NUMERICAL INVESTIGATION OF FLOW FIELDS AND FORCES FOR 2-D SQUEEZE FILM DAMPERS

A Thesis

by

TERDSAK NEADKRATOKE

Submitted to the Office of Graduate Studies of
Texas A&M University
in partial fulfillment of the requirements for the degree of

MASTER OF SCIENCE

May 2011

Major Subject: Mechanical Engineering

Numerical Investigation of Flow Fields and Forces for 2-D

Squeeze Film Dampers

Copyright 2011 Terdsak Neadkratoke

NUMERICAL INVESTIGATION OF FLOW FIELDS AND FORCES FOR 2-D SQUEEZE FILM DAMPERS

A Thesis

by

TERDSAK NEADKRATOKE

Submitted to the Office of Graduate Studies of
Texas A&M University
in partial fulfillment of the requirements for the degree of

MASTER OF SCIENCE

Approved by:

Chair of Committee,	Gerald L. Morrison
Committee Members,	Robert E. Randall
	Luis A. San Andrés
Head of Department,	Dennis O'Neal

May 2011

Major Subject: Mechanical Engineering

ABSTRACT

Numerical Investigation of Flow Fields and Forces for 2-D Squeeze Film Dampers.

(May 2011)

Terdsak Neadkratoke, B.Eng., Kasetsart University

Chair of Advisory Committee: Dr. Gerald L. Morrison

A numerical method is used to predict flow fields and forces for squeeze film dampers (SFDs). A two dimensional SFD is modeled with different amplitudes and frequencies of the journal orbiting inside the wall. In addition to the typical *circular centered orbit* (CCO) motion prescribed in most studies, orbits can vary greatly from circular to linear. The study is divided into two distinctive models including single phase flow model and two phase flow model. The single phase flow model cases including three amplitudes, i.e. 0.002, 0.001, and 0.0005 inches, and three frequencies, i.e. 10, 50, and 200 Hz, of journal motions are conducted to portray flow fields and forces and ultimately determine their relationships. The numerical prediction shows that the journal amplitude and frequency affect flow and consequently force in the SFD. The force is directly proportional to frequency and motion amplitude. Owing to the presence of cavitation in the practical SFD, the two phase flow model is also presented with the journal amplitude of 0.0002 and three frequencies of 10, 50, and 100 Hz, respectively. The ambient pressure condition was set up for numerical processing ranging from 0.001 Mpa to 100 Mpa. The results indicate that the operating pressure has an integral role in suppressing the presence of the cavitation. The caviation disappears if the operating pressure is high enough above the vapor pressure of the lubricant.

DEDICATION

To my family and close friends

ACKNOWLEDGEMENTS

I would like to express my appreciation to my advisors. Thanks to Dr. Gerald Morrison for his patience and insightful guidance. I am also grateful to my academic committee members, Dr. Robert Randall and Dr. Luis San Andrés, for their valuable time and helpful guidance.

Acknowledgements should also go to my colleagues, Aarthi Sekaran and Milind Khandare, who also work under the supervision of Dr. Morrison for their valuable discussions with me. I also would like to thank Dr. Sang Hyun Park who provided his precious instruction manual for my study.

Finally, thanks to my father and mother for their encouragement and to my siblings for their support.

NOMENCLATURE

c	SFD radial clearance [L]
CCO	Circular centered orbit
$C_{1\varepsilon}, C_{2\varepsilon}, C_{\mu}$	Constant in eq. (3) and (4)
F_d	Drag force, [N]
Fe	Frequency, [Hz]
G_b	Defined by eq. (8)
G_k	Defined by eq. (5)
g_i	Gravity in i-direction [L/T^2]
h	Dynamic film thickness [L]
k	Turbulent kinetic energy
M_t	Defined by eq. (10)
n	Number of phase
P	Pressure [N/m^2]
Pr_t	Turbulent Prandtl number
Re	Reynolds number
Re_s	Squeeze film Reynolds number
S_k, S_ε	User defined source term
T	Temperature [K]

u, v	Velocity [L/T]
$\overline{u}, \overline{v}$	Mean velocity [L/T]
u', v'	Fluctuation velocity [L/T]

Greek Symbol

μ	Dynamic viscosity [M/LT]
ρ	Fluid density [M/L^3]
α_k	Volume fraction of phase k
ϕ	Scalar quantity
ε	Rate of dissipation
θ	Polar coordinate in azimuthal direction

Subscripts

i, j	Direction
m	Mixture
p	Secondary phase
k	Turbulent kinetic energy
ε	Rate of dissipation

TABLE OF CONTENTS

Page

ABSTRACT iii

DEDICATION iv

ACKNOWLEDGEMENTS v

NOMENCLATURE vi

TABLE OF CONTENTS viii

LIST OF FIGURES x

LIST OF TABLES xxiv

CHAPTER

I INTRODUCTION 1

1.1 Background 1
1.2 Literature Review 2
1.3 Objective 6

II NUMERICAL MODEL AND PROCEDURE 7

2.1 Governing Equation 7
2.2 The Standard k-ε Model 8
2.3 Multiphase Flow Modeling 11
2.4 User Defined Function and Dynamic Mesh Method 15
2.5 The Simplified Model, Material Properties, and Boundary Conditions 16
2.6 Numerical Method of Solution 17

III SINGLE PHASE FLOW IN SQUEEZE FILM DAMPERS 19

3.1 Description of Problem 19
3.2 Grid Independence Study 20
3.3 Time Independence Study 36

CHAPTER Page

3.4 The Fluent Solution in Comparison to Reynolds Equation Solutions and Reynolds Equation with Fluid Inertia Solutions 47
3.5 The Pressure Fields 75
3.6 The Velocity Fields 81
3.7 The Drag Forces 93

IV MULTIPHASE FLOW IN SQUEEZE FILM DAMPERS 97

4.1 Description of Problem 97
4.2 Grid and Time Independence 98
4.3 Pressure Fields 98
4.4 Velocity Fields 115
4.5 The Volume Fraction of the Vapor 140
4.6 The Drag Forces 152

V SUMMARY AND CONCLUSION 158

REFERENCES 160

APPENDIX A 164

VITA 167

LIST OF FIGURES

FIGURE		Page
1.1	Typical squeeze film damper (SFD) configuration	1
2.1	The simplified model of a squeeze film damper	16
3.1	2-D simulated geometry of the SFD	19
3.2	The magnified geometry with numerical grid	20
3.3	The comparison of the flow for a journal position at 270 degrees with the frequency of 10 Hz.	21
3.4	The comparison of the flow for a journal position at 315 degrees with the frequency of 10 Hz	22
3.5	The comparison of the flow for a journal position at 360 degrees with the frequency of 10 Hz	23
3.6	The comparison of the flow for a journal position at 405 degrees with the frequency of 10 Hz	24
3.7	The comparison of the flow for a journal position at 450 degrees with the frequency of 10 Hz	25
3.8	The comparison of the flow for a journal position at 270 degrees with the frequency of 100 Hz	26
3.9	The comparison of the flow for a journal position at 315 degrees with the frequency of 100 Hz	27
3.10	The comparison of the flow for a journal position at 360 degrees with the frequency of 100 Hz	28
3.11	The comparison of the flow for a journal position at 405 degrees with the frequency of 100 Hz	29
3.12	The comparison of the flow for a journal position at 450 degrees with the frequency of 100 Hz	30

FIGURE Page

3.13 The comparison of the flow for a journal position at 270 degrees with the frequency of 500 Hz 31
3.14 The comparison of the flow for a journal position at 315 degrees with the frequency of 500 Hz 32
3.15 The comparison of the flow for a journal position at 360 degrees with the frequency of 500 Hz 33
3.16 The comparison of the flow for a journal position at 405 degrees with the frequency of 500 Hz 34
3.17 The comparison of the flow for a journal position at 450 degrees with the frequency of 500 Hz 35
3.18 The comparison of the flow for a journal position at 270 degrees with the frequency of 10 Hz 37
3.19 The comparison of the flow for a journal position at 315 degrees with the frequency of 10 Hz 38
3.20 The comparison of the flow for a journal position at 360 degrees with the frequency of 10 Hz 39
3.21 The comparison of the flow for a journal position at 405 degrees with the frequency of 10 Hz 40
3.22 The comparison of the flow for a journal position at 450 degrees with the frequency of 10 Hz 41
3.23 The comparison of the flow for a journal position at 270 degrees with the frequency of 500 Hz 42
3.24 The comparison of the flow for a journal position at 315 degrees with the frequency of 500 Hz 43
3.25 The comparison of the flow for a journal position at 360 degrees with the frequency of 500 Hz 44
3.26 The comparison of the flow for a journal position at 405 degrees with the frequency of 500 Hz 45

FIGURE Page

3.27 The comparison of the flow for a journal position at 450 degrees with the frequency of 500 Hz 46
3.28 The positions of the journal's center for pressure comparison 48
3.29 Pressure comparison for Fe = 200 Hz (Re_s = 10.13), e = 0.002 inches: a) Fluent b) Reynolds equation c) Reynolds equation with fluid inertia effect 48
3.30 Pressure comparison for Fe = 200 Hz (Re_s = 10.13), e = 0.001 inches: a) Fluent b) Reynolds equation c) Reynolds equation with fluid inertia effect 49
3.31 Pressure comparison for Fe = 200 Hz (Re_s = 10.13), e = 0.0005 inches: a) Fluent b) Reynolds equation c) Reynolds equation with fluid inertia effect 49
3.32 Pressure comparison for Fe = 50 Hz (Re_s = 2.53), e = 0.002 inches: a) Fluent b) Reynolds equation c) Reynolds equation with fluid inertia effect 51
3.33 Pressure comparison for Fe = 50 Hz (Re_s = 2.53), e = 0.001 inches: a) Fluent b) Reynolds equation c) Reynolds equation with fluid inertia effect 52
3.34 Pressure comparison for Fe = 50 Hz (Re_s = 2.53), e = 0.0005 inches: a) Fluent b) Reynolds equation c) Reynolds equation with fluid inertia effect 52
3.35 Pressure comparison for Fe = 10 Hz (Re_s = 0.51), e = 0.002 inches: a) Fluent b) Reynolds equation c) Reynolds equation with fluid inertia effect 54
3.36 Pressure comparison for Fe = 10 Hz (Re_s = 0.51), e = 0.001 inches: a) Fluent b) Reynolds equation c) Reynolds equation with fluid inertia effect 54

FIGURE Page

3.37 Pressure comparison for Fe = 10 Hz (Re_s = 0.51), e = 0.0005 inches: a) Fluent b) Reynolds equation c) Reynolds equation with fluid inertia effect 55

3.38 Pressures at different times (angles) for Fluent solutions, $\theta_{Fluent} = \pi$, Fe = 200 Hz (Re_s = 10.13)..... 56

3.39 Pressures at different times (angles) for Fluent solutions, $\theta_{Fluent} = \pi$, Fe = 50 Hz (Re_s = 2.53)..... 57

3.40 Pressures at different times (angles) for Fluent solutions, $\theta_{Fluent} = \pi$, Fe = 10 Hz (Re_s = 0.51)..... 57

3.41 Pressures at different times (angles) for Reynolds equations, $\theta_{Reynolds} = \pi/2$, Fe = 200 Hz (Re_s = 10.13)..... 58

3.42 Pressures at different times (angles) for Reynolds equations, $\theta_{Reynolds} = \pi/2$, Fe = 50 Hz (Re_s = 2.53)..... 58

3.43 Pressures at different times (angles) for Reynolds equations, $\theta_{Reynolds} = \pi/2$, Fe = 10 Hz (Re_s = 0.51)..... 59

3.44 Pressures at different times (angles) for Reynolds equations with inertia, $\theta_{Reynolds} = \pi$, Fe = 200 Hz (Re_s = 10.13)..... 59

3.45 Pressures at different times (angles) for Reynolds equations with inertia, $\theta_{Reynolds} = \pi$, Fe = 50 Hz (Re_s = 2.53)..... 60

3.46 Pressures at different times (angles) for Reynolds equations with inertia, $\theta_{Reynolds} = \pi$, Fe = 10 Hz (Re_s = 0.51)..... 60

3.47 Angle difference ($Angle_{Reynolds\ eqn} - Angle_{Reynolds\ eqn\ with\ inertia}$) for the location of max/min pressure 61

3.48 Angle difference ($Angle_{Reynolds\ eqn} - Angle_{Fluent}$) for the location of max/min pressure 61

3.49 Positive maximum pressure comparison..... 64

3.50 Negative maximum pressure comparison 64

3.51 $P_{max,Fluent}/P_{max,Reynolds}$ comparison; a) Re b) Re_s 65

FIGURE Page

3.52 Fluent solutions for *Fe* = 200 Hz, *e* = 0.002 inches; a) velocity vector b) contours of turbulent intensity 67
3.53 Fluent solutions for *Fe* = 200 Hz, *e* = 0.001 inches; a) velocity vector b) contours of turbulent intensity 67
3.54 Fluent solutions for *Fe* = 200 Hz, *e* = 0.0005 inches; a) velocity vector b) contours of turbulent intensity 68
3.55 Fluent solutions for *Fe* = 50 Hz, *e* = 0.002 inches; a) velocity vector b) contours of turbulent intensity 68
3.56 Fluent solutions for *Fe* = 50 Hz, *e* = 0.001 inches; a) velocity vector b) contours of turbulent intensity 69
3.57 Fluent solutions for *Fe* = 50 Hz, *e* = 0.0005 inches; a) velocity vector b) contours of turbulent intensity 69
3.58 Fluent solutions for *Fe* = 10 Hz, *e* = 0.002 inches; a) velocity vector b) contours of turbulent intensity 70
3.59 Fluent solutions for *Fe* = 10 Hz, *e* = 0.001 inches; a) velocity vector b) contours of turbulent intensity 70
3.60 Fluent solutions for *Fe* = 10 Hz, *e* = 0.0005 inches; a) velocity vector b) contours of turbulent intensity 71
3.61 Velocity profile at $\tau = \pi/2$, $\theta = \pi/2$ 72
3.62 Velocity profile comparison at $\tau = \pi/2$, $\theta = \pi/2$, *e* = 0.002 inches ($\varepsilon = 0.4$) 72
3.63 Velocity profile comparison at $\tau = \pi/2$, $\theta = \pi/2$, *e* = 0.001 inches ($\varepsilon = 0.2$) 73
3.64 Velocity profile comparison at $\tau = \pi/2$, $\theta = \pi/2$, *e* = 0.0005 inches ($\varepsilon = 0.1$) 73
3.65 The pressure(Pa) field at a frequency of 10 Hz and an amplitude of 0.002 inches..... 76

FIGURE Page

3.66 The pressure(Pa) field at a frequency of 50 Hz and an amplitude of 0.002 inches 76
3.67 The pressure(Pa) field at a frequency of 200 Hz and an amplitude of 0.002 inches 77
3.68 The pressure(Pa) field at a frequency of 10 Hz and an amplitude of 0.001 inches 78
3.69 The pressure(Pa) field at a frequency of 50 Hz and an amplitude of 0.001 inches 79
3.70 The pressure(Pa) field at a frequency of 200 Hz and an amplitude of 0.001 inches 79
3.71 The pressure(Pa) field at a frequency of 10 Hz and an amplitude of 0.0005 inches 80
3.72 The pressure(Pa) field at a frequency of 50 Hz and an amplitude of 0.0005 inches 80
3.73 The pressure(Pa) field at a frequency of 200 Hz and an amplitude of 0.0005 inches 81
3.74 The x-velocity(m/s) field at a frequency of 10 Hz and an amplitude of 0.002 inches 82
3.75 The x-velocity(m/s) field at a frequency of 50 Hz and an amplitude of 0.002 inches 83
3.76 The x-velocity(m/s) field at a frequency of 200 Hz and an amplitude of 0.002 inches 83
3.77 The x-velocity(m/s) field at a frequency of 10 Hz and an amplitude of 0.001 inches 84
3.78 The x-velocity(m/s) field at a frequency of 50 Hz and an amplitude of 0.001 inches 85
3.79 The x-velocity(m/s) field at a frequency of 200 Hz and an amplitude of 0.001 inches 85

FIGURE Page

3.80 The x-velocity(m/s) field at a frequency of 10 Hz and an amplitude of 0.0005 inches 86
3.81 The x-velocity(m/s) field at a frequency of 50 Hz and an amplitude of 0.0005 inches 86
3.82 The x-velocity(m/s) field at a frequency of 200 Hz and an amplitude of 0.0005 inches 87
3.83 The y-velocity(m/s) field at a frequency of 10 Hz and an amplitude of 0.002 inches 88
3.84 The y-velocity(m/s) field at a frequency of 50 Hz and an amplitude of 0.002 inches 89
3.85 The y-velocity(m/s) field at a frequency of 200 Hz and an amplitude of 0.002 inches 89
3.86 The y-velocity(m/s) field at a frequency of 10 Hz and an amplitude of 0.001 inches 90
3.87 The y-velocity(m/s) field at a frequency of 50 Hz and an amplitude of 0.001 inches 91
3.88 The y-velocity(m/s) field at a frequency of 200 Hz and an amplitude of 0.001 inches 91
3.89 The y-velocity(m/s) field at a frequency of 10 Hz and an amplitude of 0.0005 inches 92
3.90 The y-velocity(m/s) field at a frequency of 50 Hz and an amplitude of 0.0005 inches 92
3.91 The y-velocity(m/s) field at a frequency of 200 Hz and an amplitude of 0.0005 inches 93
3.92 The drag forces/unit(N/m) on the journal moving with the different frequencies and an amplitudes 94
3.93 The maximum forces(N/m) on the journal moving with the different frequencies and an amplitudes 96

FIGURE Page

4.1 2-D simulated geometry of the SFD 97
4.2 The magnified geometry with numerical grid..... 98
4.3 The pressure(Pa) field at a frequency of 10 Hz and an amplitude of 0.002 inches (Single phase flow) 99
4.4 The pressure field at a frequency of 10 Hz, an amplitude of 0.002 inches, and an operating pressure of 0.001 MPa..... 100
4.5 The pressure(Pa) field at a frequency of 10 Hz, an amplitude of 0.002 inches, and an operating pressure of 0.01 MPa..... 101
4.6 The pressure(Pa) field at a frequency of 10 Hz, an amplitude of 0.002 inches, and an operating pressure of 0.05 MPa..... 102
4.7 The pressure(Pa) field at a frequency of 10 Hz, an amplitude of 0.002 inches, and an operating pressure of 0.1 MPa..... 103
4.8 The pressure(Pa) field at a frequency of 10 Hz, an amplitude of 0.002 inches and an operating pressure of 0.5 MPa..... 103
4.9 The pressure(Pa) field at a frequency of 10 Hz, an amplitude of 0.002 inches, and an operating pressure of 1 MPa..... 104
4.10 The pressure(Pa) field at a frequency of 10 Hz, an amplitude of 0.002 inches and an operating pressure of 10 MPa..... 104
4.11 The pressure(Pa) field at a frequency of 10 Hz, an amplitude of 0.002 inches, and an operating pressure of 50 MPa..... 105
4.12 The pressure(Pa) field at a frequency of 10 Hz, an amplitude of 0.002 inches, and an operating pressure of 100 MPa..... 105
4.13 The pressure(Pa) field at a frequency of 50 Hz and an amplitude of 0.002 inches (Single phase flow).. 106
4.14 The pressure(Pa) field at a frequency of 50 Hz, an amplitude of 0.002 inches, and an operating pressure of 0.001 MPa 108
4.15 The pressure(Pa) field at a frequency of 50 Hz, an amplitude of 0.002 inches, and an operating pressure of 1 MPa 108

FIGURE Page

4.16 The pressure(Pa) field at a frequency of 50 Hz, an amplitude of 0.002 inches, and an operating pressure of 10 MPa 109
4.17 The pressure(Pa) field at a frequency of 50 Hz, an amplitude of 0.002 inches, and an operating pressure of 50 MPa 110
4.18 The pressure(Pa) field at a frequency of 50 Hz, an amplitude of 0.002 inches, and an operating pressure of 100 MPa 110
4.19 The pressure(Pa) field at a frequency of 100 Hz and an amplitude of 0.002 inches (Single phase flow).. 112
4.20 The pressure(Pa) field at a frequency of 100 Hz, an amplitude of 0.002 inches, and an operating pressure of 0.001 MPa 112
4.21 The pressure(Pa) field at a frequency of 100 Hz, an amplitude of 0.002 inches, and an operating pressure of 10 MPa 113
4.22 The pressure(Pa) field at a frequency of 100 Hz, an amplitude of 0.002 inches, and an operating pressure of 50 MPa 113
4.23 The pressure(Pa) field at a frequency of 100 Hz, an amplitude of 0.002 inches, and an operating pressure of 100 MPa 114
4.24 The x-velocity(m/s) field at a frequency of 10 Hz and an amplitude of 0.002 inches (Single phase flow). 116
4.25 The x-velocity(m/s) field at a frequency of 10 Hz, an amplitude of 0.002 inches, and an operating pressure of 0.001 MPa 117
4.26 The x-velocity(m/s) field at a frequency of 10 Hz, an amplitude of 0.002 inches, and an operating pressure of 0.01 MPa 117
4.27 The x-velocity(m/s) field at a frequency of 10 Hz, an amplitude of 0.002 inches, and an operating pressure of 0.05 MPa 118
4.28 The x-velocity(m/s) field at a frequency of 10 Hz, an amplitude of 0.002 inches, and an operating pressure of 0.1 MPa 118
4.29 The x-velocity(m/s) field at a frequency of 10 Hz, an amplitude of 0.002 inches, and an operating pressure of 0.5 MPa 119

FIGURE Page

4.30 The x-velocity(m/s) field at a frequency of 10 Hz, an amplitude of 0.002 inches, and an operating pressure of 1 MPa 119
4.31 The x-velocity(m/s) field at a frequency of 10 Hz, an amplitude of 0.002 inches, and an operating pressure of 10 MPa 120
4.32 The x-velocity(m/s) field at a frequency of 10 Hz, an amplitude of 0.002 inches, and an operating pressure of 50 MPa 120
4.33 The x-velocity(m/s) field at a frequency of 10 Hz, an amplitude of 0.002 inches, and an operating pressure of 100 MPa 121
4.34 The x-velocity(m/s) field at a frequency of 50 Hz and an amplitude of 0.002 inches (Single phase flow)..... 122
4.35 The x-velocity(m/s) field at a frequency of 50 Hz, an amplitude of 0.002 inches, and an operating pressure of 0.001 MPa 122
4.36 The x-velocity(m/s) field at a frequency of 50 Hz, an amplitude of 0.002 inches, and an operating pressure of 1 MPa 123
4.37 The x-velocity(m/s) field at a frequency of 50 Hz, an amplitude of 0.002 inches, and an operating pressure of 10 MPa 123
4.38 The x-velocity(m/s) field at a frequency of 50 Hz, an amplitude of 0.002 inches, and an operating pressure of 50 MPa 124
4.39 The x-velocity(m/s) field at a frequency of 50 Hz, an amplitude of 0.002 inches, and an operating pressure of 100 MPa 124
4.40 The x-velocity(m/s) field at a frequency of 100 Hz and an amplitude of 0.002 inches (Single phase flow)..... 125
4.41 The x-velocity(m/s) field at a frequency of 100 Hz, an amplitude of 0.002 inches, and an operating pressure of 0.001 MPa 126
4.42 The x-velocity(m/s) field at a frequency of 100 Hz, an amplitude of 0.002 inches, and an operating pressure of 10 MPa 126
4.43 The x-velocity(m/s) field at a frequency of 100 Hz, an amplitude of 0.002 inches, and an operating pressure of 50 MPa 127

FIGURE Page

4.44 The x-velocity(m/s) field at a frequency of 100 Hz, an amplitude of 0.002 inches, and an operating pressure of 100 MPa 127
4.45 The y-velocity(m/s) field at a frequency of 10 Hz and an amplitude of 0.002 inches (Single phase flow). 129
4.46 The y-velocity(m/s) field at a frequency of 10 Hz, an amplitude of 0.002 inches, and an operating pressure of 0.001 MPa 129
4.47 The y-velocity(m/s) field at a frequency of 10 Hz, an amplitude of 0.002 inches, and an operating pressure of 0.01 MPa 130
4.48 The y-velocity(m/s) field at a frequency of 10 Hz, an amplitude of 0.002 inches, and an operating pressure of 0.05 MPa 130
4.49 The y-velocity(m/s) field at a frequency of 10 Hz, an amplitude of 0.002 inches, and an operating pressure of 0.1 MPa 131
4.50 The y-velocity(m/s) field at a frequency of 10 Hz, an amplitude of 0.002 inches, and an operating pressure of 0.5 MPa 131
4.51 The y-velocity(m/s) field at a frequency of 10 Hz, an amplitude of 0.002 inches, and an operating pressure of 1 MPa 132
4.52 The y-velocity(m/s) field at a frequency of 10 Hz, an amplitude of 0.002 inches, and an operating pressure of 10 MPa 132
4.53 The y-velocity(m/s) field at a frequency of 10 Hz, an amplitude of 0.002 inches, and an operating pressure of 50 MPa 133
4.54 The y-velocity(m/s) field at a frequency of 10 Hz, an amplitude of 0.002 inches, and an operating pressure of 100 MPa 133
4.55 The y-velocity(m/s) field at a frequency of 50 Hz and an amplitude of 0.002 inches (Single phase flow) 134
4.56 The y-velocity(m/s) field at a frequency of 50 Hz and an amplitude of 0.002 inches and an operating pressure of 0.001 MPa 135
4.57 The y-velocity(m/s) field at a frequency of 50 Hz, an amplitude of 0.002 inches, and an operating pressure of 1 MPa 135

FIGURE Page

4.58 The y-velocity(m/s) field at a frequency of 50 Hz, an amplitude of 0.002 inches, and an operating pressure of 10 MPa 136

4.59 The y-velocity(m/s) field at a frequency of 50 Hz, an amplitude of 0.002 inches, and an operating pressure of 50 MPa 136

4.60 The y-velocity(m/s) field at a frequency of 50 Hz, an amplitude of 0.002 inches, and an operating pressure of 100 MPa 137

4.61 The y-velocity(m/s) field at a frequency of 100 Hz and an amplitude of 0.002 inches (Single phase flow) 138

4.62 The y-velocity(m/s) field at a frequency of 100 Hz, an amplitude of 0.002 inches, and an operating pressure of 0.001 MPa 138

4.63 The y-velocity(m/s) field at a frequency of 100 Hz, an amplitude of 0.002 inches, and an operating pressure of 10 MPa 139

4.64 The y-velocity(m/s) field at a frequency of 100 Hz, an amplitude of 0.002 inches, and an operating pressure of 50 MPa 139

4.65 The y-velocity(m/s) field at a frequency of 100 Hz, an amplitude of 0.002 inches, and an operating pressure of 100 MPa 140

4.66 The volume fraction of the vapor at a frequency of 10 Hz, an amplitude of 0.002 inches and an operating pressure of 0.001 MPa 142

4.67 The volume fraction of the vapor at a frequency of 10 Hz, an amplitude of 0.002 inches, and an operating pressure of 0.01 MPa 142

4.68 The volume fraction of the vapor at a frequency of 10 Hz, an amplitude of 0.002 inches, and an operating pressure of 0.05 MPa 143

4.69 The volume fraction of the vapor at a frequency of 10 Hz, an amplitude of 0.002 inches, and an operating pressure of 0.1 MPa 143

4.70 The volume fraction of the vapor at a frequency of 10 Hz, an amplitude of 0.002 inches, and an operating pressure of 0.5 MPa 144

4.71 The volume fraction of the vapor at a frequency of 10 Hz, an amplitude of 0.002 inches, and an operating pressure of 1 MPa 144

FIGURE Page

4.72 The volume fraction of the vapor at a frequency of 10 Hz, an amplitude of 0.002 inches, and an operating pressure of 10 MPa 145
4.73 The volume fraction of the vapor at a frequency of 10 Hz, an amplitude of 0.002 inches, and an operating pressure of 50 MPa 145
4.74 The volume fraction of the vapor at a frequency of 10 Hz, an amplitude of 0.002 inches, and an operating pressure of 100 MPa 146
4.75 The volume fraction of the vapor at a frequency of 50 Hz, an amplitude of 0.002 inches, and an operating pressure of 0.001 MPa 147
4.76 The volume fraction of the vapor at a frequency of 50 Hz, an amplitude of 0.002 inches, and an operating pressure of 1 MPa 147
4.77 The volume fraction of the vapor at a frequency of 50 Hz, an amplitude of 0.002 inches, and an operating pressure of 10 MPa 148
4.78 The volume fraction of the vapor at a frequency of 50 Hz, an amplitude of 0.002 inches, and an operating pressure of 50 MPa 148
4.79 The volume fraction of the vapor at a frequency of 50 Hz, an amplitude of 0.002 inches, and an operating pressure of 100 MPa 149
4.80 The volume fraction of the vapor at a frequency of 100 Hz, an amplitude of 0.002 inches, and an operating pressure of 0.001 MPa 150
4.81 The volume fraction of the vapor at a frequency of 100 Hz, an amplitude of 0.002 inches, and an operating pressure of 10 MPa 150
4.82 The volume fraction of the vapor at a frequency of 100 Hz, an amplitude of 0.002 inches, and an operating pressure of 50 MPa 151
4.83 The volume fraction of the vapor at a frequency of 100 Hz, an amplitude of 0.002 inches, and an operating pressure of 100 MPa 151
4.84 The drag forces(N/m) for the single phase flow. 153
4.85 The drag forces(N/m) for the multiphase flow at the frequency of 10 Hz (all operating pressure cases) 154

FIGURE Page

4.86 The drag forces(N/m) for the multiphase flow at the frequency of 10 Hz (certain operating pressure cases) 154
4.87 The drag forces(N/m) for the multiphase flow at the frequency of 50 Hz 155
4.88 The drag forces(N/m) for the multiphase flow at the frequency of 100 Hz 155

LIST OF TABLES

TABLE		Page
3.1	Maximum pressure and turbulence intensity	63
3.2	Maximum and minimum pressures at three different frequencies and amplitudes..	81
3.3	The maximum positive/negative drag forces for all cases.	95
4.1	The maximum and minimum pressures for single phase flow cases	115
4.2	The maximum and minimum pressures for multiphase flow cases	115
4.3	The maximum volume fraction of vapor for multiphase flow cases	152
4.4	The maximum forces for single phase flow cases	156
4.5	The maximum forces for multiphase flow cases and the frequency of 10 Hz.	156
4.6	The maximum forces for multiphase flow cases and the frequency of 50 Hz.	157
4.7	The maximum forces for multiphase flow cases and the frequency of 100 Hz.	157

CHAPTER I

INTRODUCTION

1.1 Background

A Squeeze Film Damper (SFD) is a bearing assembly used to provide external damping in turbomachinery such as aircraft gas turbines supported on rolling element bearings and hydrocarbon compressors. An SFD aids to reduce the vibration level owing to synchronous imbalanced response of the rotor-bearing system at traversed critical speeds and to suppress subsynchronous rotor instabilities. A typical SFD (Figure 1.1) consists of a cylindrical housing, a journal represented by the shaft & ball bearing assembly, a small gap filled with lubricant and an anti-rotation pin preventing the journal from rotating. In operation, the dynamic vibratory motion of the journal squeezes the lubricant film, thus generating hydrodynamic pressures and forces contributing to the dissipation of the mechanical energy.

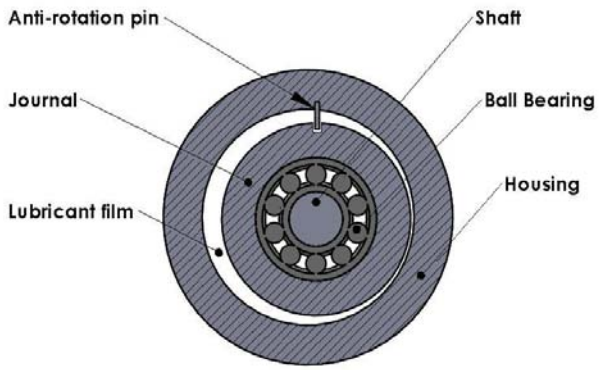

Figure 1.1 Typical squeeze film damper (SFD) configuration

This thesis follows the style of ASME Journal of Tribology.

1.2 Literature Review

The development of SFDs is based upon both experimental measurements and theoretical calculations (Renolds-equation-based solutions, for example) to gain insight into their characteristics. Zeidan et al. [1] summarized a comprehensive report of the design and application of squeeze film dampers detailing the history, theory, and practical limitations. In addition, Pietra and Adiletta [2-3] published articles summarizing the squeeze film damper over four decades of investigations. According to these reports, the study of SFDs mainly focused on the dynamic behavior of rotor-support systems equipped with them such as imbalance response of the rigid/flexible rotor supported on them. In addition, sealing and feeding-geometry effects and the effects of certain phenomena such as air entrainment, lubricant vapor cavitation, and fluid inertia are also taken into account to gain insight into their features and to improve their performance.

For the study of the dynamic behavior of rotor-bearing system equipped with SFDs, the theory of force coefficients including the direct and cross-coupled damping and inertia force coefficients were introduced by Vance [4]. Examples of interesting research follow. Diaz and San Andrés [5] presented two methods for the identification of damping force coefficient in rotor-damper system. The first method applied a least-square curve fitting to the damping force (LS orbit method), while the second determined the elliptic orbit that best approximated the actual one (filtered orbit method). Due to its practical implementation, the filtered orbit method was applied to identify the damping force coefficients from measurements of the synchronous response on a test rotor mounted on off-center SFDs. It was found that identified system damping coefficients are not a function of the rotor motion.

El-Shafei and Eranki [6] presented the technique of equivalent linearization to perform nonlinear dynamic analysis of SFDs supported rotors using linear rotor-dynamic methods. This aided to lessen the difficulty and time consuming tasks of solving nonlinear equations. Lubell and San Andrés [7] presented a test apparatus and

measurements of the imbalance response of the rotor-bearing system supported on squeeze film dampers. It was found that synchronous rotor response of a rotor-bearing system at critical speeds is linearly dependent to the imbalance level and further show that the presence of little lubricant, just a few drops, can enable SDFs to attenuate rotor vibrations.

The study of rotordynamics behavior also plays an integral role in improvements and innovative designs such as integral squeeze film dampers designed for a reduction in dimension with respect to conventional SFDs. De Santiago and San Andrés [8-10] presented an extensive experimentation for integral squeeze film dampers (ISFDs) to verify their dynamic forced performance and to determine their reliability for application on high performance turbomachinery. Measurements of the synchronous response of a test rotor supported on ISFDs were presented. System damping coefficients for the rotor motions are extracted from amplification factors of the synchronous response. The results confirmed the damping capacity of ISFDs to reduce rotor vibrations.

The effects of sealing and feeding-geometry are also addressed in studies of SFDs. Arauz and San Andrés [11-13] investigated experimentally the effects a circumferential feeding groove on the dynamic force response. Open end and sealed damper configurations are tested for different groove depths, journal orbit radii, whirl frequency and fluid viscosity conditions. It was found that the use of end seals is an effective method to reduce leakage and increase the performance of the SFD and the dynamic pressures detected at the groove also contributed to the damping characteristics of the SFD. The results also showed the effect of groove depth on the forced response of SFDs. Arauz and San Andrés [14] also studied the effect of a circumferential feeding groove on the damper force response presenting a model for short open-end, uncavitated dampers that included the fluid flow at the groove volume. It was found that the groove with depths as large as ten times the radial film clearance generated significantly the damping force and dynamic pressures at the shallow groove were comparable to those at the film lands. San Andrés [15] presented the analysis of short squeeze film dampers

with a central groove. It was found that an SFD with the two lands separated by a central groove behaved like an SFD with a single land whose length was the sum of the two land lengths and the groove width.

In addition, the effect of certain phenomena such as air entrainment, fluid initia, and lubricant vapor cavitation must be taken into account when studying SFDs. Diaz and San Andrés [16-17] presented experiments and reported pressures in the squeeze film zone as journal at motion for increasing content of air in a controlled lubricant mixture (from pure oil to 100 percent air). The results show there is a decrease in pressure resulting in the reduction of SFD damping force thanks to increasing air content in the lubricant. San Andrés and Diaz [18] presented measurements of dynamic film pressures and high speed-speed photographs (video recordings) of the flow field in a SFD operating with natural air entrainment for an open-ended damper with moderately large journal orbital motions ($\varepsilon_c \rightarrow$ 0.55-0.75) and increasing whirl frequencies (8.33-50 Hz). The results show that air entrainment results in the formation of irregular gas fingering and striation patterns in SFDs with low feed pressure. A high feed pressure and low operating speeds could delay air entrainment in SFD operations. Tao *et al*. [19] proposed a continuum model describing the motion of a bubbly fluid in an open ended SFD operating with circular centered journal orbits. The predictions for dynamic pressures and fluid film forces agree well with experimental measurements conducted on a SFD test rig operating with a controlled air in oil mixture.

Zeidan and Vance [20] present a controlled orbit test rig operating with increasing speeds and classified the possible operation of squeeze film, with regard to the rupture as 5 regimes i.e. uncavitated 2π-film, cavitation bubble following the journal, oil-air mixture, vapor cavitation, and vapor and gaseous cavitation, respectively. San Andrés [21] presented theoretical and experimental comparisons for damping coefficients of short-length open squeeze film damper. The film forces are directly proportional to whirl frequencies and lubricant viscosity. The test damping coefficient correlate well with the π-film cavitation model at the high frequency reflecting the great

influence of cavitation on the squeeze film force. Robinson *et al*. [22] describe a test rig for the measurement of rotordynamic coefficients of generic fluid film bearing elements. It was found that damping force coefficients for a short length, open ended SFD obtained from the experiment agreed well with theoretical predictions. However, most test inertia force coefficients are larger than theoretical predictions since the test SFD did not present cavitation regime that the theory assumed. San Andrés and Vance [23] presented the effect of inertia on the performance of squeeze film damper supported rotor. The theoretical results show that fluid inertia in SFDs under certain operating conditions and bearing characteristics significantly impact the SFD performance.

Although the experiment is the universal and fundamental approach in the research and development of SFDs, the numerical investigation is also applied to study the squeeze film flow in the SFD. Chen and Hahn [24] investigated the suitability of applying CFD to Squeeze Film Dampers by employing a 2D steady state laminar flow model based upon the Reynolds equation to validate the CFD results. It was found that the inertia effects predicted by CFD agreed well with results in the literature. The results confirmed the assumption of constant pressure across the film. It was concluded that CFD software is capable of accurately solving steady state hydrodynamic lubrication problems.

Xing *et al*. [25] use the CFD-ACE+ commercial software based on Navier-Stokes equations (NSE) to show the effect of inertia in a squeeze film zone for short and long dampers. The inertia coefficients derived from a linearized dynamic theory [4] are compared to those from Reynolds equation based models. The results show that there are some differences between these two approaches due to the three-dimensional effects included in the NSE. Besides, Xing *et al*. [26] also used the CFD-ACE+ commercial software based on Navier-Stokes equations (NSE) to study the effect of Gaseous cavitation. The pressure profiles, velocities and damping coefficients generated from a steady-state, circular centerd orbit SFD operating with different amounts of gas mass fraction were numerically calculated and presented comparing to those from established

models such as the π-film cavitation model. It was found that the results, in general, agreed well with the simpler theoretical and experimental works. Besides, the study was extended to using the damping coefficients obtained from previous works to further study the effects of gaseous cavitation on the behavior of SFDs [27]. By applying the methods called the point mass rotor model and the direct numerical simulation, the trajectory of the rotor was determined for both steady-state circular centered orbit and transient motion. It was found that the presence of gaseous cavitation resulted in the different dynamics behaviors of SFDs. However, it was noted from this study that the cavitation due to a phase change in the lubricant, or vapor cavitation, and fluid inertia were disregard.

1.3 Objective

In this study, the Fluent software package [28] is used to calculate the hydrodynamic forces generated by the fluid in the squeeze film damper using the "dynamic mesh" technique. A two dimensional SFD is modeled with operation of different amplitudes and frequencies of an infinitely long journal motion. Computational flow depicts the parameters, i.e., pressure and velocity within the squeeze zone due to the motion of the journal in the SFD. The result of this study will enable better understanding of the squeeze film flow including lubricant vapor cavitation corresponding to feed pressure. This will be useful for the prediction of the lubricant pressure to avoid the chance of cavitation in the SFD.

CHAPTER II

NUMERICAL MODEL AND PROCEDURE

Numerical methods can provide the information that is difficult to obtain by experimental means. In addition, the increases in computation power of the desktop computers had made it economical to optimize the design parameters based on numerical analyses. Based on the number of equations to be solved, turbulence modeling approaches can be broadly classified as one-equation, two-equation, and second-moment closure models. Development of faster computers with more memory makes it feasible to compute more details of flow analysis. The main difficulties in predictions are proper turbulence models, including wall functions.

As mentioned before, numerical analysis was conducted to better understanding the two dimensional flow in squeeze film dampers with different amplitudes (0.0005, 0.001, and 0.002 inches) and frequencies of the journal motion, i.e 10, 50, 100, and 200 Hz. The standard k-ε model with enhanced wall treatment in FLUENT code was used to perform the calculations.

Not only is the fluid in SFDs is modeled as a single phase but to approach more applicable a two phase model was employed. The multiphase flow model was also performed in order to depict the cavitation phenomenon due to a phase change of the fluid in SFDs when experiencing the pressure below its vapor pressure.

2.1 Governing Equation

In Reynolds averaging, the solution variables in the instantaneous Navier-Stokes equations are decomposed into the mean and fluctuating components. For the velocity components: $u_i = \overline{u_i} + u_i'$ where $\overline{u_i}$ and u_i' are the mean and fluctuating velocity

components. Likewise, for pressure and other scalar quantities: $\phi = \bar{\phi} + \phi'$ where ϕ denotes a scalar such as pressure, energy, or species concentration. Taking a time average to the instantaneous Navier-Stokes equations and dropping the over bar yield the ensemble-averaged equations. The continuity and momentum equations can be written in Cartesian tensor form as:

$$\frac{\partial \rho}{\partial t} + \frac{\partial}{\partial x_i}(\rho u_i) = 0 \tag{1}$$

$$\frac{\partial}{\partial t}(\rho u_i) + \frac{\partial}{\partial x_j}(\rho u_i u_j) = -\frac{\partial P}{\partial x_i} + \frac{\partial}{\partial x_j}\left[\mu\left(\frac{\partial u_i}{\partial x_j} + \frac{\partial u_j}{\partial x_i} - \frac{2}{3}\delta_{ij}\frac{\partial u_l}{\partial x_l}\right)\right] + \frac{\partial}{\partial x_j}\left(-\rho\overline{u_i' u_j'}\right) \tag{2}$$

Equations (1) and (2) are called Reynolds-Averaged Navier-Stokes (RANS) equations. Additional terms now appear that represent the effects of turbulence. These Reynolds stresses, $-\rho\overline{u_i' u_j'}$ must be modeled in order to close Eq. (2).

2.2 The Standard k-ε Model

The standard k-ε Model is also known as a two-equation closure model in which the solution of two separate transport equations allows the turbulent velocity and length scales to be independently determined. The standard k-ε model is widely used in industrial flow and heat transfer simulations because of its robustness, economy, and reasonable accuracy for a wide range of turbulent flows. It is a semi-empirical model, and the derivation of the model equations relies on phenomenological considerations and empiricism.

The standard k-ε model is a semi-empirical model based on model transport equations for the turbulence kinetic energy (k) and its dissipation rate (ε). The model transport equation for k is derived from the exact equation, while the model transport

equation for ε was obtained using physical reasoning and bears little resemblance to its mathematically exact counterpart.

In the derivation of the k-ε model, the assumption is that the flow is fully turbulent, and the effects of molecular viscosity are negligible. The standard k-ε model is therefore valid only for fully turbulent flows.

According to **FLUENT** [27], the turbulence kinetic energy, k, and its rate of dissipation, ε, are obtained from the following transport equations:

$$\frac{\partial}{\partial t}(\rho k)+\frac{\partial}{\partial x_i}(\rho k u_i)=\frac{\partial}{\partial x_j}\left[\left(\mu+\frac{u_t}{\sigma_k}\right)\frac{\partial k}{\partial x_j}\right]+G_k+G_b-\rho\varepsilon-Y_M+S_k \tag{3}$$

and

$$\frac{\partial}{\partial t}(\rho \varepsilon)+\frac{\partial}{\partial x_i}(\rho \varepsilon u_i)=\frac{\partial}{\partial x_j}\left[\left(\mu+\frac{u_t}{\sigma_\varepsilon}\right)\frac{\partial \varepsilon}{\partial x_j}\right]+C_{1\varepsilon}\frac{\varepsilon}{k}\left(G_k+C_{3\varepsilon}G_b\right)-C_{2\varepsilon}\rho\frac{\varepsilon^2}{k}+S_\varepsilon \tag{4}$$

According to the Eq. (3) and Eq. (4):

G_k represents the generation of turbulence kinetic energy due to the mean velocity gradients, defined as

$$G_k=-\rho\overline{u_i'u_i'}\frac{\partial u_j}{\partial x_i} \tag{5}$$

To evaluate G_k in a manner consistent with the Boussinesq hypothesis,

$$G_k=\mu_t S^2 \tag{6}$$

where S is the modulus of the mean rate-of-strain tensor, defined as

$$S=\sqrt{2S_{ij}S_{ij}} \tag{7}$$

G_b represents the generation of turbulence due to buoyancy, given by

$$G_b = \beta g_i \frac{\mu_t}{\mathrm{Pr}_t} \frac{\partial T}{\partial x_i} \tag{8}$$

where Pr_t is the turbulent Prandtl number for energy with a default value of 0.85 and g_i is the component of the gravitational vector in the i th direction.

The buoyancy effects on the generation of k in Eq. (3) are relatively well understood whereas the effect on ε in Eq.(4) is less clear. In FLUENT, by default, the buoyancy effects on ε are neglected simply by setting G_b to zero in the transport equation for ε.

Y_m represents the contribution of the fluctuating dilatation in compressible turbulence to the overall dissipation rate, calculated as

$$Y_m = 2\rho\varepsilon M_t^2 \tag{9}$$

where M_t is the turbulent Mach number, defined as

$$M_t = \sqrt{\frac{k}{a^2}} \tag{10}$$

where $a(\equiv \sqrt{\gamma RT})$ is the speed of sound.

This compressibility modification always takes effect when the compressible form of the ideal gas law is used.

$C_{1\varepsilon}$, $C_{2\varepsilon}$, and $C_{3\varepsilon}$ are constants. σ_k and σ_ε are the turbulent Prandtl numbers for k and ε, respectively. S_k and S_ε are user-defined source terms.

The model constants $C_{1\varepsilon}$, $C_{2\varepsilon}$, C_μ, σ_k, and σ_ε have the following default values :

$C_{1\varepsilon} = 1.44$, $C_{2\varepsilon} = 1.92$, $C_\mu = 0.09$, $\sigma_k = 1.0$, $\sigma_\varepsilon = 1.3$

The turbulent (or eddy) viscosity , μ_t, is computed by combining k and as ε follows:

$$\mu_t = \rho C_\mu \frac{k^2}{\varepsilon} \tag{11}$$

where C_μ is a constant.

The k-ε model is based upon Boussinsq's hypothesis assuming that the turbulence is assumed to be isotropic. According to Boussinesq hypothesis, it assumes, μ_t, is an isotropic scalar quantity, which is not strictly true. However, this approach performs very well and is less computational cost comparing to Reynold stress model (RSM) which is suitable for the anisotropic turbulence having dominant effect on the mean flow.

2.3 Multiphase Flow Modeling

The mixture of phase is prevalent in general flows. For this study, gas-liquid flow regime appears when pressure of the lubricant falls below vapor pressure itself resulted from the journal's movement in the SFD. Such phenomenon is known as cavitation.

In the Euler-Euler approach, the different phases are considered mathematically as interpenetrating continua. Since the volume of a phase cannot be occupied by the other phases, the concept of phasic volume fraction is addressed. These volume fractions are considered as temporally and spatially continuous functions and their sum is equal to one. Conservation equations for each phase are derived to obtain a set of equations, which have identical structure for all phases.

Among the multiphase flow models, the mixture model was chosen owing to its simplicity and having applicable concept for the study of SFDs.

As a simplified multiphase model, the mixture model described in **FLUENT** can be used to model multiphase flows where the phases move at either different velocities

or the same velocity. In some cases, the mixture model can be applied for the full Eulerian multiphase model which may not be feasible when there is a wide distribution of the particulate phase or when the interphase laws cannot be determined or their reliability is questionable. The mixture model is a simple model which can perform as well as a full multiphase model while solving a smaller number of variables than the full multiphase model.

The continuity equation for the mixture can be expressed as

$$\frac{\partial}{\partial t}(\rho_m) + \nabla.(\rho_m \vec{v}_m) = 0 \tag{12}$$

where $\vec{v}_m$ is the mass-averaged velocity:

$$\vec{v}_m = \frac{\sum_{k=1}^{n} \alpha_k \rho_k \vec{v}_k}{\rho_m} \tag{13}$$

and ρ_m is the mixture density:

$$\rho_m = \sum_{k=1}^{n} \alpha_k \rho_k \tag{14}$$

α_k is the volume fraction of phase *k*.

The momentum equation for the mixture can be determined by summing the individual momentum equations for all phases. It can be expressed as

$$\frac{\partial}{\partial t}(\rho_m \vec{v}_m) + \nabla.(\rho_m \vec{v}_m \vec{v}_m) = -\nabla p + \nabla.\left[\mu_m \left(\nabla \vec{v}_m + \nabla \vec{v}_m^T\right)\right] +$$

$$\rho_m \vec{g} + \vec{F} + \nabla.\left(\sum_{k=1}^{n} \alpha_k \rho_k \vec{v}_{dr,k} \vec{v}_{dr,k}\right) \tag{15}$$

where n is the number of phases, $\vec{F}$ is a body force, and μ_m is the viscosity of the mixture:

$$\mu_m = \sum_{k=1}^{n} \alpha_k \mu_k \tag{16}$$

$\vec{v}_{dr,k}$ is the drift velocity for secondary phase k :

$$\vec{v}_{dr,k} = \vec{v}_k - \vec{v}_m \tag{17}$$

From the continuity equation for secondary phase p, the volume fraction equation for secondary phase p can be determined:

$$\frac{\partial}{\partial t}\left(\alpha_p \rho_p\right) + \nabla.\left(\alpha_p \rho_m \vec{v}_m\right) = -\nabla.\left(\alpha_p \rho_p \vec{v}_{dr,p}\right) + \sum_{q=1}^{n}\left(\dot{m}_{qp} - \dot{m}_{pq}\right) \tag{18}$$

FLUENT describes a cavitation model as a mass transfer model in multiphase flow with the assumption that the investigated system involves only two phases (a liquid and its vapor), and a certain fraction of separately modeled noncondensable gases known in advance and both bubble formation (evaporation) and collapse (condensation) are taken into consideration.

A vapor transport equation governs the vapor mass fraction, f, expressed as:

$$\frac{\partial}{\partial t}\left(\rho_m f\right) + \nabla.\left(\rho_m \vec{v}_v f\right) = \nabla\left(\gamma \nabla f\right) + R_e - R_c \tag{19}$$

where ρ_m is the mixture density, $\vec{v}_v$ is the velocity vector of the vapor phase, γ is the effective exchange coefficient, and R_e and R_c are the vapor generation and condensation rate terms, or phase change rates.

These rates are given by:

when $p < p_{sat}$

$$R_e = C_e \frac{V_{ch}}{\sigma} \rho_l \rho_v \sqrt{\frac{2(p_{sat} - p)}{3\rho_l}} (1 - f) \tag{20}$$

when $p > p_{sat}$

$$Rc = C_c \frac{V_{ch}}{\sigma} \rho_l \rho_v \sqrt{\frac{2(p - p_{sat})}{3\rho_l}} f \tag{21}$$

where the suffixes l and v denote the liquid and vapor phases, V_{ch} is a characteristic velocity, which is approximated by the local turbulence intensity, (i.e. $V_{ch} = \sqrt{k}$), σ is the surface tension coefficient of the liquid, p_{sat} is the liquid saturation vapor pressure at the given temperature, and C_e and C_c are empirical constants. The default values are C_e = 0.02 and C_c = 0.01.

FLUENT accounts for the turbulence-induced pressure fluctuations by changing the phase-change threshold pressure from p_{sat} to

$$p_v = \frac{1}{2}(p_{sat} + p_{turb}) \tag{22}$$

where

$$p_{turb} = 0.39 \rho k \tag{23}$$

where k is the local turbulence kinetic energy.

For cavitation model, the density of the mixture, ρ_m , is expressed as

$$\rho_m = \alpha_v \rho_v + \rho_g \rho_g + (1 - \alpha_v - \alpha_g) \rho_l \tag{20}$$

where ρ_l, ρ_v , and ρ_g are the densities of the liquid, the vapor, and the noncondensable gases, respectively, and , α_v, and α_g are the respective volume fractions. The volume fraction (α_i) is related to mass fraction (f_i) as

$$\alpha_i = f_i \frac{\rho_m}{\rho_i} \tag{21}$$

The combined volume fraction of vapor and gas (i.e., $\alpha_v + \alpha_g$) is known the void fraction (α).

2.4 User Defined Function and Dynamic Mesh Method

A user-defined function, or UDF, is a function that the user programs and can be dynamically loaded with the **FLUENT** solver to enhance the standard features of the code. UDF's can be used to define your own boundary conditions, material properties, and other additional customized model parameters.

UDF's are written in the C programming language using any text editor. The source code file containing UDF's can be either interpreted or compiled in **FLUENT**. Once interpreted or compiled, UDF's will become visible and selectable in **FLUENT** graphics panels, and can be tied to a solver by choosing the function name in the appropriate panel.

In this study, a UDF is used to prescribe the motion of the journal in the SFD. The source code files define that the journal's orbits vary greatly from circular to linear at a certain frequency.

The prescribed motion of the SFD affects the shape of the domain for which we are studying. The dynamic mesh model in **FLUENT** was used to model flows where the shape of the domain is changing with time due to motion on the domain boundaries. The volume mesh will be updated automatically by **FLUENT** at each time step based on the new positions of the boundaries. By providing a starting volume mesh and the description of the motion of any moving zones in the model, the dynamic mesh model can perform its task.

2.5 The Simplified Model, Material Properties, and Boundary Conditions

The model simplified the SFD as two cylinders (Figure 2.1), one inside the other. The inside circle represents the integration of the shaft, bearing, and journal whereas the outer represents the housing. Eccentricity indicates the distance between the centers of the two circles. The clearance, (c) = 0.005 inches, represents the difference in circle radii. The radius of the journal (R), or inner circle, is 2.5 inches. The journal orbits inside the wall. The orbits experienced by SFDs vary greatly from circular to linear. Therefore a linear sinusoidal motion along the X-axis will be applied with the amplitude (e) of 0.0005, 0.001, and 0.002 inches (e/c = 0.1, 0.2, and 0.4) with frequencies (Fe) of 10, 50, 100, and 200, and 500 Hz.

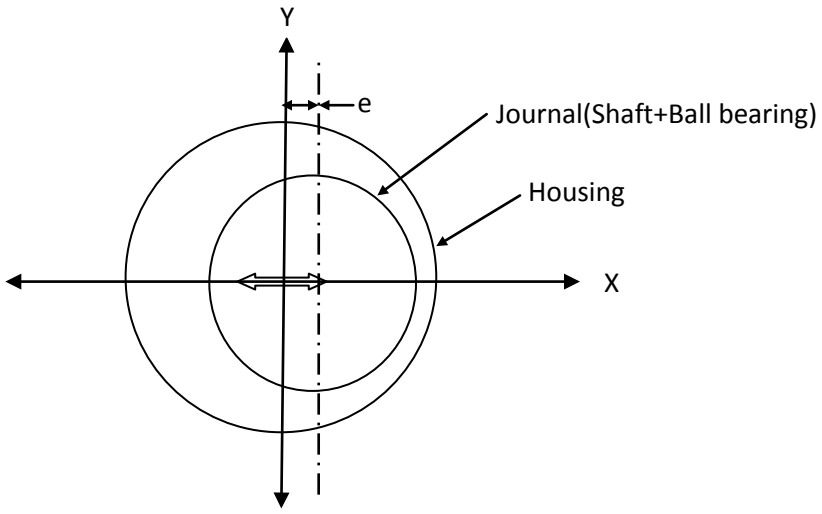

Figure 2.1 The simplified model of a squeeze film damper

The translational movement of a journal can be described as:

$$x = e\cos(\omega t) \tag{22}$$

$$y = 0 \tag{23}$$

where ω is angular velocity (rad/sec) equal to $2\pi(Fe)$ and t represents time(s).

The fluid in the squeeze film zone is ISO VG 2 with a density and viscosity of 800 kg/m^3 and 2 cst. respectively.

In the case of cavitation, the water was considered as the subject since **FLUENT** provides all required properties to be used in numerical calculation. According to the two-phase flow, the primary phase was the liquid water with a density and dynamic viscosity of 1000 kg/m^3 and 0.001 kg/m-s, respectively whereas the secondary phase was water-vapor with a density and dynamic viscosity of 0.02558 kg/m^3 and 1.26e-06 kg/m-s, respectively. The cavitation parameters include 3540 Pa of vaporization pressure, 0.0717 N/m of surface tension coefficient, and 1.5e-05 of non-condensable gas mass fraction (f_g). We assume the closed system which means no flow across the boundary.

2.6 Numerical Method of Solution

The numerical study used the finite difference method to convert the governing equations into algebraic equations that could be solved numerically. The **FLUENT 6.3** program was applied to integrate the governing equations for each control volume and to yield discrete equations conserving each quantity.

For the single phase flow, the pressure based solver with implicit formulation was chosen using the standard k-ε model. The unsteady flow with dynamic mesh method was applied to solve the flow and turbulence equation. For the pressure-velocity coupling, the SIMPLE (Semi-Implicit Method for Pressure-Linked Equation) algorithm was used to solve the continuity equation. For the pressure discretization, the standard scheme was chosen. The equations for the momentum, turbulent dissipation, and

turbulent kinetic energy were discretized spatially with a first-order upwind scheme. The convergence criteria are 10^{-5} for all parameters.

For the multiphase flow, the mixture model was applied in addition to the k-ε model and the wall function based on enhanced wall treatment. The unsteady solution with dynamic mesh method was also used to determine the flow and turbulence. For the pressure-velocity coupling, the SIMPLEC (SIMPLE-Consistent) algorithm was used to solve the continuity equation. For the pressure discritization, the standard scheme was chosen. The equations for the density, momentum, vapor, turbulent dissipation, and turbulent kinetic energy were discretized spatially with a first-order upwind scheme. The convergence criteria are 10^{-5} for all parameters except 0.001 for the volume fraction of the vapor, or the vf-vapor.

The commercial software package GAMBIT grid generator was used to generate the 2-D structured grid. The gravitational effect on the geometry was neglected in this study.

CHAPTER III

SINGLE PHASE FLOW IN SQUEEZE FILM DAMPERS

In this chapter, the computations performed for 2-D SFDs in which the journal moves inside solved using the k-ε model in FLUENT are presented.

3.1 Description of Problem

Figure 3.1 shows the simulated geometry for the SFD whereas Figure 3.2 represents the magnified geometry with a numerical grid. The diameter of the journal, or inner circle was 5 inches, while the clearance was 0.005 inches. The journal orbits inside the wall. Orbits can vary greatly from circular to linear. For this study, single phase flow and a linear sinusoidal motion along the X-axis will be applied with amplitudes(e) of 0.0005, 0.001, and 0.002 inches and frequencies of 10,100, and 200 Hz.

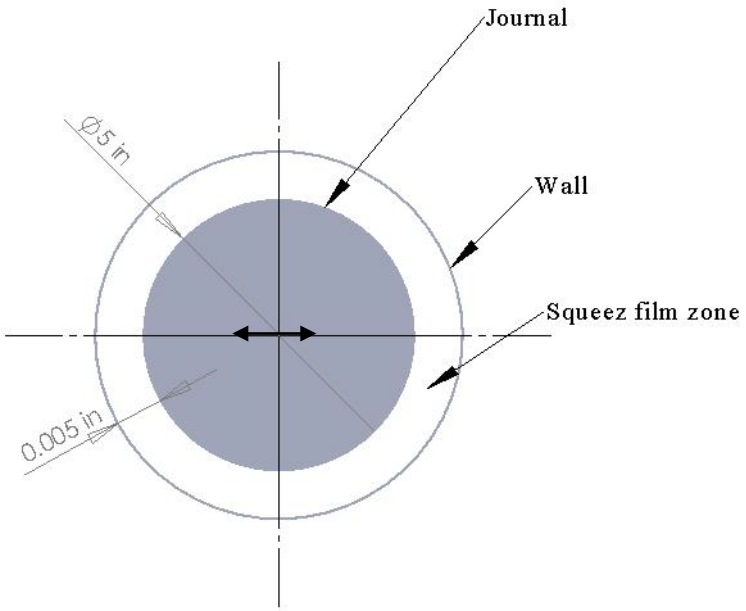

Figure 3.1 2-D simulated geometry of the SFD

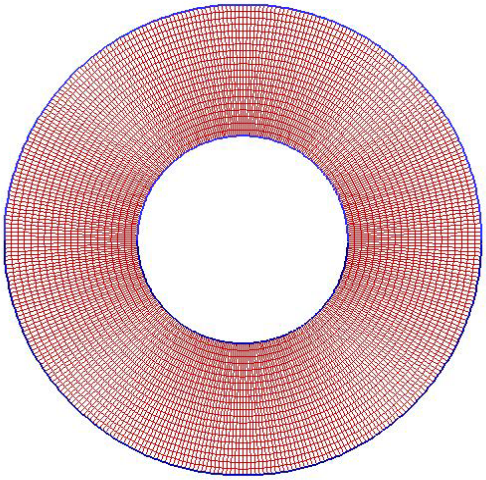

Figure 3.2 The magnified geometry with numerical grid

3.2 Grid Independence Study

The grid independent study was performed for three different grids of 10x180, 20x360, and 20x1440. For a motion of the journal, the amplitude was 0.002 with 5 degrees/step movement and three different frequencies of 10, 100, and 500 Hz, respectively. At five different journal positions, i.e. 270, 315, 360, 405, and 450 degrees, the comparison among three different grids was depicted with the flow values of the pressure, x-velocity, and y-velocity in the squeeze film zone. The Figures 3.3 through 3.7 portrayed the comparison of three different grids at different five positions with the journal's frequency of 10 Hz. The Figures 3.8 through 3.12 showed the comparison at the frequency of 100 Hz whereas the Figures 3.13 through 3.17 depicted the comparison at the frequency of 500 Hz. According to the comparison, the 20x360 grid was chosen for further studies because there is no significant change in the flow comparing with the 20x1440 grid.

Grid 10x180 20x360 20 x1440

(a) Pressure (Pa)

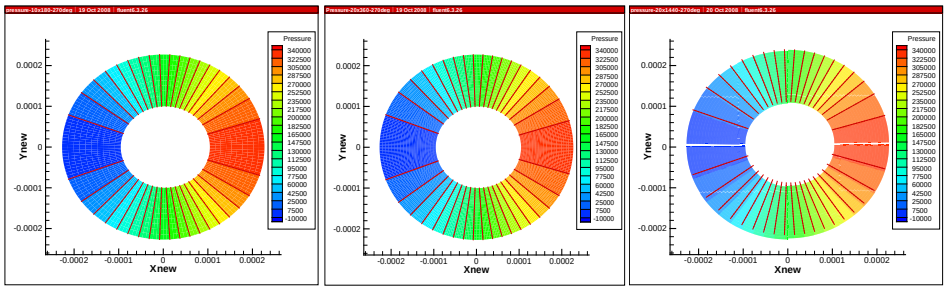

(b) X velocity(m/s)

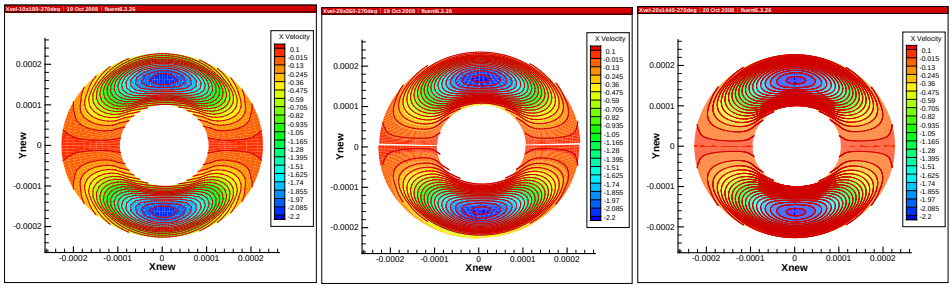

(c) Y velocity (m/s)

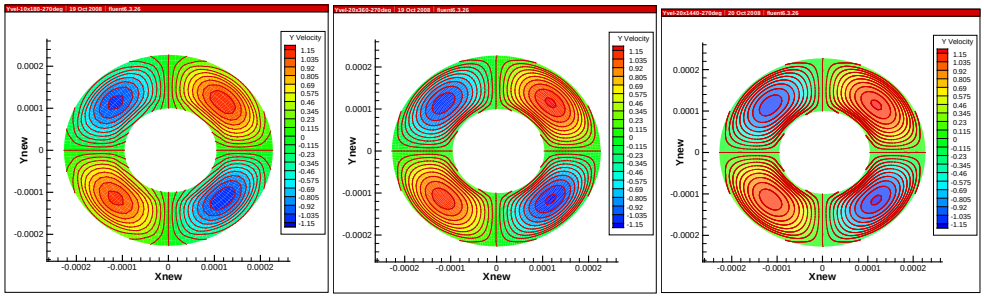

Figure 3.3 The comparison of the flow for a journal position at 270 degrees with the frequency of 10 Hz

Grid 10x180 20x360 20 x1440

(a) Pressure (Pa)

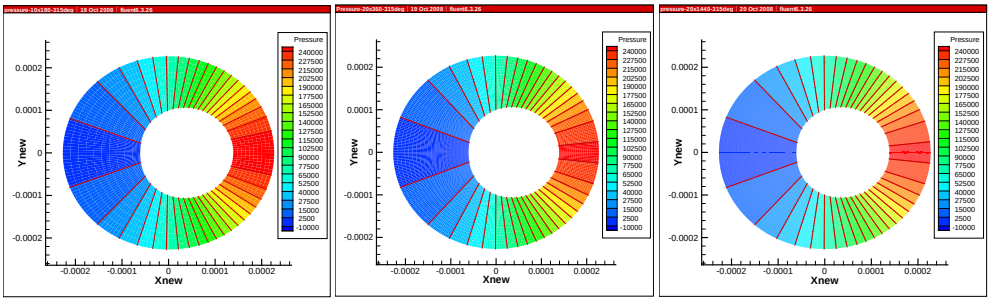

(b) X velocity(m/s)

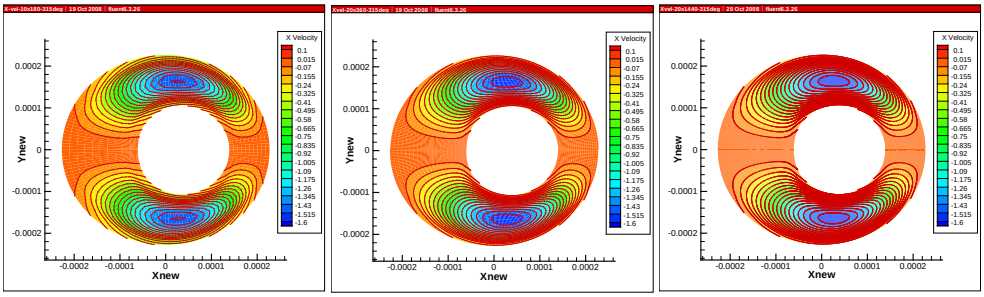

(c) Y velocity (m/s)

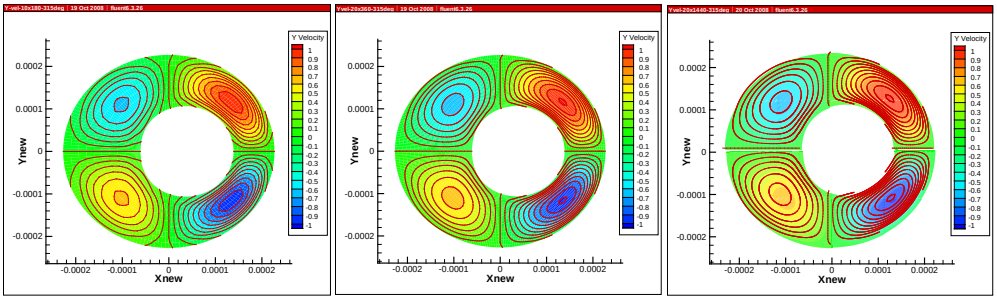

Figure 3.4 The comparison of the flow for a journal position at 315 degrees with the frequency of 10 Hz

Grid 10x180 20x360 20 x1440

(a) Pressure (Pa)

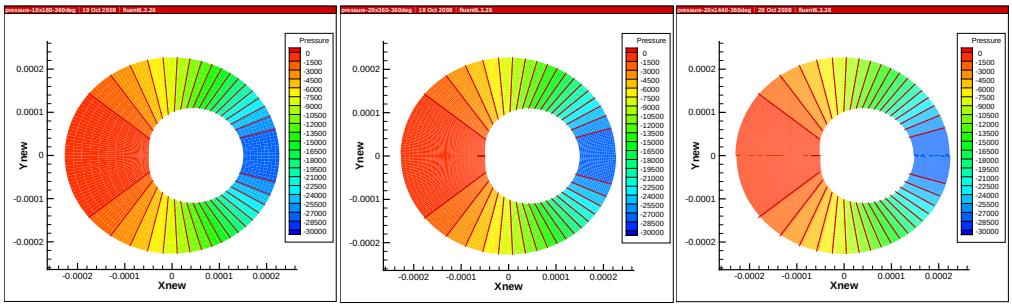

(b) X velocity(m/s)

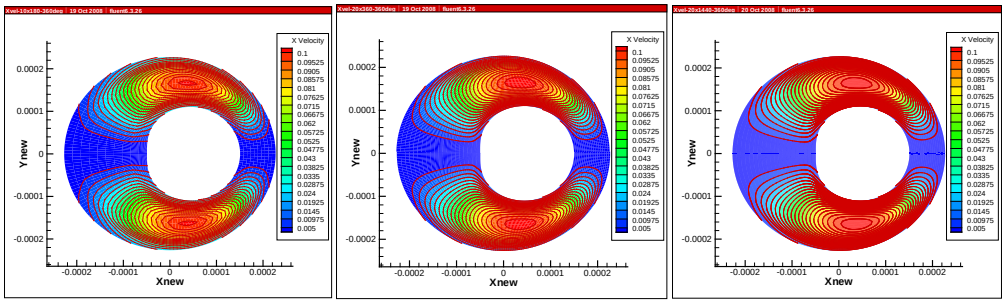

(c) Y velocity (m/s)

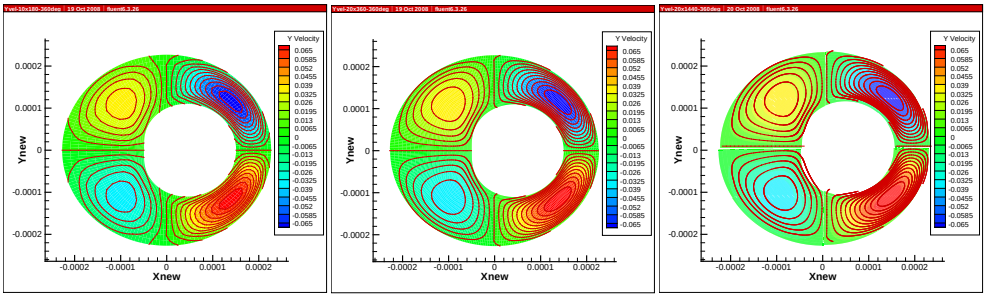

Figure 3.5 The comparison of the flow for a journal position at 360 degrees with the frequency of 10 Hz

Grid 10x180 20x360 20 x1440

(a) Pressure (Pa)

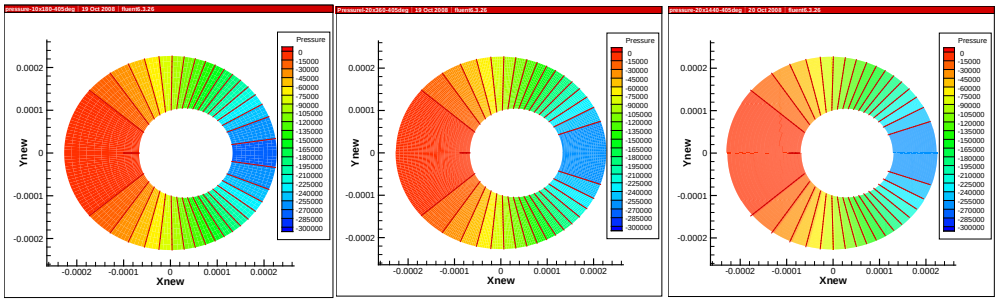

(b) X velocity(m/s)

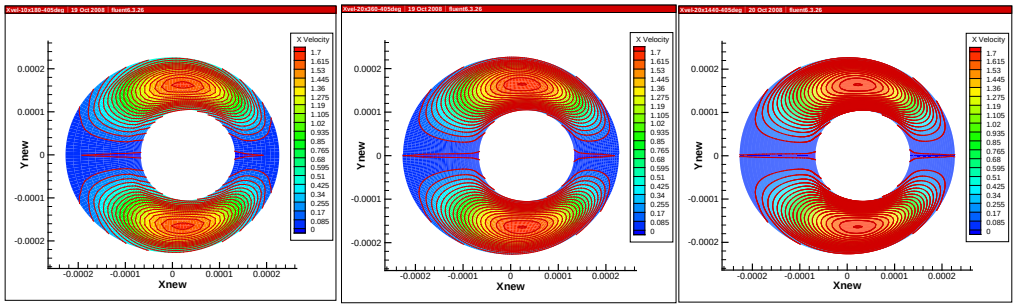

(c) Y velocity (m/s)

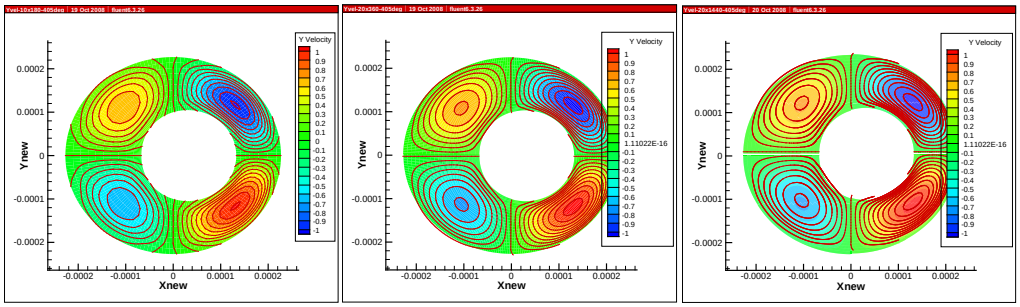

Figure 3.6 The comparison of the flow for a journal position at 405 degrees with the frequency of 10 Hz

Grid 10x180 20x360 20 x1440

(a) Pressure (Pa)

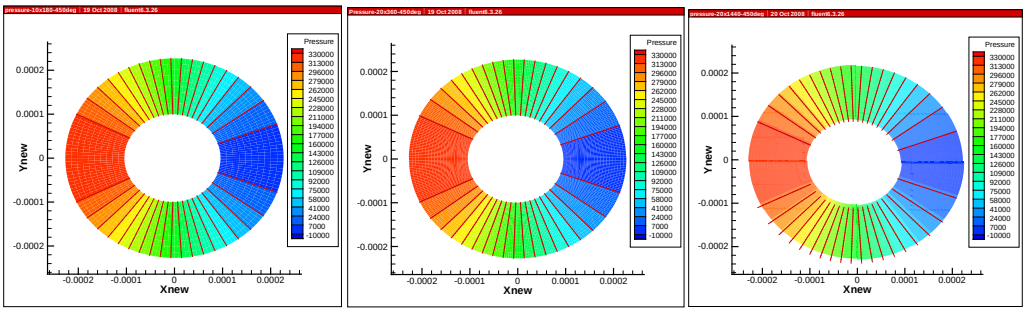

(b) X velocity(m/s)

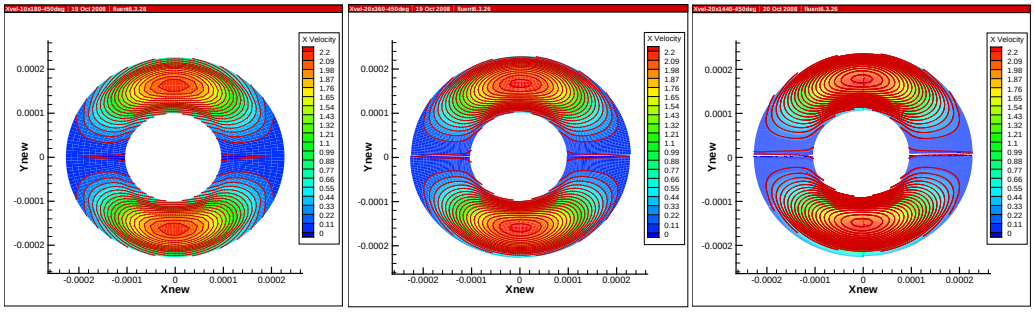

(c) Y velocity (m/s)

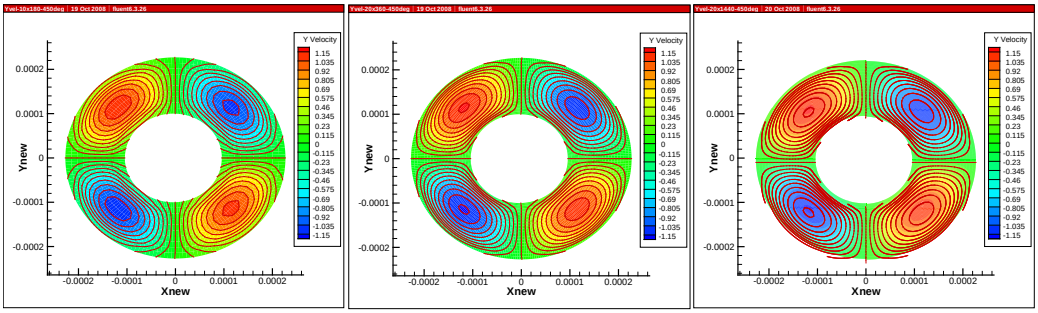

Figure 3.7 The comparison of the flow for a journal position at 450 degrees with the frequency of 10 Hz

Grid 10x180 20x360 20 x1440

(a) Pressure (Pa)

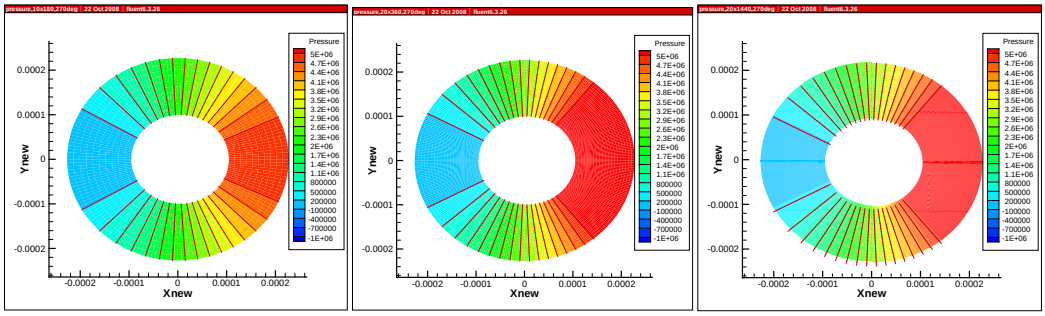

(b) X velocity(m/s)

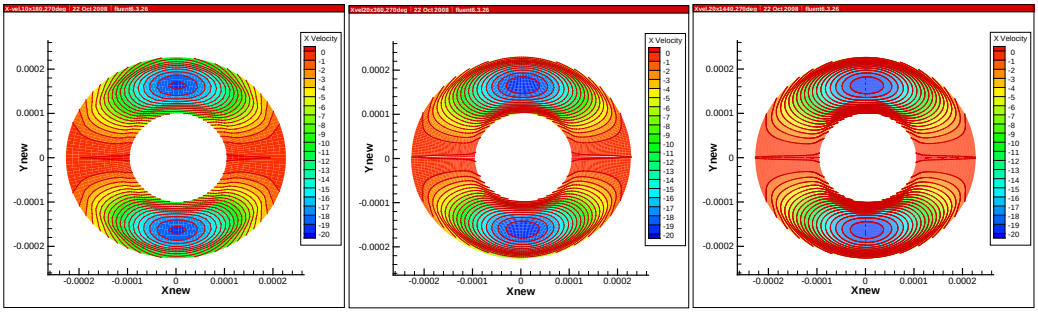

(c) Y velocity (m/s)

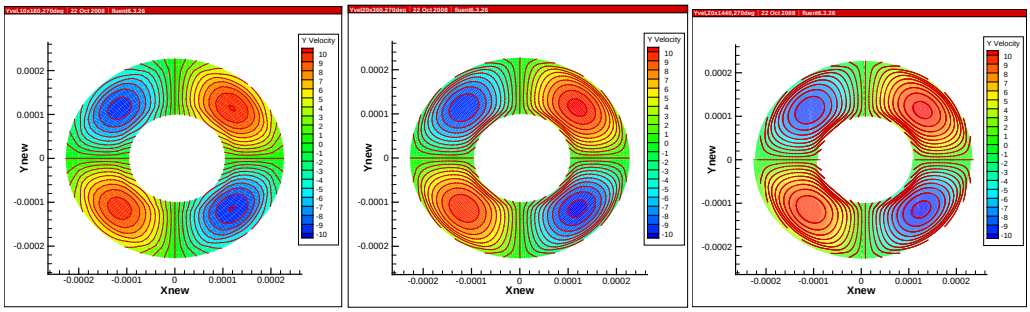

Figure 3.8 The comparison of the flow for a journal position at 270 degrees with the frequency of 100 Hz

Grid 10x180 20x360 20 x1440

(a) Pressure (Pa)

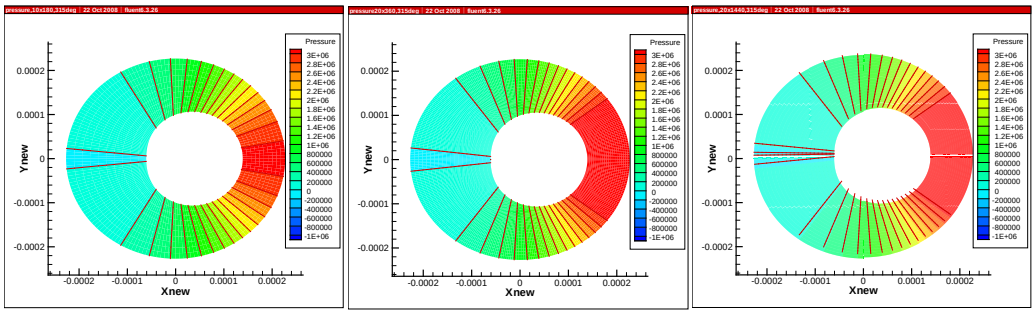

(b) X velocity(m/s)

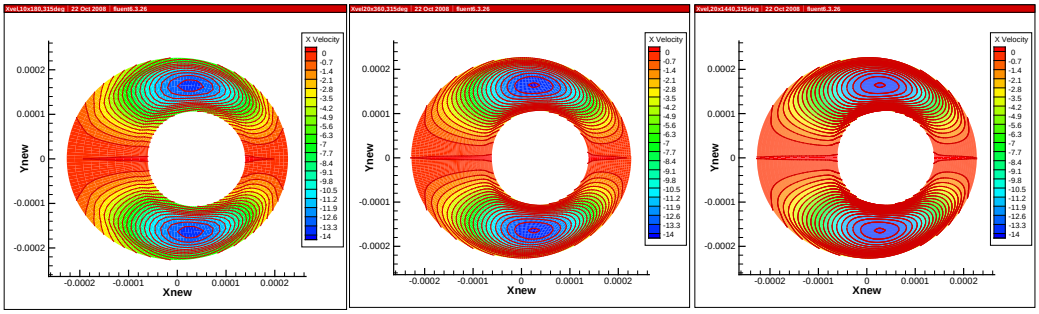

(c) Y velocity (m/s)

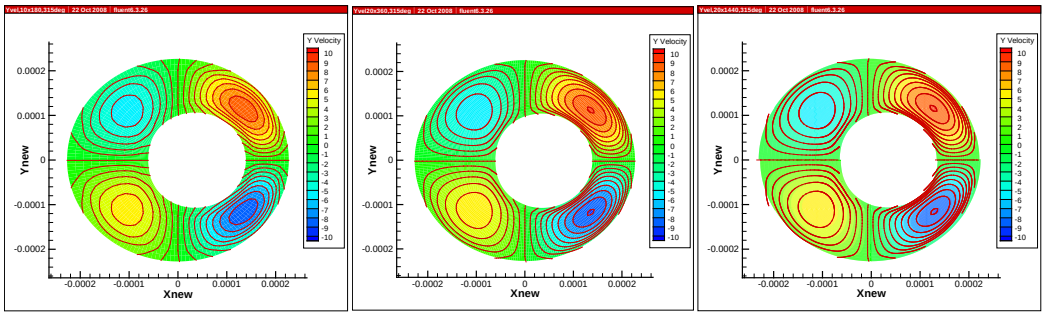

Figure 3.9 The comparison of the flow for a journal position at 315 degrees with the frequency of 100 Hz

Grid 10x180 20x360 20 x1440

(a) Pressure (Pa)

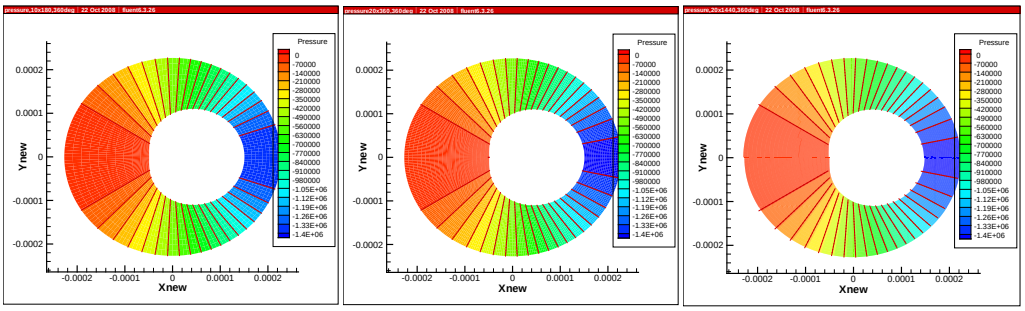

(b) X velocity(m/s)

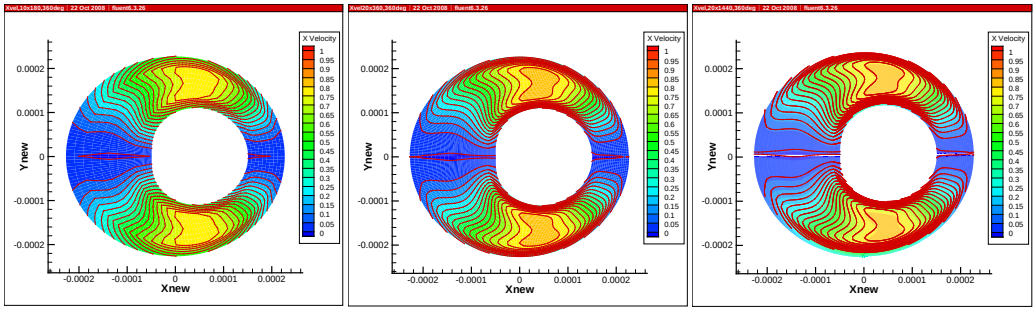

(c) Y velocity (m/s)

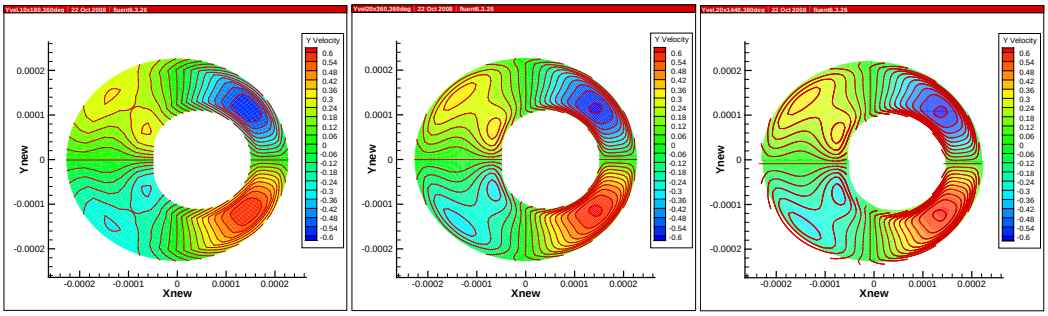

Figure 3.10 The comparison of the flow for a journal position at 360 degrees with the frequency of 100 Hz

Grid 10x180 20x360 20 x1440

(a) Pressure (Pa)

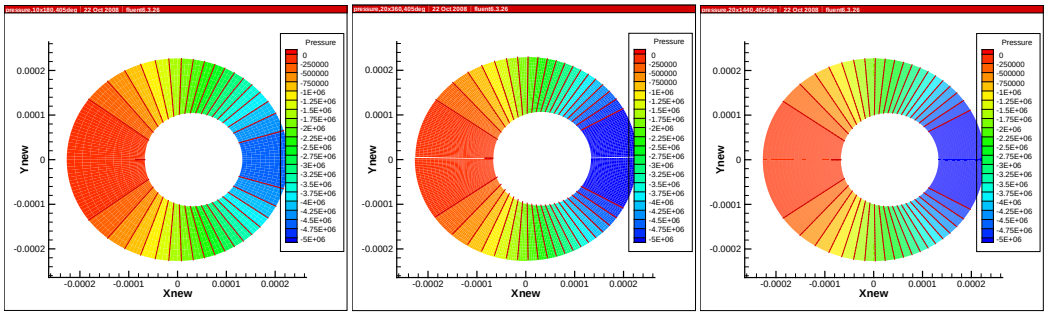

(b) X velocity(m/s)

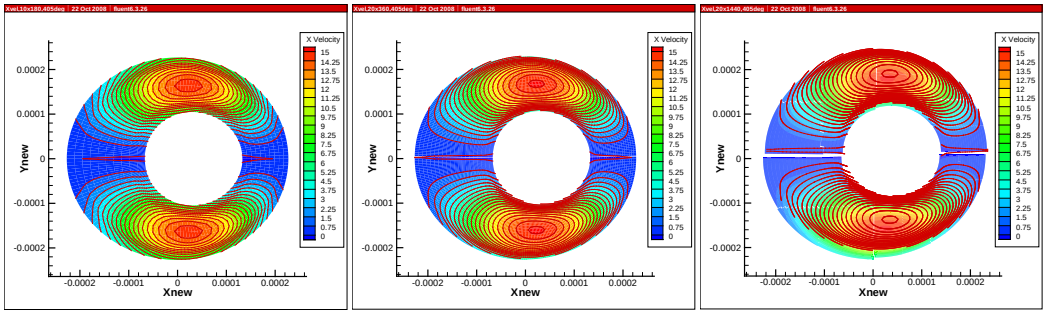

(c) Y velocity (m/s)

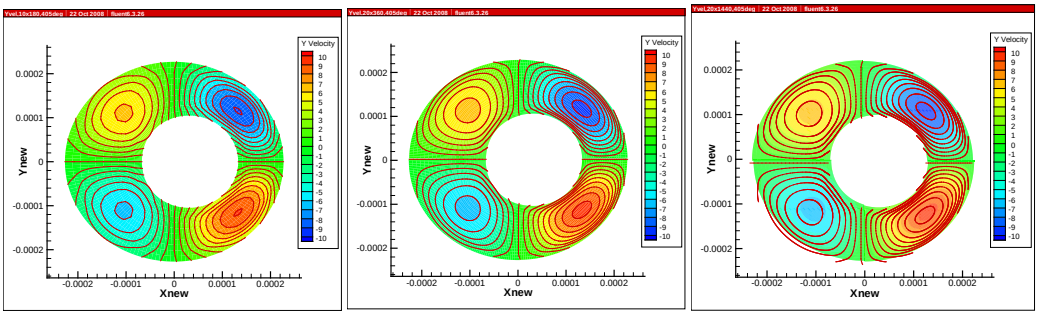

Figure 3.11 The comparison of the flow for a journal position at 405 degrees with the frequency of 100 Hz

Grid 10x180 20x360 20 x1440

(a) Pressure (Pa)

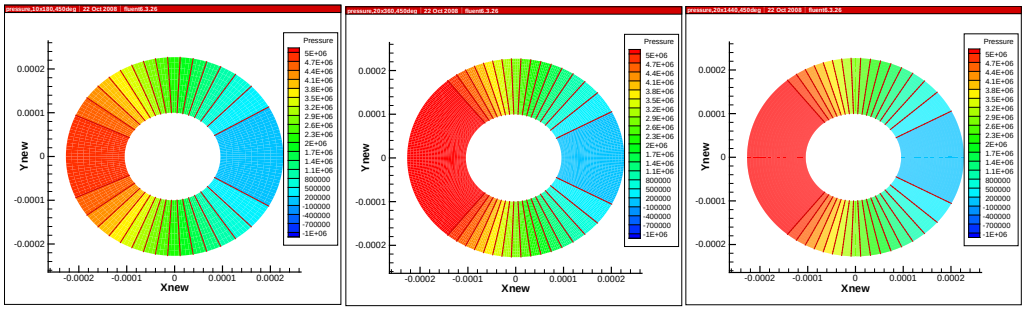

(b) X velocity(m/s)

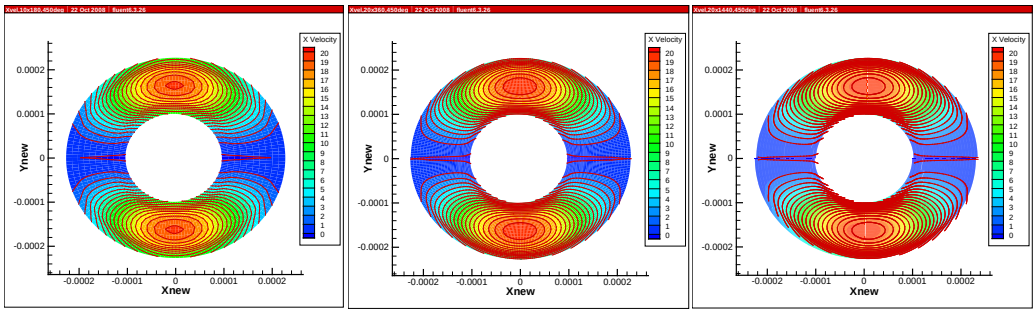

(c) Y velocity (m/s)

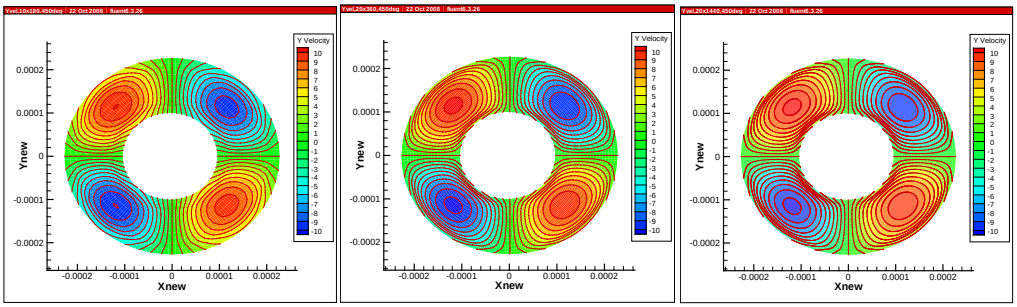

Figure 3.12 The comparison of the flow for a journal position at 450 degrees with the frequency of 100 Hz

Grid 10x180 20x360 20 x1440

(a) Pressure (Pa)

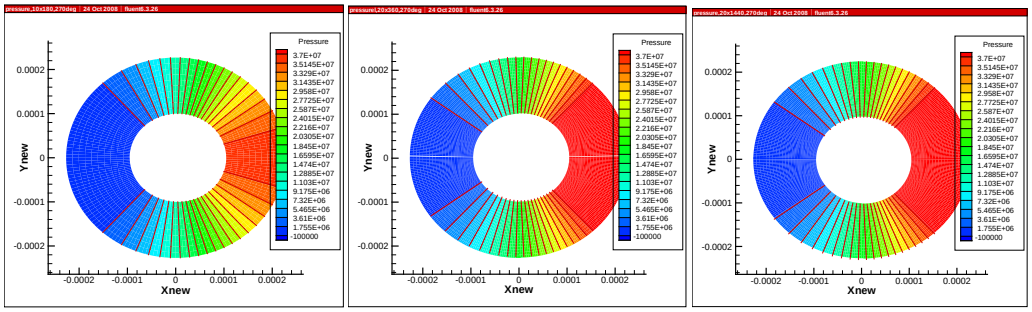

(b) X velocity(m/s)

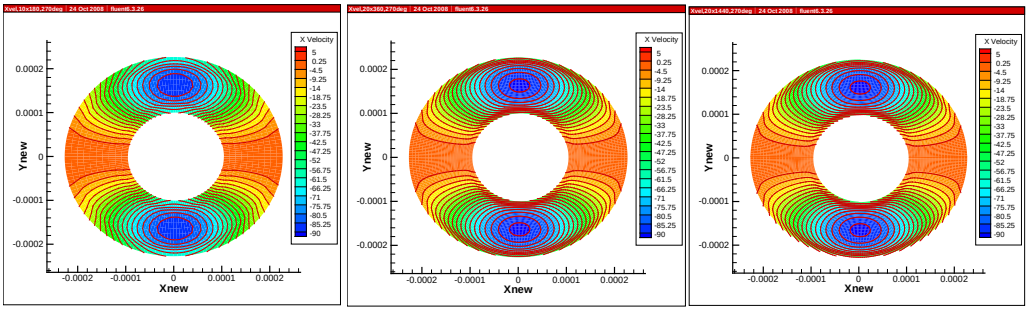

(c) Y velocity (m/s)

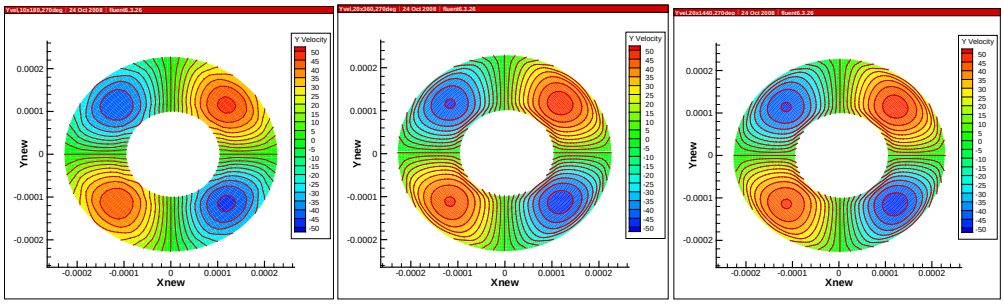

Figure 3.13 The comparison of the flow for a journal position at 270 degrees with the frequency of 500 Hz

Grid 10x180 20x360 20 x1440

(a) Pressure (Pa)

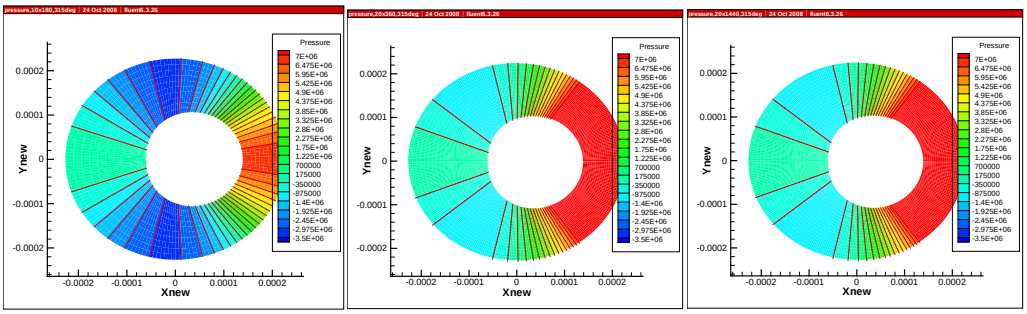

(b) X velocity(m/s)

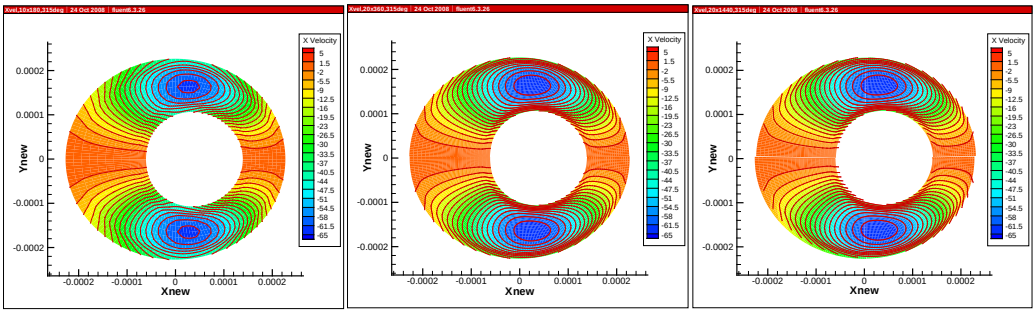

(c) Y velocity (m/s)

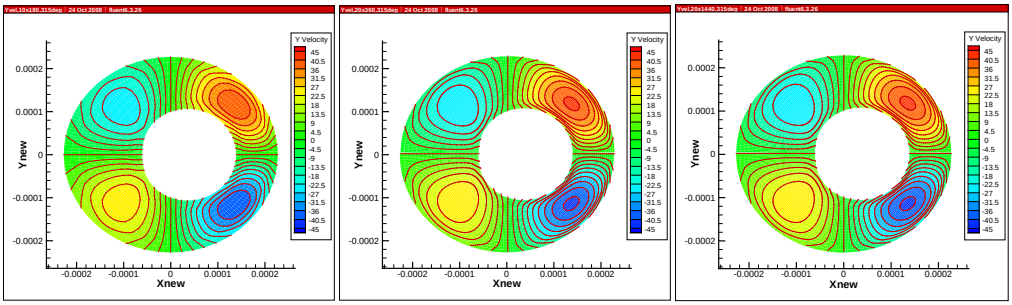

Figure 3.14 The comparison of the flow for a journal position at 315 degrees with the frequency of 500 Hz

Grid 10x180 20x360 20 x1440

(a) Pressure (Pa)

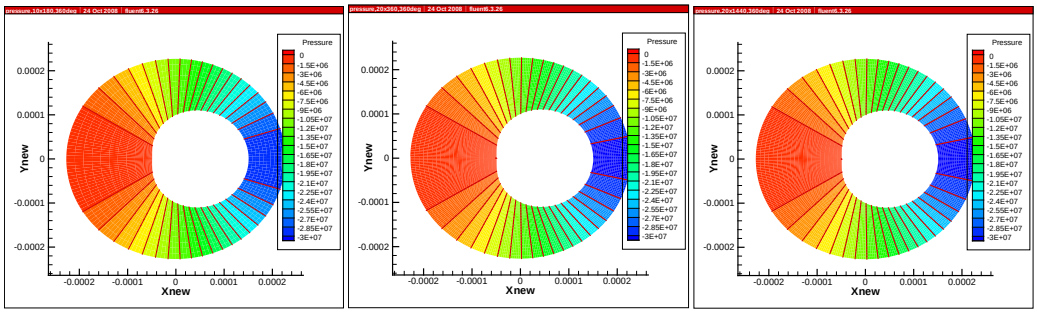

(b) X velocity(m/s)

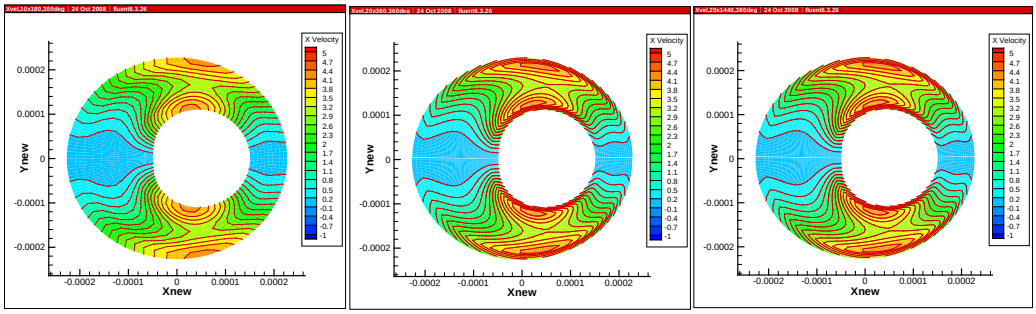

(c) Y velocity (m/s)

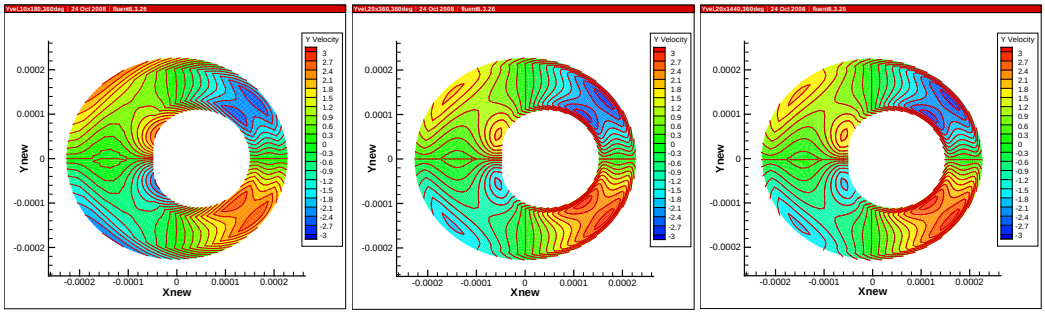

Figure 3.15 The comparison of the flow for a journal position at 360 degrees with the frequency of 500 Hz

Grid 10x180 20x360 20 x1440

(a) Pressure (Pa)

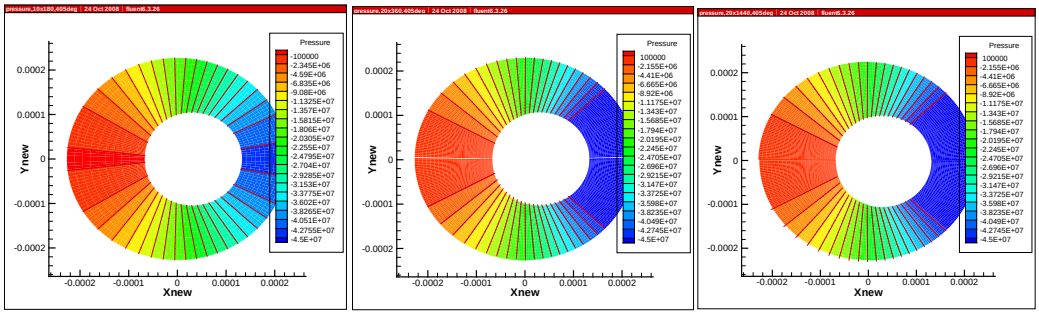

(b) X velocity(m/s)

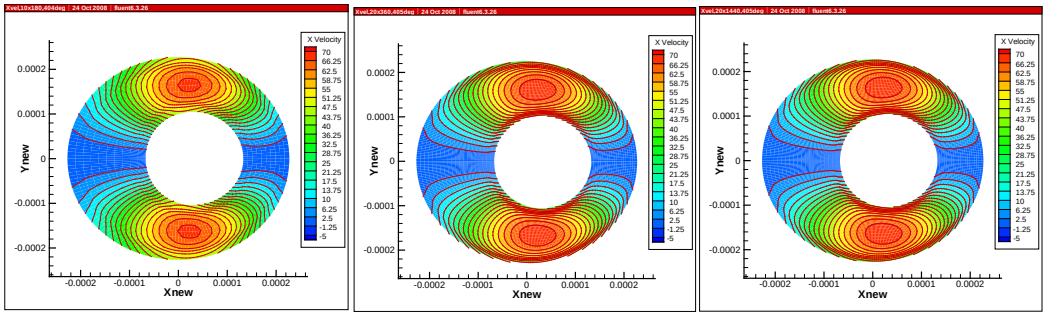

(c) Y velocity (m/s)

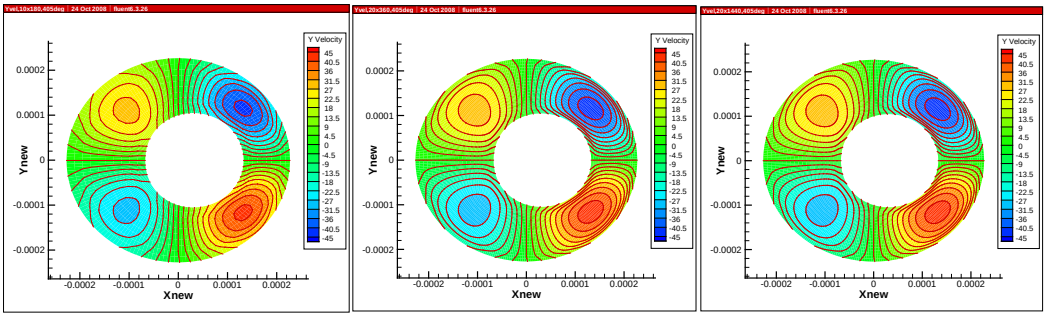

Figure 3.16 The comparison of the flow for a journal position at 405 degrees with the frequency of 500 Hz

Grid 10x180 20x360 20 x1440

(a) Pressure (Pa)

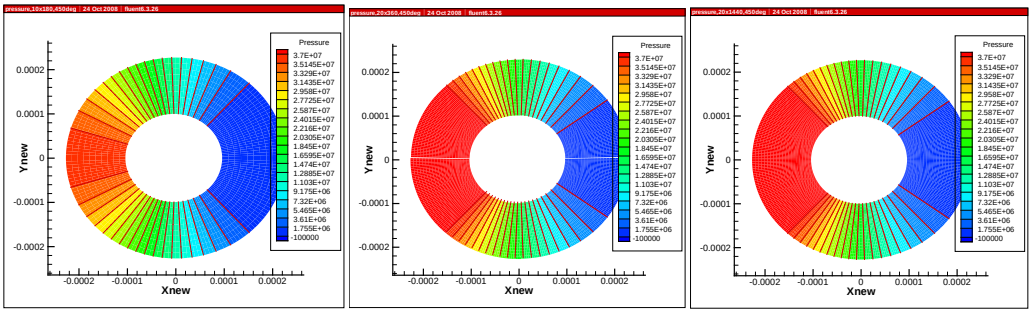

(b) X velocity(m/s)

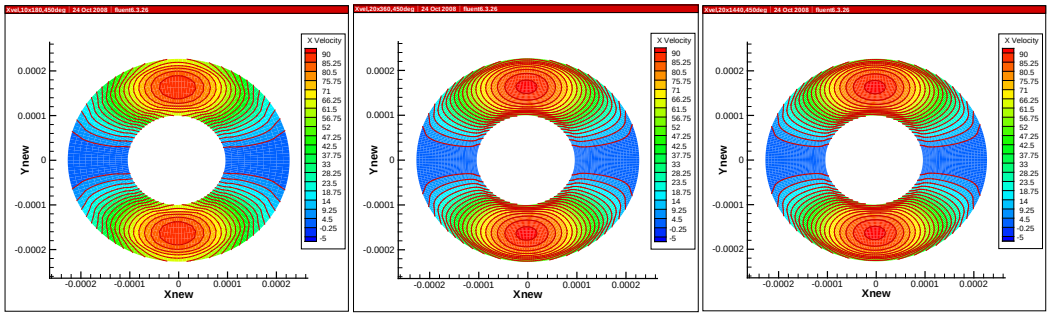

(c) Y velocity (m/s)

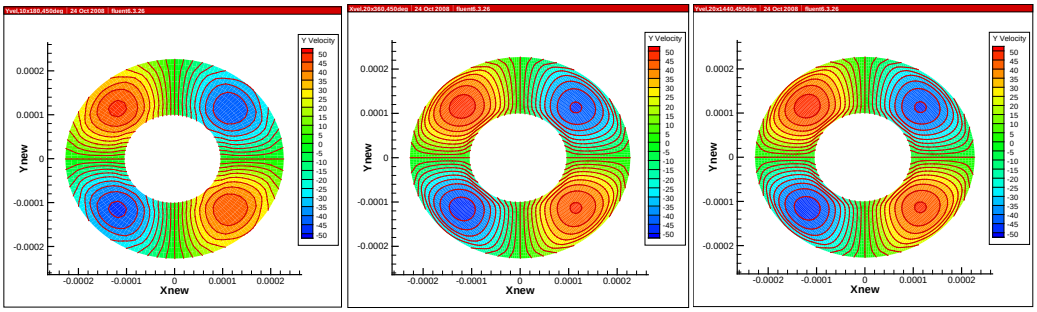

Figure 3.17 The comparison of the flow for a journal position at 450 degrees with the frequency of 500 Hz

3.3 Time Independence Study

Since the domain of the squeeze film zone has been changing corresponding to the journal motion, **FLUENT** performed the unsteady-state calculation to determine the flow properties in the squeeze film zone. So an appropriate distance for journal moving one step was determined by time independence study.

After the 20x360 grid was chosen, the time independent study was also performed for different time intervals of a journal's motion including 5, 2.5, 1, and 0.5 degrees/step. There are two different frequencies of 10 and 500 Hz with the same grid and amplitude of 20x360 and 0.002 inches, respectively. At five different journal positions, i.e. 270, 315, 360, 405, and 450 degrees, the comparison between the different degrees/step rates for the three different oscillation rates was depicted with the flow values of the pressure, x-velocity, and y-velocity in the squeeze film zone. The Figures 3.18 through 3.27 portrayed the comparison of four different time intervals, i.e. 5, 1, and 0.5 degrees/step at five different positions with the journal of 10 and 500 Hz.

According to the comparison, the 1 degree/step was chosen for further studies because there is no significant change in the flow comparing with the 0.5 degrees/step. The analysis of the results will be presented using the 1 degree/step time increments.

Time step 5 deg/step 1 deg/step 0.5 deg/step

(a) Pressure (Pa)

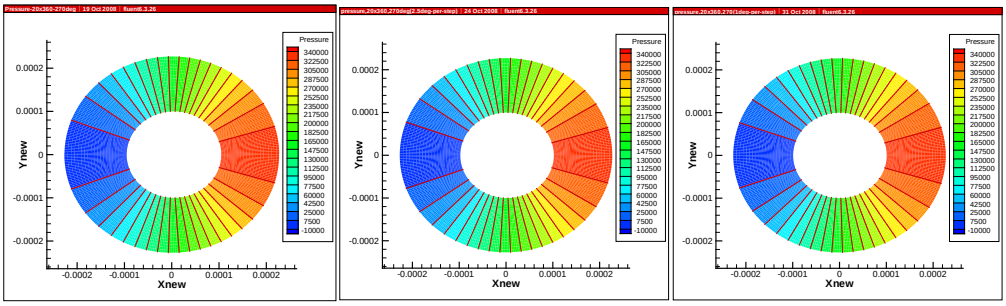

(b) X velocity(m/s)

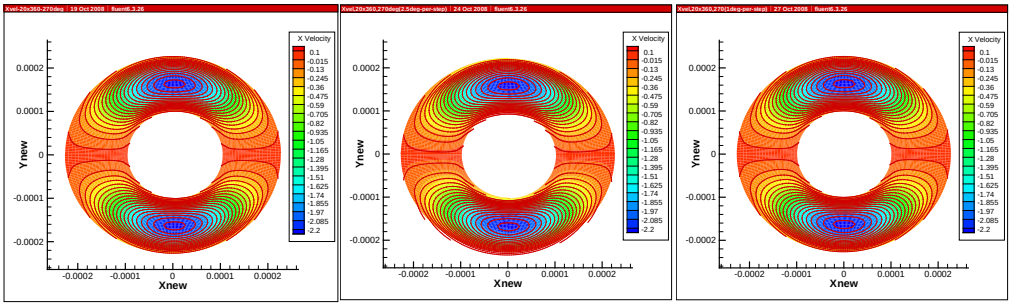

(c) Y velocity (m/s)

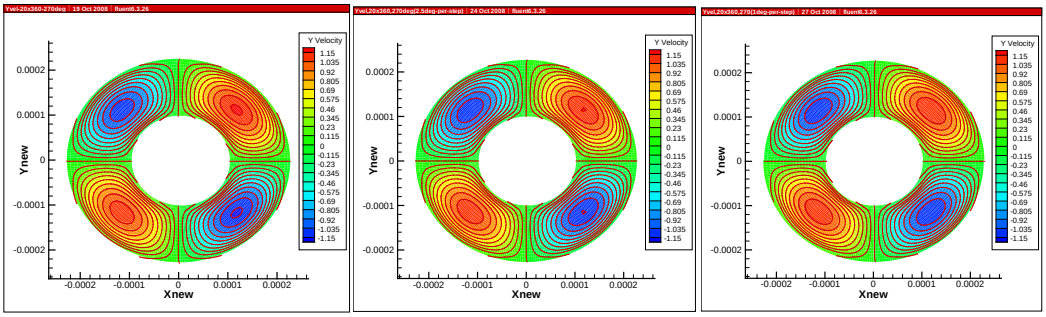

Figure 3.18 The comparison of the flow for a journal position at 270 degrees with the frequency of 10 Hz

Time step 5 deg/step 1 deg/step 0.5 deg/step

(a) Pressure (Pa)

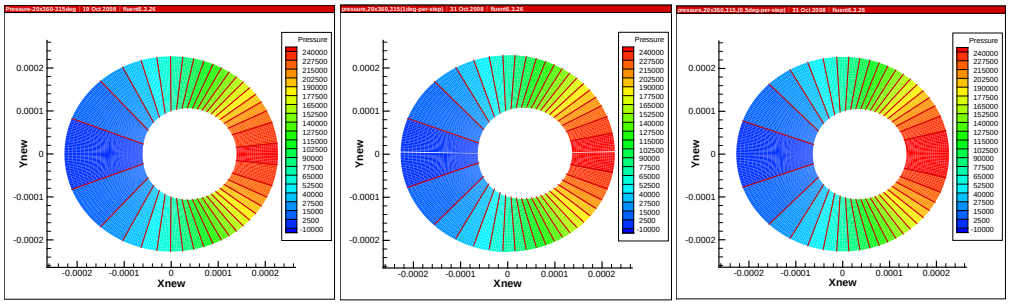

(b) X velocity(m/s)

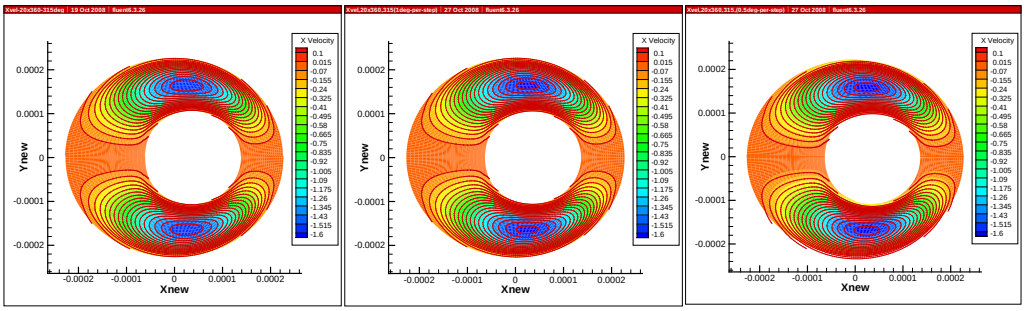

(c) Y velocity(m/s)

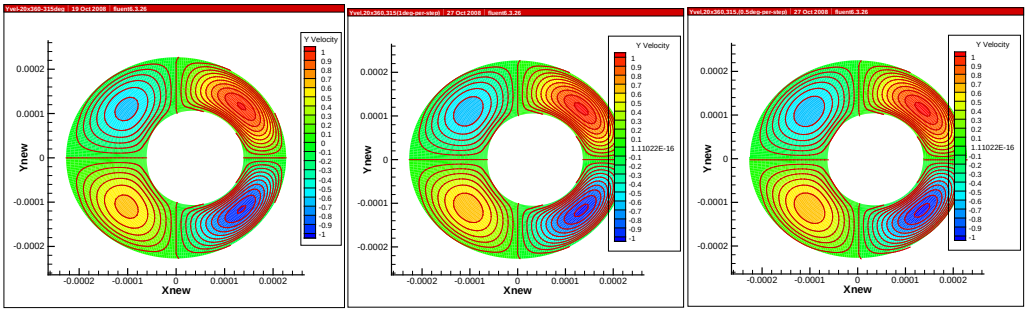

Figure 3.19 The comparison of the flow for a journal position at 315 degrees with the frequency of 10 Hz

Time step 5 deg/step 1 deg/step 0.5 deg/step

(a) Pressure (Pa)

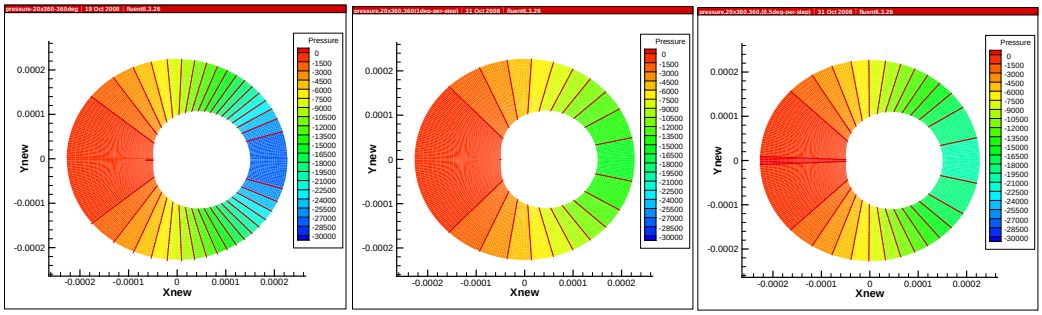

(b) X velocity(m/s)

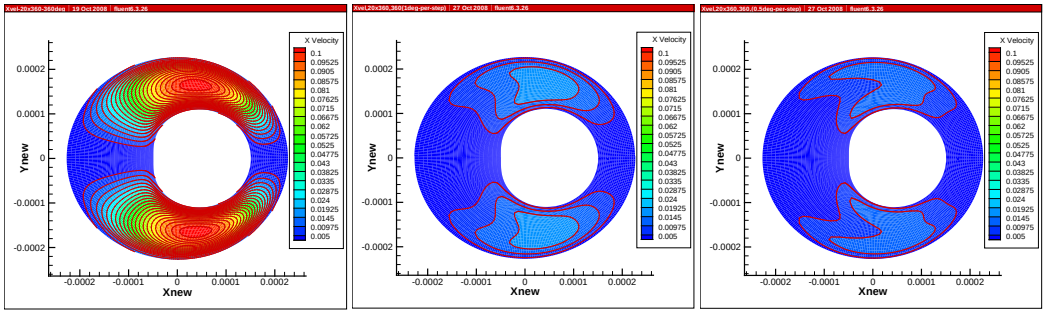

(c) Y velocity(m/s)

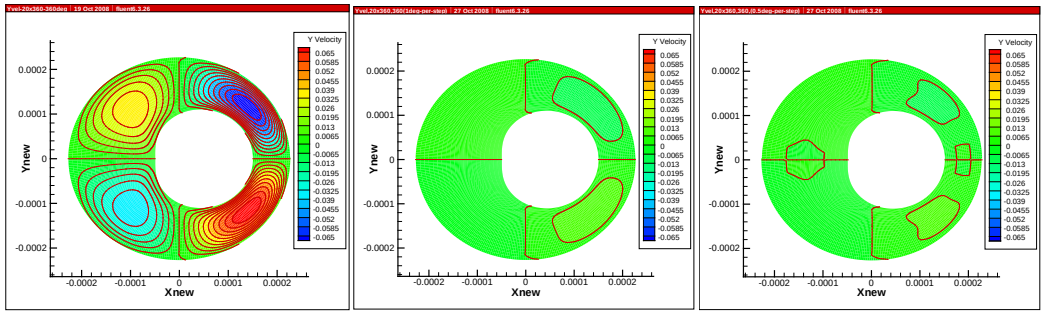

Figure 3.20 The comparison of the flow for a journal position at 360 degrees with the frequency of 10 Hz

Time step 5 deg/step 1 deg/step 0.5 deg/step

(a) Pressure (Pa)

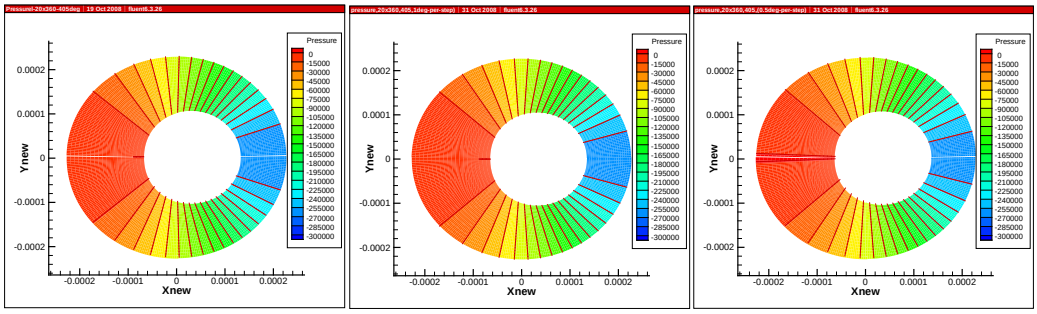

(b) X velocity(m/s)

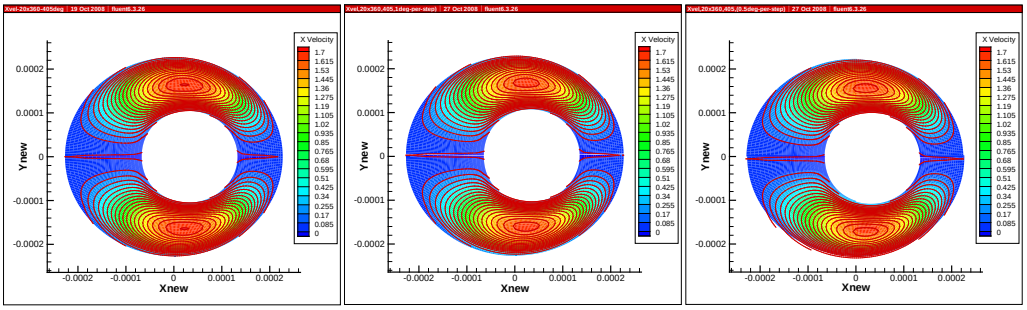

(c) Y velocity(m/s)

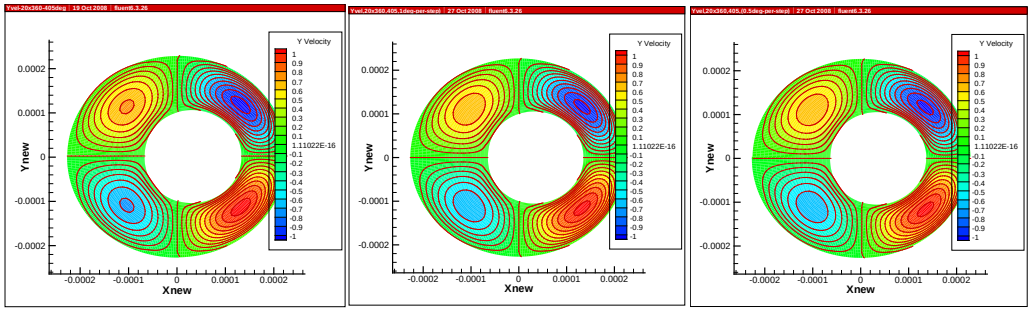

Figure 3.21 The comparison of the flow for a journal position at 405 degrees with the frequency of 10 Hz

Time step 5 deg/step 1 deg/step 0.5 deg/step

(a) Pressure (Pa)

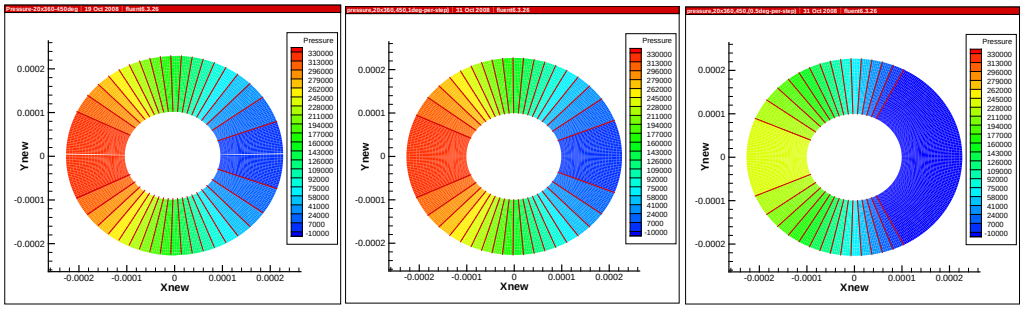

(b) X velocity(m/s)

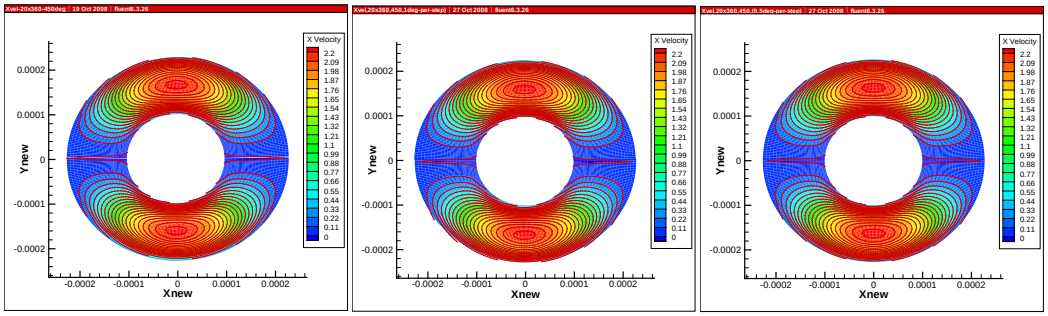

(c) Y velocity(m/s)

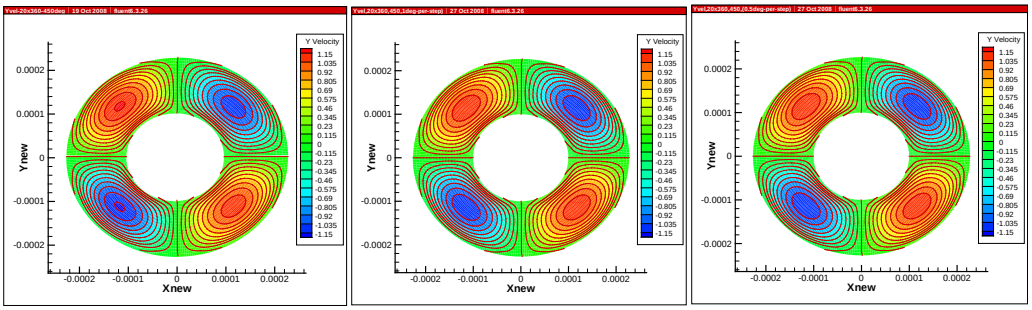

Figure 3.22 The comparison of the flow for a journal position at 450 degrees with the frequency of 10 Hz

Time step 5 deg/step 1 deg/step 0.5 deg/step

(a) Pressure (Pa)

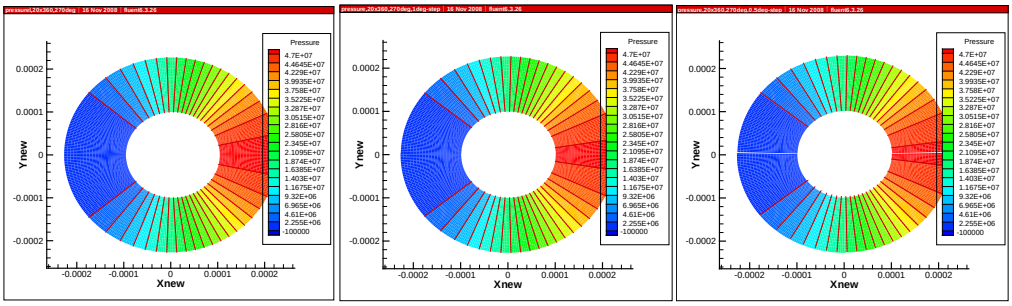

(b) X velocity(m/s)

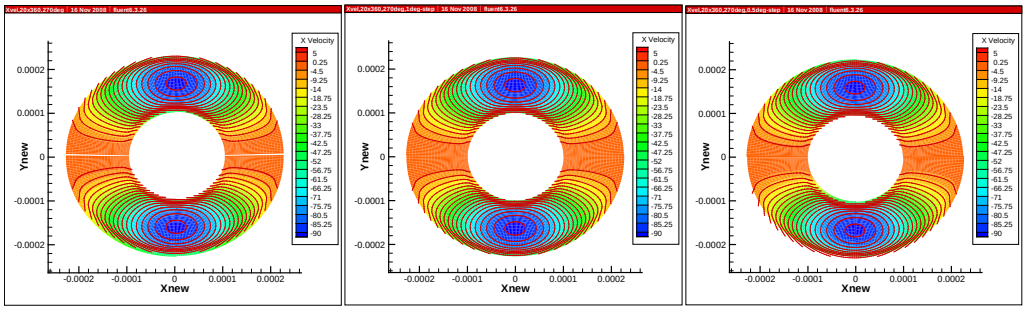

(c) Y velocity(m/s)

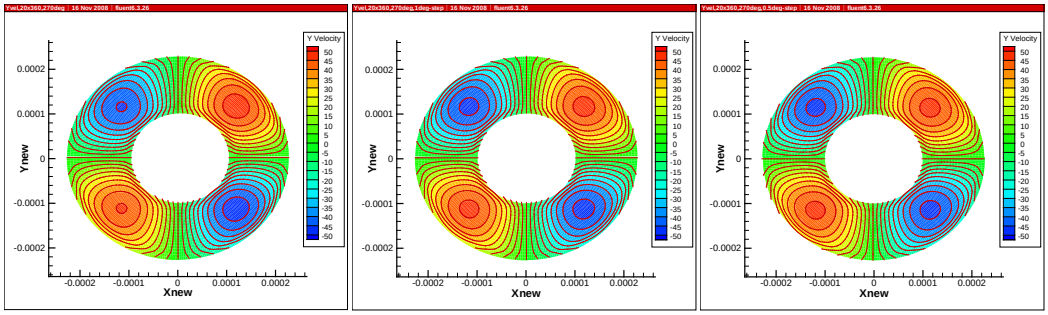

Figure 3.23 The comparison of the flow for a journal position at 270 degrees with the frequency of 500 Hz

Time step 5 deg/step 1 deg/step 0.5 deg/step

(a) Pressure (Pa)

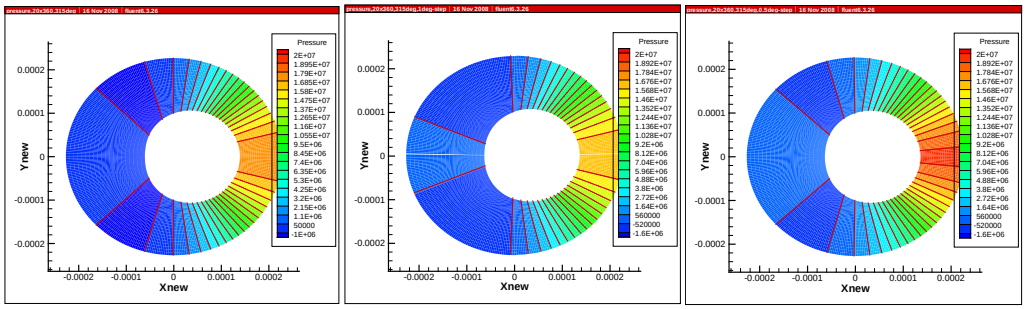

(b) X velocity(m/s)

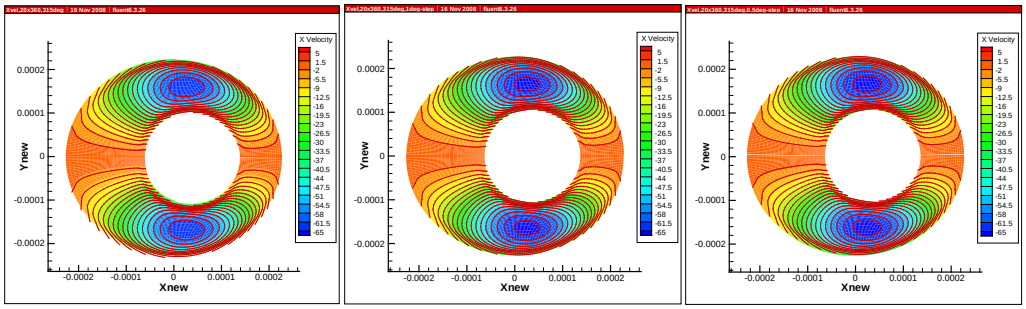

(c) Y velocity(m/s)

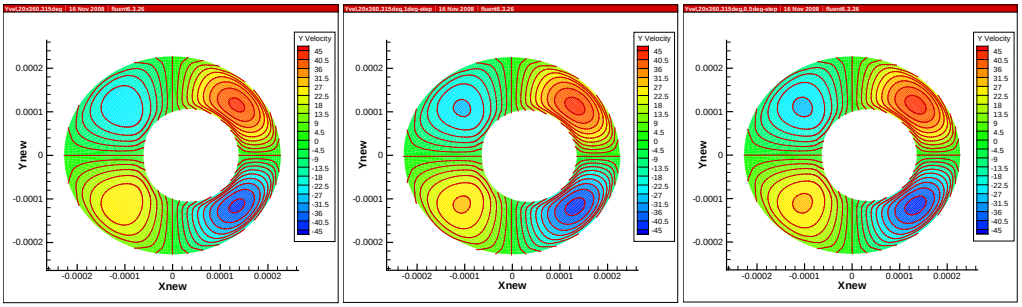

Figure 3.24 The comparison of the flow for a journal position at 315 degrees with the frequency of 500 Hz

Time step 5 deg/step 1 deg/step 0.5 deg/step

(a) Pressure (Pa)

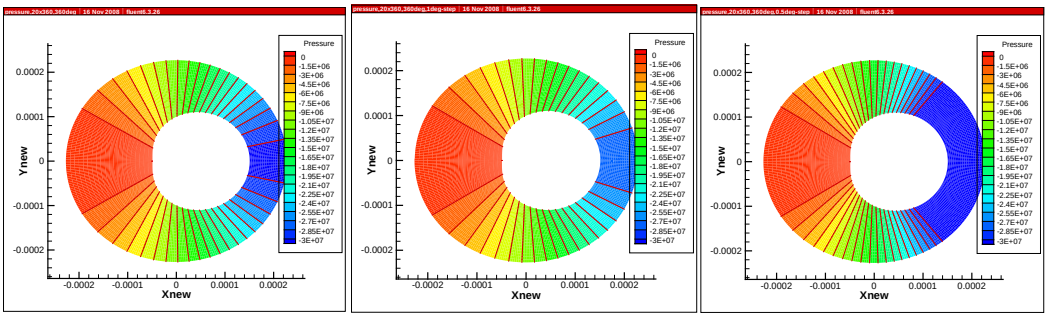

(b) X velocity(m/s)

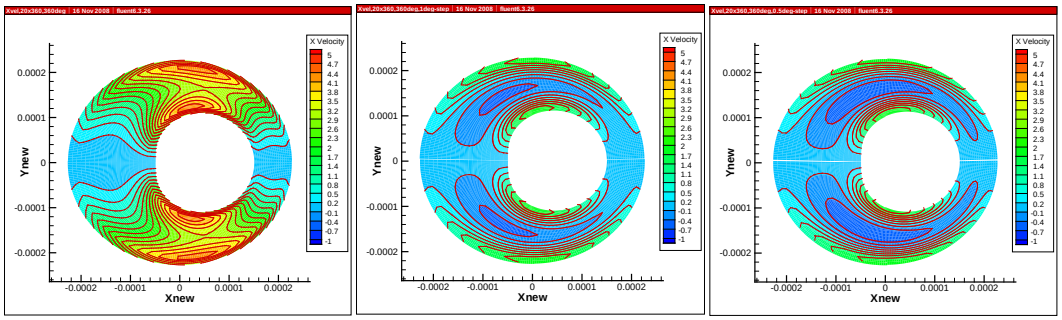

(c) Y velocity(m/s)

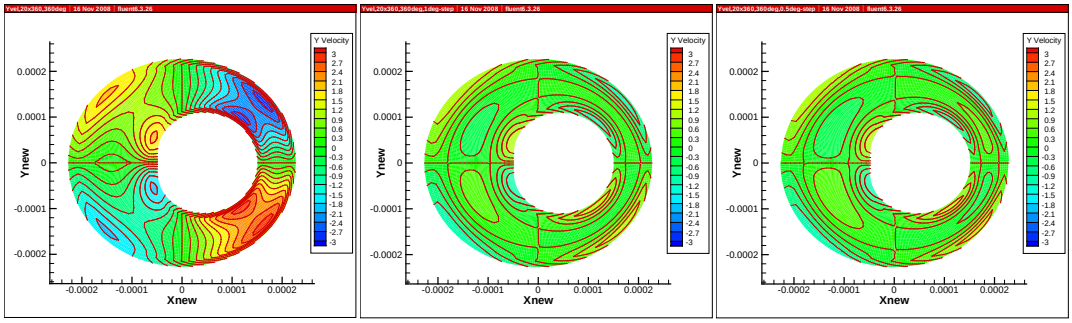

Figure 3.25 The comparison of the flow for a journal position at 360 degrees with the frequency of 500 Hz

Time step 5 deg/step 1 deg/step 0.5 deg/step

(a) Pressure (Pa)

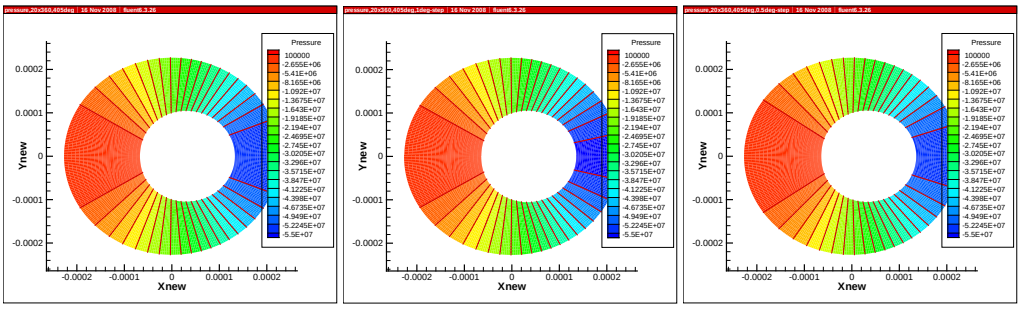

(b) X velocity(m/s)

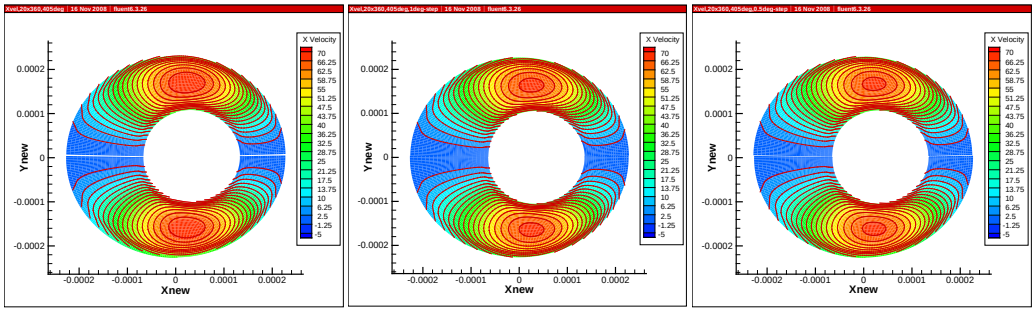

(c) Y velocity(m/s)

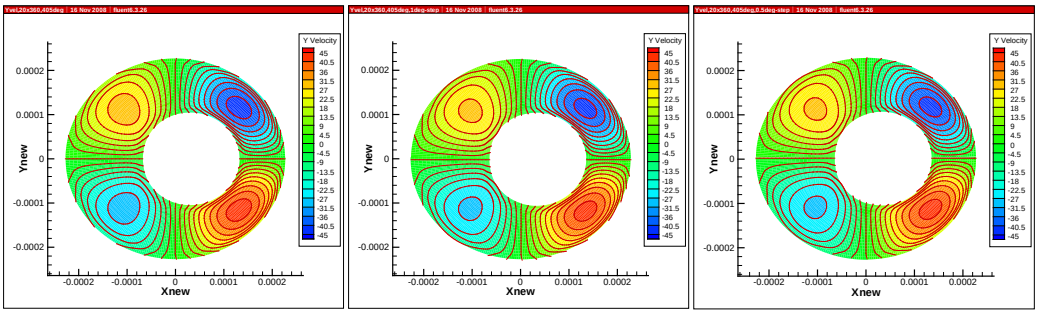

Figure 3.26 The comparison of the flow for a journal position at 405 degrees with the frequency of 500 Hz

Time step 5 deg/step 1 deg/step 0.5 deg/step

(a) Pressure (Pa)

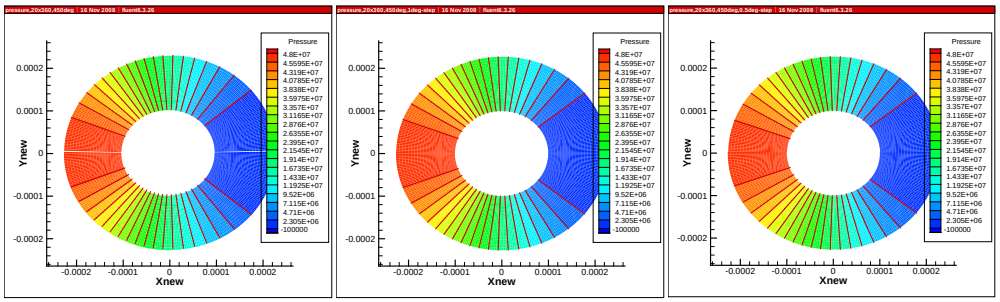

(b) X velocity(m/s)

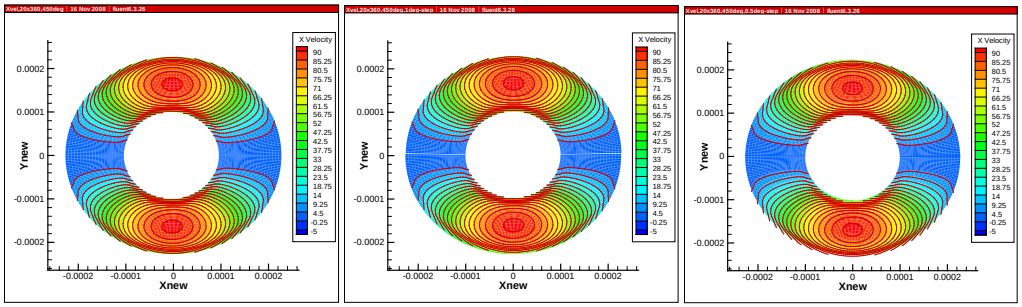

(c) Y velocity(m/s)

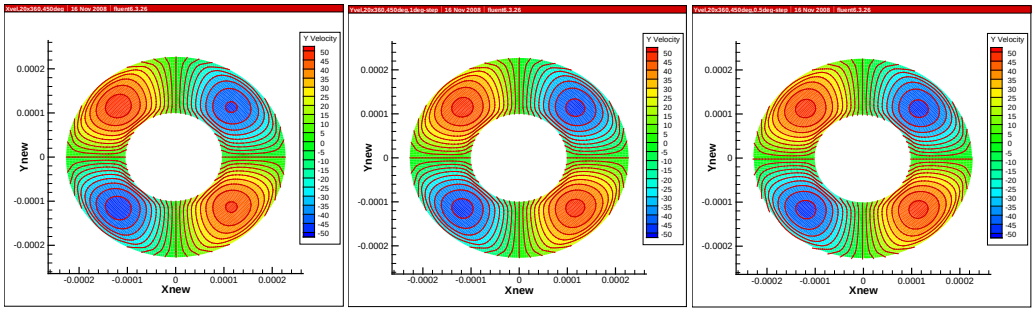

Figure 3.27 The comparison of the flow for a journal position at 450 degrees with the frequency of 500 Hz

3.4 The Fluent Solution in Comparison to Reynolds Equation Solutions and Reynolds Equation with Fluid Inertia Solutions

To facilitate comparison of the CFD results to standard Reynolds equation based solutions the CFD results were transformed to the same format. This section will be the section presented in this format.

FLUENT performed numerical calculations for 2-D squeeze film dampers for different cases including three journal frequencies, i.e. 200, 50, and 10 Hz, and three different amplitudes (e), i.e. 0.002, 0.001, and 0.0005 inches (eccentricity ε = 0.4, 0.2, and 0.1) were made. The pressure solutions obtained from **FLUENT** were compared to those obtained from Reynolds equations. The comparison and the conclusion follow.

Figures 3.29 through 3.30 show curves of pressure at journal positions defined in Figure 3.28 obtained by Fluent, Reynolds equation, and Reynolds equation with fluid inertia effect, respectively. According to the figures, it should be noted that the same line colors for each figure indicate the same positions of the journal. The journal positions start form $P(\theta_i,0)$ which is the position at the center of SFD to $P(\theta_i,\pi)$, that is the second angle represents the angle of the journal orbit with respect to one orbit being 0 to 2π. Since π to 2π is symmetric to 0 to π only the 0 to π journal angle are shown.

The pressure comparison for the journal frequency of 200 Hz and an amplitude of 0.002 inches in Figure 3.29 indicates that the pressure curves for all three cases are asymmetric since the magnitude of pressures at the upper part (θ = 0 - π) are larger than those at lower part ($\theta = \pi - 2\pi$). There is large deviation in pressure since the maximum pressure of Fluent (Figure 3.29a) is approximately three times higher than that of Reynolds equation (Figure 3.29b). It also is noted that the fluid inertia effect apparently contributes to the deviation in pressure as it can be clearly seen from the flat-line pressure curve of Reynolds equation at $P(\theta_i,\pi/2)$ which is totally different from the sinusoidal pressure curve of Fluent at the same journal position.

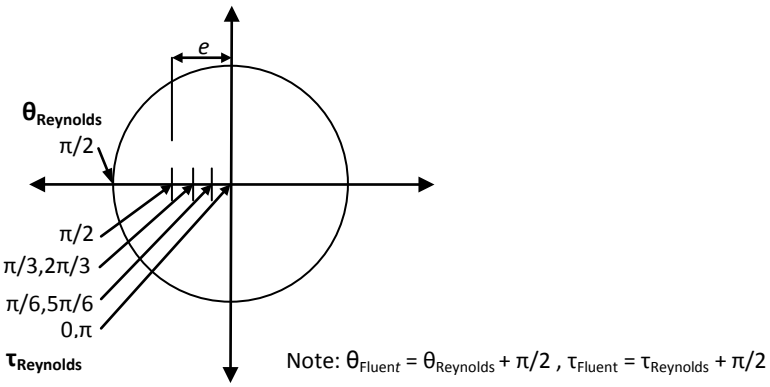

Figure 3.28 The positions of the journal's center for pressure comparison

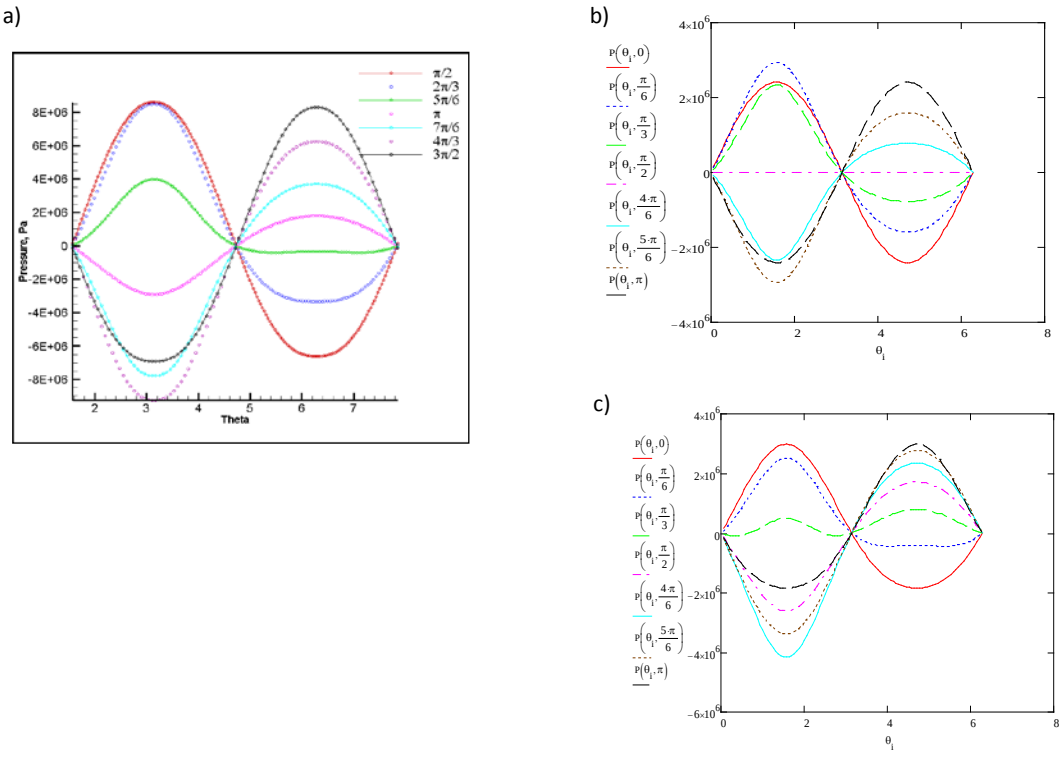

Figure 3.29 Pressure comparison for *Fe* = 200 Hz (Re_s = 10.13), *e* = 0.002 inches: a) Fluent b) Reynolds equation c) Reynolds equation with fluid inertia effect

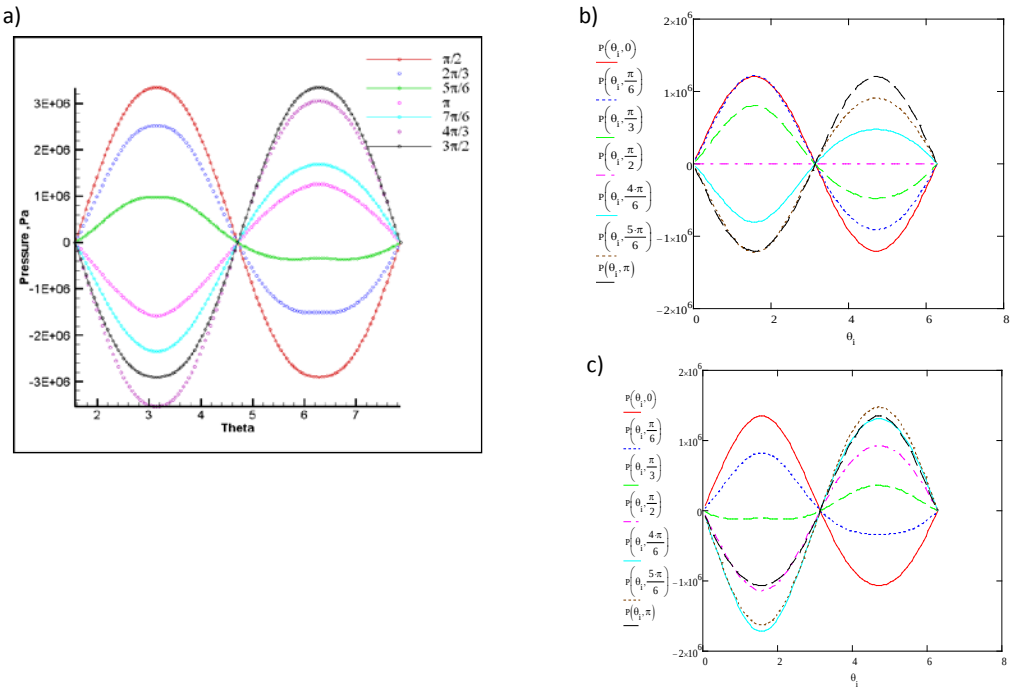

Figure 3.30 Pressure comparison for *Fe* = 200 Hz (Re_s = 10.13), *e* = 0.001 inches: a) Fluent b) Reynolds equation c) Reynolds equation with fluid inertia effect

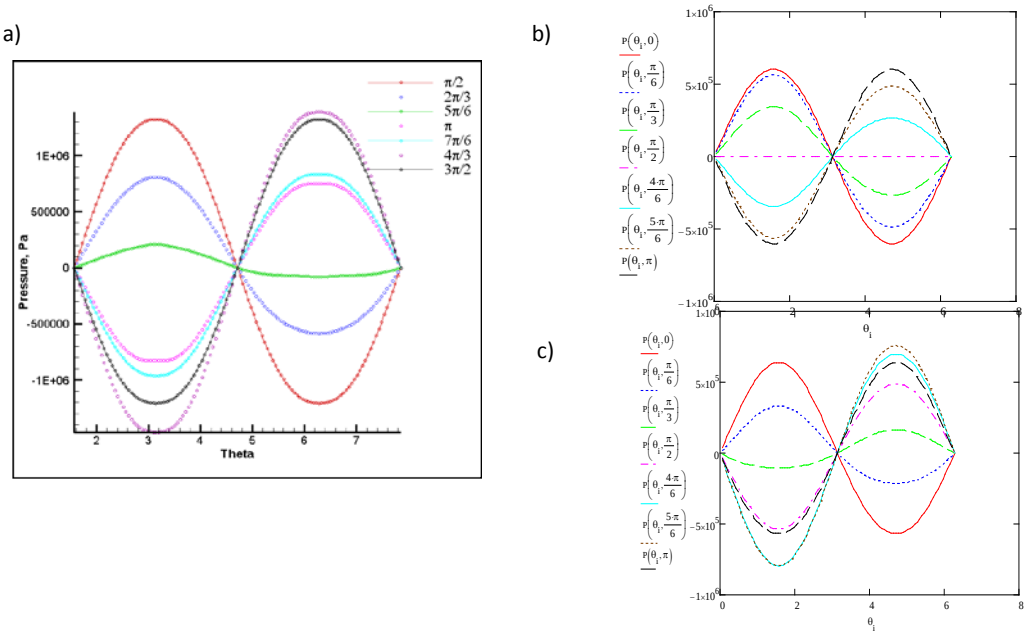

Figure 3.31 Pressure comparison for *Fe* = 200 Hz (Re_s = 10.13), *e* = 0.0005 inches: a) Fluent b) Reynolds equation c) Reynolds equation with fluid inertia effect

Figure 3.30 represents the pressure comparison for the journal frequency of 200 Hz and an amplitude of 0.001 inches. The pressure curves for the Reynolds equation case (Figure 3.30b) are symmetric whereas they are asymmetric for Fluent (Figure 3.30a) and Reynolds equation with fluid inertia effect cases (Figure 3.30c). The magnitude of maximum pressure of Fluent is almost three times higher than that of Reynolds equation. In addition, the fluid inertia effect apparently contributes to the deviation of the pressure curve of laminar flow obtained from Reynolds equation when comparing the Figure 3.30b to Figure 3.30c portraying the differences in both pattern and magnitude of pressure curves.

Figure 3.31 represents the pressure comparison for the journal frequency of 200 Hz and an amplitude of 0.0005 inches. The pressure curves are as the same in the pattern as those of those in Figure 3.31 but magnitudes are less than those of higher amplitudes.

The pressure comparison for the journal frequency of 50 Hz in Figures 3.32 through 3.34 also indicates, as well as for the 200 Hz case, that the pressure from Fluent does not agree well with the pressure from Reynolds equation. Figure 3.32 portrays the pressure comparison for the journal frequency of 50 Hz and an amplitude of 0.002 inches. The pressure curves for all three cases are asymmetric since the magnitude of pressures at the upper part are larger than those at lower part. There is large deviation in pressure since the maximum pressure of Fluent (Figure 3.32a) is approximately twice as large as that of Reynolds equation (Figure 3.32b). The fluid inertia effect also contributes to the deviation of pressures when comparing the laminar flow from Figure 3.32b to the laminar flow with fluid inertia effect from Figure 3.32c.

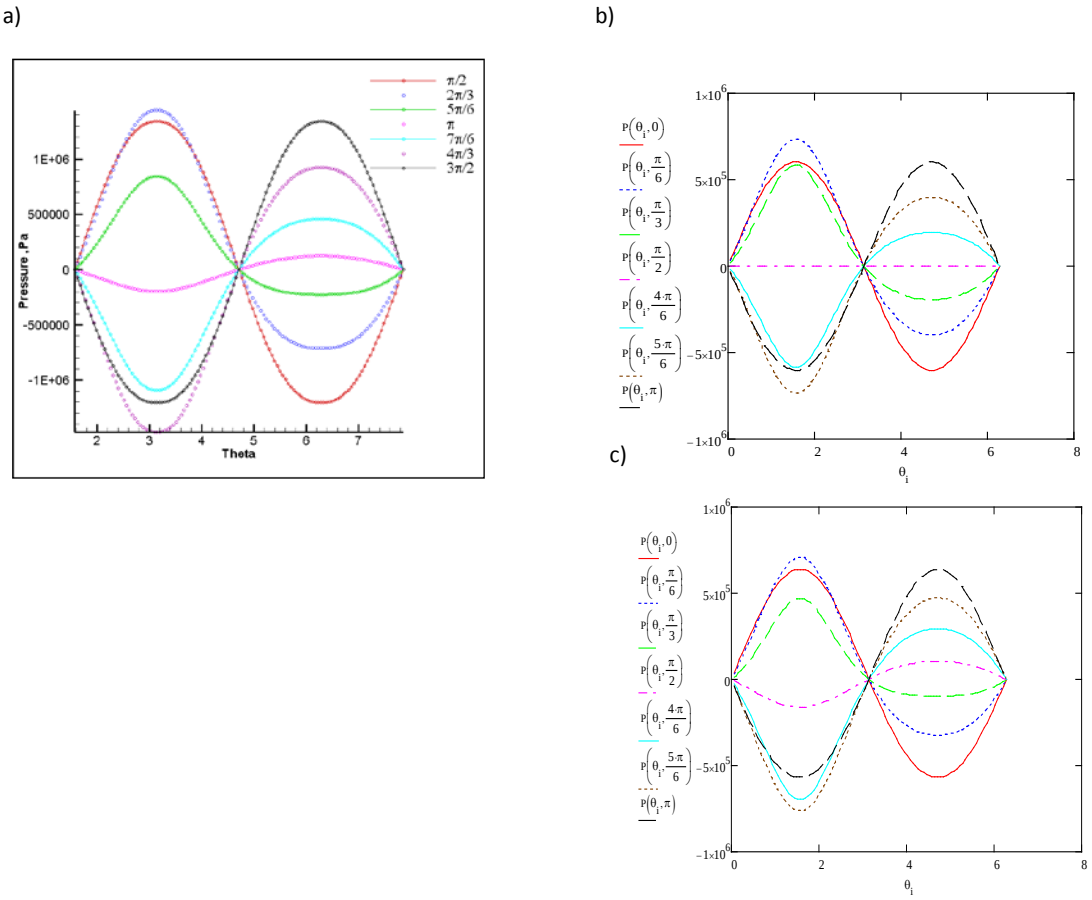

Figure 3.32 Pressure comparison for *Fe* = 50 Hz (Re_s = 2.53), *e* = 0.002 inches: a) Fluent b) Reynolds equation c) Reynolds equation with fluid inertia effect

Figure 3.33 represents the pressure comparison for the journal frequency of 50 Hz and an amplitude of 0.001 inches. The pressure curves for are comparably symmetric since the magnitudes of pressures at the upper part ($\theta = 0 - \pi$) are comparable to those at lower part ($\theta = \pi - 2\pi$). The magnitude of maximum pressure of Fluent is approximately one and a haft times higher than that of Reynolds equation. In addition, the fluid inertia effect apparently contributes to the deviation of the pressure curve from laminar flow obtained from Reynolds equation when comparing the Figure 3.33b to Figure 3.33c indicating the differences in both pattern and magnitude of pressure curves.

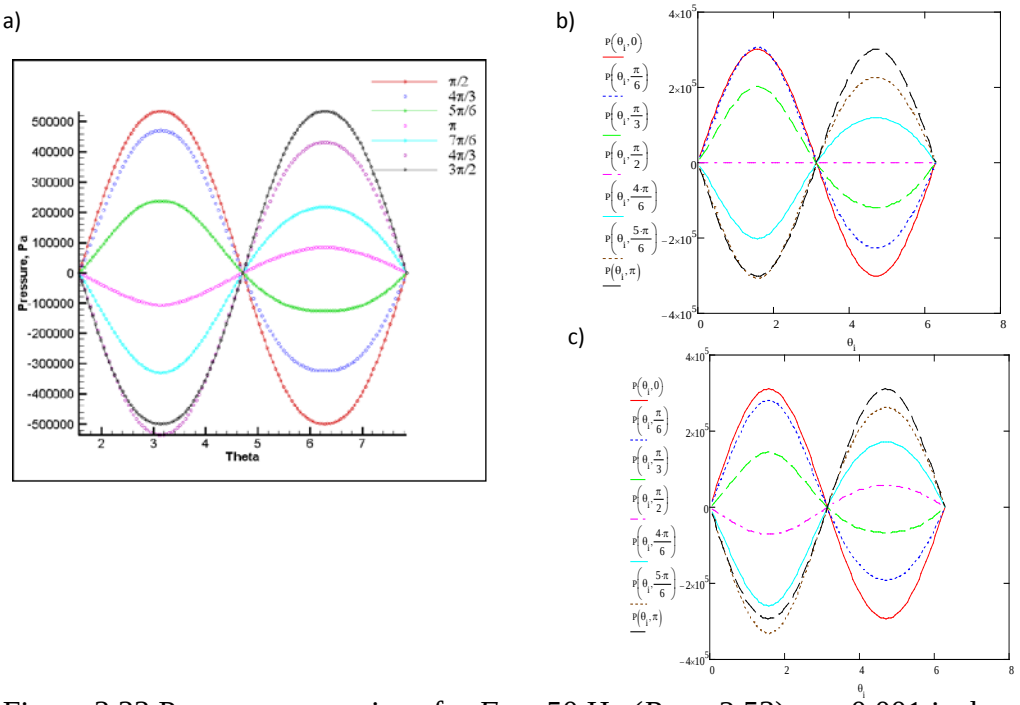

Figure 3.33 Pressure comparison for *Fe* = 50 Hz (Re_s = 2.53), *e* = 0.001 inches: a) Fluent b) Reynolds equation c) Reynolds equation with fluid inertia effect

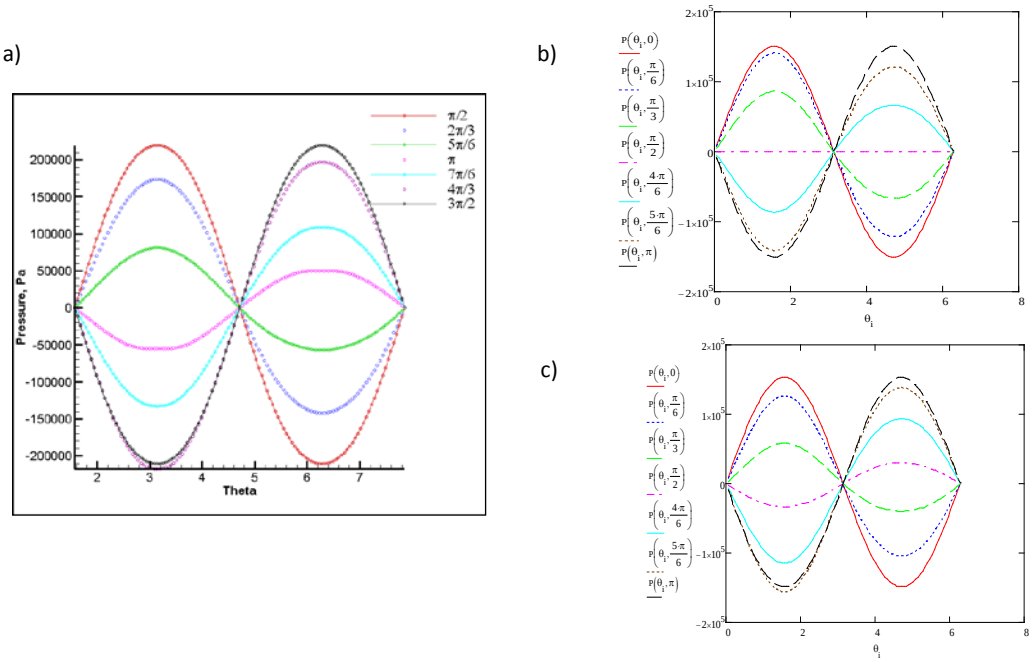

Figure 3.34 Pressure comparison for *Fe* = 50 Hz (Re_s = 2.53), *e* = 0.0005 inches: a) Fluent b) Reynolds equation c) Reynolds equation with fluid inertia effect

Figure 3.34 represents the pressure comparison for the journal frequency of 50 Hz and an amplitude of 0.0005 inches. The pressure curves portray the deviation of pressures identical to that from the 0.001 inches case in Figure 3.33.

Figures 3.35 through 3.37 represent the pressure comparison for the journal frequency of 10 Hz. The pressure curves indicate that the deviation of pressures from Reynolds equation is less than that from the cases of 50 Hz and 200 Hz. Figure 3.35 portrays the pressure comparison for the journal frequency of 10 Hz and an amplitude of 0.002 inches. The pressure curves for all three cases are symmetric. There is less deviation in pressures since the maximum pressure of Fluent (Figure 3.35a) is comparable to that of Reynolds equation (Figure 3.35b). The fluid inertia effect also barely contributes to the deviation of pressures when comparing the laminar flow from Figure 3.35b to the laminar flow with fluid inertia effect from Figure 3.35c.

Figure 3.36 represents the pressure comparison for the journal frequency of 10 Hz and an amplitude of 0.001 inches. The pressure curves are symmetric since the magnitudes of pressures at the upper part are almost identical to those at lower part. The magnitude of maximum pressure of Fluent is a little bit higher than that of Reynolds equation. In addition, the fluid inertia effect hardly contributes to the deviation of the pressure curve from laminar flow obtained from Reynolds equation when comparing the Figure 3.36b to Figure 3.36c.

Figure 3.37 represents the pressure comparison for the journal frequency of 10 Hz and an amplitude of 0.0005 inches. The pressure curves portray the deviation of pressures identical to that from the 0.001 inches case in Figure 3.36. With the lowest journal amplitude and frequency, it indicates that there is the least deviation of the pressure curves from the laminar flow.

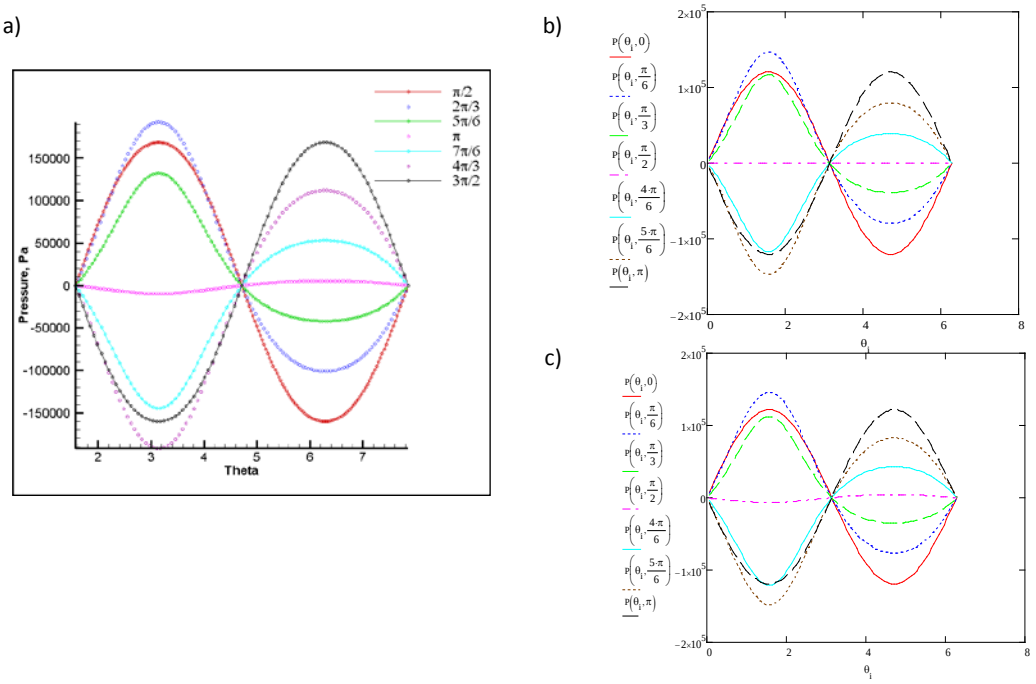

Figure 3.35 Pressure comparison for *Fe* = 10 Hz (Re_s = 0.51), *e* = 0.002 inches: a) Fluent b) Reynolds equation c) Reynolds equation with fluid inertia effect

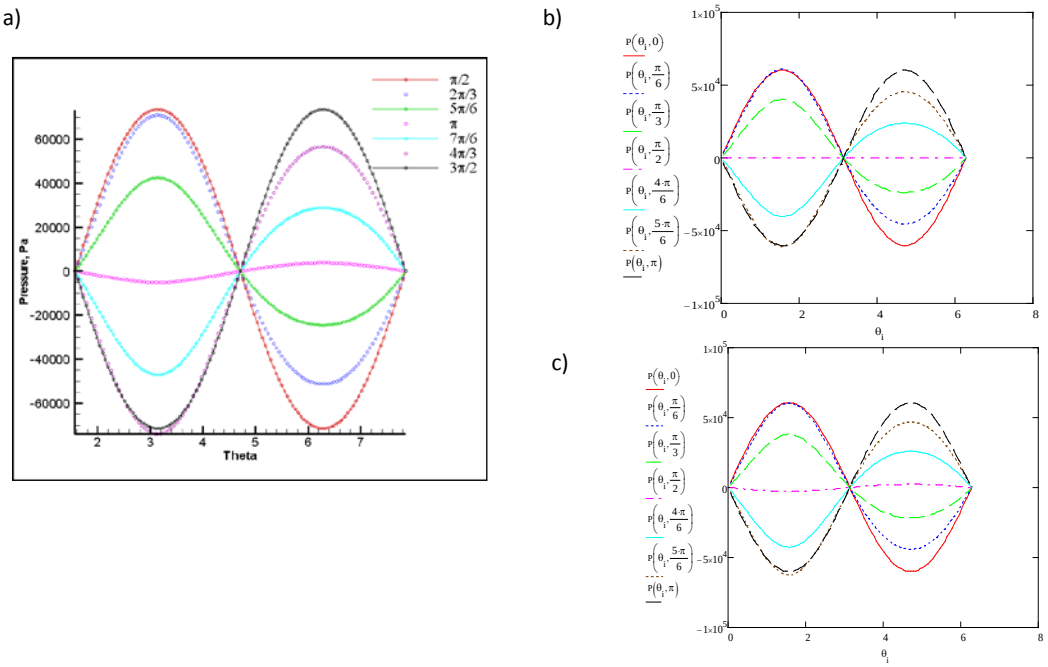

Figure 3.36 Pressure comparison for *Fe* = 10 Hz (Re_s = 0.51), *e* = 0.001 inches: a) Fluent b) Reynolds equation c) Reynolds equation with fluid inertia effect

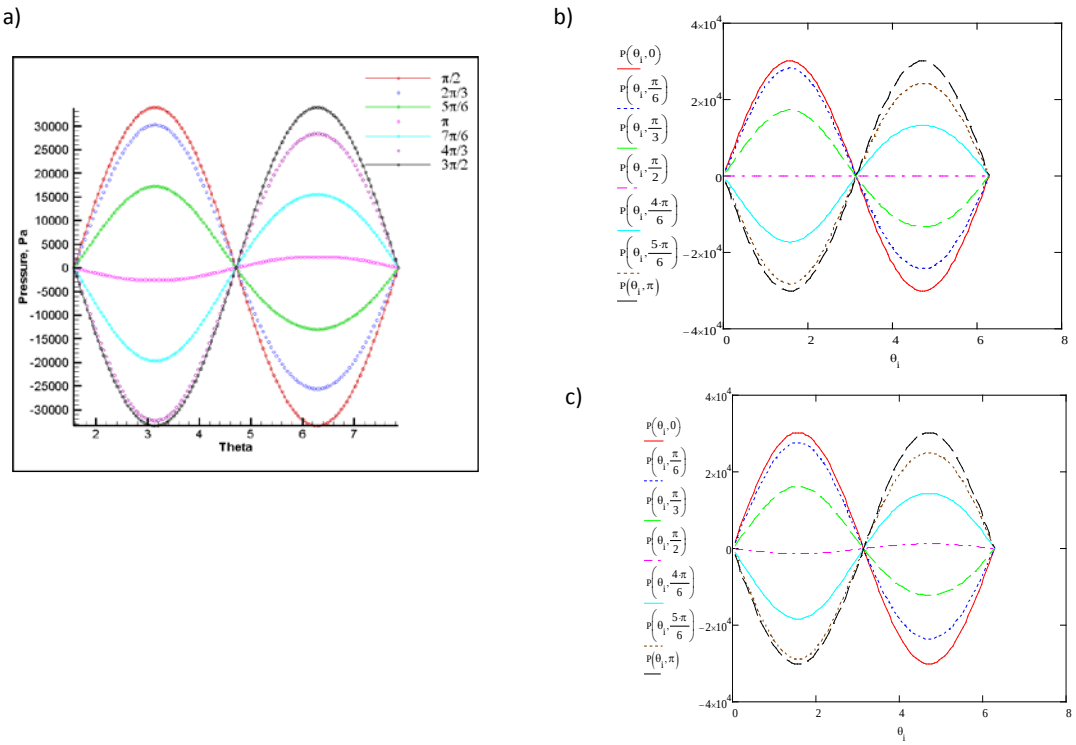

Figure 3.37 Pressure comparison for *Fe* = 10 Hz (Re_s = 0.51), *e* = 0.0005 inches: a) Fluent b) Reynolds equation c) Reynolds equation with fluid inertia effect

Figures 3.38 through 3.40 show curves of pressures from Fluent solutions versus times for a fixed point on the journal ($\theta_{Fluent} = \pi$) and the journal frequencies of 200 , 50, and 10 Hz, respectively. The pressure curves for all cases indicate a phase shift for the location of the maximum pressure as the journal amplitude increases. The maximum pressure at the journal amplitude of 0.0005 inches is almost in-phase with the journal position whereas the phase is shifted as the journal amplitude is increased to 0.001 inches and the phase shift is at maximum for the journal amplitude of 0.002 inches. It is noted that the pressures fluctuate in values for the 200 Hz case whereas the pressure curve is a smooth line for the 10 Hz case which is similar to that for the laminar flow from Reynolds equation solutions. This indicates that the flow is likely to be turbulent at the high frequencies, or high Re_s.

The phase shift also shows the same trend with the pressure curves from Reynolds equation solutions and Reynolds equation with fluent inertia solutions as depicted in Figures 3.41 through 3.46.

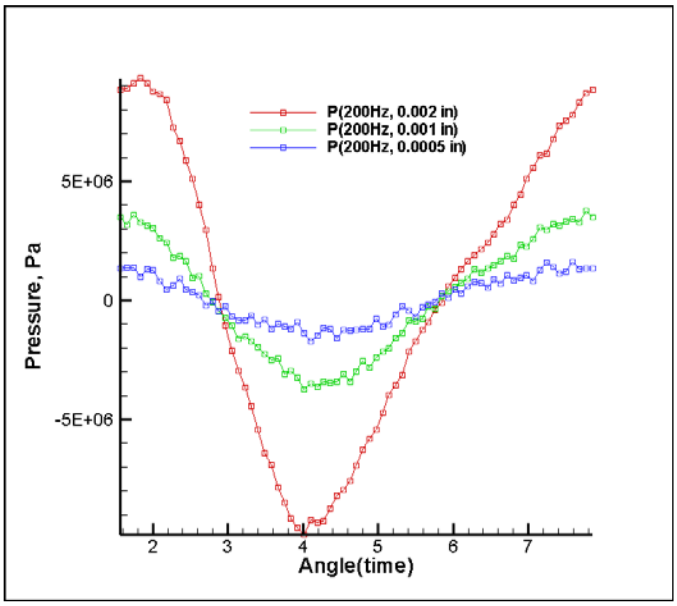

Figure 3.38 Pressures at different times (angles) for Fluent solutions, $\theta_{Fluent} = \pi$, Fe = 200 Hz (Re_s = 10.13)

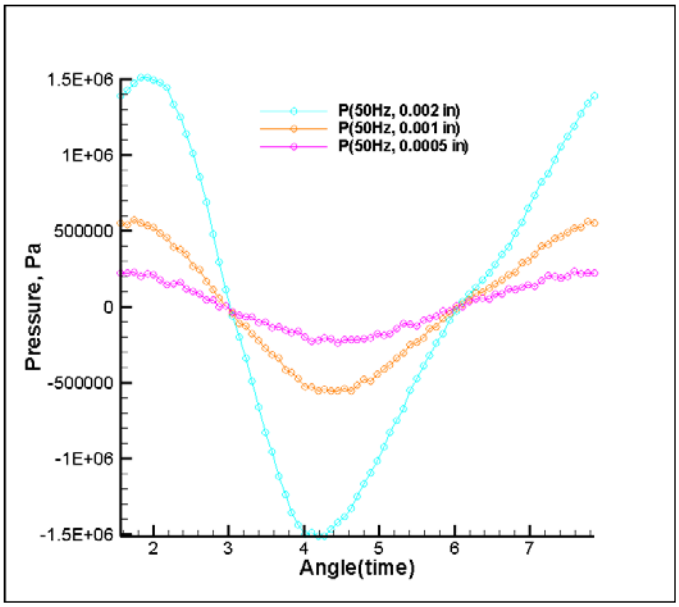

Figure 3.39 Pressures at different times (angles) for Fluent solutions, $\theta_{Fluent} = \pi$, Fe = 50 Hz (Re_s = 2.53)

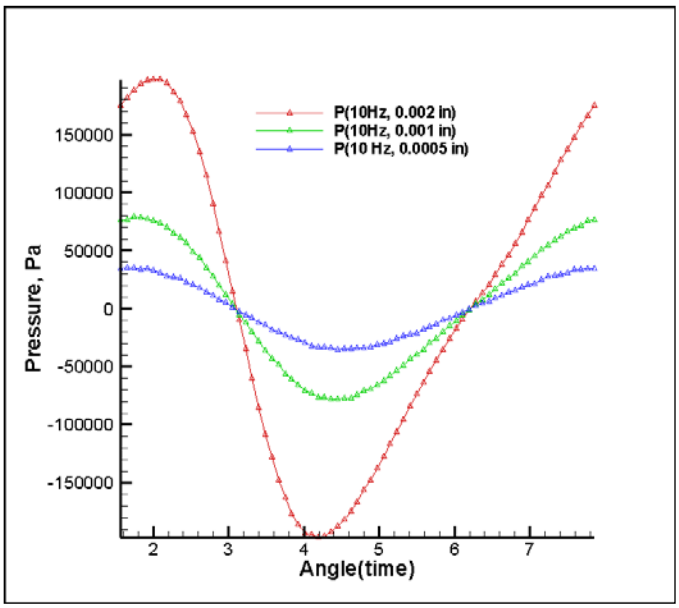

Figure 3.40 Pressures at different times (angles) for Fluent solutions, $\theta_{Fluent} = \pi$, Fe = 10 Hz (Re_s = 0.51)

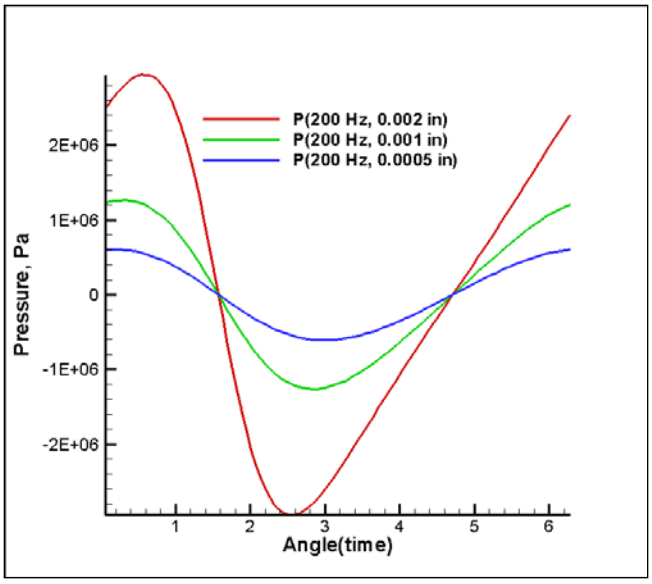

Figure 3.41 Pressures at different times (angles) for Reynolds equations, $\theta_{Reynolds} = \pi/2$, Fe = 200 Hz (Re_s = 10.13)

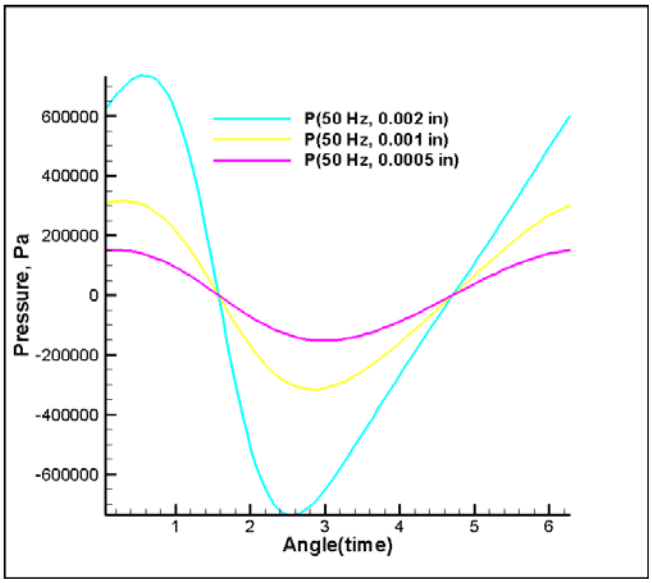

Figure 3.42 Pressures at different times (angles) for Reynolds equations $\theta_{Reynolds} = \pi$, Fe = 50 Hz (Re_s = 2.53)

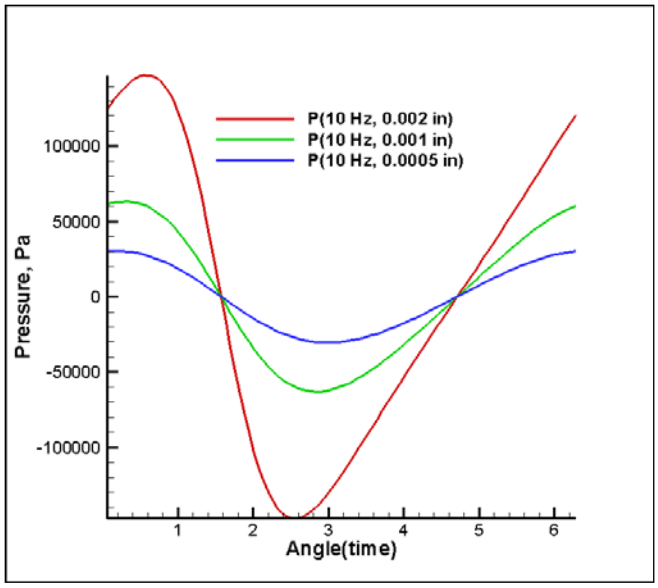

Figure 3.43 Pressures at different times (angles) for Reynolds equations $\theta_{Reynolds} = \pi$, Fe = 10 Hz (Re_s = 0.51)

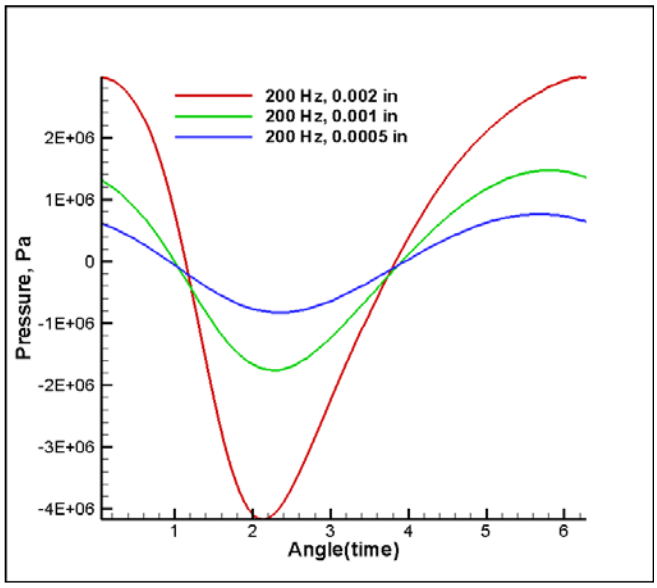

Figure 3.44 Pressures at different times (angles) for Reynolds equations with inertia, $\theta_{Reynolds} = \pi$, Fe = 200 Hz (Re_s = 10.13)

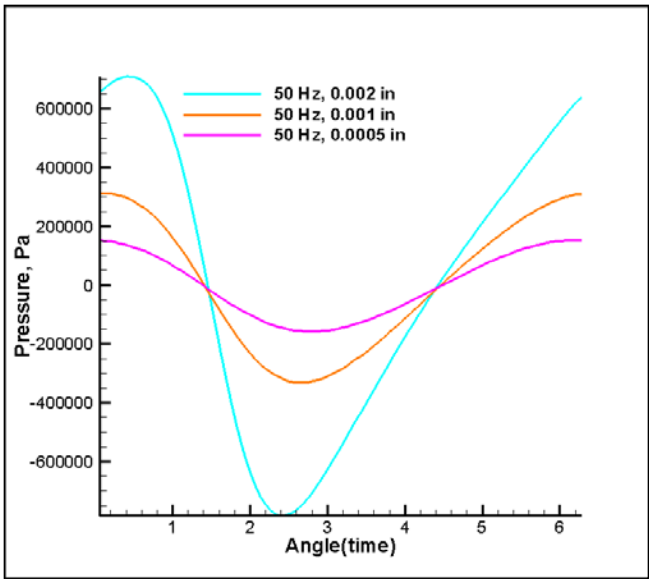

Figure 3.45 Pressures at different times (angles) for Reynolds equations with inertia, $\theta_{\text{Reynolds}} = \pi$, Fe = 50 Hz (Re_s = 2.53)

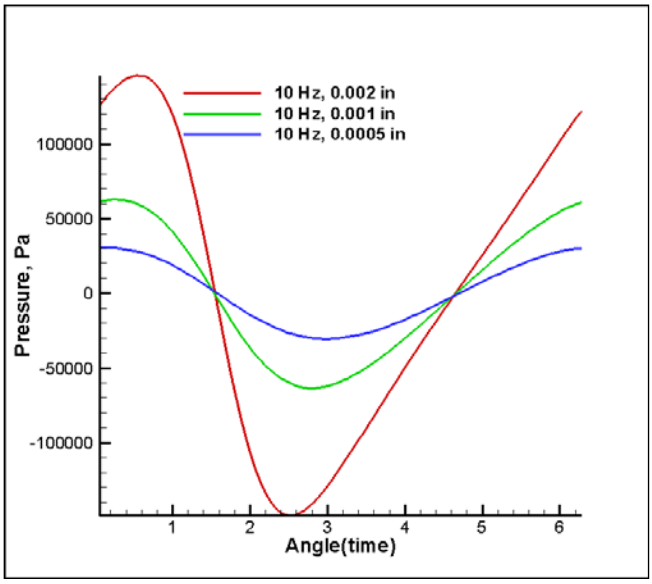

Figure 3.46 Pressures at different times (angles) for Reynolds equations with inertia, $\theta_{Reynolds} = \pi$, Fe = 10 Hz (Re_s = 0.51)

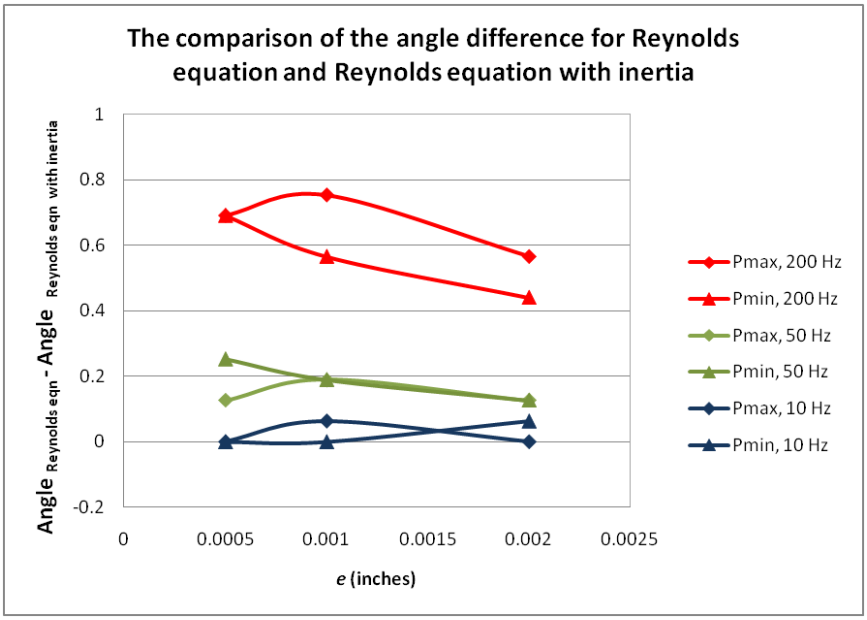

Figure 3.47 Angle difference ($Angle_{Reynolds\ eqn} - Angle_{Reynolds\ eqn\ with\ inertia}$) for the location of max/min pressure

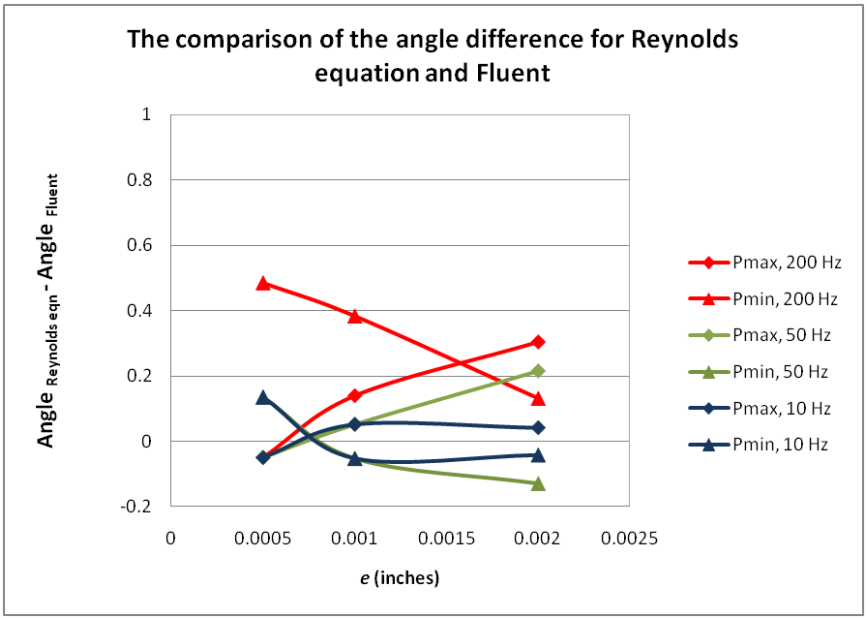

Figure 3.48 Angle difference ($Angle_{Reynolds\ eqn} - Angle_{Fluent}$) for the location of max/min pressure

Figure 3.47 shows the angle differences between Reynolds equation solutions and Reynolds equation with fluid inertia solutions with respect to the journal amplitudes and frequencies for the location of maximum and minimum pressure. The angle differences are highest for the 200 Hz case whereas they are insignificant for the 10 Hz case. This indicates that, at high journal frequencies, the fluid inertia effect also contributes to the deviation of the angle of maximum and minimum pressures.

Figure 3.48 shows the angle differences between Reynolds equation solutions and Fluent solutions for the location of maximum and minimum pressure. The angle differences are lower than those from previous cases and insignificant for the low frequency cases. At high frequencies, the angle differences for minimum pressure case decrease as the amplitudes increase whereas the angle differences for maximum pressure case increase as the amplitudes increase. This indicates that, at high frequencies, the significant deviation of the angle of maximum and minimum pressures is due to the non-laminar flow in SFDs.

The deviation of the pressure for all cases is examined by observing maximum pressures portrayed in Table 3.1. It is noted that the pressures vary directly to the journal eccentricity and frequency. In addition, the maximum bulk velocity, U_{max}, the Squeeze film Reynolds number, and the Reynolds number, *Re*, are also specified in this table. To compare with pipe flow, the Reynolds number, $Re = \rho U_{max}(2c)/\mu$, is defined with hydraulic diameter, $D_H = 2c$. This maximizes at 4,053.84 which is in transition zone for pipes.

Table 3.1 Maximum pressure and turbulence intensity

ε	Hz	U_{max}	$Re=\rho U_{max}(2c)/\mu$	$Res=\rho\omega c^2/\mu$	$P_{max,Fluent}$	$P_{max,\ Reynolds\ eqn}$	$P_{max,inertia}$	$P_{neg.\ max,Fluent}$	$P_{neg.\ max,Reynolds}$	$P_{neg.\ max,inertia}$	$turbulence\ intensity_{max}$
		m/s			Pa	Pa	Pa	Pa	Pa	Pa	
0.4	200	31.92	4053.84	10.13	8.59E+06	2.94E+06	2.98E+06	-9.25E+06	-2.94E+06	-4.16E+06	4.70E+00
0.4	50	7.98	1013.46	2.53	1.44E+06	7.35E+05	7.07E+05	-1.47E+06	-7.35E+05	-7.62E+05	3.02E+00
0.4	10	1.6	203.2	0.51	1.93E+05	1.47E+05	1.46E+05	-1.92E+05	-1.47E+05	-1.48E+05	1.93E+00
0.2	200	15.96	2026.92	10.13	3.34E+06	1.23E+06	1.48E+06	-3.54E+06	-1.23E+06	-1.72E+06	1.93E+00
0.2	50	3.99	506.73	2.53	5.34E+05	3.06E+05	3.11E+05	-5.36E+05	-3.06E+05	-3.31E+05	1.23E+00
0.2	10	0.8	101.6	0.51	7.36E+04	6.13E+04	6.07E+04	-7.40E+04	-6.13E+04	-6.23E+04	7.80E-01
0.1	200	7.98	1013.46	10.13	1.39E+06	6.03E+05	7.58E+05	-1.47E+06	-6.03E+05	-7.96E+05	6.80E-01
0.1	50	1.99	252.73	2.53	2.19E+05	1.51E+05	1.53E+05	-2.18E+05	-1.51E+05	-1.56E+05	4.50E-01
0.1	10	0.4	50.8	0.51	3.39E+04	3.02E+04	3.03E+04	-3.34E+04	-3.02E+04	-3.01E+04	3.00E-01

Positive maximum pressure for all cases in Table 3.1 are plotted in Figure 3.49 to show the trend of pressure versus $\rho.(U_{max})^2/2$. According to the curves, the pressures increase as $\rho.(U_{max})^2/2$ increases. The curves are divided into two groups including the laminar flow which is the group of pressures from Reynolds equation and pressures from Reynolds equation with fluid inertia effect and the group of pressure from Fluent. The difference in pressure between these two groups increases as $\rho.(U_{max})^2/2$ increases and this difference is due to the non-laminar flow.

Negative maximum pressure for all cases in Table 3.1 are plotted in Figure 3.50 to portray the trend of pressures versus $\rho.(U_{max})^2/2$. According to the curves, the pressure magnitudes increase as $\rho.(U_{max})^2/2$ increase. The curves can be divides into two groups including the laminar flow which is the group of pressures from Reynolds equation and pressures from Reynolds equation with fluid inertia effect and the group of pressure from Fluent. In addition, the curves which show significant difference in pressures between Reynolds equation and Reynolds equation with fluid inertia effect indicate inertia effect contribute to the deviation of pressure from laminar flow. The difference in pressure between these two group increases as $\rho.(U_{max})^2/2$ increases and this difference is due to the non-laminar flow.

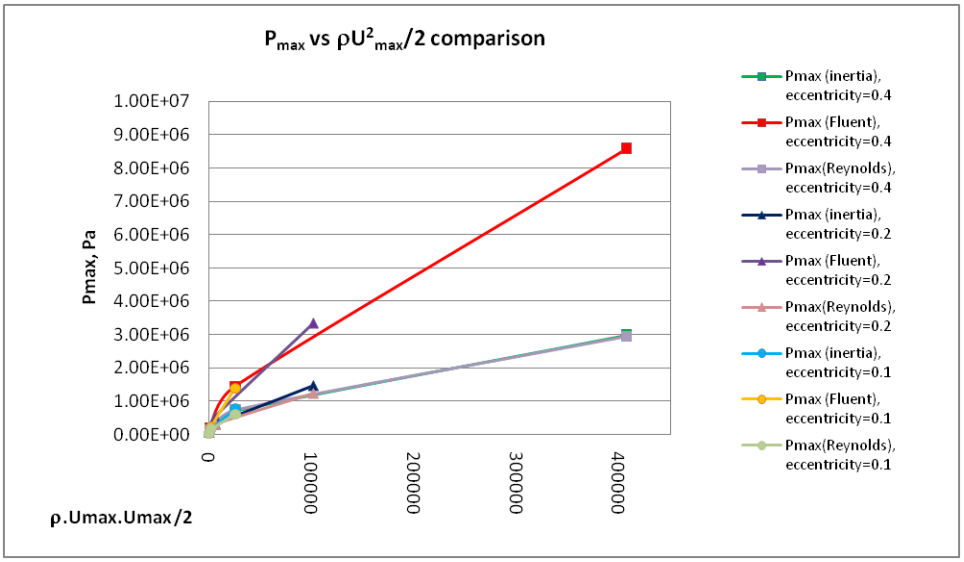

Figure 3.49 Positive maximum pressure comparison

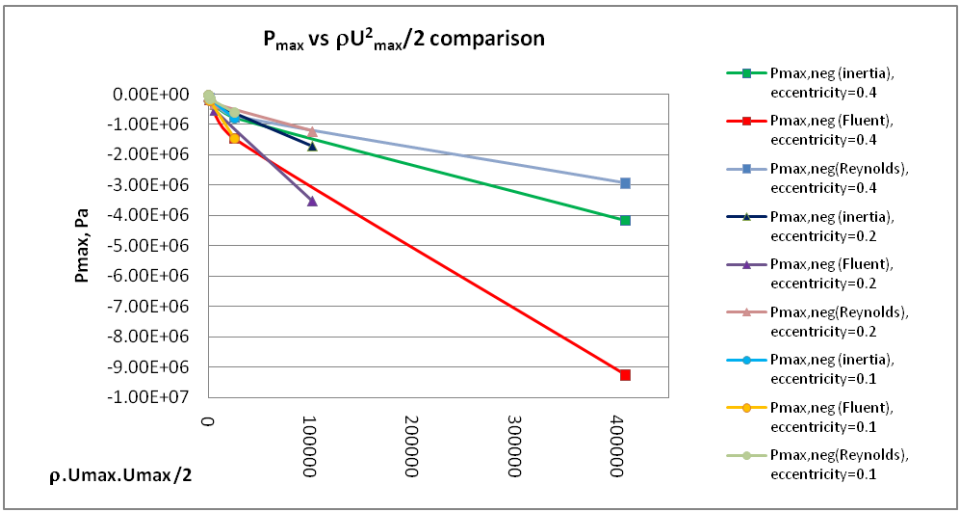

Figure 3.50 Negative maximum pressure comparison

a)

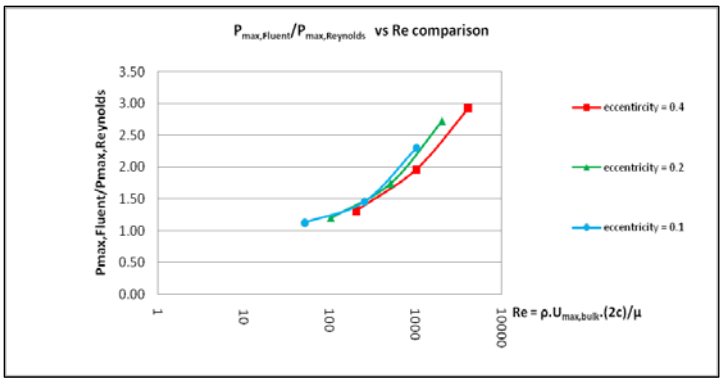

b)

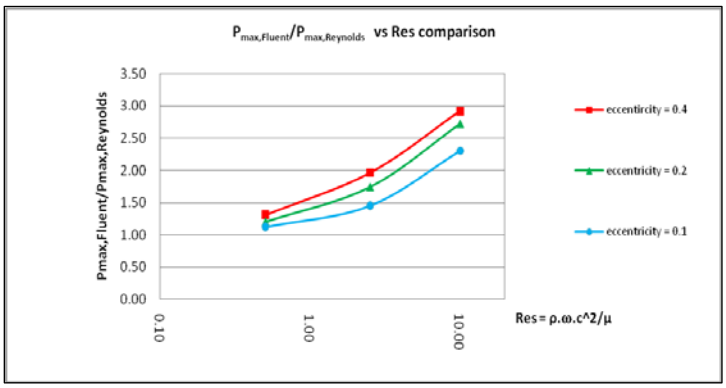

Figure 3.51 $P_{max,Fluent}/P_{max,Reynolds}$ comparison; a) *Re* b) Re_s

Figure 3.51 shows the maximum pressures from Fluent compared to those from Reynolds equation. The figure indicates that the deviation of pressure increases as *Re* and Re_s increase. It is noted that the pressures from Fluent are comparable to those from Reynolds equation at low *Re* and Re_s and consequently the laminar flow is regarded as the only flow accounted for SFDs at low frequencies. However, at high *Re* and Re_s, the laminar flow is not the only flow accounted for SFDs at all since there is significant deviation in pressure. The fluid inertia effect and non-laminar flow are accounted for SFDs operating at a high frequency. The Reynolds number based upon the maximum velocity does a better job of collapsing all the data to a common curve than does the

Reynolds number based upon journal frequency, Re_s. The squeeze film damper is different from a journal bearing as both surfaces do not rotate. Therefore ω represents the rate of compression which generates V_{max} as opposed to the rate of viscous drag generating the tangential velocity. The difference in fluid velocity production is the reason *Re* is more appropriate than Re_s.

In order to observe indications of turbulent flow from the Fluent solutions, Figures 3.52 through 3.54 show the velocity vector radial profiles and the turbulent intensity for journal frequency of 200 Hz and the journal amplitudes of 0.002, 0.001, and 0.0005 inches, respectively. It is noted that the velocity vector radial profile and the turbulent intensity vary directly to the journal amplitude. The turbulence intensity is a maximum in the boundary layer where U_{max} occurs. The velocity profiles are not parabolic and are tending towards a turbulent flow profile.

Figures 3.55 through 3.57 show the velocity vector radial profiles and the turbulent intensity for journal frequency of 50 Hz and the journal amplitudes of 0.002, 0.001, and 0.0005 inches, respectively. It is also noted that the velocity vector and the turbulent intensity vary directly to the journal amplitude. In addition, for the same journal amplitude, the values from 50 Hz case are less than those from the 200 Hz case.

Figures 3.58 through 3.60 show the velocity vector radial profiles and the turbulent intensity for journal frequency of 10 Hz and the journal amplitudes of 0.002, 0.001, and 0.0005 inches, respectively. The velocity vector radial profiles are more parabolic as assumed for the Reynolds equation solution. This is consistent with the pressure fields for this case being the most similar to the Reynolds equation solution. The turbulence intensities have decreased significantly in value again indicating the flow is tending towards laminar flow.

a) b)

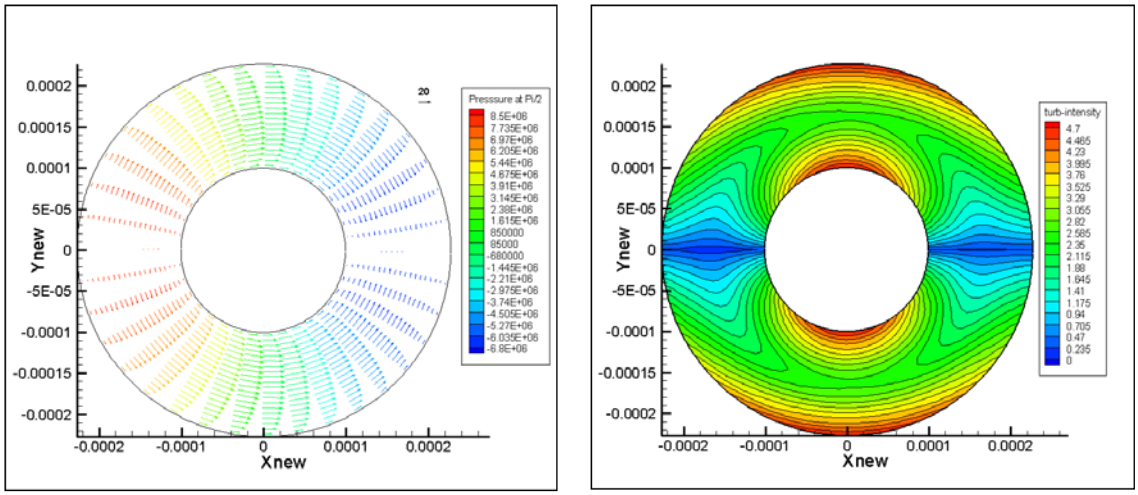

Figure 3.52 Fluent solutions for Fe=200 Hz, e=0.002 inches; a) velocity vector b) contours of turbulence intensity

a) b)

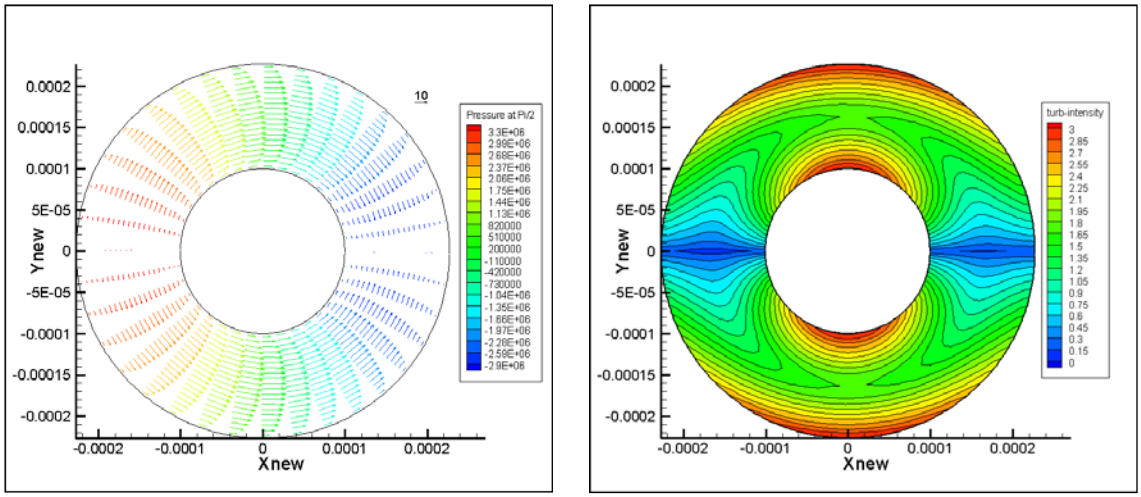

Figure 3.53 Fluent solutions for Fe=200 Hz, e=0.001 inches; a) velocity vector b) contours of turbulence intensity

a) b)

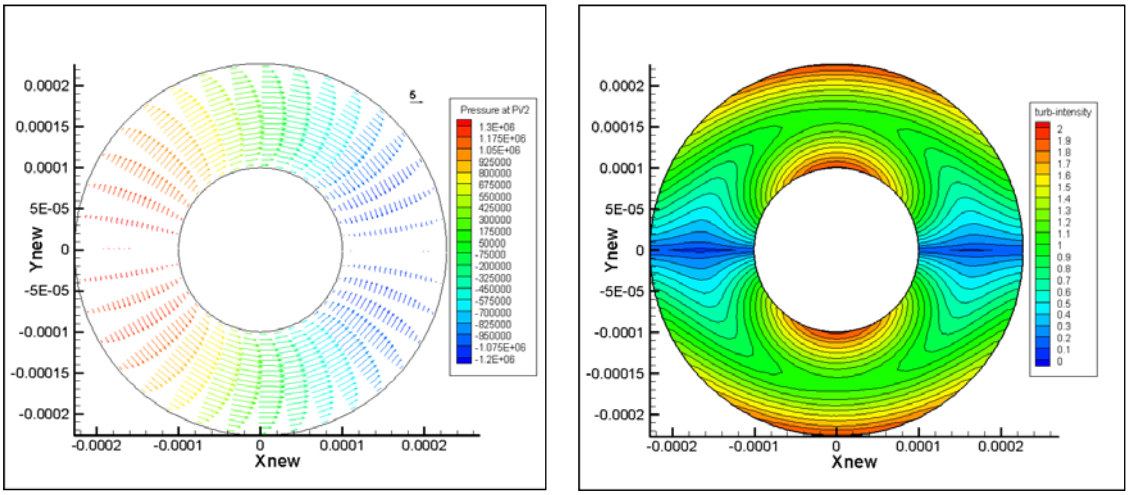

Figure 3.54 Fluent solutions for Fe=200 Hz, e=0.0005 inches; a) velocity vector b) contours of turbulence intensity

a) b)

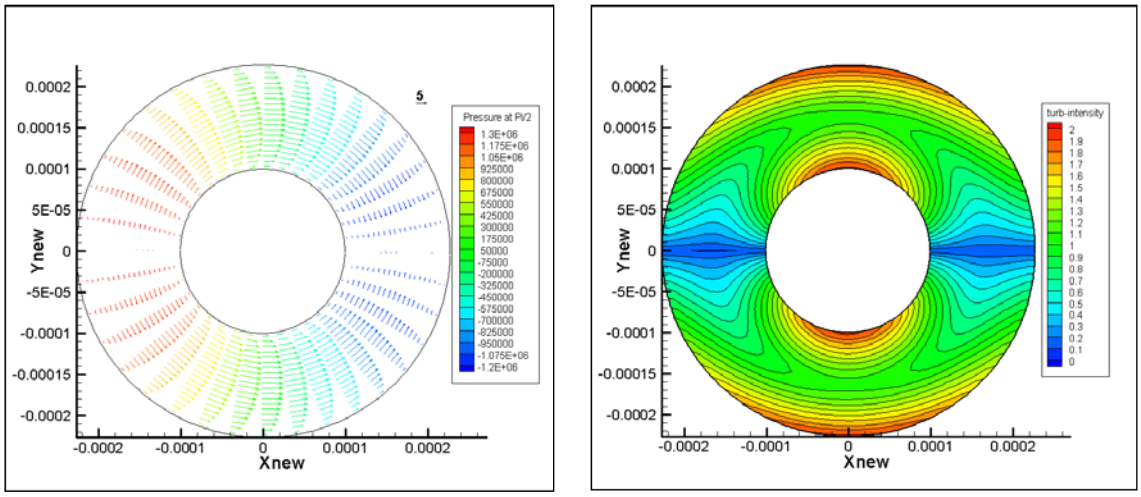

Figure 3.55 Fluent solutions for Fe=50 Hz, e=0.002 inches; a) velocity vector b) contours of turbulence intensity

a) b)

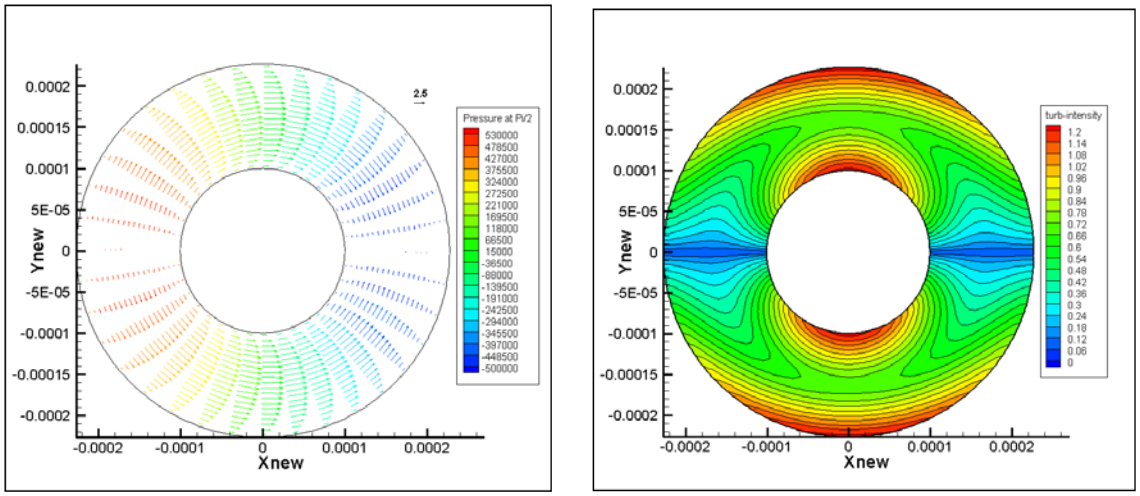

Figure 3.56 Fluent solutions for Fe=50 Hz, e=0.001 inches; a) velocity vector b) contours of turbulence intensity

a) b)

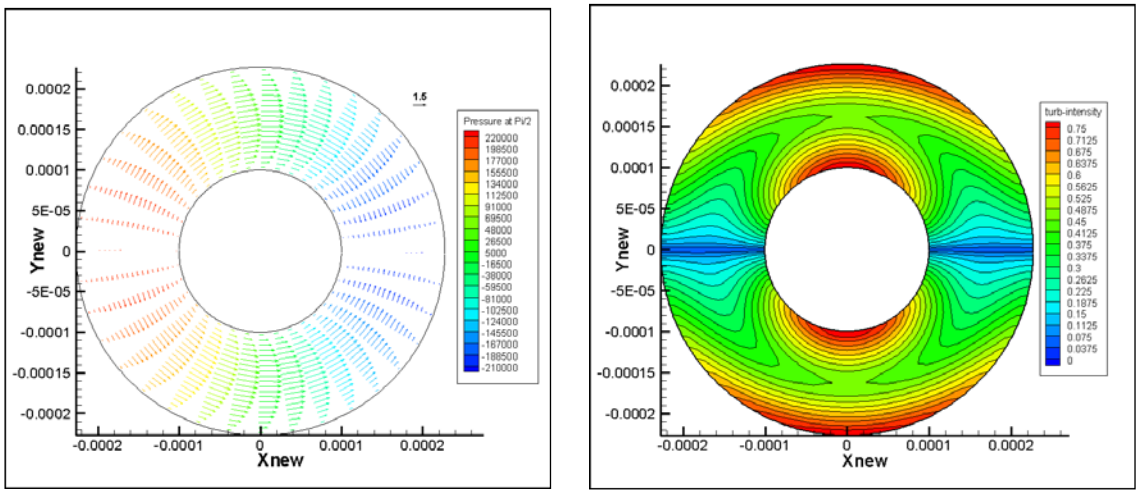

Figure 3.57 Fluent solutions for Fe=50 Hz, e=0.0005 inches; a) velocity vector b) contours of turbulence intensity

a) b)

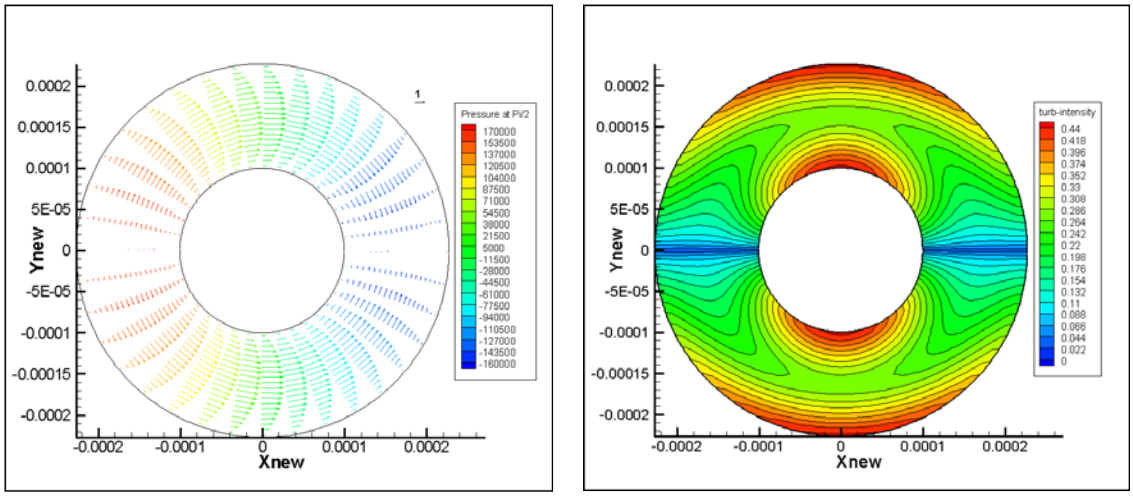

Figure 3.58 Fluent solutions for Fe=10 Hz, e=0.002 inches; a) velocity vector b) contours of turbulence intensity

a) b)

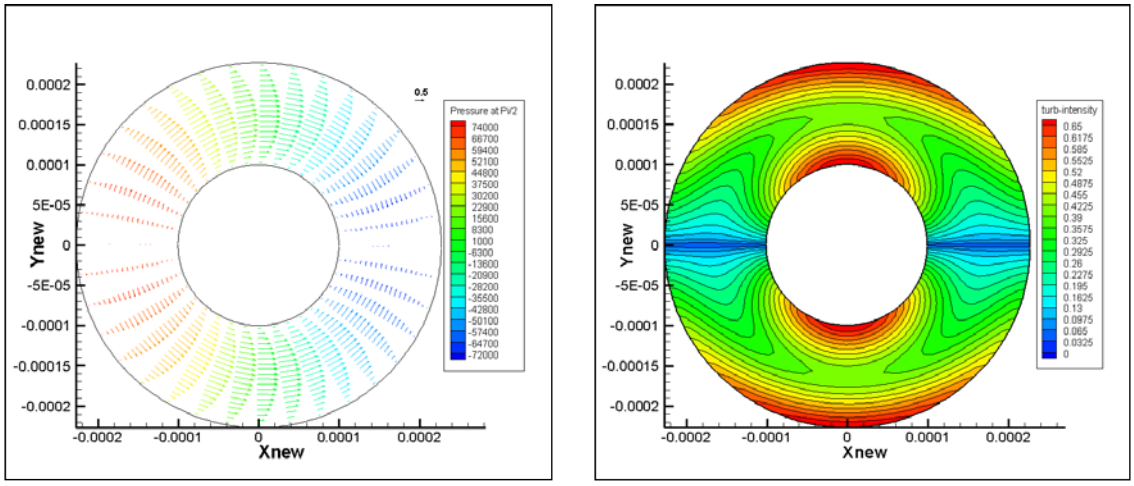

Figure 3.59 Fluent solutions for Fe=10 Hz, e=0.001 inches; a) velocity vector b) contours of turbulence intensity

a) b)

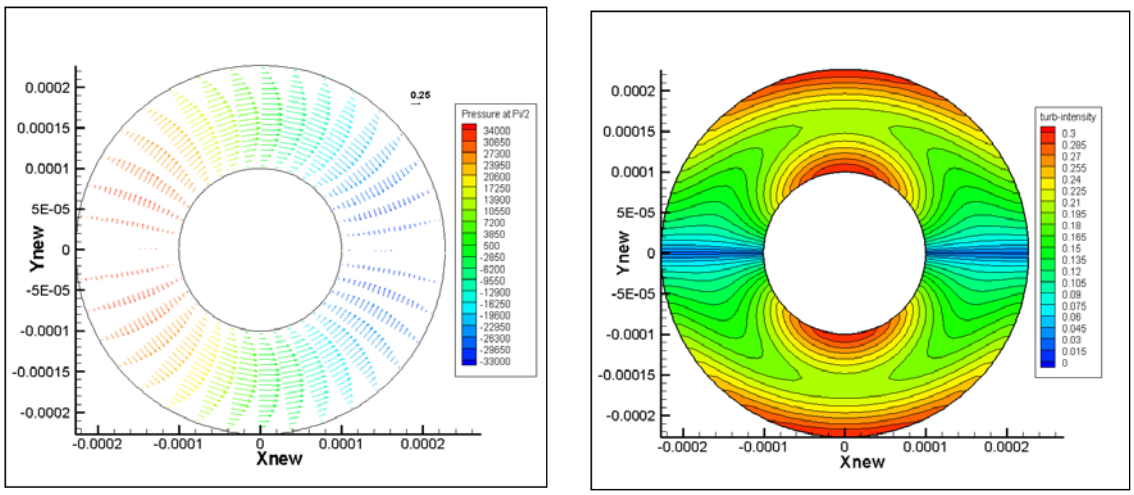

Figure 3.60 Fluent solutions for Fe=10 Hz, e=0.0005 inches; a) velocity vector b) contours of turbulence intensity

To better quantify the information presented in Figures 3.52 through 3.60, the velocity profile at $\theta = \pi/2$ (Figure 3.61) was extracted from the velocity vector data. The velocity profiles are also plotted along with polynomial curve fits in order to determine the trend line of the solutions. Figures 3.62 through 3.64 represent the velocity profile comparison for the journal amplitude of 0.002, 0.001, and 0.0005 inches, respectively. The velocity profile at low frequency, 10 Hz, is very well represented by a parabola curve of $U/U_{max} = 1-(y/(c/2))^2$ predicted by the solution of the laminar flow. The curve fits deviate from the parabola curves as the frequency increases. The curve fits of the velocities for the journal frequencies of 50 Hz and 200 are polynomial with the degree of 4 and 6, respectively.

Regarding to velocity profile in general, the abrupt change in velocity from zero at the wall ($y/(c/2) = 1$ and -1) to a certain value and almost remain at the positions away from wall is the indication of turbulence. The significant deviation of velocity profile from laminar flow velocity profile for the 50 Hz and 200 Hz case indicates the non-

laminar flow in SFDs operating at high frequency. The velocity profile at these high frequencies shows the flow is in transitional regime undergoing from laminar to turbulence since it has not yet developed in to a $U/U_{max} = (|y|/(c/2))^{1/n}$ where $n > 6$.

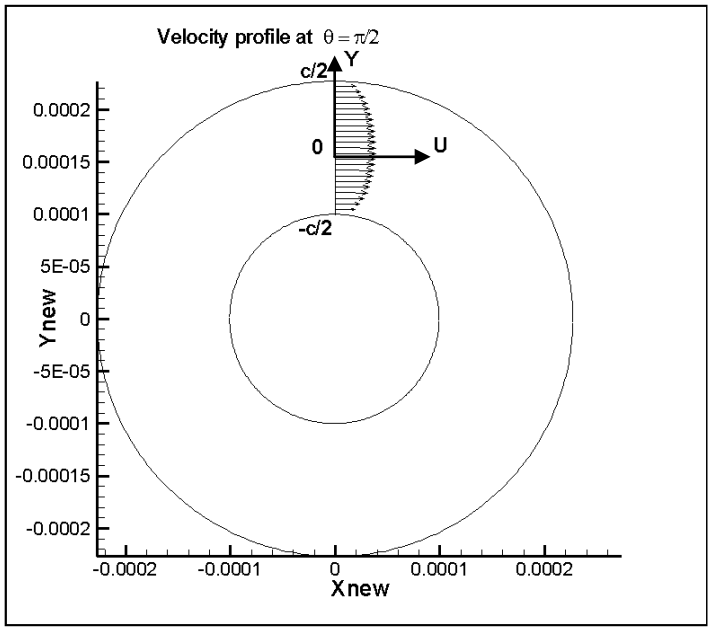

Figure 3.61 Velocity profile at $\tau = \pi/2$, $\theta = \pi/2$

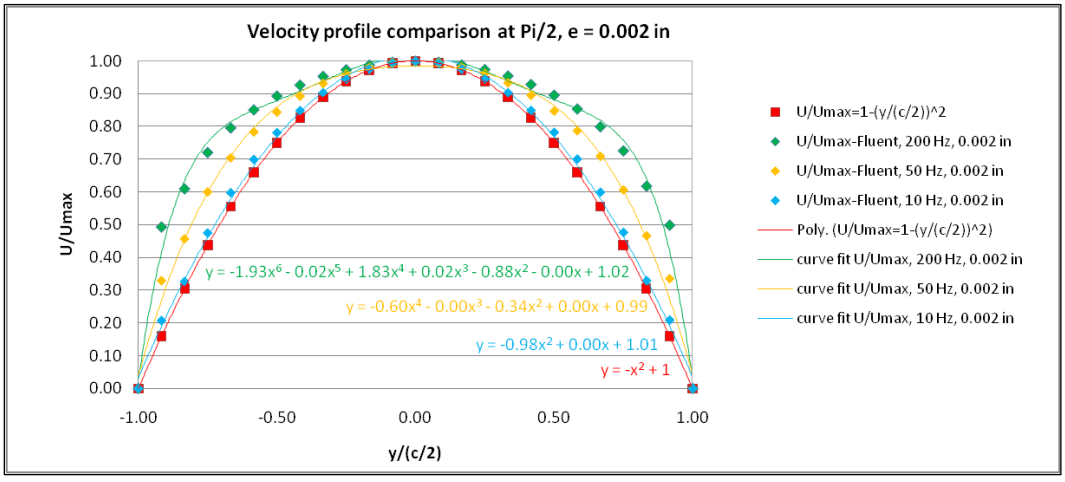

Figure 3.62 Velocity profile comparison at $\tau = \pi/2$, $\theta = \pi/2$, $e = 0.002$ inches ($\varepsilon = 0.4$)

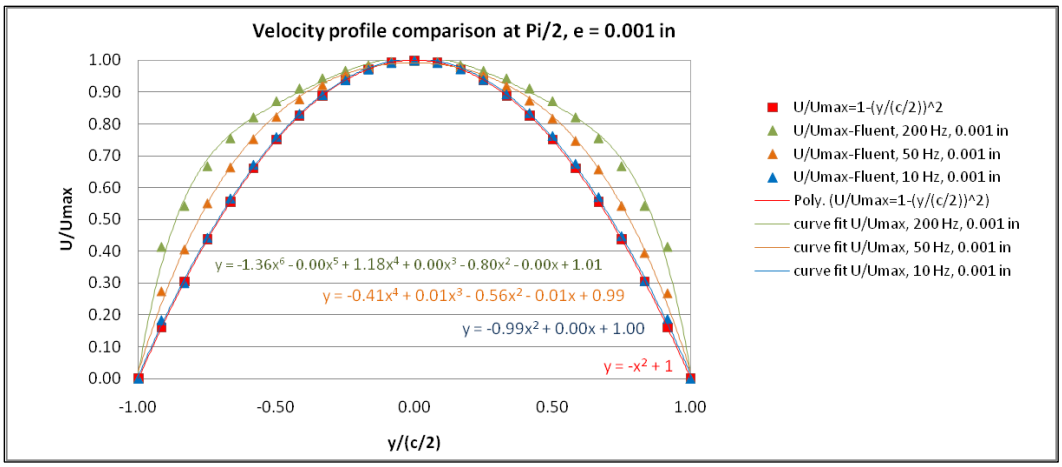

Figure 3.63 Velocity profile comparison at $\tau = \pi/2$, $\theta = \pi/2$, $e = 0.001$ inches ($\varepsilon = 0.2$)

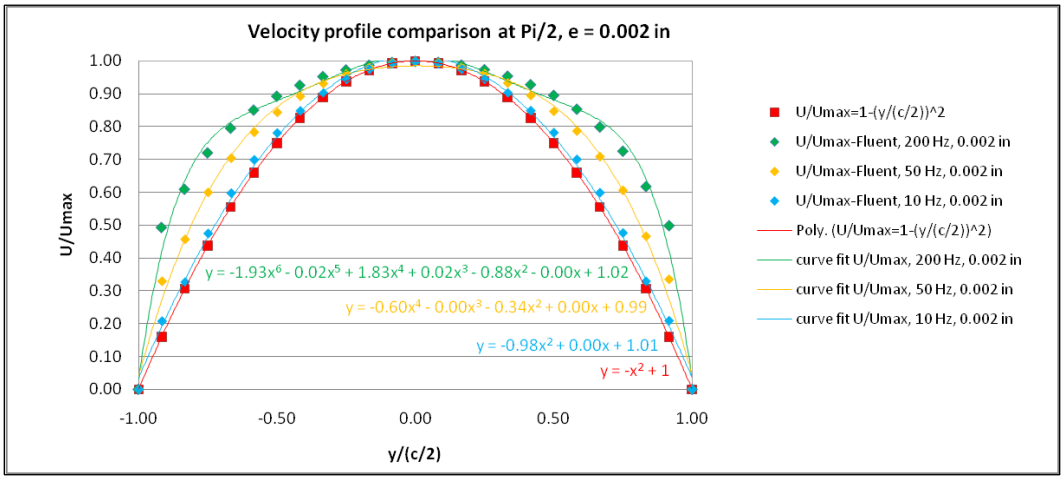

Figure 3.64 Velocity profile comparison at $\tau = \pi/2$, $\theta = \pi/2$, $e = 0.0005$ inches ($\varepsilon = 0.1$)

According to the comparison, the conclusion follows:

1. The pressure comparison (Figure 3.29-3.37) shows that there is larger deviation in pressure fields between the Reynolds and Fluent solutions at high frequencies than at low frequencies.

2. When considering the pressure curve for Fluent solutions (Figure 3.38-3.40), Reynolds equation solutions (Figure 3.41-3.43), and Reynolds equation with fluid inertia solutions (Figure 3.44-3.46) versus times for a certain point on the journal, the pressure curves for all cases indicate the phase shift of maximum pressure as the journal amplitude increases. In addition, the fluctuation of the pressure curves for Fluent solutions at high frequencies indicates the presence of turbulence. Moreover, the angle differences between Reynolds equation solutions and Reynolds equation with fluid inertia solutions for the locations of the maximum and minimum pressures (Figure 3.47) and the angle differences between Reynolds equation solutions and Fluent solutions for the locations of the maximum and minimum pressures (Figure 3.48) indicate the effect of inertia and the non-laminar flow contribute the significant deviation of the angle of maximum and minimum pressures.

3. When comparing the maximum pressures (Figure 3.49-3.50), the fluid inertia effect increases as the frequency increases especially for the negative maximum pressures. In addition, the curves can be divides into two groups including the laminar flow which is the group of pressures from Reynolds equation, pressures from Reynolds equation with fluid inertia effect, and the group of pressure from Fluent. It also confirms that there is larger deviation in pressure for these two groups at high frequencies than at low frequencies.

4. $P_{max,Fuent}/P_{max,Reynolds}$ comparison in Figure 3.51 indicates that there is large deviation in pressures at a high frequency whereas the values tend toward 1 as frequencies approach low frequencies. It can be concluded that the non-laminar flow as well as the fluid inertia effect could be accounted for the flow in SFDs at high frequencies. It is seen that *Re* better defines the change in this ratio than Re_s

5. When considering velocity vectors, Turbulence intensities (Figure 3.52-3.60), and velocity profiles (Figure 3.62-3.64), it is indicated that the flow is likely to be turbulent at high frequencies as the increase in turbulent intensity at higher frequencies and the curve fit for velocity profiles indicating a high order of

polynomial. The velocity profile at high frequencies indicates the transitional regime going from laminar to turbulence. There need to be some experiments performed to well define the transitional regime.

6. According to numerical investigation, it indicates that the non-laminar flow and fluid inertia effect should be included for flow in SFDs at high frequencies. However, the experimental investigation should be performed to confirm the observation from numerical solution and to determine the exact values of interested operating points.

3.5 The Pressure Fields

For the pressure field study, the comparison between journal frequencies, i.e. 10, 50, and 200 Hz., as well as the journal amplitude, i.e. 0.002, 0.001, and 0.0005 inches are taken into account. The animation of the pressure field for the journal amplitude of 0.002 inches at three different frequencies of 10, 50, and 200 Hz. are shown in Figures 3.65 through 3.67. The pressures presented are the deviation from the operating pressure. At the starting position, the squeeze film zone has a constant of the operating pressure. When the journal moves forward to the positive degree, or the left hand side, the squeeze film zone has the distribution of pressure consisting of the gradually increasing pressure upstream and dropping pressure downstream. The upstream pressure experiences drastic change and reaches the maximum positive pressure at a position of 90 degrees whereas the downstream pressure approaches the minimum pressure (negative pressure). At the positions between 90 degrees and 180 degrees, the upstream pressure gradually decreases and finally reaches the operating pressure at 180 degrees whereas the downstream pressure gradually increases and also possesses the uniform initial pressure at 180 degrees. The distribution of the pressure of the squeeze film zone at the position between the positions of 180 degrees and 360 degrees has the similar pattern to that of the squeeze film zone from 0 to 180 degrees but is the mirror image.

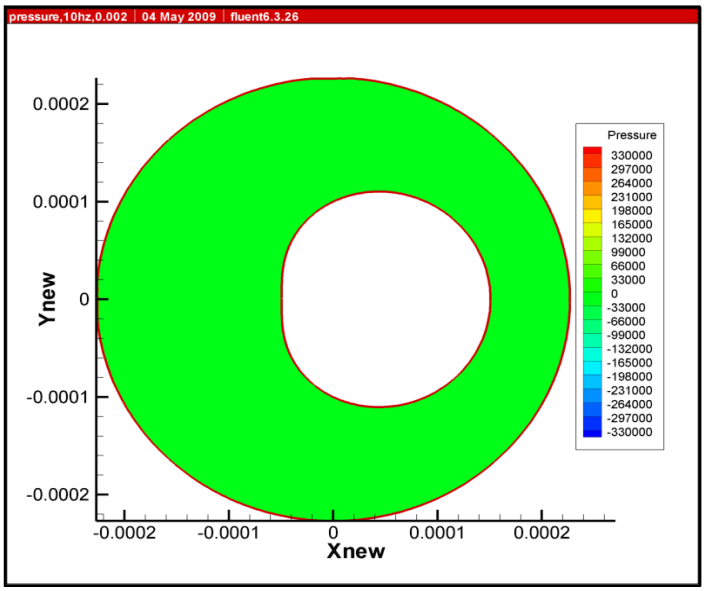

Figure 3.65 The pressure (Pa) field at a frequency of 10 Hz and an amplitude of 0.002 inches

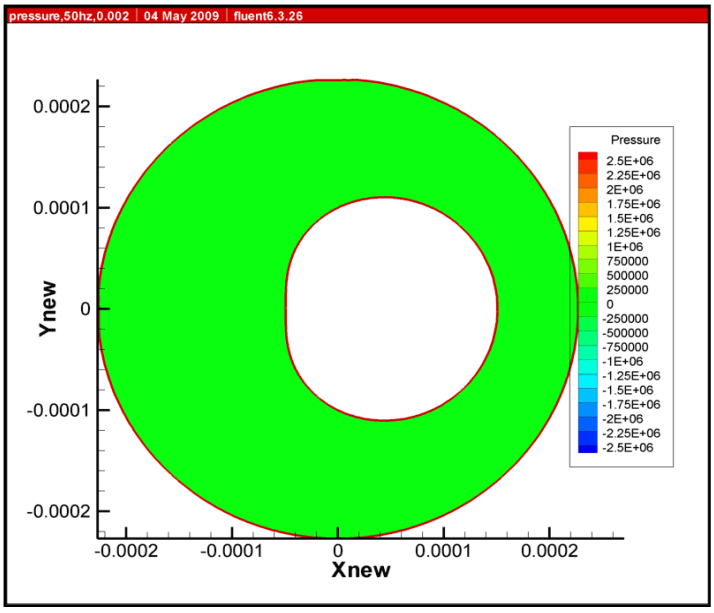

Figure 3.66 The pressure (Pa) field at a frequency of 50 Hz and an amplitude of 0.002 inches

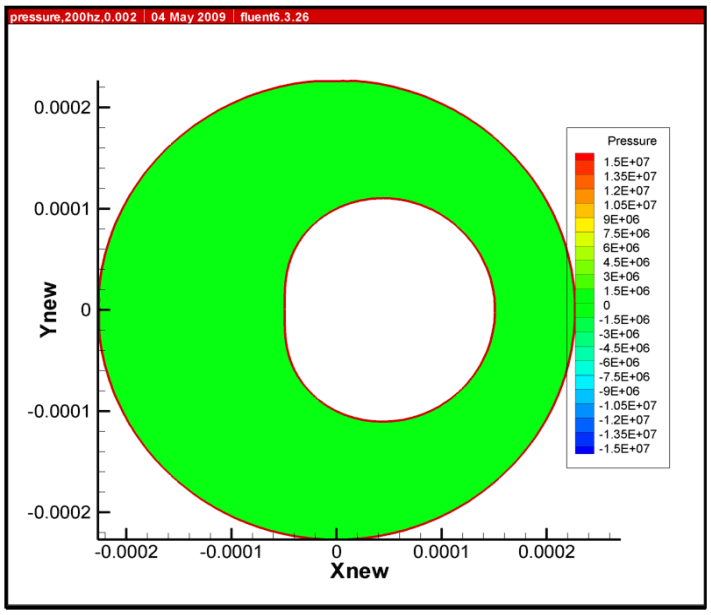

Figure 3.67 The pressure (Pa) field at a frequency of 200 Hz and an amplitude of 0.002 inches

In addition, Figures 3.68 through 3.70 show the animation of the pressure field for three different frequencies of 10, 50, and 100 Hz and a journal's amplitude of 0.001 inches whereas Figures 3.71 through 3.73 animate the pressure field for three different frequencies and a journal's amplitude of 0.0005 inches.

Table 3.2 shows maximum and minimum pressures for three different frequencies and amplitudes. When comparing among three different frequencies for the same journal motion amplitude, the pressure fields have the same pattern of pressure distributions for the three different frequencies. The highest value, or maximum positive and negative pressure, is present for 200 Hz frequency whereas the lowest is for 10 Hz frequency.

At the same frequency, the pressure fields have the same pressure distribution for three different amplitudes. The highest value, or maximum positive and negative

pressure, is present for 0.002 inch amplitude whereas the lowest is for the 0.0005 inch amplitude.

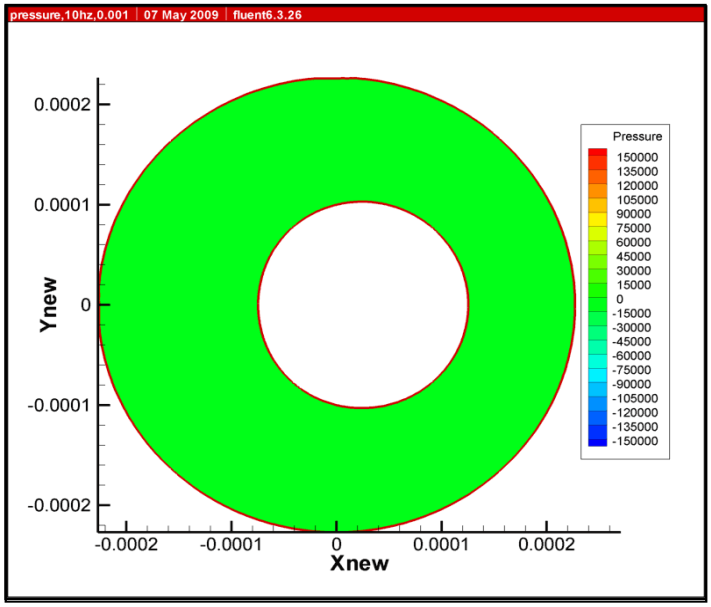

Figure 3.68 The pressure (Pa) field at a frequency of 10 Hz and an amplitude of 0.001 inches

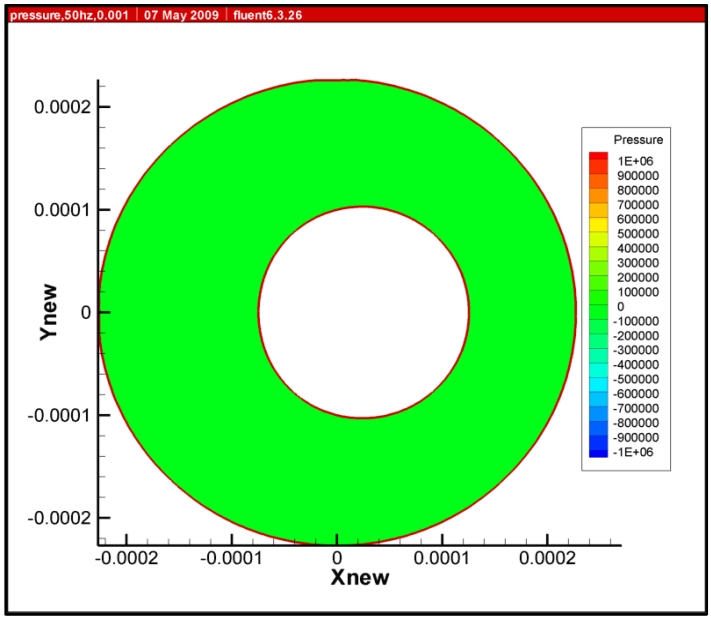

Figure 3.69 The pressure(Pa) field at a frequency of 50 Hz and an amplitude of 0.001 inches

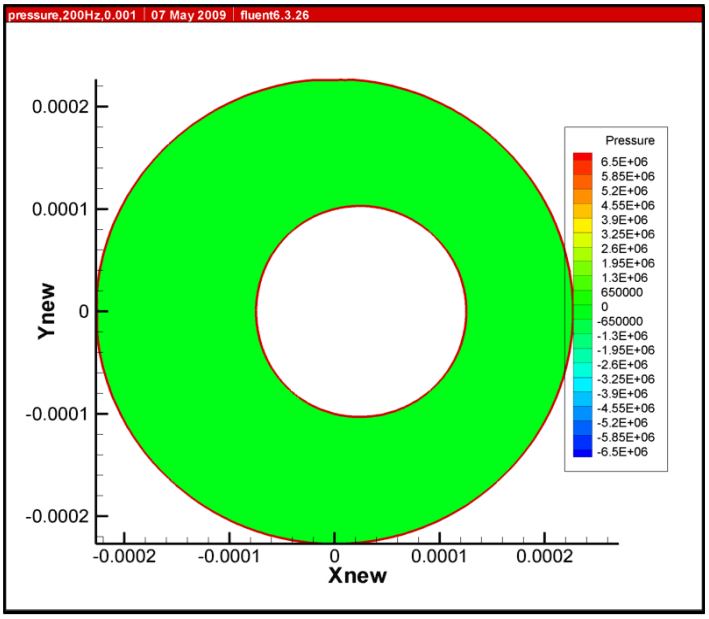

Figure 3.70 The pressure(Pa) field at a frequency of 200 Hz and an amplitude of 0.001 inches

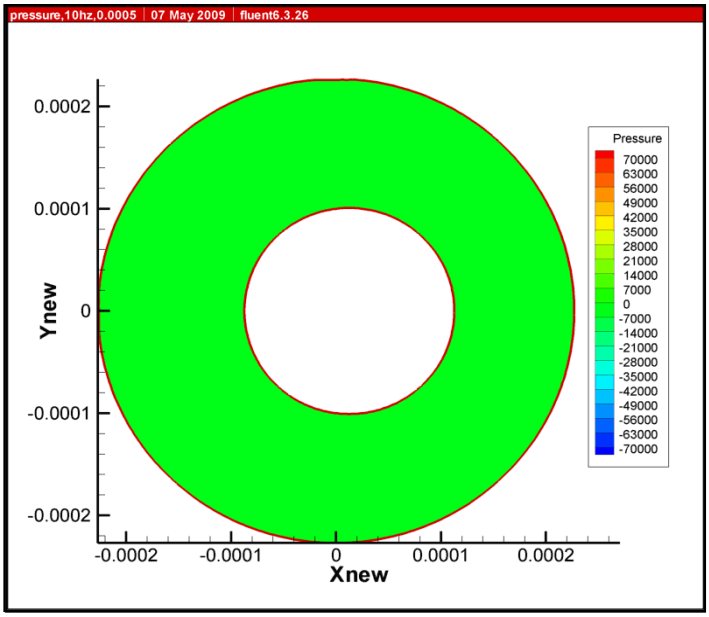

Figure 3.71 The pressure(Pa) field at a frequency of 10 Hz and an amplitude of 0.0005 inches

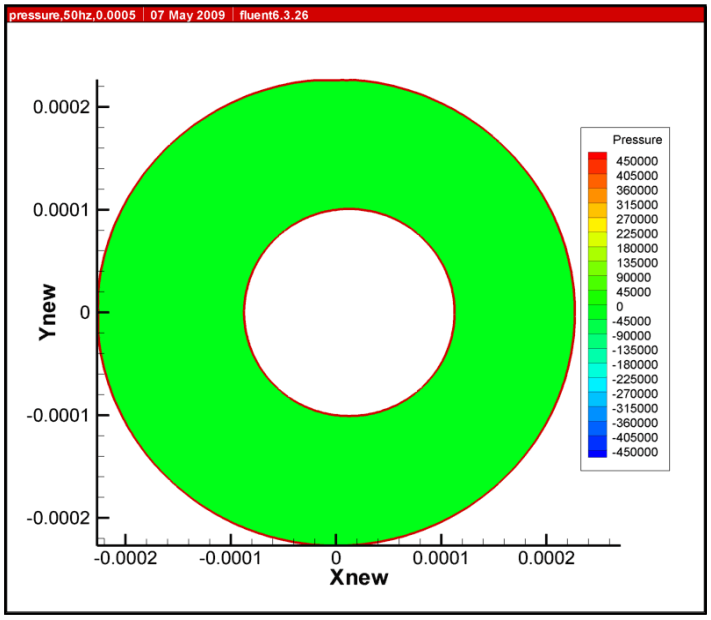

Figure 3.72 The pressure(Pa) field at a frequency of 50 Hz and an amplitude of 0.0005 inches

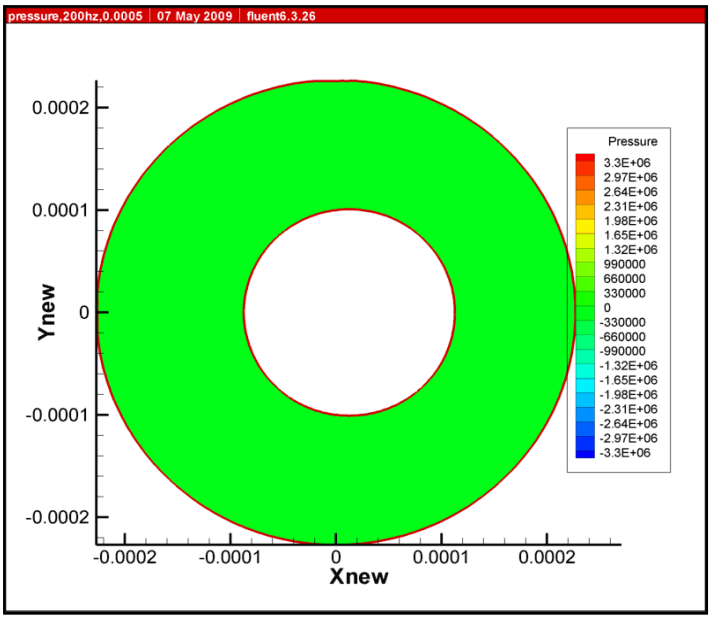

Figure 3.73 The pressure(Pa) field at a frequency of 200 Hz and an amplitude of 0.0005 inches

Table 3.2 Maximum and minimum pressures at three different frequencies and amplitudes

Frequency(Hz)	Amplitude = 0.002 inches		Amplitude = 0.001 inches		Amplitude = 0.0005 inches	
	Pmax(Pa)	Pmin(Pa)	Pmax(Pa)	Pmin(Pa)	Pmax(Pa)	Pmin(Pa)
10	328,643	-329,276	144,792	-147,064	66,012	-67,684
50	2,545,770	-2,572,090	1,031,740	-1,077,590	429,858	-463,621
200	15,207,200	-15,992,000	6,236,780	-6924,890	2,501,250	-3,152370

3.6 The Velocity Fields

The velocity filed consisting of x and y in direction was portrayed in the same way as the pressure field. The animation of the x-velocity, or the velocity in x direction, for the journal amplitude of 0.002 inches at three different frequencies of 10, 50, and 200

Hz are shown in Figures 3.74 through 3.76. The squeeze film zone has the symmetric distribution of x-velocity if the mirror line is the x-axis. The velocity gradually increases as the journal moves forward to the positive degree, or the left hand side. At squeeze film zone, the velocity increases from zero at the walls, i.e. journal and housing's wall, to maximum right above and below the journal at middle point between the two walls.

The x-velocity reaches the maximum at a position of 90 degrees and gradually decreases as the journal moves further forward and approaches the zero at a position of 180 degrees. The distribution of the x-velocity of the squeeze film zone at the position between 180 degrees and 360 degrees has the similar pattern to that of the squeeze film zone from 0 to 180 degrees but having negative values because of the negative direction of the journal.

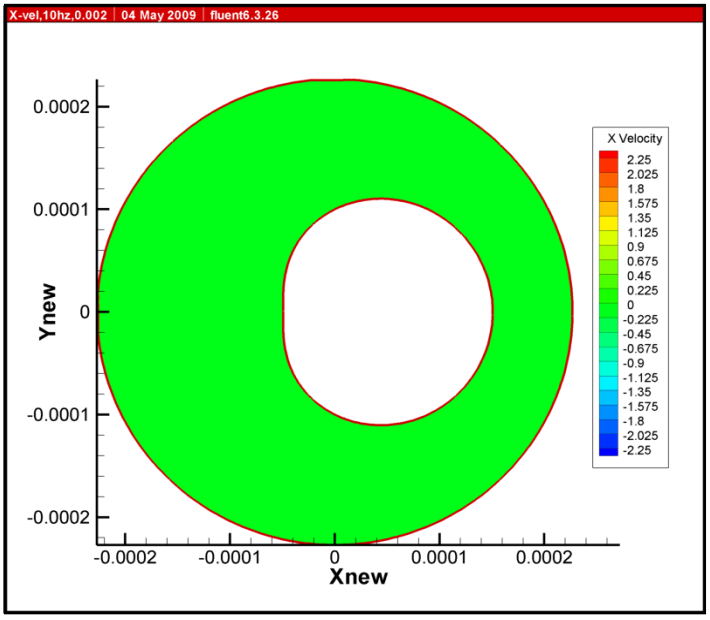

Figure 3.74 The x-velocity(m/s) field at a frequency of 10 Hz and an amplitude of 0.002 inches

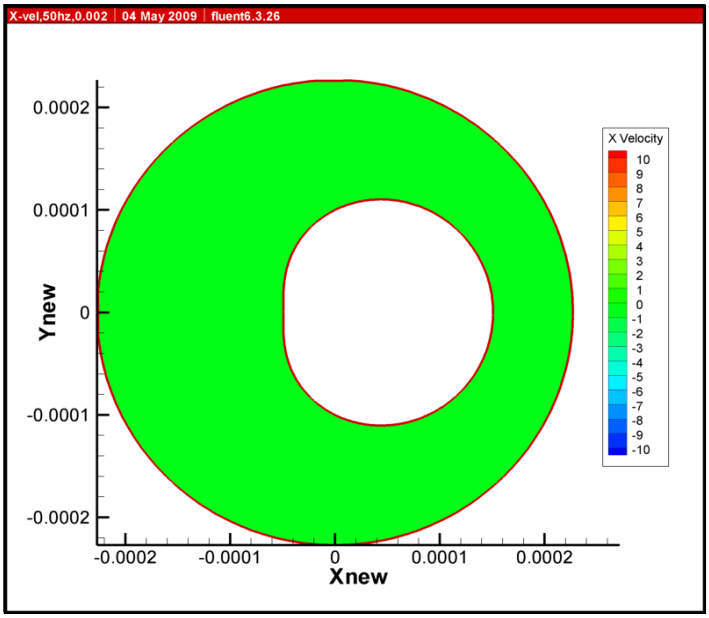

Figure 3.75 The x-velocity(m/s) field at a frequency of 50 Hz and an amplitude of 0.002 inches

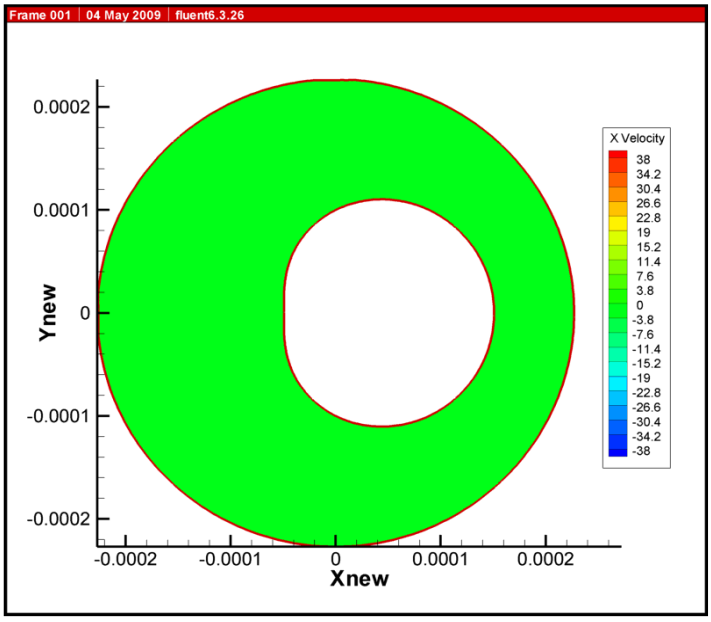

Figure 3.76 The x-velocity(m/s) field at a frequency of 200 Hz and an amplitude of 0.002 inches

In addition, Figures 3.77 through 3.79 show the animation of the x-velocity field for three different frequencies of 10, 50, and 200 Hz and a journal's amplitude of 0.001 inches whereas Figures 3.80 through 3.82 animate the x-velocity field for three different frequencies and a journal's amplitude of 0.0005 inches.

When comparing among three different frequencies for the same journal's amplitude, the x-velocity fields have the same x-velocity distribution for the three different frequencies. The highest value, or maximum positive and negative x-velocity, is present for the 200 Hz frequency whereas the lowest is for the 10 Hz frequency.

At the same frequency, the x-velocity fields have the same distribution for three different amplitudes. The highest value, or maximum positive and negative x-velocity, is of 0.002 inch amplitude whereas the lowest is for 0.0005 inch amplitude.

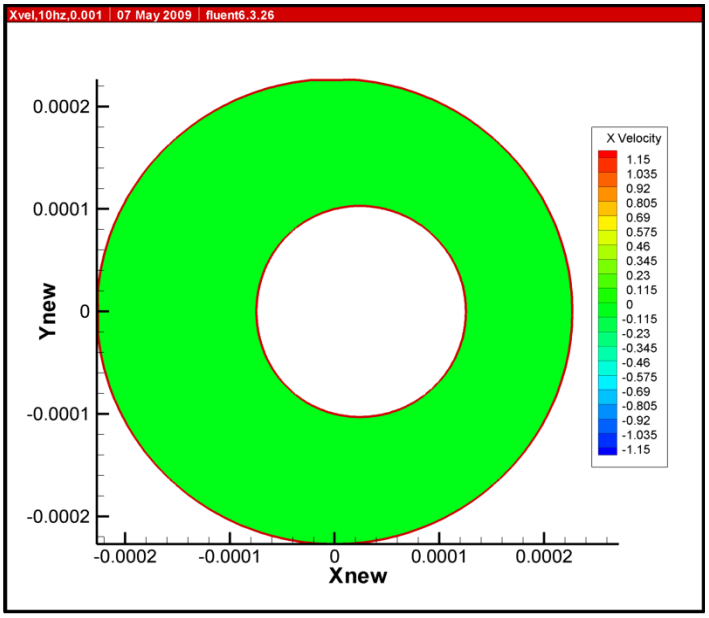

Figure 3.77 The x-velocity(m/s) field at a frequency of 10 Hz and an amplitude of 0.001 inches

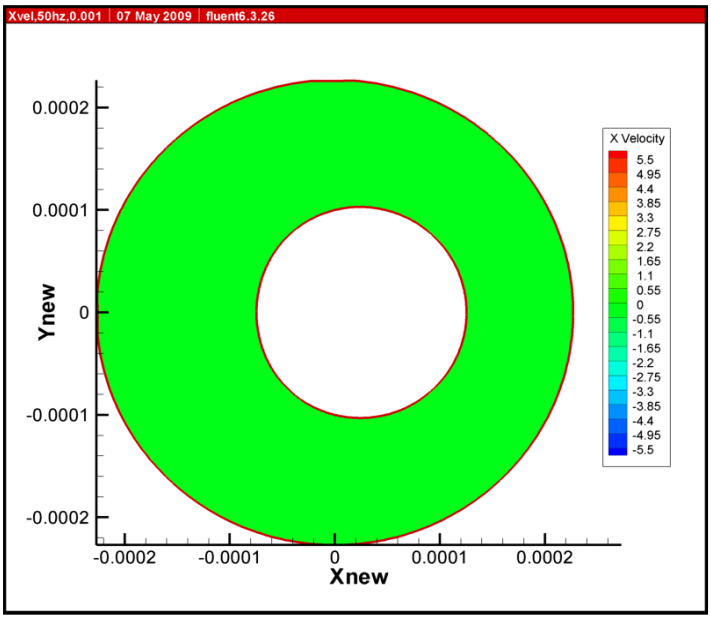

Figure 3.78 The x-velocity(m/s) field at a frequency of 50 Hz and an amplitude of 0.001 inches

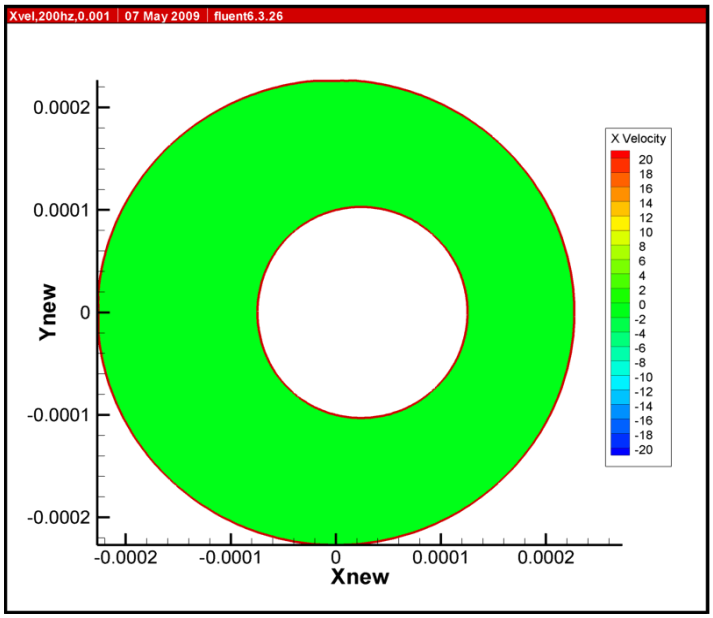

Figure 3.79 The x-velocity(m/s) field at a frequency of 200 Hz and an amplitude of 0.001 inches

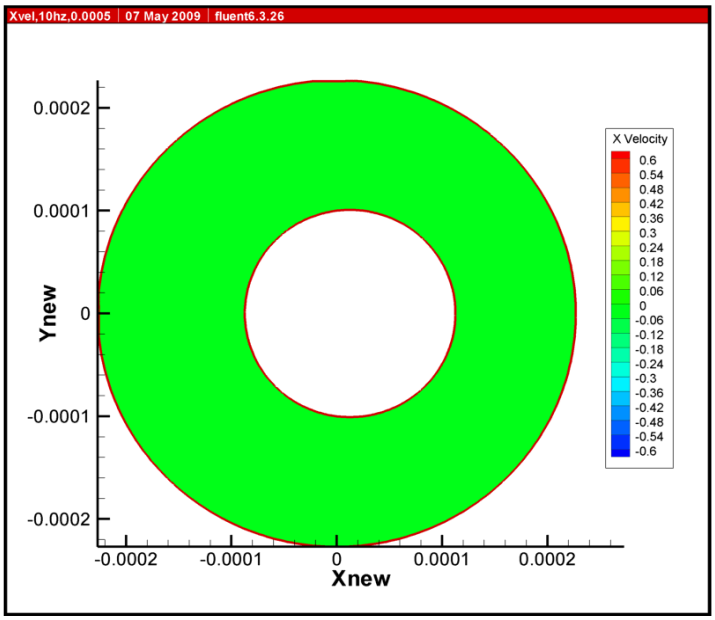

Figure 3.80 The x-velocity(m/s) field at a frequency of 10 Hz and an amplitude of 0.0005 inches

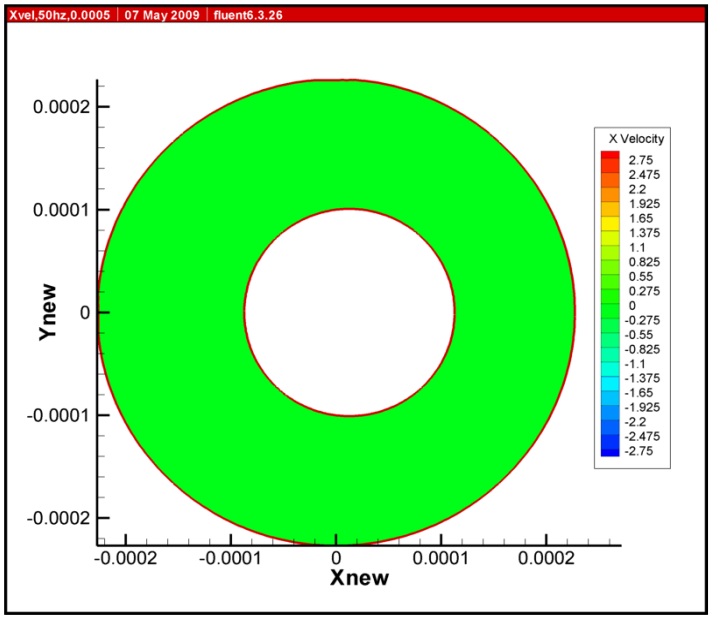

Figure 3.81 The x-velocity(m/s) field at a frequency of 50 Hz and an amplitude of 0.0005 inches

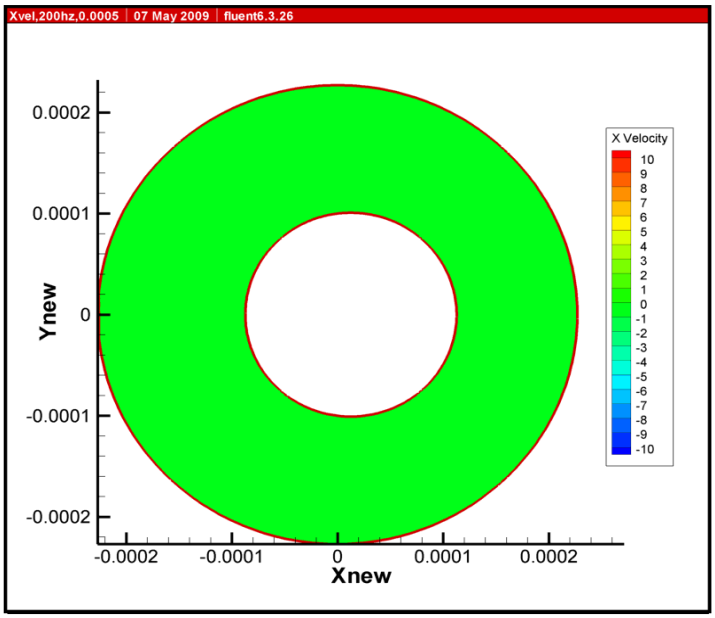

Figure 3.82 The x-velocity(m/s) field at a frequency of 200 Hz and an amplitude of 0.0005 inches

The animation of the y-velocity, or the velocity in y direction, for the journal amplitude of 0.002 inches at three different frequencies of 10, 50, and 200 Hz are shown in Figures 3.83 through 3.85. To ease portraying the y-velocity distribution, the squeeze film zone can be divided equally into four parts. The first quadrant has the same distribution as the third quadrant whereas the second has the same as the fourth. The velocity in the second quadrant as well as the fourth gradually increases as the journal is moving forward to the positive degree, or the left hand side. On the other hand, the velocity in the first quadrant as well as the third gradually decreases as the journal is moving forward to the positive degree. At each quadrant of the squeeze film zone, the velocity increases/decreases from zero at the walls, i.e. journal and housing's wall, to maximum positive/negative at center point between the two walls.

The y-velocity reaches the maximum positive/negative value at a position of 90 degrees and gradually decreases when moving further forward and approaches the zero

at a position of 180 degrees. The distribution of the y-velocity of the squeeze film zone at the position between 180 degrees and 360 degrees has the similar pattern to that of the squeeze film zone from 0 to 180 degrees but having negative values because of the negative direction of the journal.

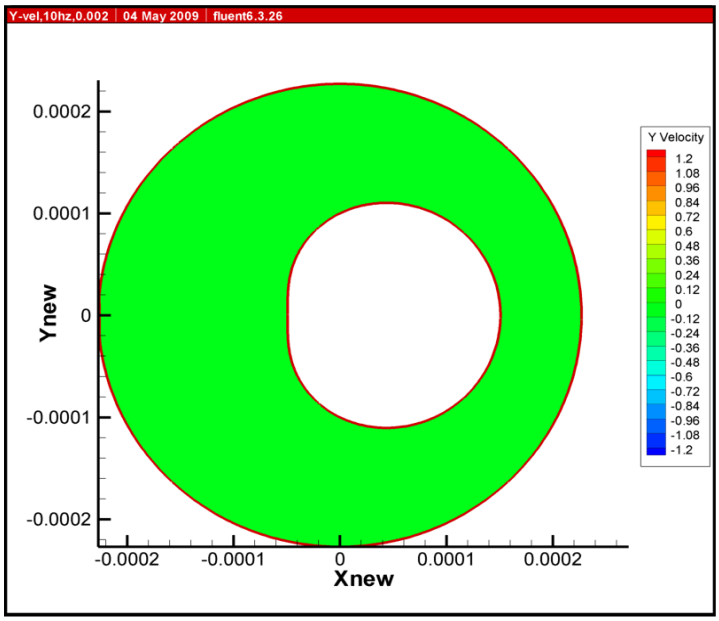

Figure 3.83 The y-velocity(m/s) field at a frequency of 10 Hz and an amplitude of 0.002 inches

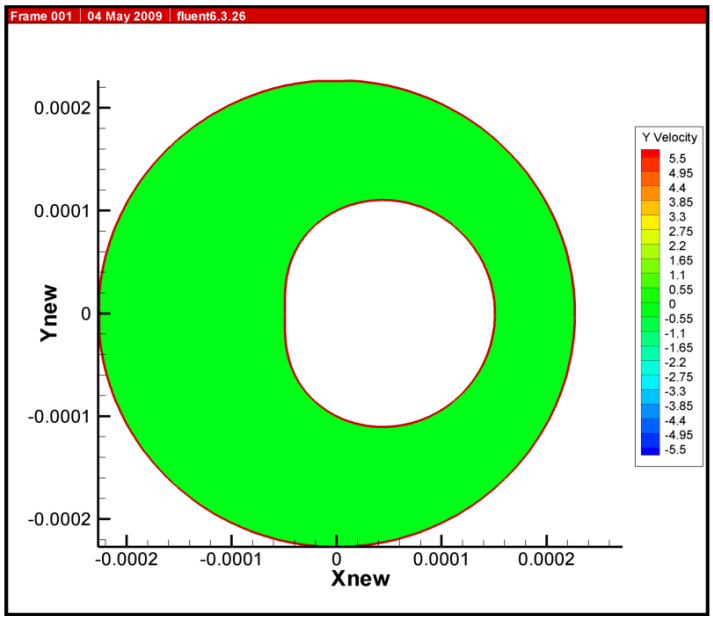

Figure 3.84 The y-velocity(m/s) field at a frequency of 50 Hz and an amplitude of 0.002 inches

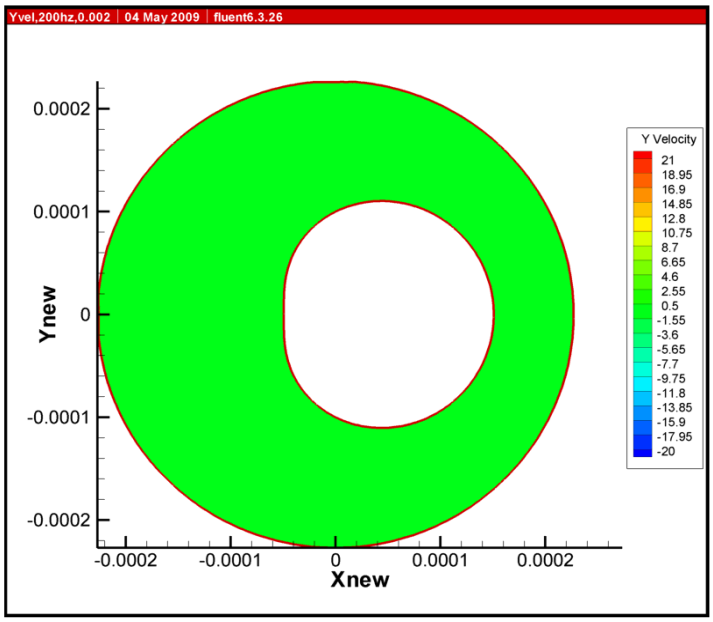

Figure 3.85 The y-velocity(m/s) field at a frequency of 200 Hz and an amplitude of 0.002 inches

In addition, the Figures 3.86 through 3.88 show the animation of the y-velocity field for three different frequencies of 10, 50, and 200 Hz and a journal's amplitude of 0.001 inches whereas the Figures 3.89 through 3.91 animate the x-velocity field for three different frequencies and a journal's amplitude of 0.0005 inches.

When comparing among three different frequencies for the same journal's amplitude, the y-velocity fields have the same pattern of y-velocity distribution for the three different frequencies. The highest value, or maximum positive and negative x-velocity, is present for the 200 Hz. frequency whereas the lowest is for the 10 Hz. frequency.

At the same frequency, the y-velocity fields have the same distribution for three different amplitudes. The highest value, or maximum positive and negative y-velocity, is of 0.002 inch amplitude whereas the lowest is for 0.0005 inch amplitude.

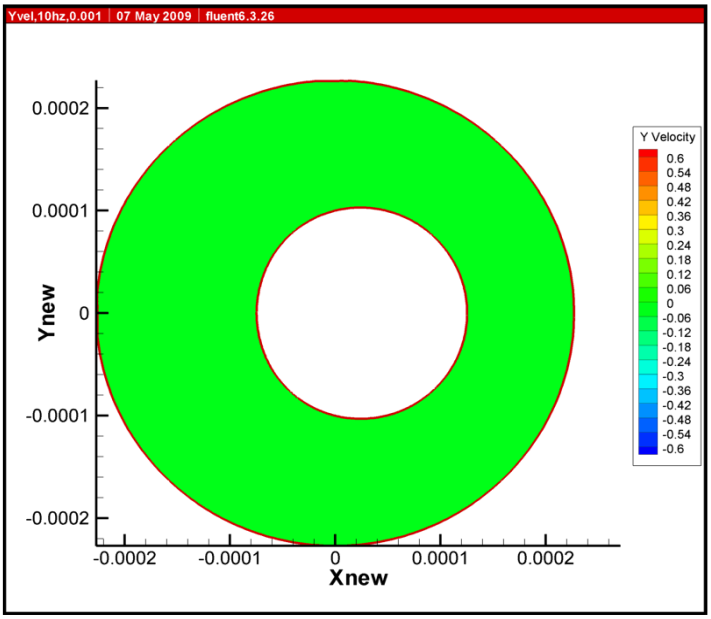

Figure 3.86 The y-velocity(m/s) field at a frequency of 10 Hz and an amplitude of 0.001 inches

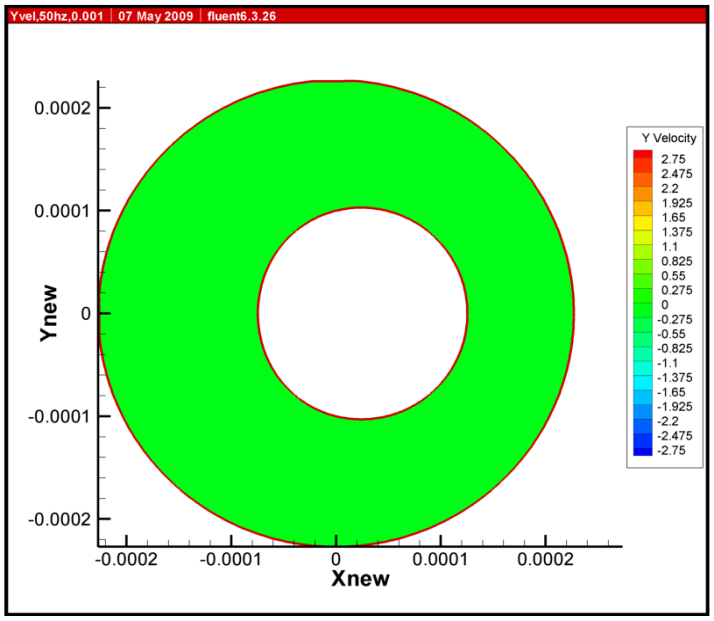

Figure 3.87 The y-velocity(m/s) field at a frequency of 50 Hz and an amplitude of 0.001 inches

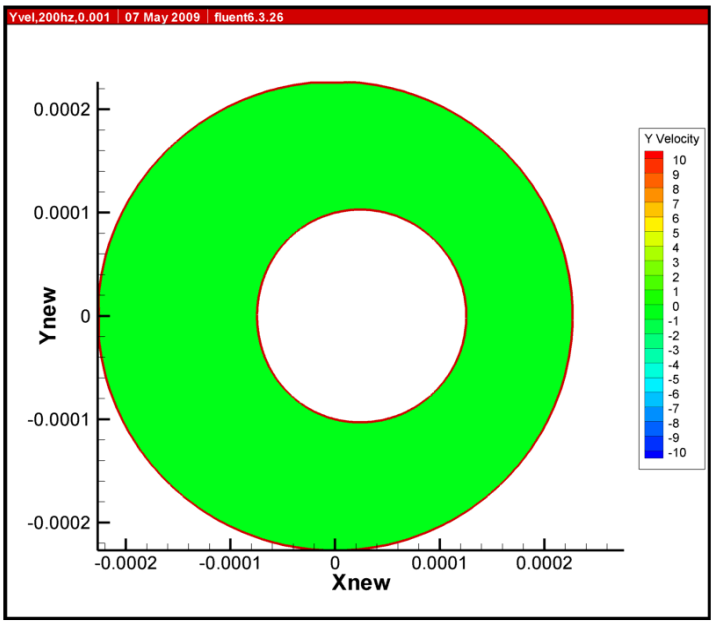

Figure 3.88 The y-velocity(m/s) field at a frequency of 200 Hz and an amplitude of 0.001 inches

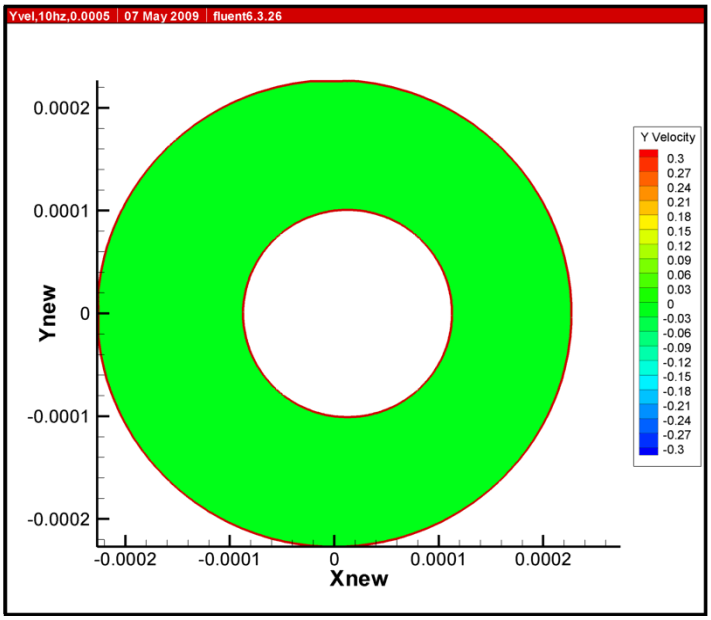

Figure 3.89 The y-velocity(m/s) field at a frequency of 10 Hz and an amplitude of 0.0005 inches

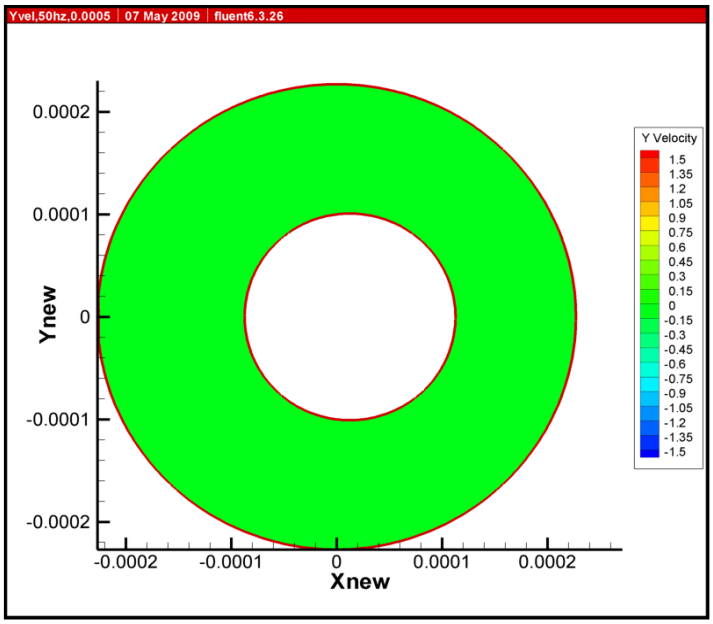

Figure 3.90 The y-velocity(m/s) field at a frequency of 50 Hz and an amplitude of 0.0005 inches

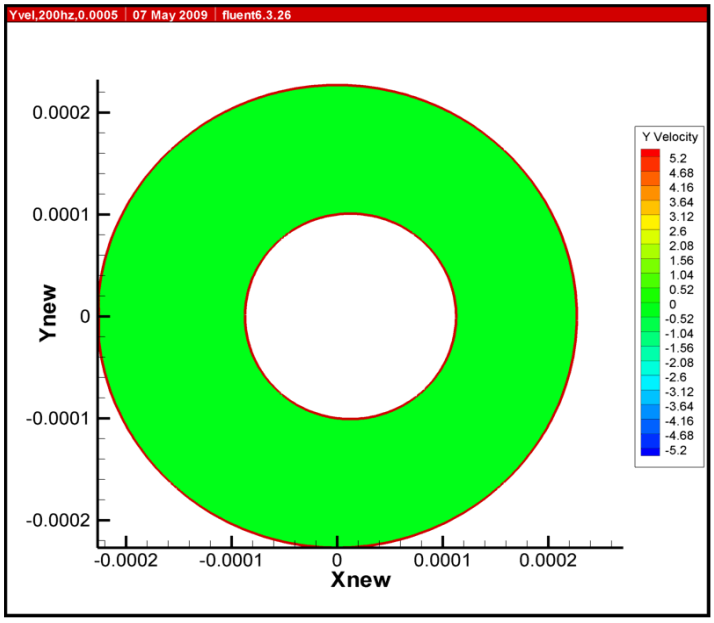

Figure 3.91 The y-velocity(m/s) field at a frequency of 200 Hz and an amplitude of 0.0005 inches

3.7 The Drag Forces

The drag force, F_d, exerting on the journal is a significant concern in this study. Figure 3.92 depicts the drag forces versus the angles for all cases. The force is sinusoidal for all cases. As the journal moves forward to the positive degrees, the drag forces gradually increase and reach the maximum value approximately at 90 degree. As the journal moves further degrees, the drag forces decrease and reach the zero approximately at 180 degrees. For the journal positions between 180 and 360, the forces are negative but have similar pattern to that of the positions between 0 and 180.

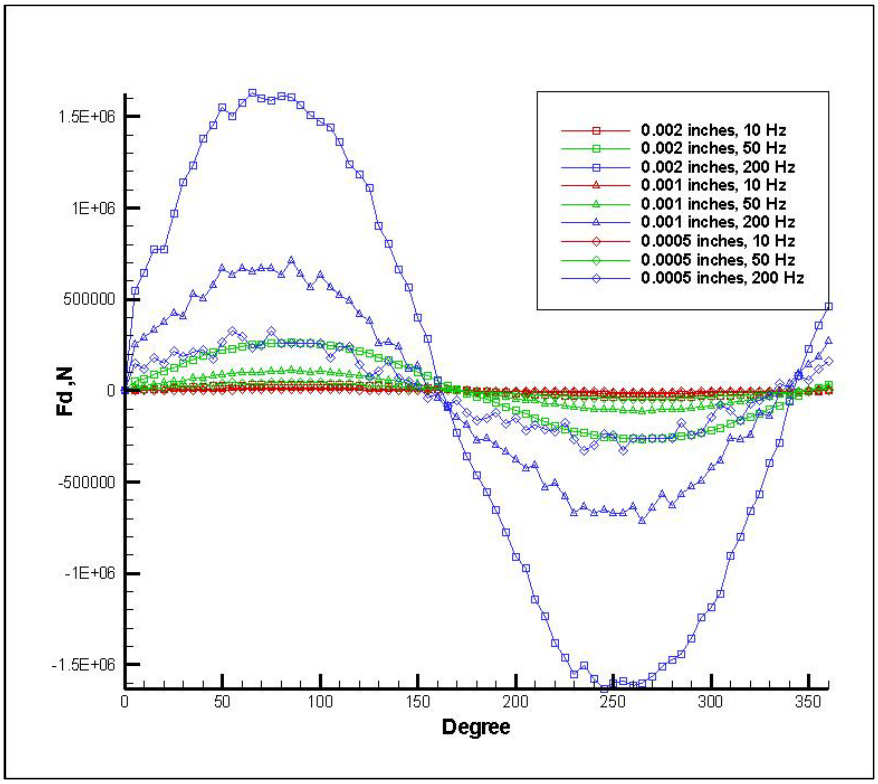

Figure 3.92 The drag forces/unit(N/m) on the journal moving with the different frequencies and amplitudes

Table 3.3 shows the maximum positive/negative drag forces for all cases. For the same amplitude, the drag forces vary directly to the frequencies. The 200 Hz frequency possesses the highest force whereas the 10 Hz frequency possesses the lowest. In addition, the drag forces also vary directly to the journal amplitudes. The 0.002 inch amplitude possesses the highest force whereas the 0.0005 inch amplitude possesses the lowest.

Table 3.3 The maximum positive/negative drag forces for all cases.

Amplitude(inches)	Frequency(Hz)	Maximum positive force, N/m	Maximum negative force, N/m
0.002	10	33,449.43	-33,447.67
	50	263,940.72	-263,936.31
	200	1,613,564.10	-1,613,883.90
0.001	10	14,862.28	-14,862.28
	50	110,565.21	-110,563.88
	200	713,600.24	-713,567.66
0.0005	10	6,767.75	-6,767.70
	50	43,939.96	-43,939.17
	200	262,576.14	-262,565.19

Figure 3.93 depicts the maximum force-amplitude relationship for three different frequencies. The fit lines are created in order to portray such relationships. The maximum positive forces and frequencies have linear relationship. According to the goodness of fit, r^2, the linear equation suit well for the relationship. The fit lines obviously have different slopes for the different frequencies. The 200 Hz line possesses the highest slope whereas the 10 Hz line possesses the lowest.

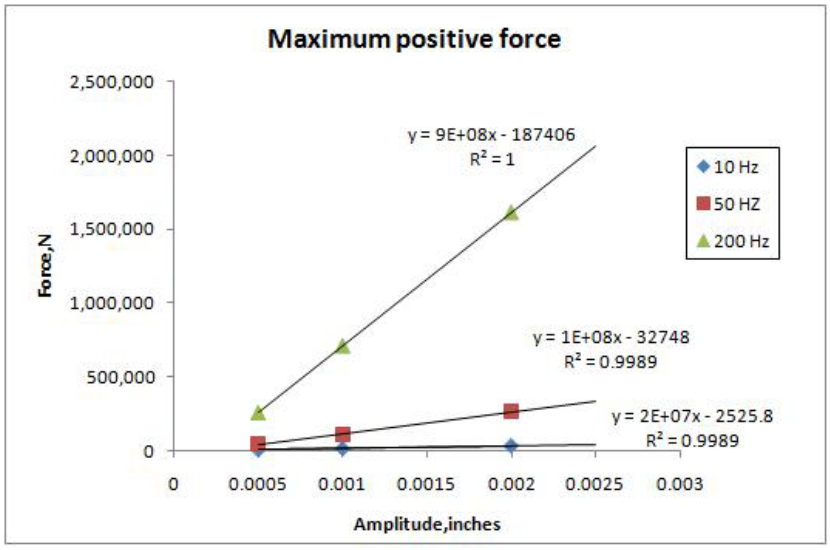

Figure 3.93 The maximum forces(N/m) on the journal moving with the different frequencies and amplitudes

CHAPTER IV

MULTIPHASE FLOW IN SQUEEZE FILM DAMPERS

In this chapter, the computations performed for 2-D SFDs in which the journal moves inside solved using the mixture model in addition to the k-ε model in FLUENT are presented.

4.1 Description of Problem

Figure 4.1 shows the simulated geometry for the SFD whereas Figure 4.2 represents the magnified geometry with a numerical grid. The diameter of the journal, or inner circle was 5 inches, while the clearance was 0.005 inches. The journal orbits inside the wall. Orbits can vary greatly from circular to linear. For this study, multiphase flow and a linear sinusoidal motion along the X-axis will be applied with amplitudes of 0.002 inches and frequencies of 10, 50, and 100 Hz and operating pressures of 0.001, 0.01, 0.05, 0.1, 0.5, 1, 10, 50, and 100 Mpa.

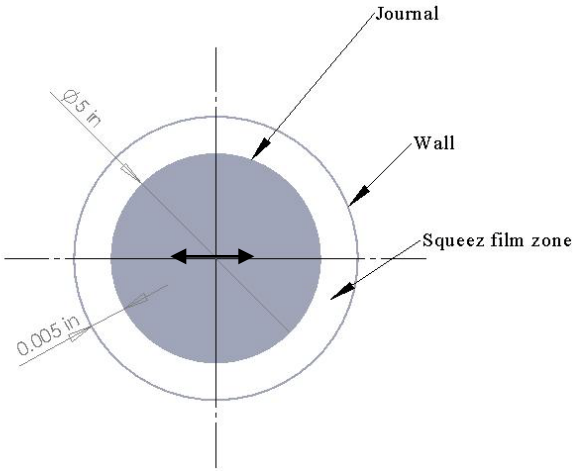

Figure 4.1 2-D simulated geometry of the SFD

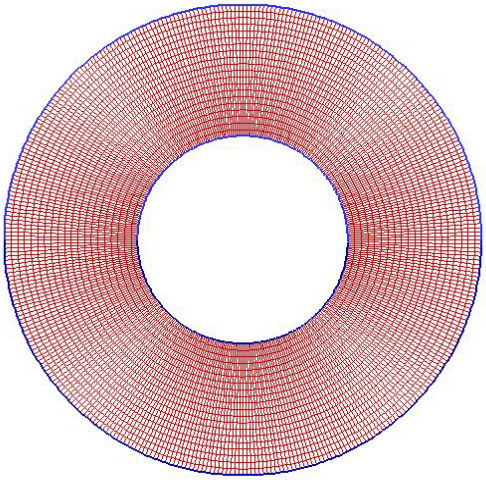

Figure 4.2 The magnified geometry with numerical grid

4.2 Grid and Time Independence

The grid and time independence followed the study in Chapter III. According to the study, the 20 x360 grid and 1 degree/ step are chosen. However, the time increment may be reduced in order to run the numerical solution successfully.

4.3 The Pressure Fields

For the pressure field study, the comparison between journal frequencies, i.e. 10, 50, and 100 Hz, the journal amplitude of 0.002 inches, and the operating pressures of 0.001, 0.01, 0.05, 0.1, 0.5, 1, 10, 50, and 100 MPa are taken into account.

The Figure 4.3 shows the pressure fields for the single phase model for the frequency of 10 Hz. For the multiphase flow, the animation of the pressure field for the journal amplitude of 0.002 inches and the frequency of 10 Hz at different operating pressures of 0.001, 0.01, 0.05, 0.1, 0.5, 1, 10, 50, and 100 MPa are depicted in the

Figures 4.4 through 4.12. The pressures presented are the deviation from the operating pressure.

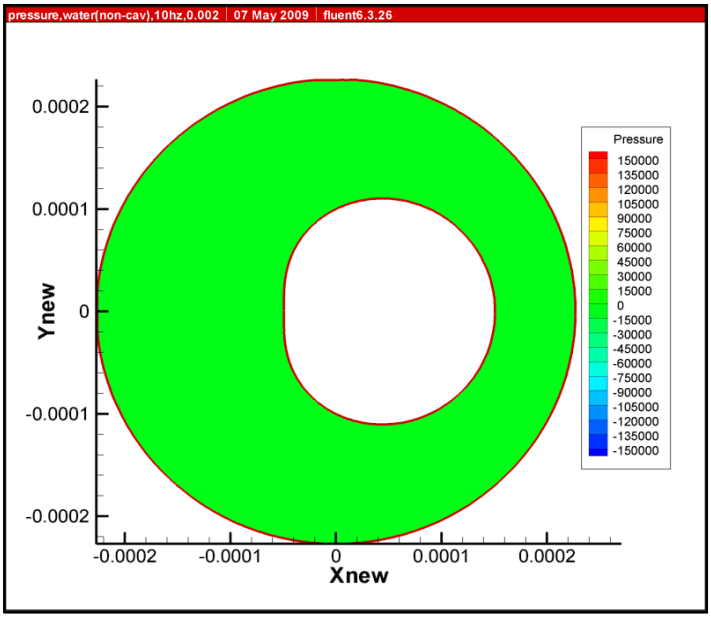

Figure 4.3 The pressure(Pa) field at a frequency of 10 Hz and an amplitude of 0.002 inches (Single phase flow)

For the multiphase flow cases, the pressure field of the SFD at the operating pressure of 0.001 MPa which is less than the vapor pressure of the water, i.e. 3540 Pa, is constant and equal to the static pressure as presented in Figure 4.4. In Figure 4.5, the operating pressure, i.e. 0.01 MPa, is slightly more than the vapor pressure. There is a large fluctuation of the pressure in the squeeze zone when the journal is moving through certain positions, i.e. 90 and 270 degrees. As the journal moves forward to the positive degree from the start, or the left hand side, the squeeze film zone has the distribution of pressure varying approximately between the operating pressure upstream and vapor pressure downstream. The squeeze film zone experiences a drastic change and reaches the maximum positive pressure at a position of 90 degrees and regains normal

distribution of upstream positive pressure and downstream negative pressure approximately between 95 and 145 degrees. From 145 to 180 degree, the pressure falls into the domination of negative pressure zone. The distribution of the pressure of the squeeze film zone at the position between the positions of 180 degrees and 360 degrees has the similar pattern to that of the squeeze film zone from 0 to 180 degrees but is the mirror image. At certain angles i.e. 90, 270 degrees and vicinity, the normal time increment of 1 degree/step for the Fluent program could not yield the solution because of the severe cavitation effect in the pressure ranges. The 0.1 and 0.01 degrees/step are applied to this case.

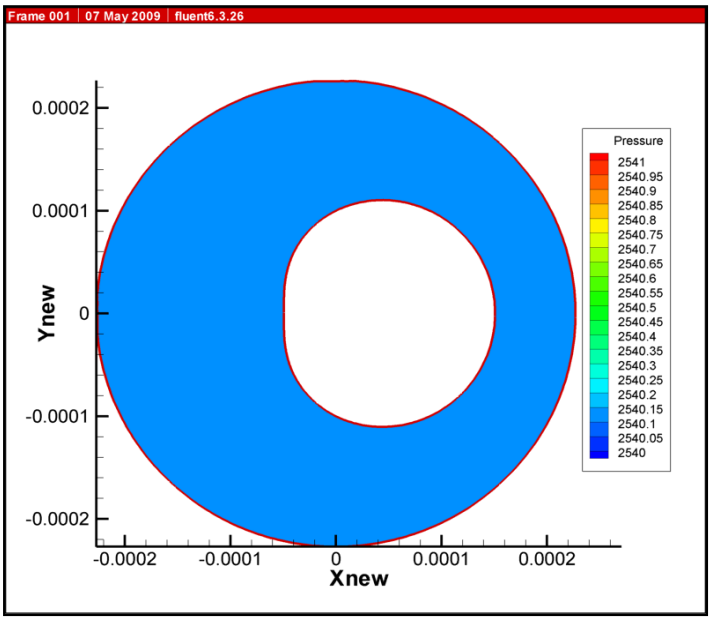

Figure 4.4 The pressure(Pa) field at a frequency of 10 Hz, an amplitude of 0.002 inches, and an operating pressure of 0.001 MPa

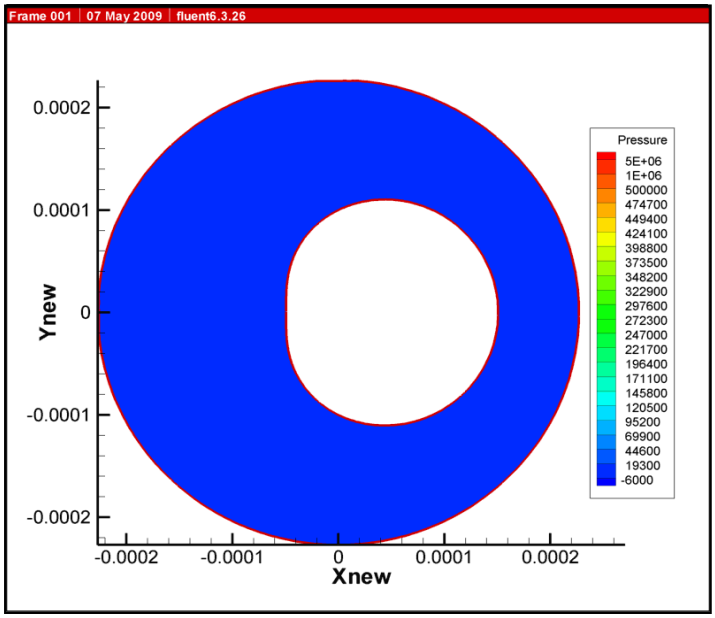

Figure 4.5 The pressure(Pa) field at a frequency of 10 Hz, an amplitude of 0.002 inches, and an operating pressure of 0.01 MPa

The figure 4.6 illustrates the pressure fields at the operating pressure of 0.05 MPa. As the journal moves forward to the positive degree from the start, or the left hand side, the squeeze film zone has the distribution of pressure varying approximately from the operating pressure upstream to vapor pressure downstream. The squeeze film zone experiences a drastic change and reaches the maximum positive pressure at a position of 90 degrees and regains the distribution varying approximately from the operating pressure upstream to vapor pressure downstream approximately between 95 and 120 degrees. As moving further degrees, the pressure falls into the domination of positive pressure zone and approaches operating pressure at 180 degrees. The distribution of the pressure of the squeeze film zone at the position between the positions of 180 degrees and 360 degrees has the similar pattern to that of the squeeze film zone from 0 to 180 degrees but is the mirror image. The sudden increase in pressure occurred as the fluid undergoes a sudden phase change with the resulting rapid fluid motion.

Figures 4.7 through 4.12 show the pressure fields at different operating pressures of 0.1, 0.5, 1, 10, 50, and 100 MPa, respectively. The pattern of the pressure fields are similar to that of the single phase case since phase change is suppressed as the ambient pressure is increased. Once the phase change is eliminated by the higher operating pressure the pressure variation due to the journal motion become the same for all operating pressure.

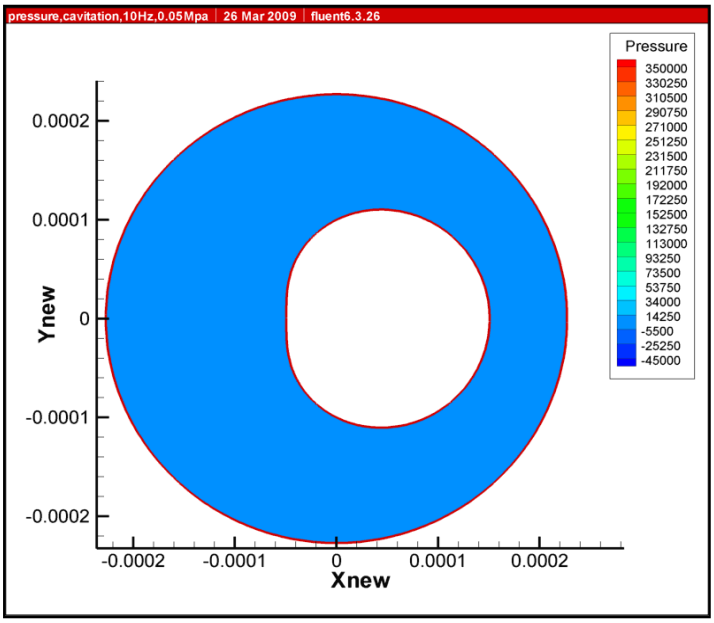

Figure 4.6 The pressure(Pa) field at a frequency of 10 Hz, an amplitude of 0.002 inches, and an operating pressure of 0.05 MPa

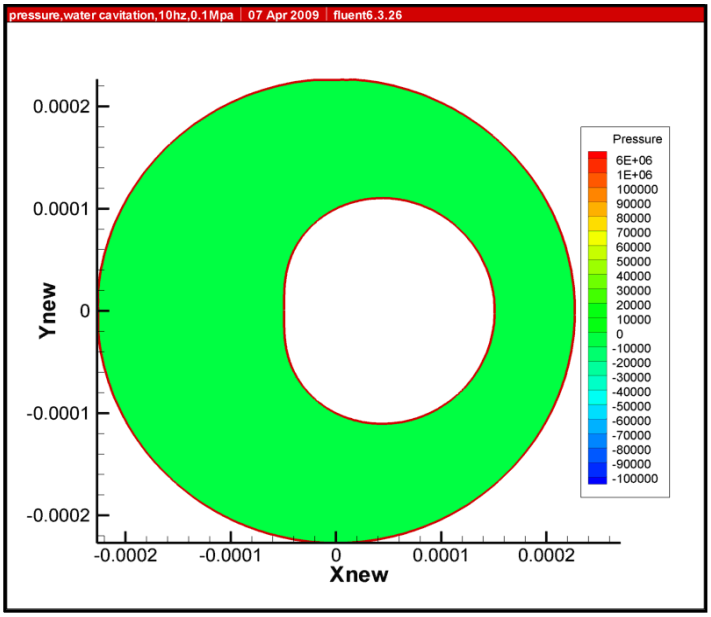

Figure 4.7 The pressure(Pa) field at a frequency of 10 Hz, an amplitude of 0.002 inches, and an operating pressure of 0.1 MPa

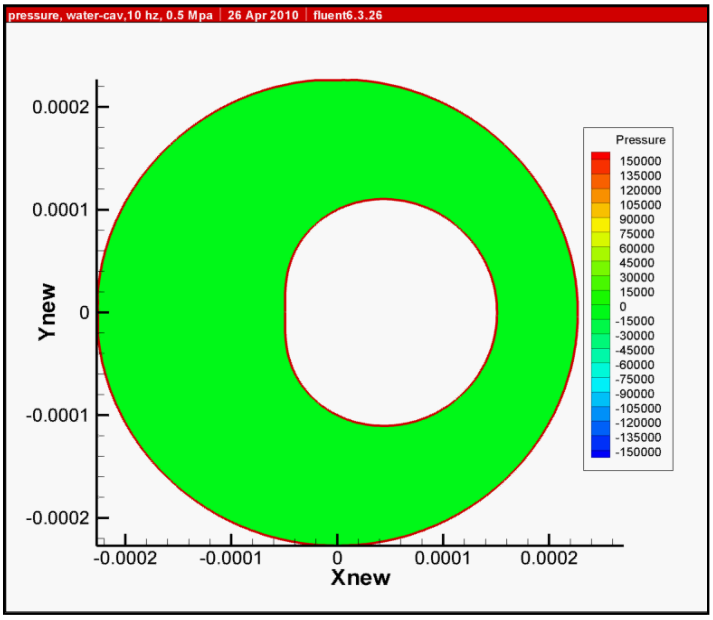

Figure 4.8 The pressure(Pa) field at a frequency of 10 Hz, an amplitude of 0.002 inches, and an operating pressure of 0.5 MPa

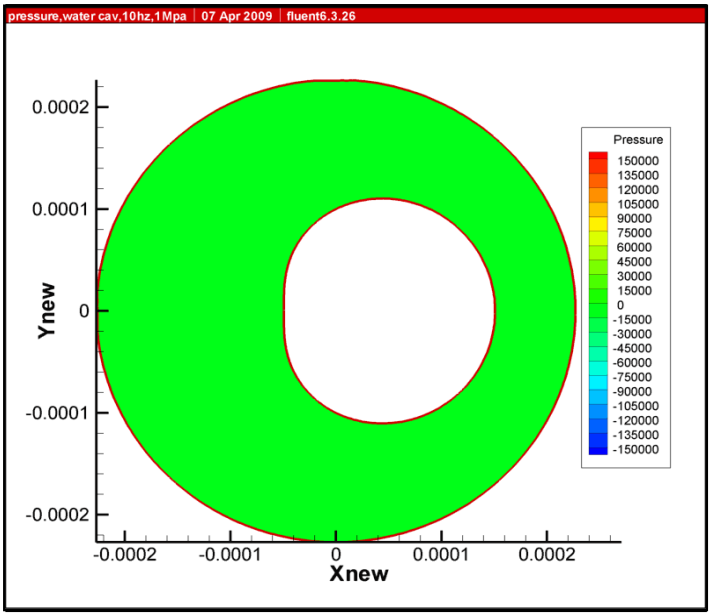

Figure 4.9 The pressure(Pa) field at a frequency of 10 Hz, an amplitude of 0.002 inches, and an operating pressure of 1 MPa

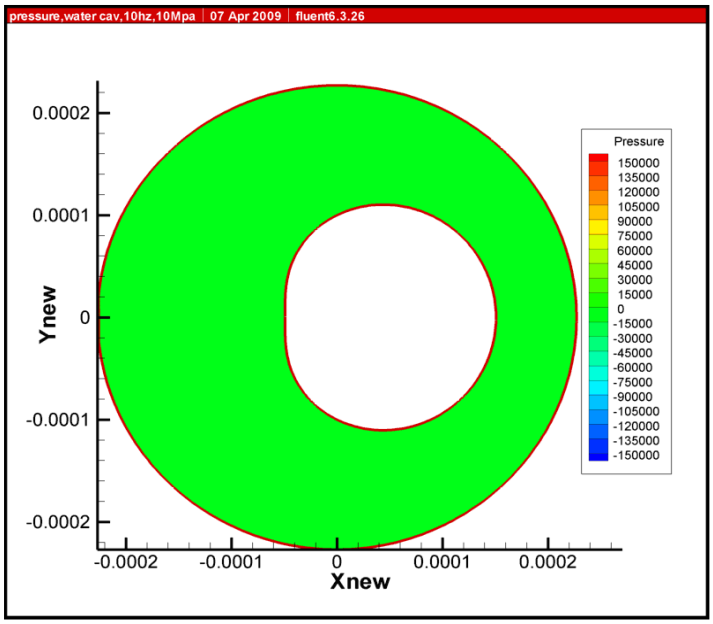

Figure 4.10 The pressure(Pa) field at a frequency of 10 Hz, an amplitude of 0.002 inches, and an operating pressure of 10 MPa

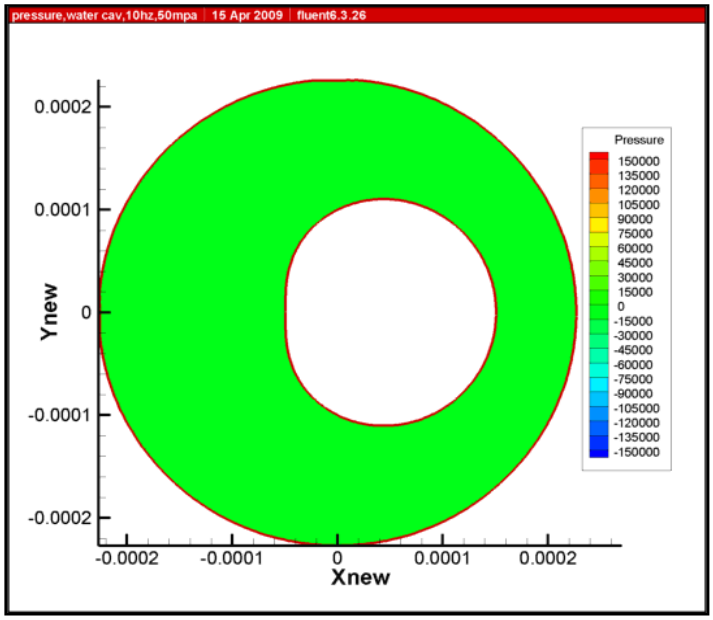

Figure 4.11 The pressure(Pa) field at a frequency of 10 Hz, an amplitude of 0.002 inches, and an operating pressure of 50 MPa

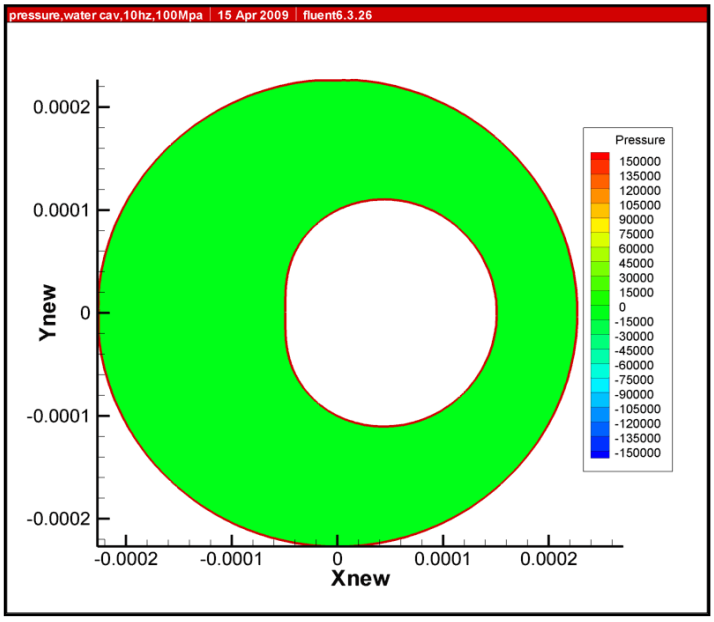

Figure 4.12 The pressure(Pa) field at a frequency of 10 Hz, an amplitude of 0.002 inches, and an operating pressure of 100 MPa

The Figure 4.13 shows the pressure fields for the single phase model for the frequency of 50 Hz. The pressure field is similar to the 10 Hz case except the pressure variance amplitude has increased as document earlier. For the multiphase flow, the animation of the pressure field for the journal amplitude of 0.002 inches and the frequency of 50 Hz at different operating pressures of 0.001, 1, 10, 50, and 100 MPa are depicted in the Figures 4.14 through 4.18. Unfortunately, the solution could not be achieved at the operating pressure of 0.01, 0.05, 0.1, and 0.5 MPa because of the limitation of numerical processing in FLUENT program. The severity of the cavitation prevented obtaining a stable solution at these values.

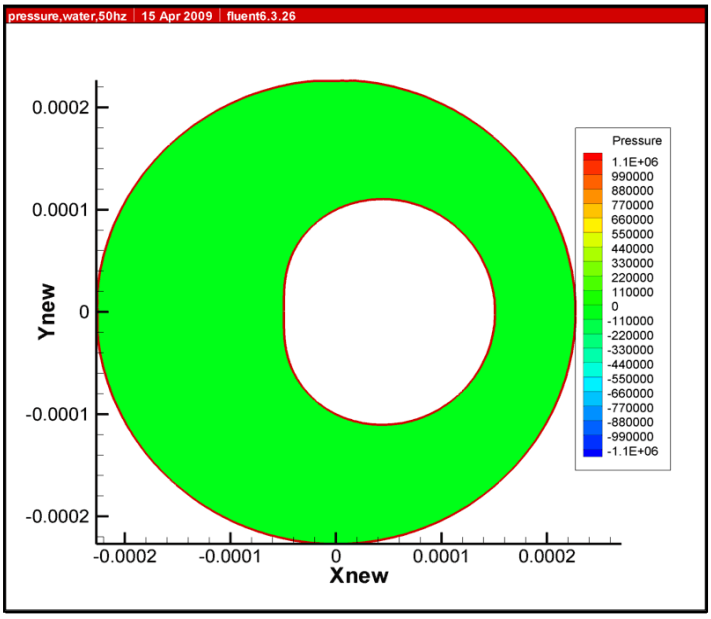

Figure 4.13 The pressure(Pa) field at a frequency of 50 Hz and an amplitude of 0.002 inches (Single phase flow)

For the multiphase flow cases, the pressure field of the SFD at the operating pressure of 0.001 MPa which is less than the vapor pressure of the water, i.e. 3540 Pa, is constant and equal to the static pressure as presented in figure 4.14. For 1 MPa operating

pressure in Figure 4.15, there is the highly fluctuation of the pressure in the squeeze zone when the journal is moving through certain positions, i.e. 90 and 270 degrees. As the journal moves forward to the positive degree from the start, or the left hand side, the squeeze film zone has the distribution of pressure varying approximately between the operating pressure upstream and vapor pressure downstream. The squeeze film zone experiences a drastic change and reaches the maximum positive pressure at a position of 90 degrees and possesses the distribution of upstream positive pressure and downstream negative pressure approximately between 95 and 110 degrees. From 110 to 180 degree, the pressure falls into the domination of positive pressure zone and approaches the operating pressure at 180 degrees. The distribution of the pressure of the squeeze film zone at the position between the positions of 180 degrees and 360 degrees has the similar pattern to that of the squeeze film zone from 0 to 180 degrees but is the mirror image. The pressure variance from the vapor pressure to over 3.5 MPa illustrates the severity of the cavitation occurring. This cavitation occurs due to the used of water in the squeeze film damper instead of oil which has a much lower vapor pressure.

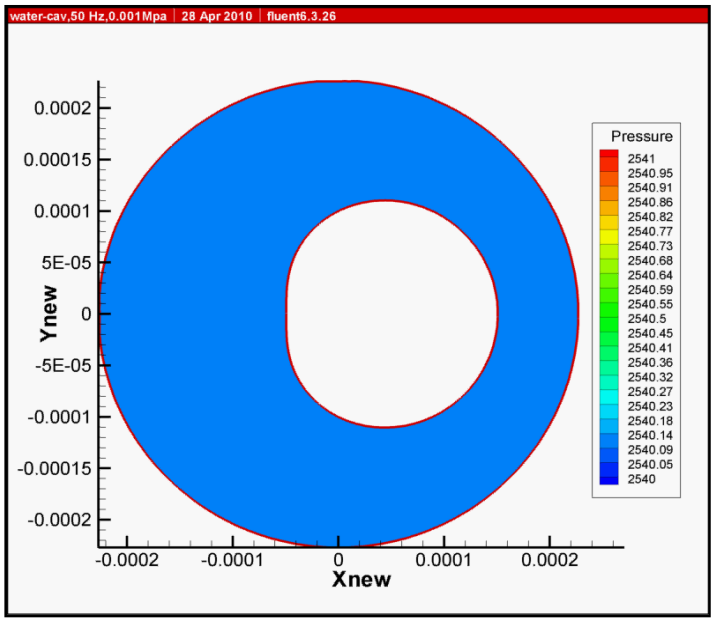

Figure 4.14 The pressure(Pa) field at a frequency of 50 Hz, an amplitude of 0.002 inches, and an operating pressure of 0.001 MPa

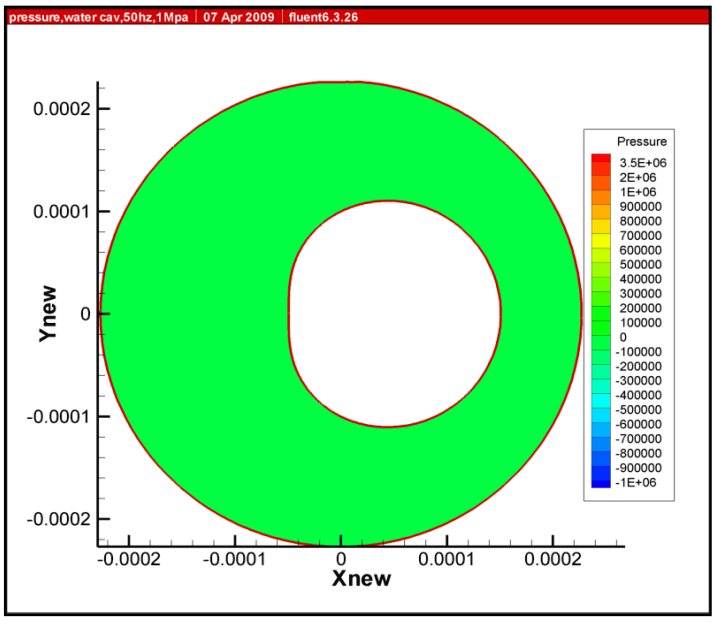

Figure 4.15 The pressure(Pa) field at a frequency of 50 Hz, an amplitude of 0.002 inches, and an operating pressure of 1 MPa

The Figures 4.16 through 4.18 show the pressure fields at different operating pressures of 10, 50, and 100 MPa, respectively. The pattern of the pressure fields is similar to that of the single phase case since the vapor pressure of the water is significantly less than the pressures generated by the dampen motion.

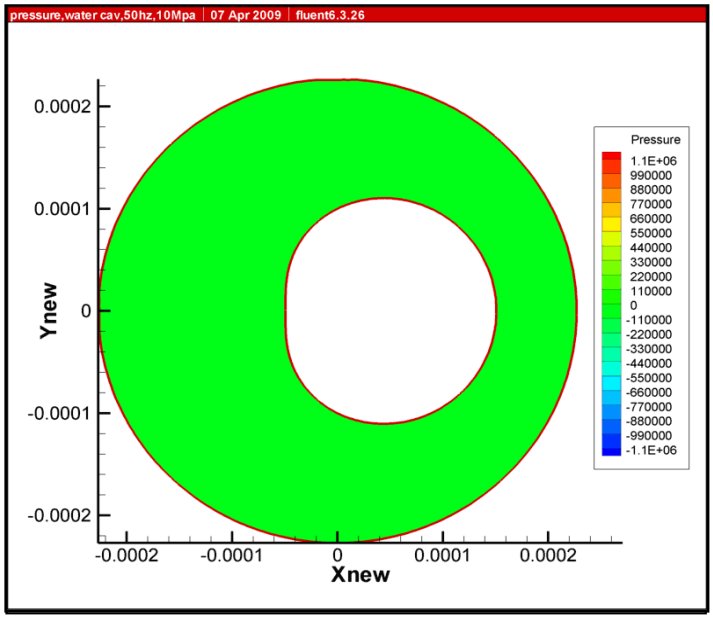

Figure 4.16 The pressure(Pa) field at a frequency of 50 Hz, an amplitude of 0.002 inches, and an operating pressure of 10 MPa

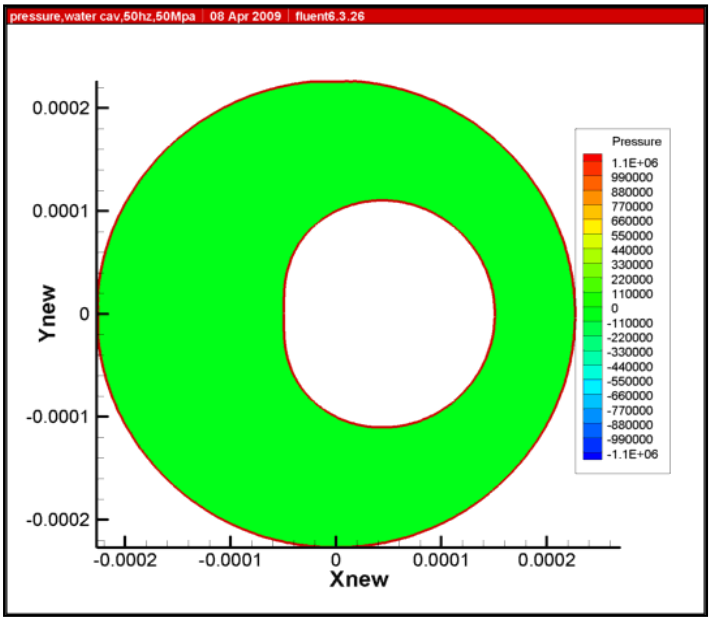

Figure 4.17 The pressure(Pa) field at a frequency of 50 Hz, an amplitude of 0.002 inches, and an operating pressure of 50 MPa

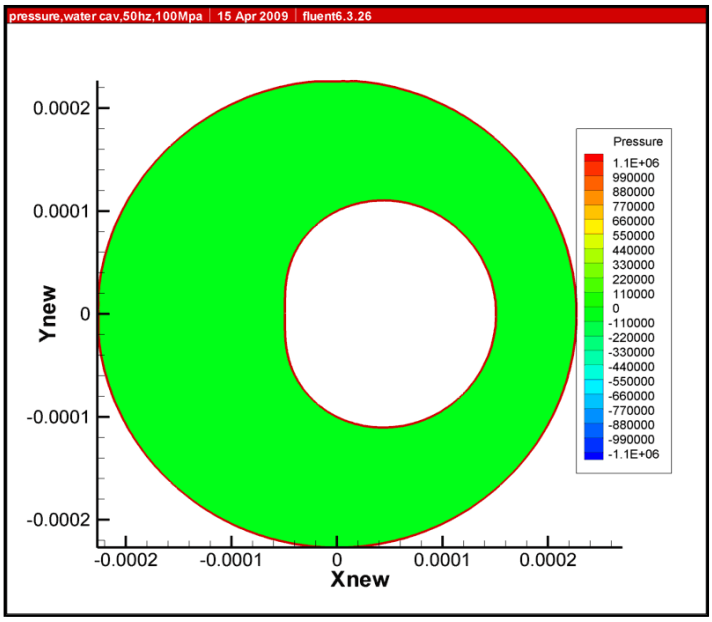

Figure 4.18 The pressure(Pa) field at a frequency of 50 Hz, an amplitude of 0.002 inches, and an operating pressure of 100 MPa

The Figure 4.19 shows the pressure fields for the single phase model for the frequency of 100 Hz. For the multiphase flow, the animation of the pressure field for the journal amplitude of 0.002 inches and the frequency of 100 Hz at different operating pressures of 0.001, 10, 50, and 100 MPa are depicted in the Figures 4.20 through 4.23. Unfortunately, the solution could not be achieved at the operating pressure of 0.01, 0.05, 0.1,0.5, and 1 MPa because of the limitation of numerical processing in the FLUENT program to follow the severe cavitation effects in these pressure ranges.

For the multiphase flow cases, the pressure field of the SFD at the operating pressure of 0.001 MPa which is less than the vapor pressure of the water, i.e. 3540 Pa, is constant and equal to the static pressure as presented in figure 4.20. The Figures 4.21 through 4.23 show the pressure fields at different operating pressures of 10, 50, and 100 MPa, respectively. The pattern of the pressure fields is similar to that of the single phase case. Again, this is due to the minimum pressure being larger than the vapor pressure of the water.

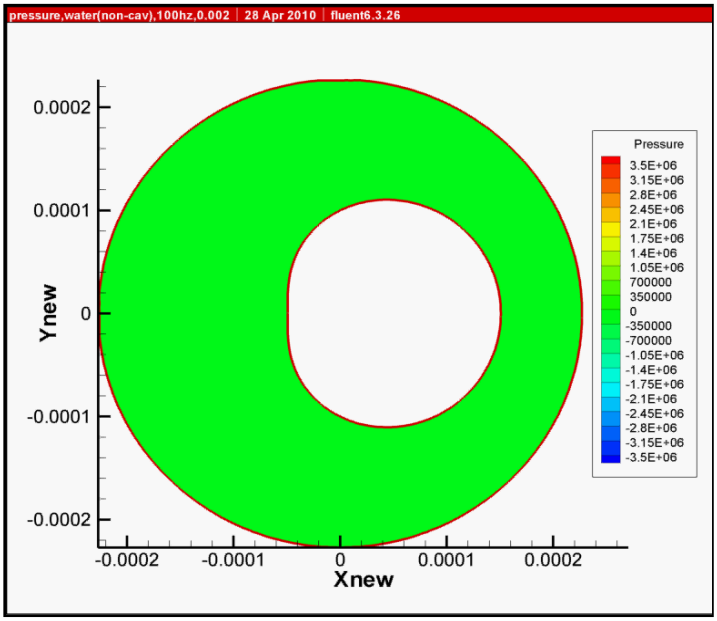

Figure 4.19 The pressure field at a frequency of 100 Hz and an amplitude of 0.002 inches (Single phase flow)

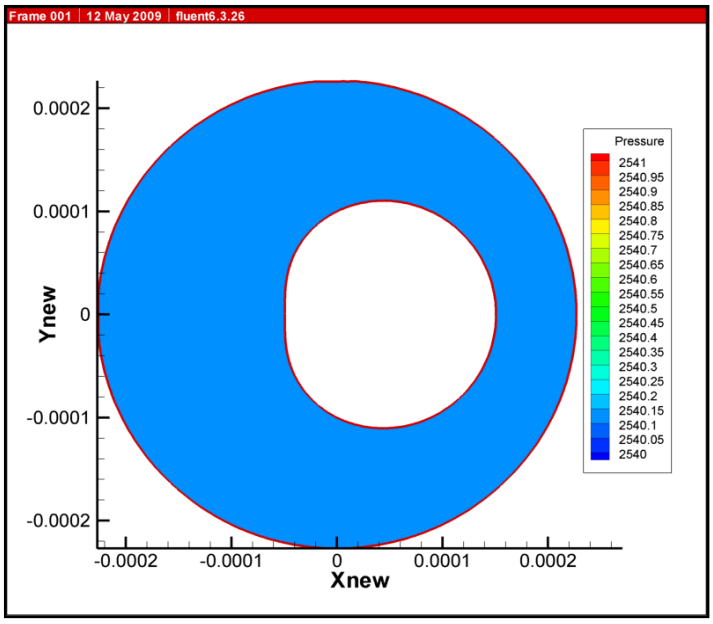

Figure 4.20 The pressure field at a frequency of 100 Hz, an amplitude of 0.002 inches, and an operating pressure of 0.001 MPa

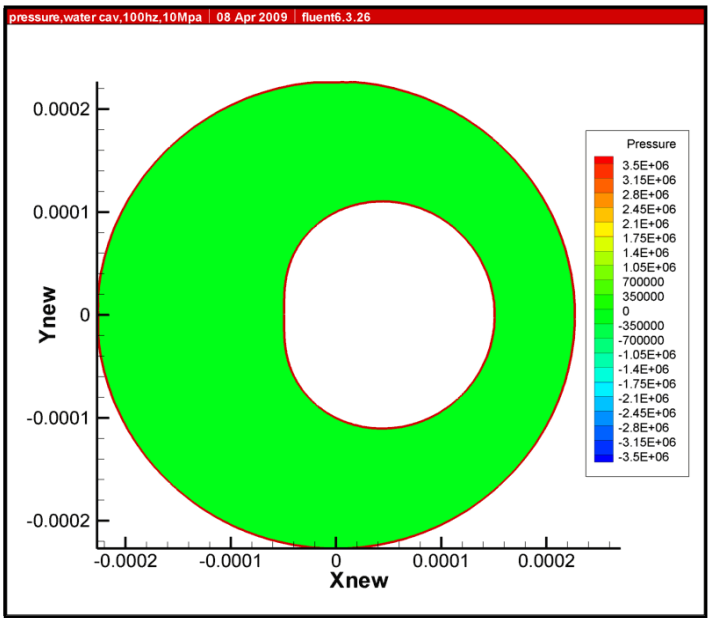

Figure 4.21 The pressure field at a frequency of 100 Hz, an amplitude of 0.002 inches, and an operating pressure of 10 MPa

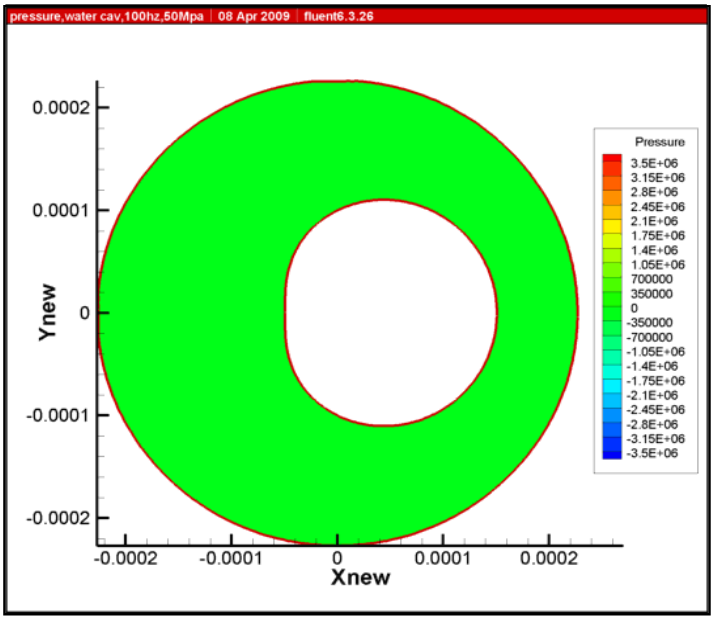

Figure 4.22 The pressure field at a frequency of 100 Hz, an amplitude of 0.002 inches, and an operating pressure of 50 MPa

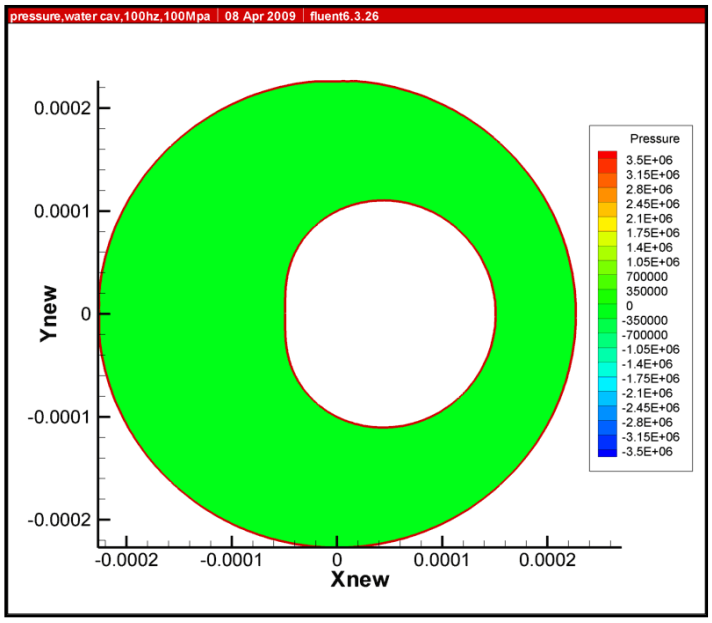

Figure 4.23 The pressure field at a frequency of 100 Hz, an amplitude of 0.002 inches, and an operating pressure of 100 MPa

The maximum and minimum pressures for all cases were shown in Tables 4.1 and 4.2. Table 4.1 shows the pressure for the single phase flow cases whereas Table 4.2 shows the pressure for the multiphase cases. According to the information in the table, the maximum and minimum pressures vary directly to the frequencies. The 100 Hz frequency possesses the highest pressure whereas the 10 Hz frequency possesses the lowest. For the multiphase flow cases in Table 4.2, there are unusual maximum and minimum pressures at certain operating pressures, i.e. at 0.01,0.05, 0.1 MPa for 10 Hz frequency and 1 MPa for 50 Hz frequency when cavitation occurs, whereas the other cases are similar to the single phase flow cases.

Table 4.1 The maximum and minimum pressures for single phase flow cases

Frequency = 10 Hz		Frequency = 50 Hz		Frequency = 100 Hz	
Pmax (Pa)	Pmin (Pa)	Pmax (Pa)	Pmin (Pa)	Pmax (Pa)	Pmin (Pa)
150,384	-152,057	1,070,200	-1,130,160	3,129,710	-3,373,210

Table 4.2 The maximum and minimum pressures for multiphase flow cases

Operating pressure	Frequency = 10 Hz		Frequency = 50 Hz		Frequency = 100 Hz	
(MPa)	Pmax (Pa)	Pmin (Pa)	Pmax (Pa)	Pmin (Pa)	Pmax (Pa)	Pmin (Pa)
0.001	2,540	2,540	2,540	2,540	2,540	2,540
0.01	9,439,010	-6,397	N/A	N/A	N/A	N/A
0.05	4,066,450	-45,306	N/A	N/A	N/A	N/A
0.1	6,531,940	-95,145	N/A	N/A	N/A	N/A
0.5	158,020	-151,450	N/A	N/A	N/A	N/A
1	151,215	-151,720	3,507,070	-983,315	N/A	N/A
10	150,909	-151,914	1,089,300	-1,152,520	3,347,600	-3,466,890
50	151,484	-152,030	1,093,640	-1,152,620	3,343,630	-3,469,320
100	151,486	-152,032	1,098,370	-1,158,580	3,343,670	-3,469,370

4.4 Velocity Fields

The velocity filed consisting of x and y in direction was portrayed in the same way as the pressure field. The Figure 4.24 shows the animation of x-velocity, or the velocity in x direction, for the single phase flow cases at the journal frequency of 10 Hz. For the multiphase flow cases, the Figure 4.25 shows the animation of x-velocity at the journal frequency of 10 Hz and the operating pressure of 0.001 MPa. The x-velocity is almost constant and close to zero due to only vapor being present.

The Figure 4.26 through 4.33 shows the animation of x-velocity at the journal frequency of 10 Hz and the operating pressures of 0.01, 0.05, 0.1, 0.5, 1, 10, 50, and 100

MPa. The squeeze film zone has the symmetric distribution of x-velocity if the mirror line is the x-axis. The velocity gradually increases along with the journal moving forward to the positive degree, or the left hand side. The velocity changes rapidly to the maximum velocity at 90 degrees and returns to the normal distribution along the way to 180 degrees. The distribution of the x-velocity of the squeeze film zone at the position between 180 degrees and 360 degrees has the similar pattern to that of the squeeze film zone from 0 to 180 degrees but having negative values because of the negative direction of the journal. The sudden large change in fluid velocity is due to the fluid phase changes causing a rush of fluid as cavitation occurs. The x-velocity for the operating pressures of 0.5, 1, 10, 50, and 100 MPa is almost the same as that of single phase flow case as the effect of cavitation diminish or vanish.

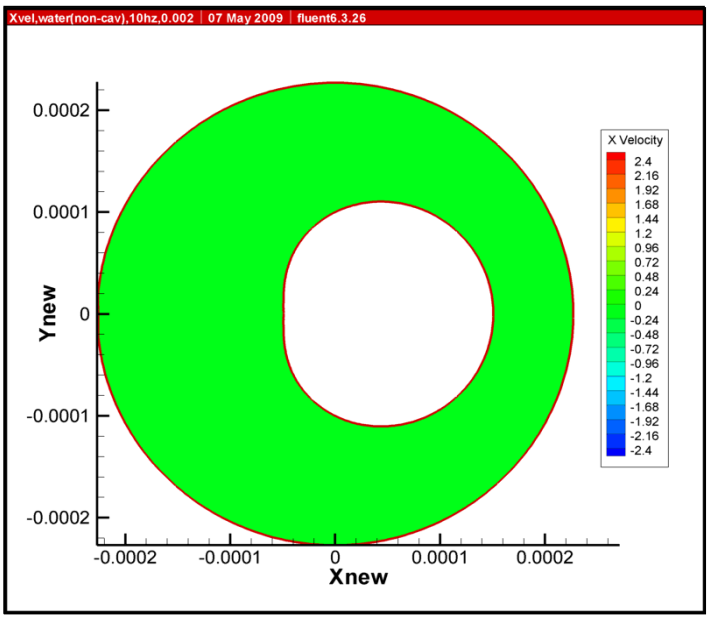

Figure 4.24 The x-velocity(m/s) field at a frequency of 10 Hz and an amplitude of 0.002 inches (Single phase flow)

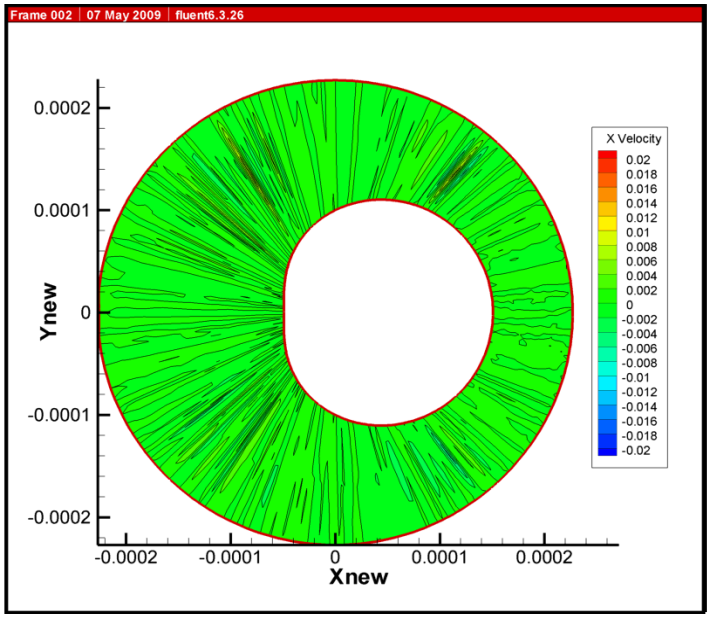

Figure 4.25 The x-velocity(m/s) field at a frequency of 10 Hz, an amplitude of 0.002 inches, and an operating pressure of 0.001 MPa

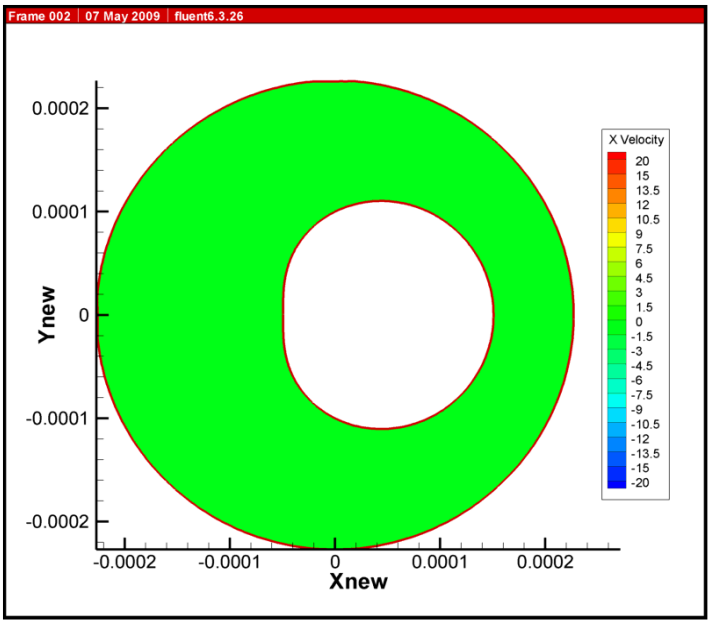

Figure 4.26 The x-velocity(m/s) field at a frequency of 10 Hz, an amplitude of 0.002 inches, and an operating pressure of 0.01 MPa

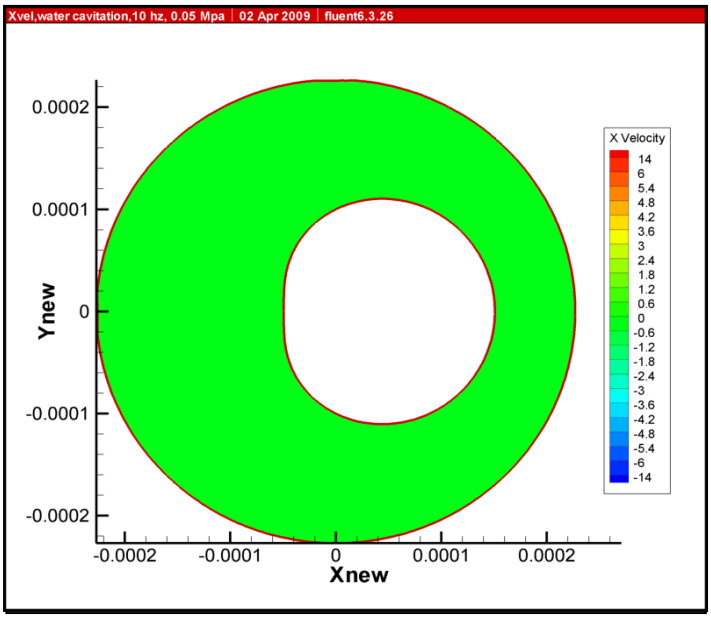

Figure 4.27 The x-velocity(m/s) field at a frequency of 10 Hz, an amplitude of 0.002 inches, and an operating pressure of 0.05 MPa

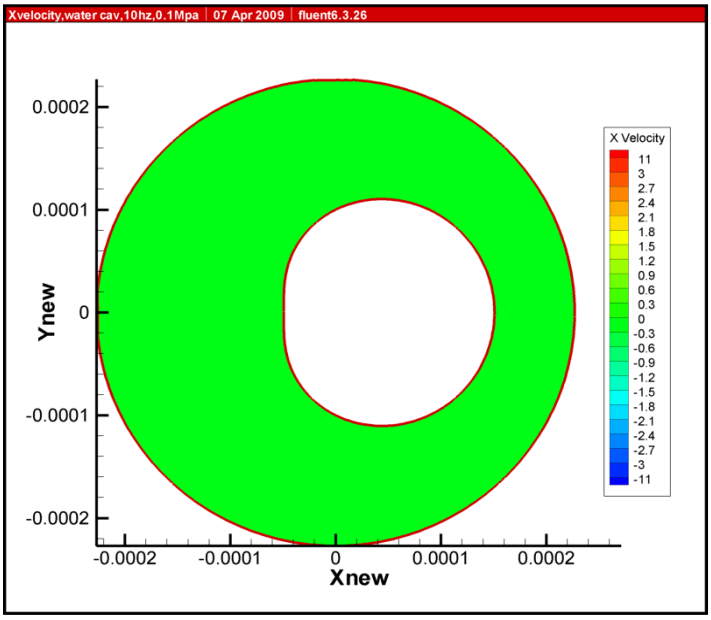

Figure 4.28 The x-velocity(m/s) field at a frequency of 10 Hz, an amplitude of 0.002 inches, and an operating pressure of 0.1 MPa

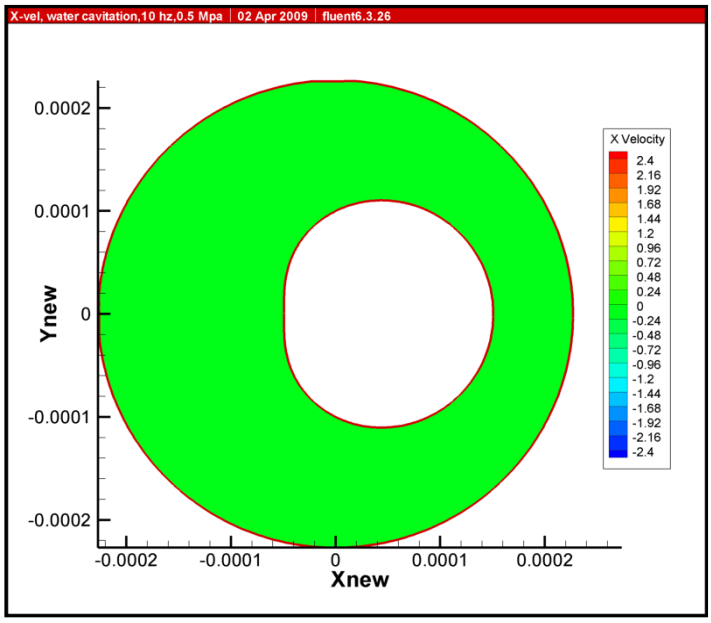

Figure 4.29 The x-velocity(m/s) field at a frequency of 10 Hz, an amplitude of 0.002 inches, and an operating pressure of 0.5 MPa

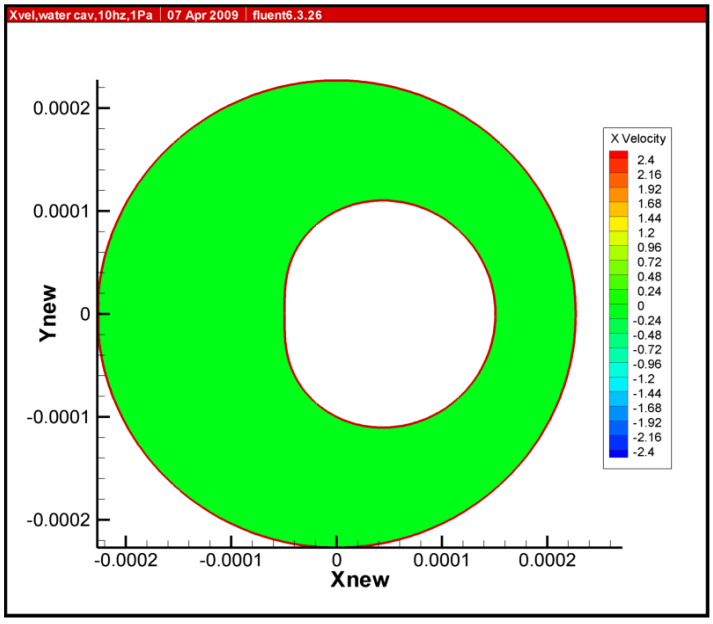

Figure 4.30 The x-velocity(m/s) field at a frequency of 10 Hz, an amplitude of 0.002 inches, and an operating pressure of 1 MPa

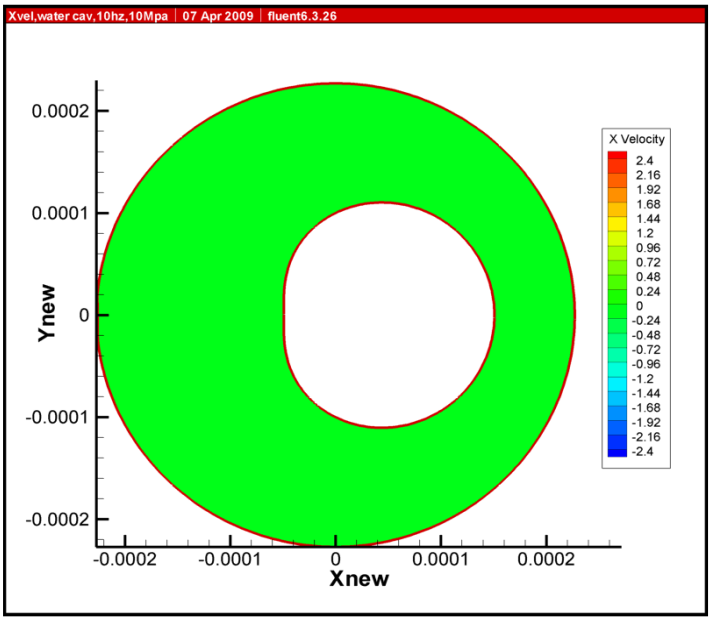

Figure 4.31 The x-velocity(m/s) field at a frequency of 10 Hz, an amplitude of 0.002 inches, and an operating pressure of 10 MPa

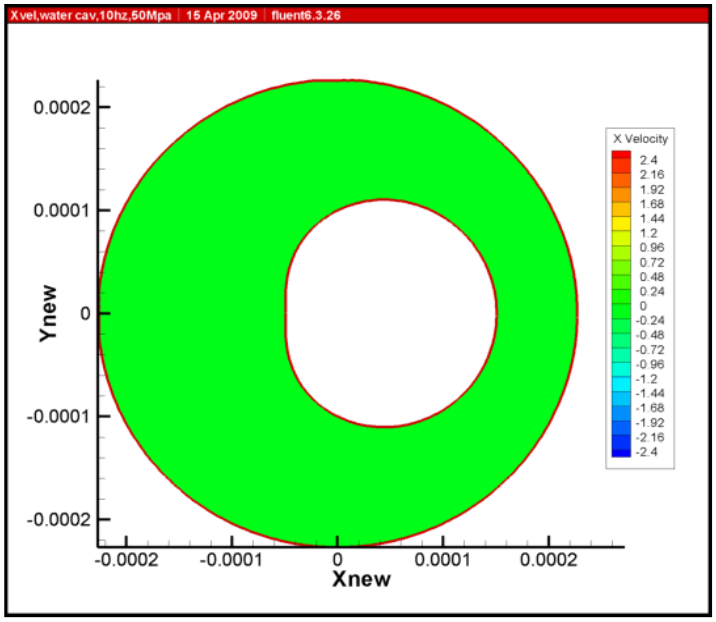

Figure 4.32 The x-velocity(m/s) field at a frequency of 10 Hz, an amplitude of 0.002 inches, and an operating pressure of 50 MPa

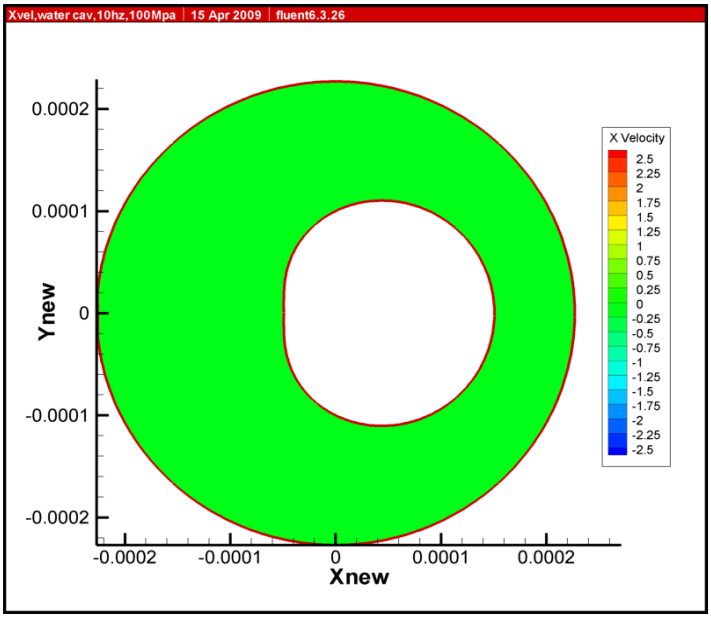

Figure 4.33 The x-velocity(m/s) field at a frequency of 10 Hz, an amplitude of 0.002 inches, and an operating pressure of 100 MPa

The Figure 4.34 shows the animation of x-velocity, or the velocity in x direction, for the single phase flow cases at the journal frequency of 50 Hz. For the multiphase flow cases, the Figure 4.35 shows the animation of x-velocity at the journal frequency of 50 Hz and the operating pressure of 0.001 MPa. The x-velocity is almost constant and close to zero as the water is in the gas phase.

The Figure 4.36 through 4.39 shows the animation of x-velocity at the journal frequency of 10 Hz and the operating pressures of 1, 10, 50, and 100 MPa. The squeeze film zone at 50 Hz frequency has the same pattern of the distribution as that at 10 Hz frequency. The x-velocity for the operating pressures of 10, 50, and 100 MPa is almost the same as that of single phase flow case. As stated before, at the larger journal frequencies, it was not possible to predict the cavitating flows at operating pressures below 1MPa.

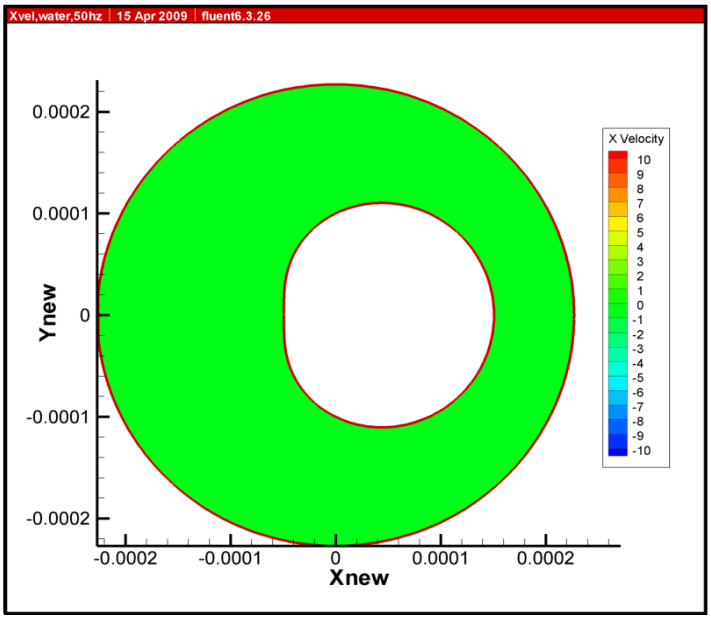

Figure 4.34 The x-velocity(m/s) field at a frequency of 50 Hz and an amplitude of 0.002 inches (Single phase flow)

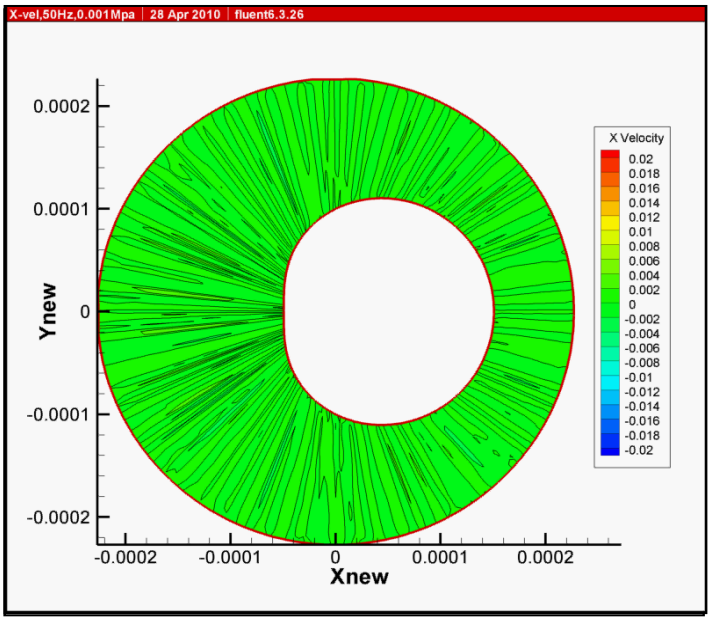

Figure 4.35 The x-velocity(m/s) field at a frequency of 50 Hz, an amplitude of 0.002 inches, and an operating pressure of 0.001 MPa

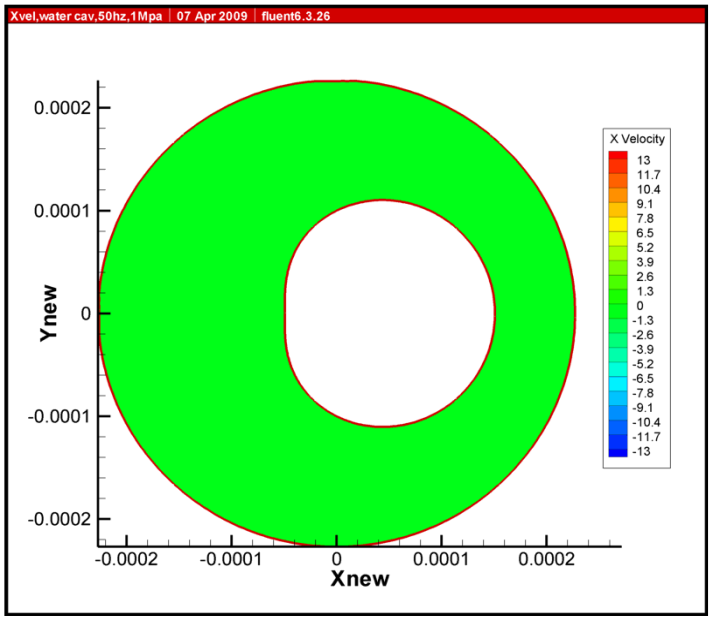

Figure 4.36 The x-velocity(m/s) field at a frequency of 50 Hz, an amplitude of 0.002 inches, and an operating pressure of 1 MPa

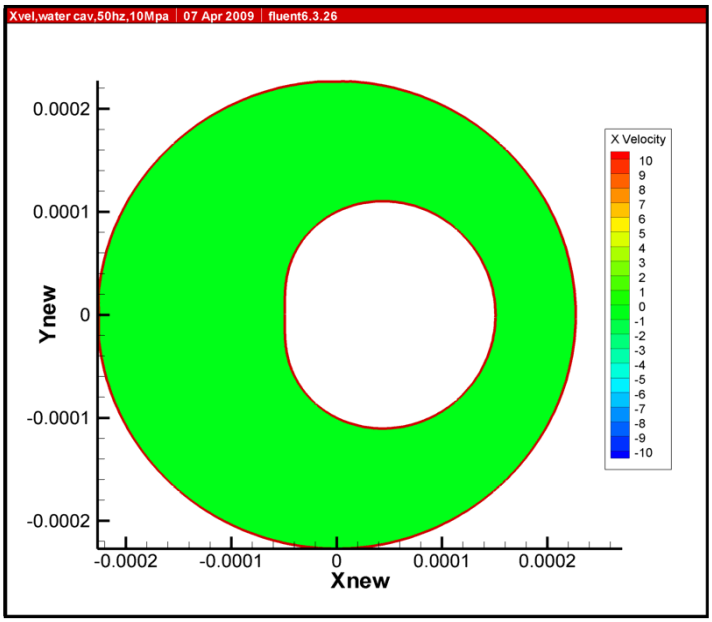

Figure 4.37 The x-velocity(m/s) field at a frequency of 50 Hz, an amplitude of 0.002 inches, and an operating pressure of 10 MPa

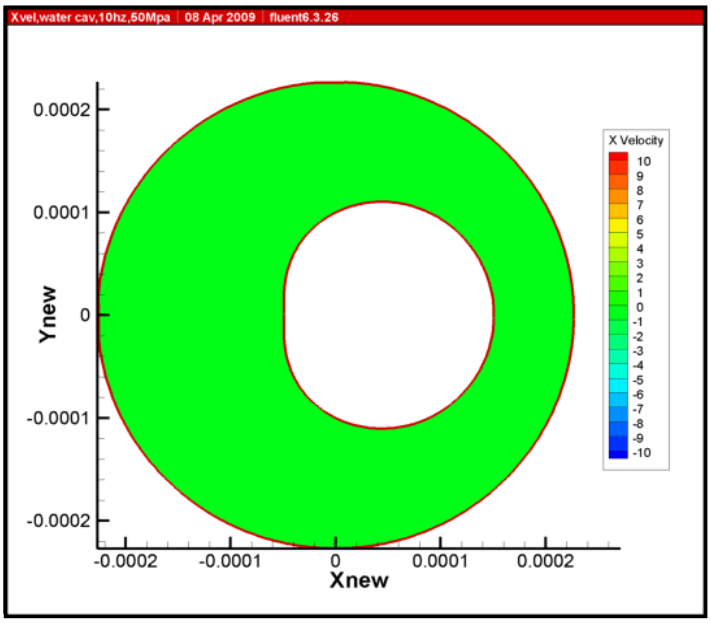

Figure 4.38 The x-velocity(m/s) field at a frequency of 50 Hz, an amplitude of 0.002 inches, and an operating pressure of 50 MPa

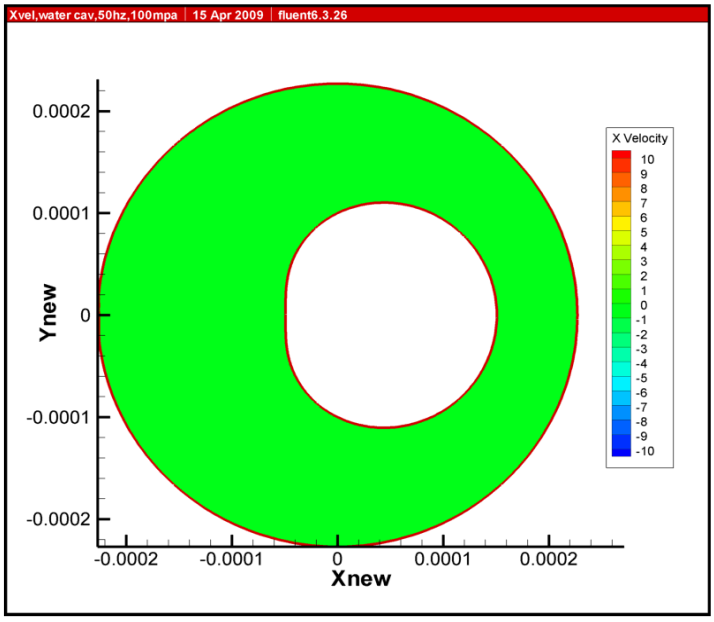

Figure 4.39 The x-velocity(m/s) field at a frequency of 50 Hz, an amplitude of 0.002 inches, and an operating pressure of 100 MPa

The Figure 4.40 shows the animation of x-velocity, or the velocity in x direction, for the single phase flow cases at a journal frequency of 100 Hz. For the multiphase flow cases, the Figure 4.41 shows the animation of x-velocity at the journal frequency of 100 Hz and the operating pressure of 0.001 MPa. The x-velocity is almost constant and close to zero.

The Figure 4.42 through 4.44 shows the animation of x-velocity at the journal frequency of 10 Hz and the operating pressures of 10, 50, and 100 MPa. The squeeze film zone at 50 Hz frequency has the same pattern of the distribution as that at 10 Hz frequency. The x-velocity for the operating pressures of 10, 50, and 100 MPa is almost the same as that of single phase flow case.

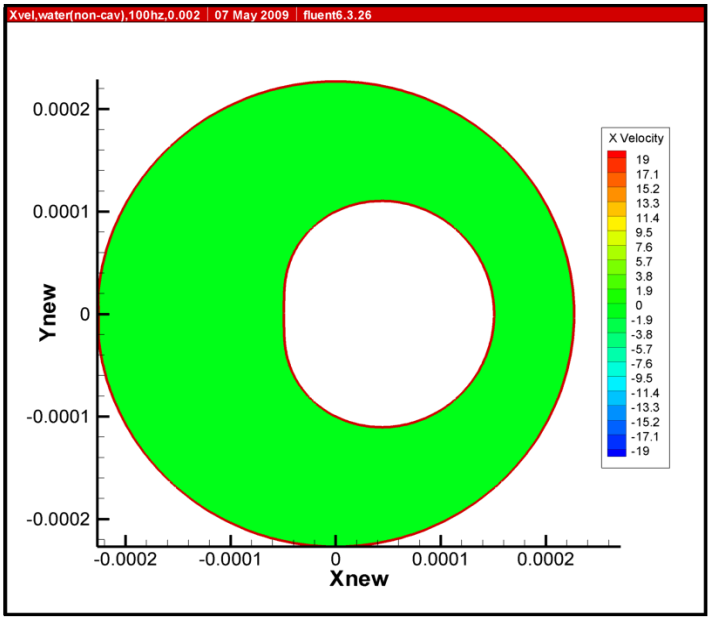

Figure 4.40 The x-velocity(m/s) field at a frequency of 100 Hz and an amplitude of 0.002 inches (Single phase flow)

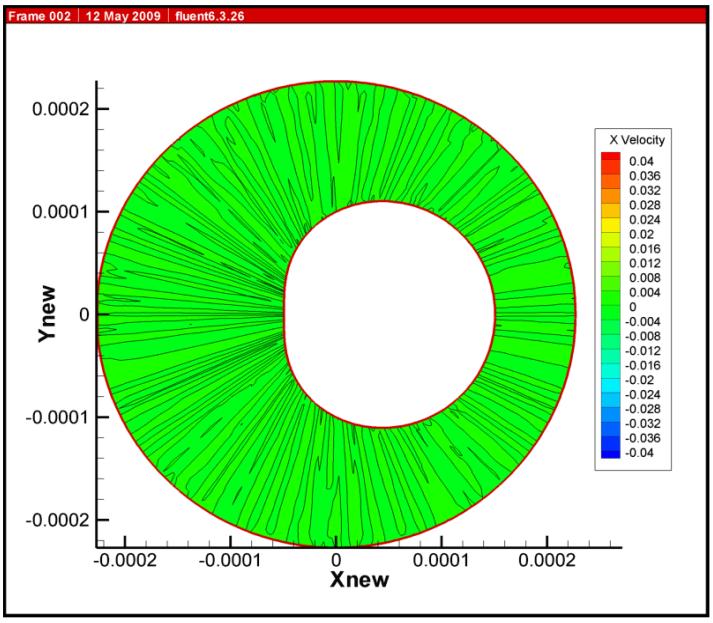

Figure 4.41 The x-velocity(m/s) field at a frequency of 100 Hz, an amplitude of 0.002 inches, and an operating pressure of 0.001 MPa

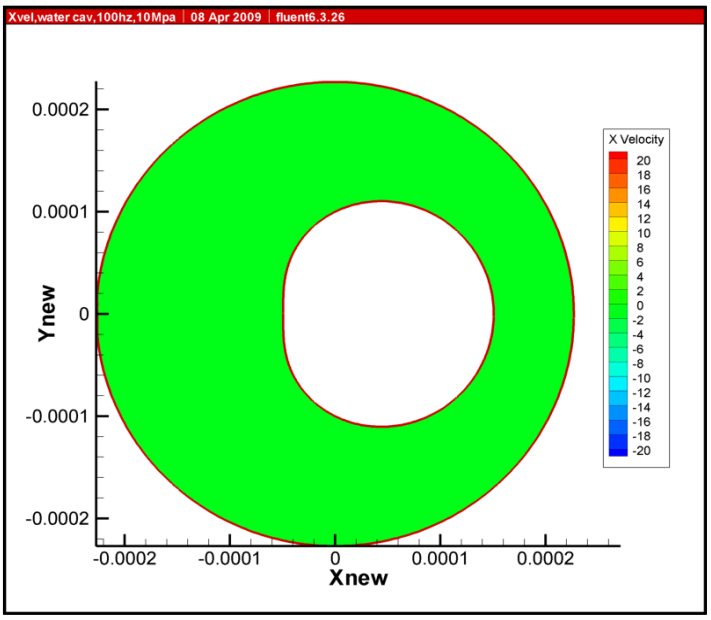

Figure 4.42 The x-velocity(m/s) field at a frequency of 100 Hz, an amplitude of 0.002 inches, and an operating pressure of 10 MPa

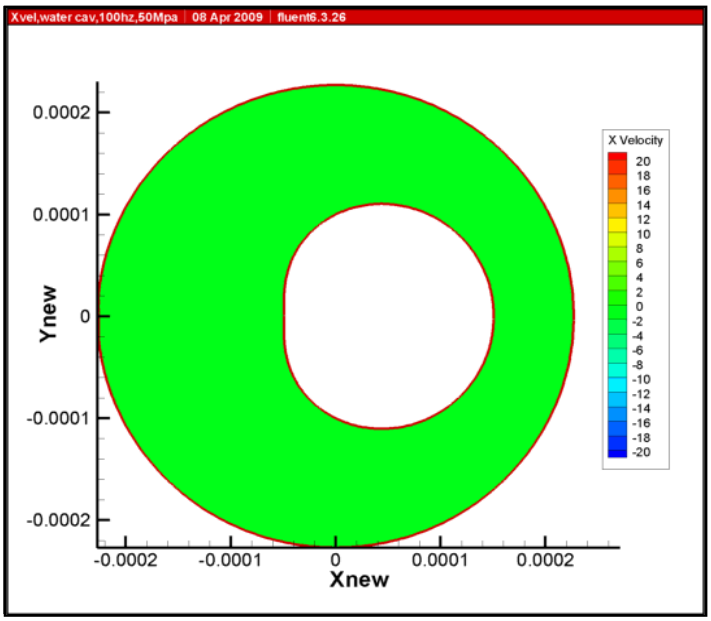

Figure 4.43 The x-velocity(m/s) field at a frequency of 100 Hz, an amplitude of 0.002 inches, and an operating pressure of 50 MPa

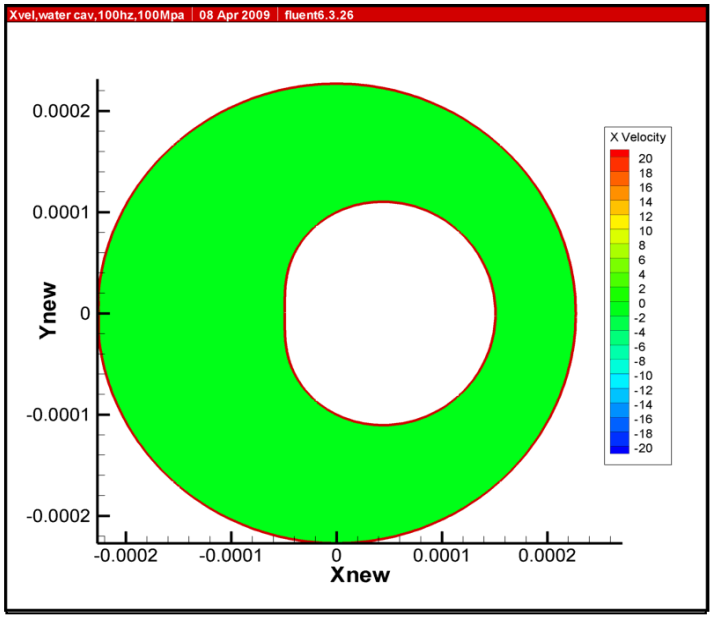

Figure 4.44 The x-velocity(m/s) field at a frequency of 100 Hz, an amplitude of 0.002 inches, and an operating pressure of 100 MPa

The animation of the y-velocity, or the velocity in y direction, is generally similar to that elaborated for the single phase case. However, there is a drastic change in velocity at certain positions, i.e. 90 and 270 degrees, for some multiphase flow cases.

The Figure 4.45 shows the animation of y-velocity for the single phase flow cases at a journal frequency of 10 Hz. For the multiphase flow cases, the Figure 4.46 shows the animation of y-velocity at the journal frequency of 10 Hz and the operating pressure of 0.001 MPa. The y-velocity is almost constant and close to zero. The Figures 4.47 through 4.54 animate the y-velocity for operating pressures of 0.01, 0.05, 0.1, 0.5, 1, 10, 50, 100 MPa. There is an extremely large change in y-velocity as the journal moving through 90 and 270 degree positions for the operating pressures of 0.001, 0.05, and 0.1 MPa whereas the y-velocity distribution for the operating pressures of 0.5, 1, 10, 50, and 100 MPa is almost the same as that of single phase flow case. The y-velocity contours show how cavitation produces large velocities. The head on collision of these large velocity along the y = 0 plane are the cause for the sudden pressure changes observed in the pressure contour animations. The spatial velocity gradients are very large when the fluid cavitates.

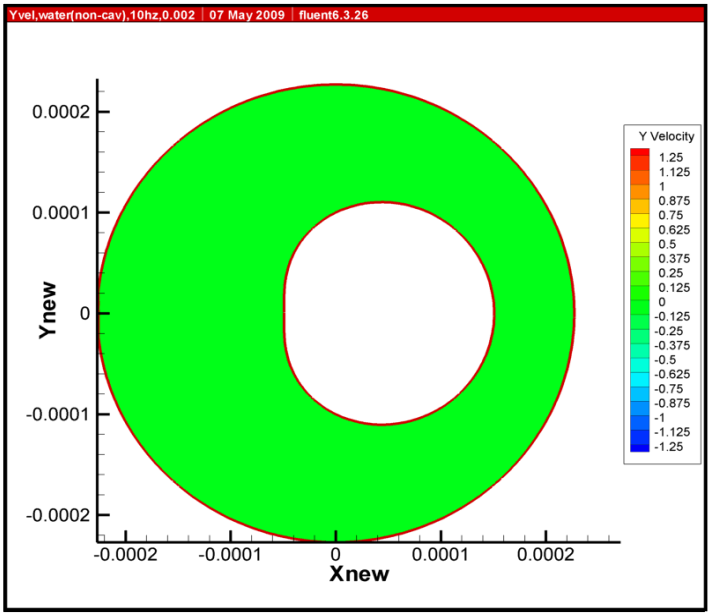

Figure 4.45 The y-velocity(m/s) field at a frequency of 10 Hz and an amplitude of 0.002 inches (Single phase flow)

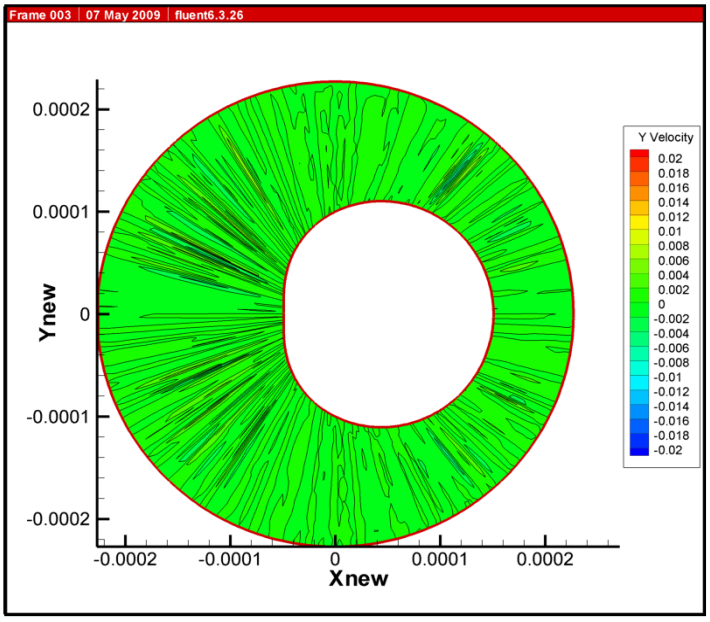

Figure 4.46 The y-velocity(m/s) field at a frequency of 10 Hz, an amplitude of 0.002 inches, and an operating pressure of 0.001 MPa

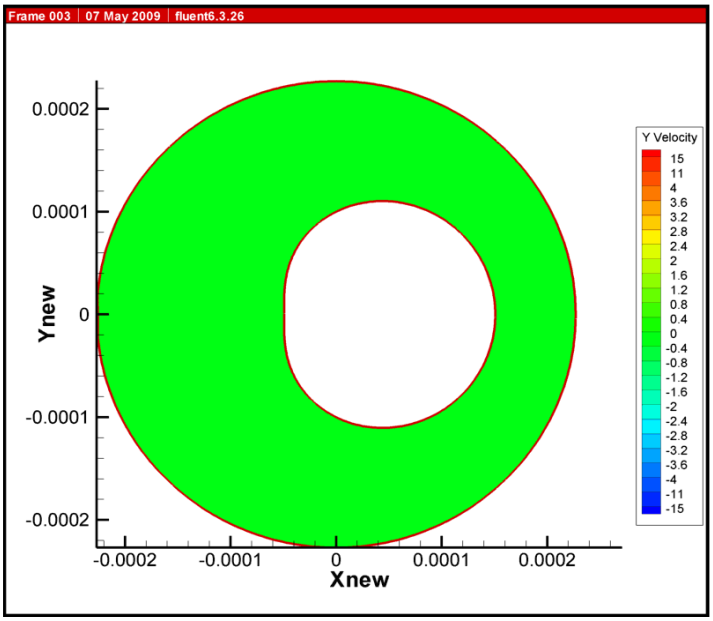

Figure 4.47 The y-velocity(m/s) field at a frequency of 10 Hz, an amplitude of 0.002 inches, and an operating pressure of 0.01 MPa

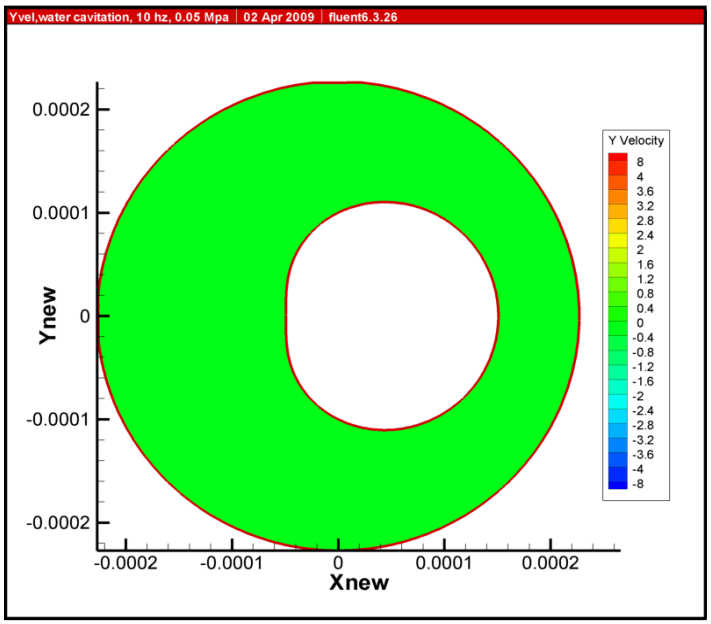

Figure 4.48 The y-velocity(m/s) field at a frequency of 10 Hz, an amplitude of 0.002 inches, and an operating pressure of 0.05 MPa

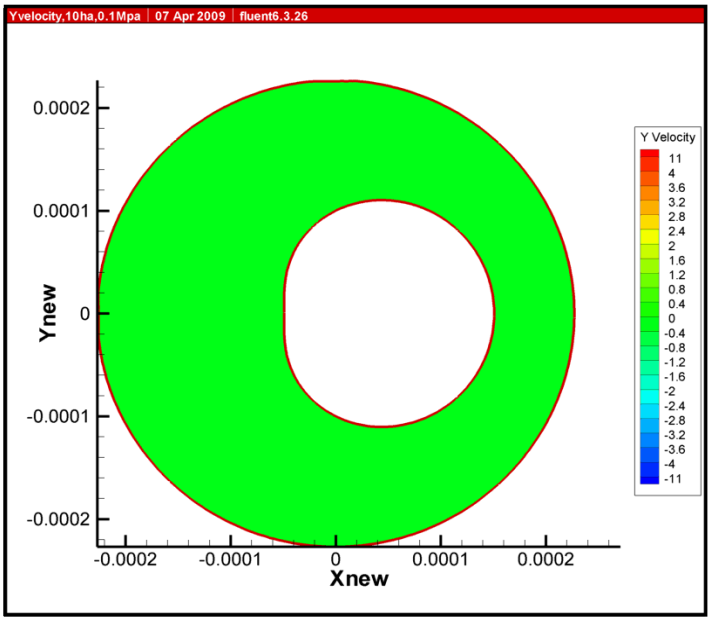

Figure 4.49 The y-velocity(m/s) field at a frequency of 10 Hz, an amplitude of 0.002 inches, and an operating pressure of 0.1 MPa

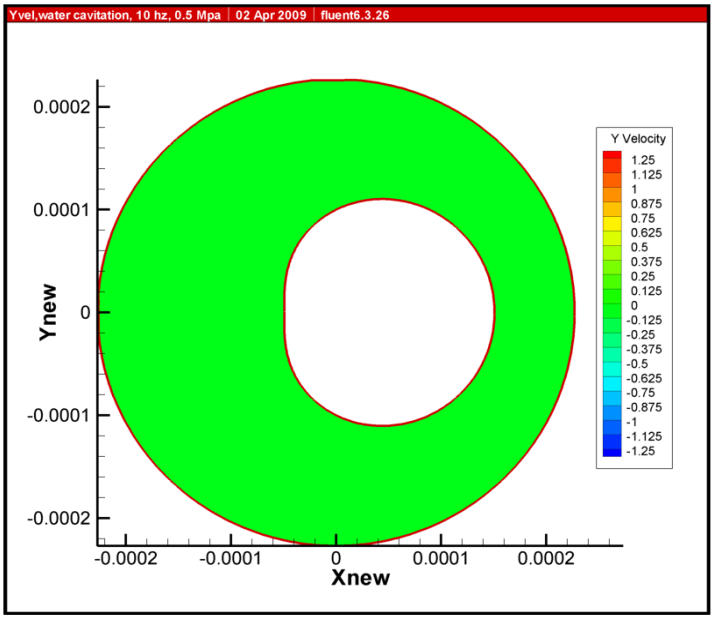

Figure 4.50 The y-velocity(m/s) field at a frequency of 10 Hz, an amplitude of 0.002 inches, and an operating pressure of 0.5 MPa

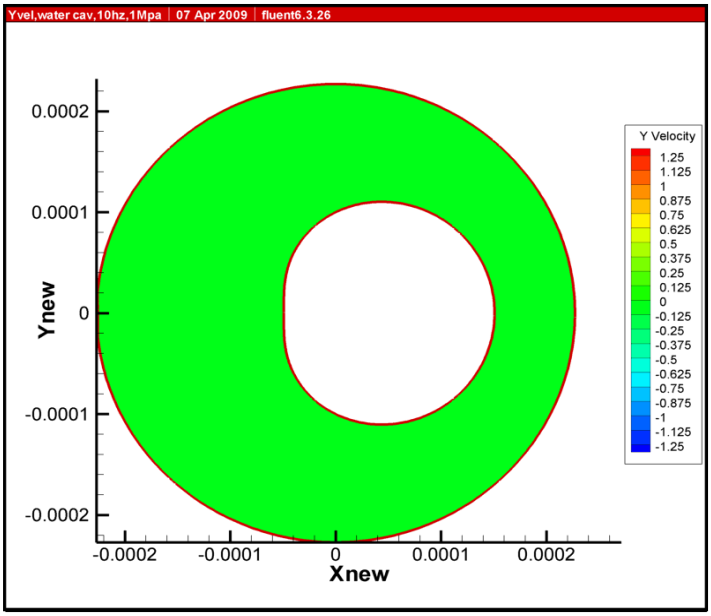

Figure 4.51 The y-velocity(m/s) field at a frequency of 10 Hz, an amplitude of 0.002 inches, and an operating pressure of 1 MPa

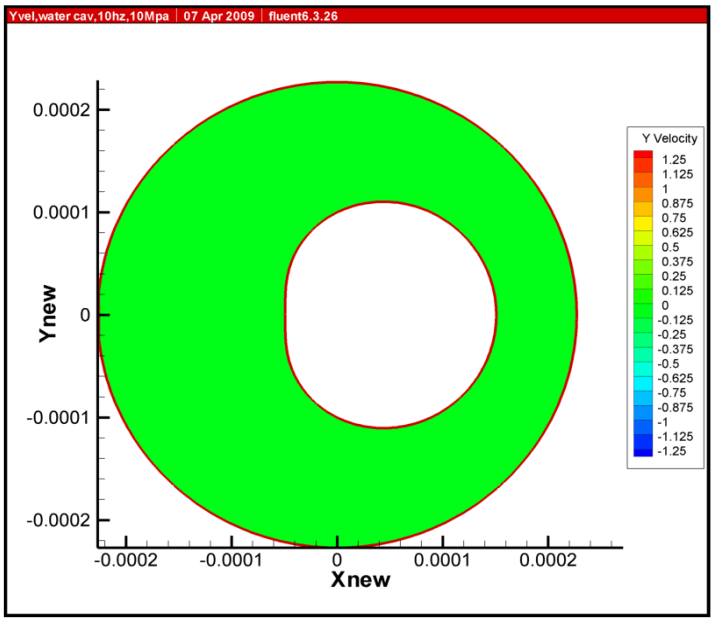

Figure 4.52 The y-velocity(m/s) field at a frequency of 10 Hz, an amplitude of 0.002 inches, and an operating pressure of 10 MPa

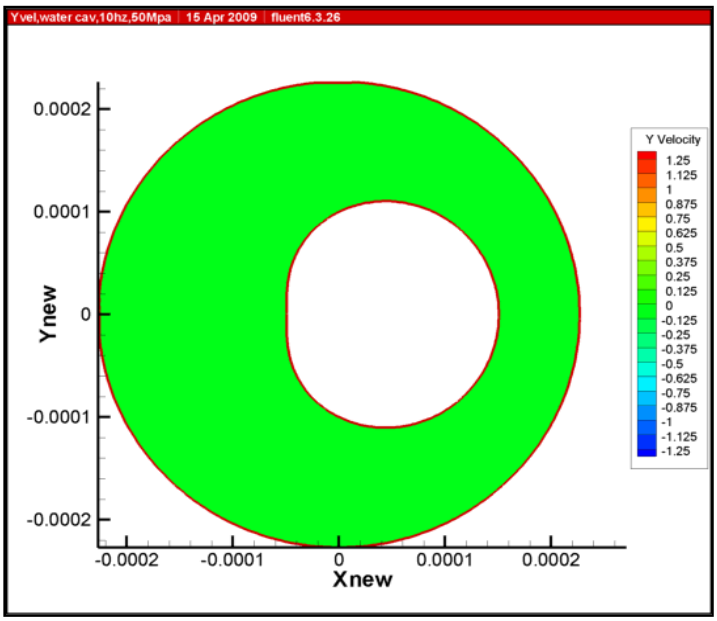

Figure 4.53 The y-velocity(m/s) field at a frequency of 10 Hz, an amplitude of 0.002 inches, and an operating pressure of 50 MPa

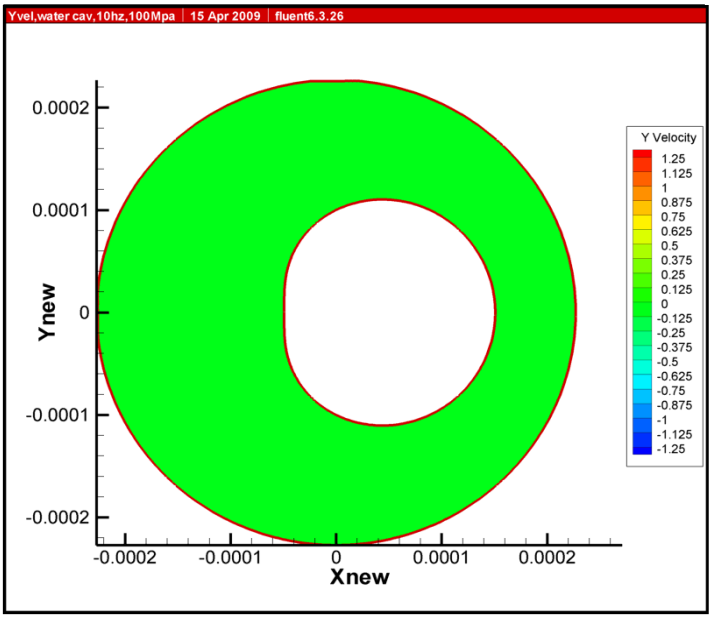

Figure 4.54 The y-velocity(m/s) field at a frequency of 10 Hz, an amplitude of 0.002 inches, and an operating pressure of 100 MPa

The Figure 4.55 shows the animation of y-velocity for the single phase flow cases at a journal frequency of 50 Hz. For the multiphase flow cases, the Figure 4.56 shows the animation of y-velocity at the journal frequency of 50 Hz and the operating pressure of 0.001 MPa. The y-velocity is almost constant and close to zero for the gas only case. The Figures 4.57 through 4.60 animate the y-velocity for operating pressures of 1, 10, 50, 100 MPa. There is extremely change in y-velocity as the journal moving through 90 and 270 degree positions for the operating pressures of 1 MPa including some phase change of the water whereas the y-velocity distribution for the operating pressures of 10, 50, and 100 MPa is almost the same as that of single phase flow case.

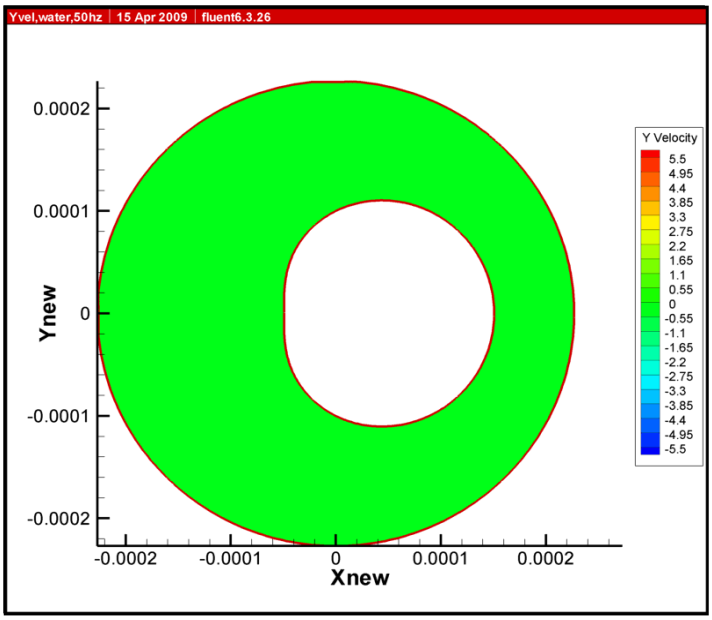

Figure 4.55 The y-velocity(m/s) field at a frequency of 50 Hz and an amplitude of 0.002 inches (Single phase flow)

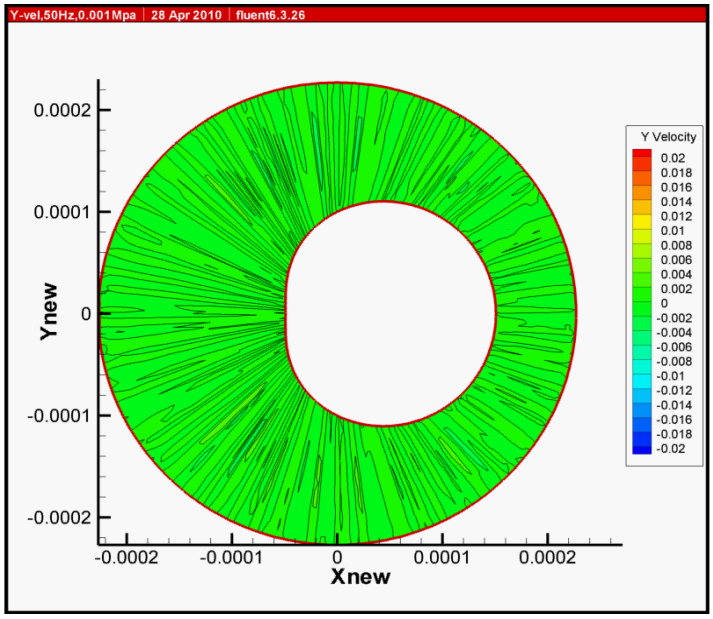

Figure 4.56 The y-velocity(m/s) field at a frequency of 50 Hz, an amplitude of 0.002 inches, and an operating pressure of 0.001 MPa

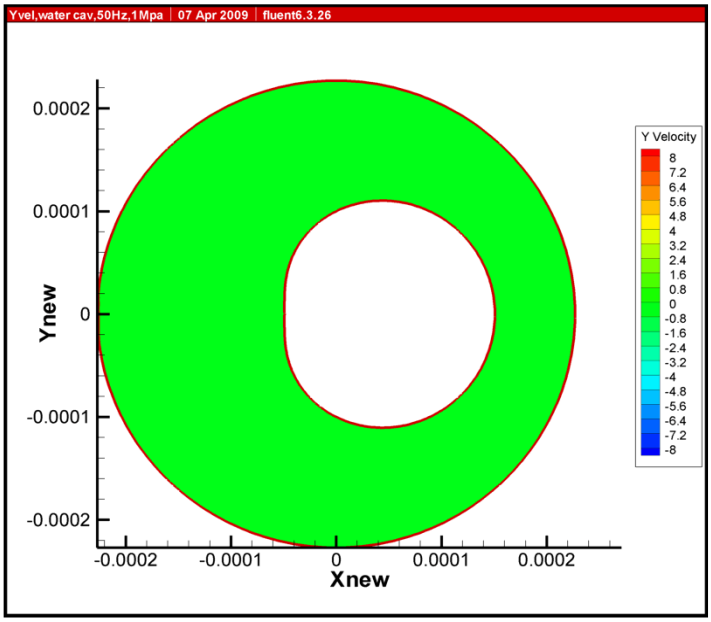

Figure 4.57 The y-velocity(m/s) field at a frequency of 50 Hz, an amplitude of 0.002 inches, and an operating pressure of 1 MPa

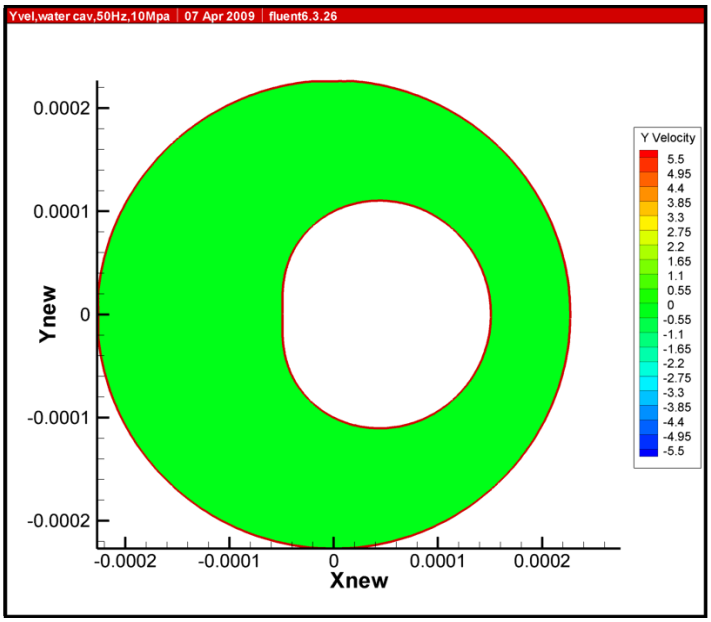

Figure 4.58 The y-velocity(m/s) field at a frequency of 50 Hz, an amplitude of 0.002 inches, and an operating pressure of 10 MPa

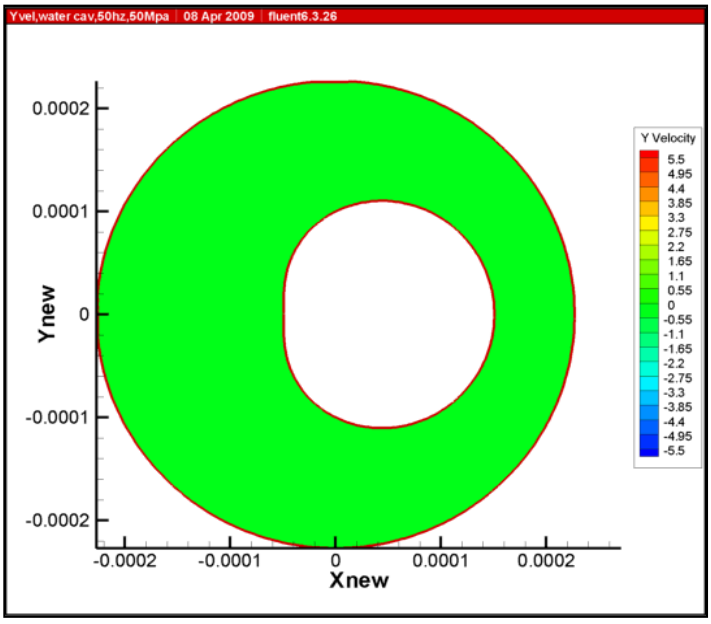

Figure 4.59 The y-velocity(m/s) field at a frequency of 50 Hz, an amplitude of 0.002 inches, and an operating pressure of 50 MPa

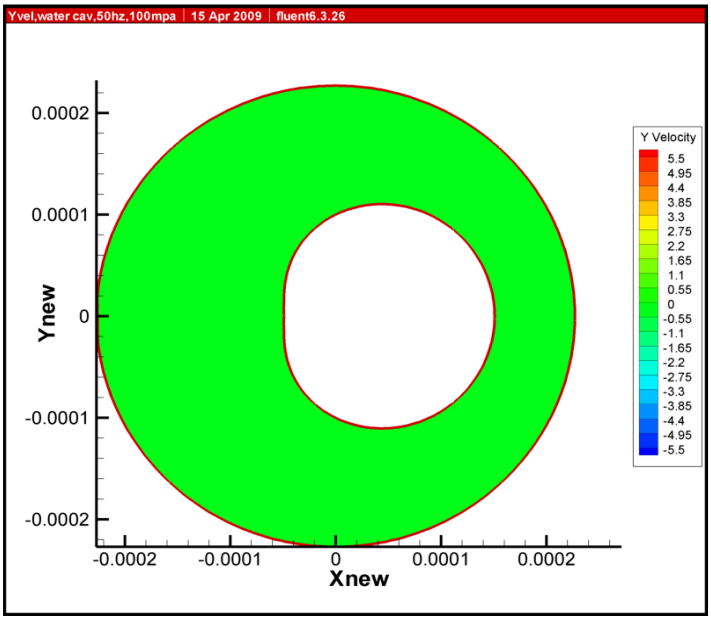

Figure 4.60 The y-velocity(m/s) field at a frequency of 50 Hz, an amplitude of 0.002 inches, and an operating pressure of 100 MPa

The Figure 4.61 shows the animation of y-velocity for the single phase flow cases at a journal frequency of 100 Hz. For the multiphase flow cases, the Figure 4.62 shows the animation of y-velocity at the journal frequency of 100 Hz and the operating pressure of 0.001 MPa. The y-velocity is almost constant and close to zero. The Figures 4.63 through 4.65 animate the y-velocity for operating pressures of 10, 50, 100 MPa. The y-velocity distribution for the operating pressures of 10, 50, and 100 MPa is almost the same as that of single phase flow case.

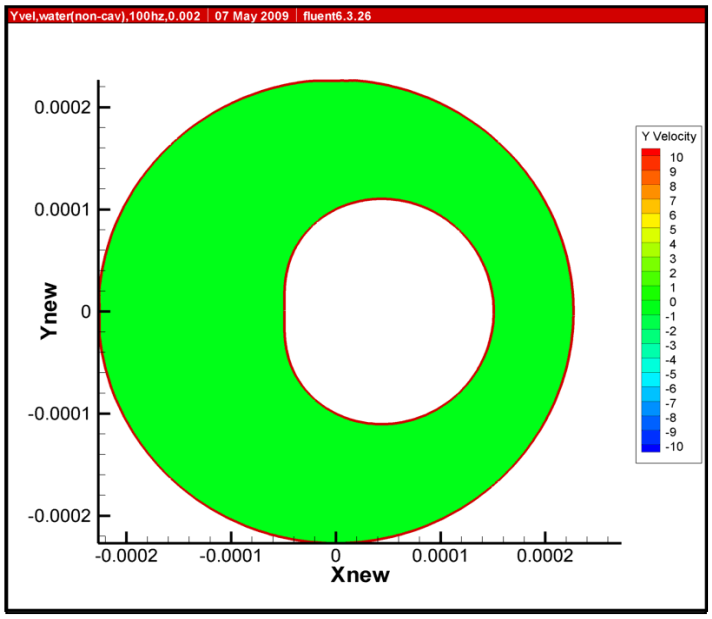

Figure 4.61 The y-velocity(m/s) field at a frequency of 100 Hz and an amplitude of 0.002 inches (Single phase flow)

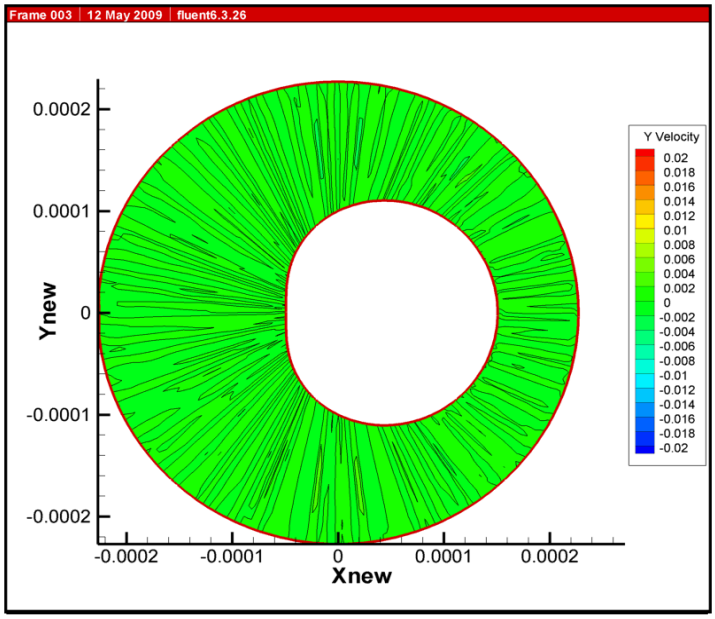

Figure 4.62 The y-velocity(m/s) field at a frequency of 100 Hz, an amplitude of 0.002 inches, and an operating pressure of 0.001 MPa

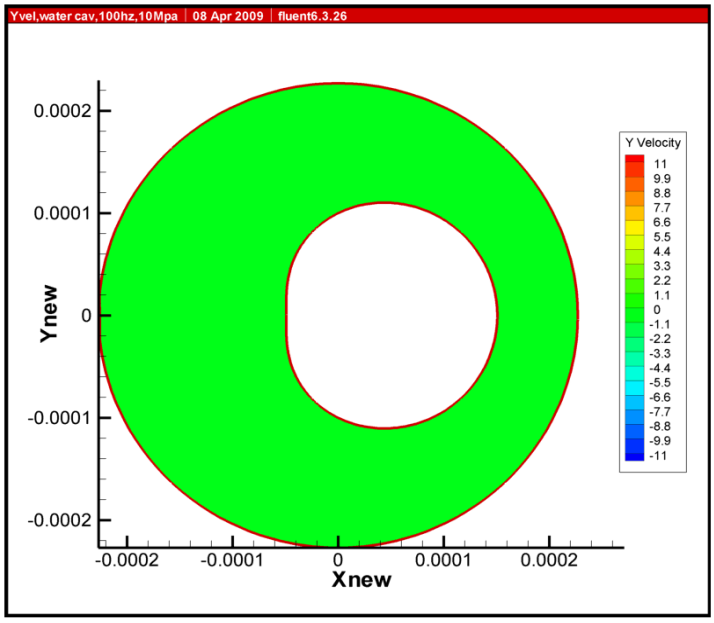

Figure 4.63 The y-velocity(m/s) field at a frequency of 100 Hz, an amplitude of 0.002 inches, and an operating pressure of 10 MPa

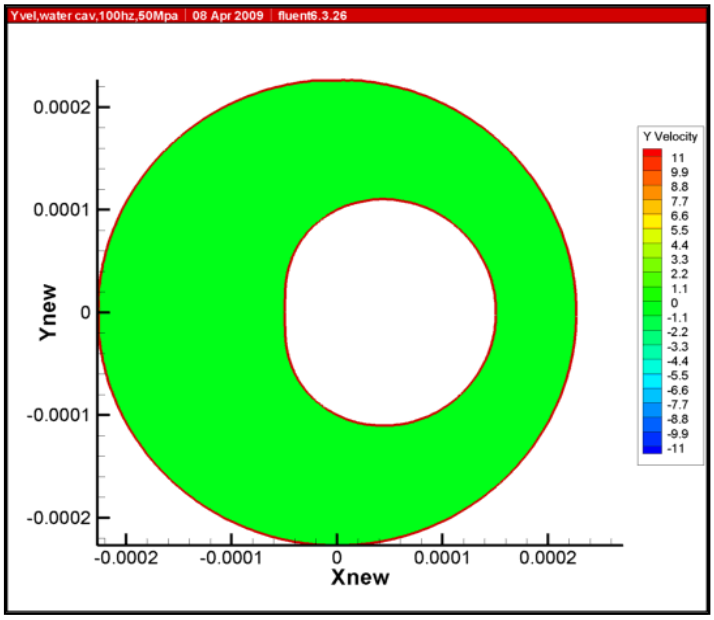

Figure 4.64 The y-velocity(m/s) field at a frequency of 100 Hz, an amplitude of 0.002 inches, and an operating pressure of 50 MPa

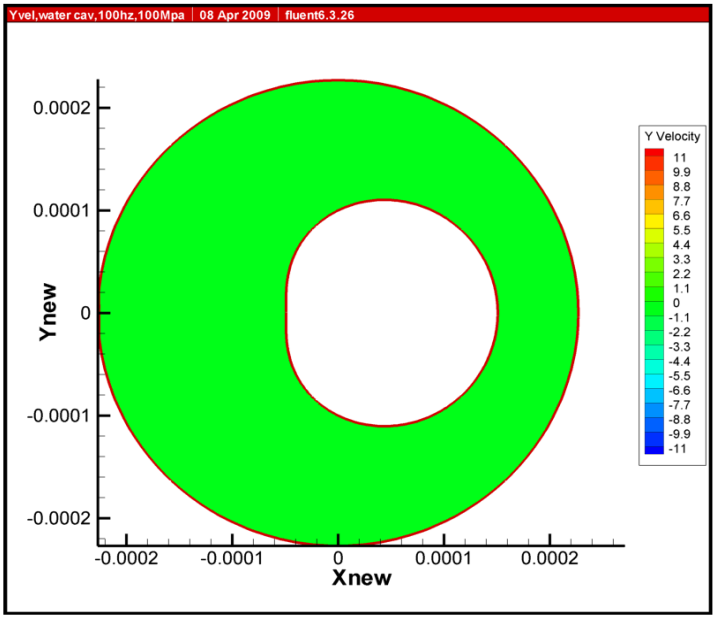

Figure 4.65 The y-velocity(m/s) field at a frequency of 100 Hz, an amplitude of 0.002 inches, and an operating pressure of 100 MPa

4.5 The Volume Fraction of the Vapor

For the volume fraction of the vapor study, the comparison between journal frequencies, i.e. 10, 50, and 100 Hz., the journal amplitude of 0.002 inches, and the operating pressures of 0.001, 0.01, 0.05, 0.1, 0.5, 1, 10, 50, and 100 MPa are taken into account.

The Figure 4.66 shows the volume fraction of the vapor for the journal frequency of 10 Hz and the operating pressure of 0.001 MPa. The squeeze film zone is totally full with vapor because the operating pressure of the system is less than fluid vapor pressure. For the operating pressure of 0.01 MPa in Figure 4.67, the distribution of the volume fraction as the journal moves forward to the positive degree from the start consists of gradually increasing of the volume fraction from upstream to downstream and reaches

the maximum value downstream at the position approaching to 90 degrees. The volume fraction of vapor suddenly falls to almost zero at 90 degrees. From 145 to 180 degrees, the distribution consists of gradually decreasing of the volume fraction from upstream to downstream. The distribution of the volume fraction for the journal position from 180 to 360 is almost identical to that from 0 to 180 but is a mirror image.

The animation of the pressure field for the journal amplitude of 0.002 inches and the frequency of 10 Hz at different operating pressures of 0.05, 0.1, 0.5, 1, 10, 50, and 100 MPa are depicted in the Figures 4.68 through 4.74. As the journal moves forward to the positive degrees from the start, the distribution consists of gradually increasing of the volume fraction from upstream to downstream and reaches the maximum value downstream at the position approaching to 90 degrees. The volume fraction of vapor suddenly falls to almost zero at 90 degrees and remain almost the same pattern until 180 degrees. The distribution of the volume fraction for the journal position from 180 to 360 is almost identical to that from 0 to 180 but is a mirror image. The rapid motion of the gaseous phase around the circumference is in agreement with the sudden velocity and pressure changes.

From 0.5 Mpa and above the gas volume fraction increases in the wake of cylinder until the cylinder has pass the half way mark. Then the gas volume fraction decreases.

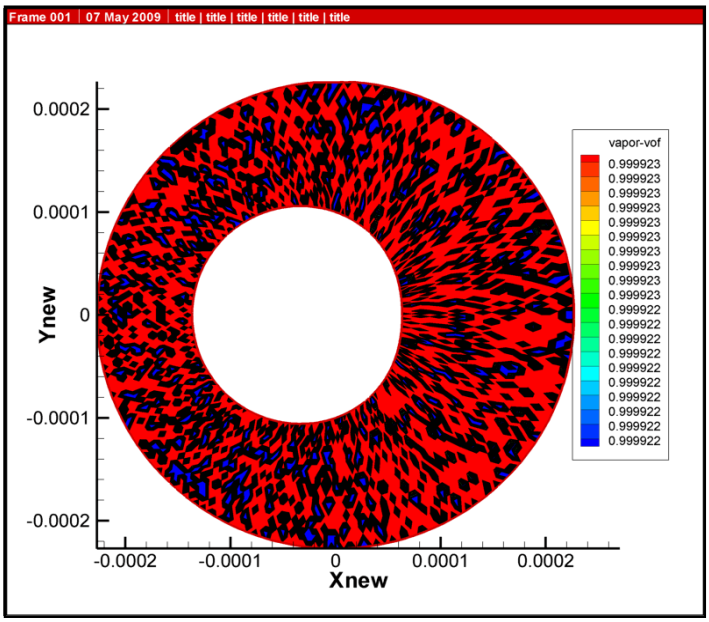

Figure 4.66 The volume fraction of the vapor at a frequency of 10 Hz, an amplitude of 0.002 inches, and operating pressure of 0.001 MPa

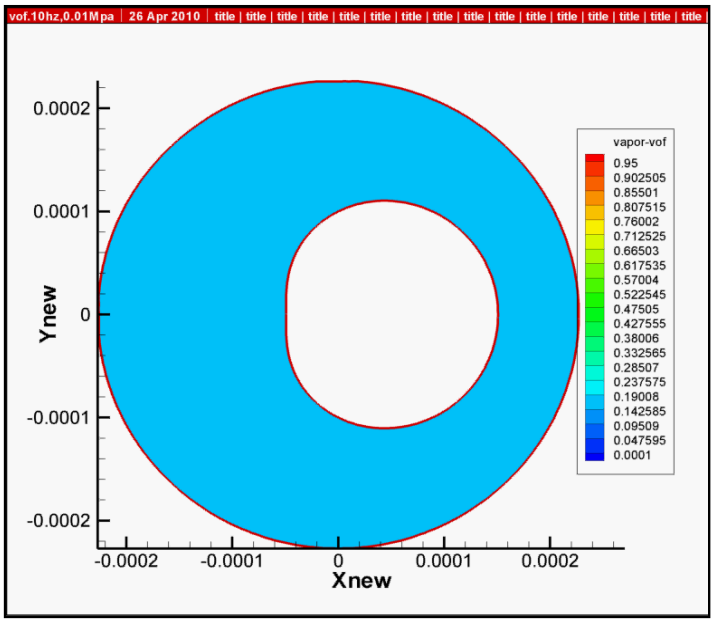

Figure 4.67 The volume fraction of the vapor at a frequency of 10 Hz, an amplitude of 0.002 inches, and operating pressure of 0.01 MPa

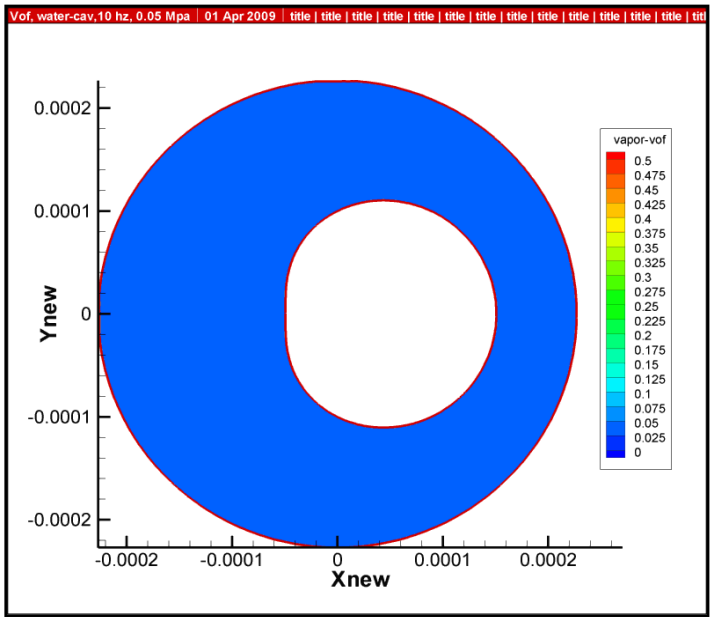

Figure 4.68 The volume fraction of the vapor at a frequency of 10 Hz, an amplitude of 0.002 inches, and operating pressure of 0.05 MPa

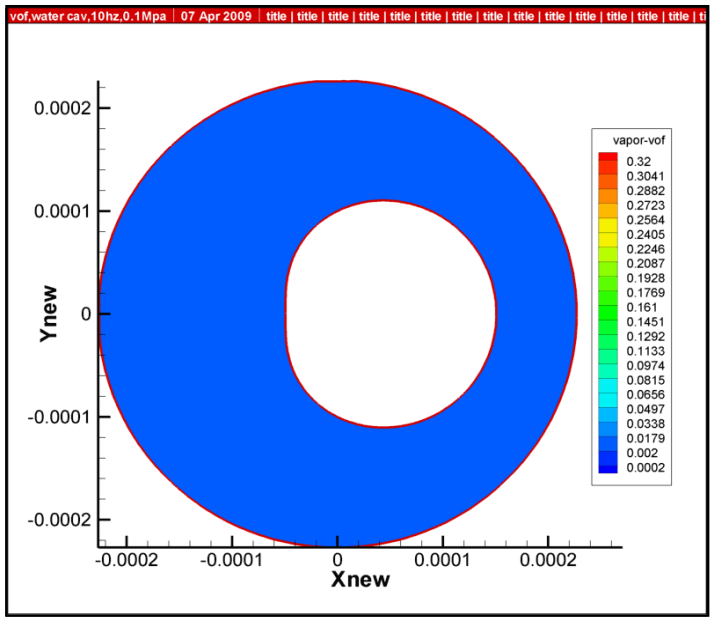

Figure 4.69 The volume fraction of the vapor at a frequency of 10 Hz, an amplitude of 0.002 inches, and operating pressure of 0.1 MPa

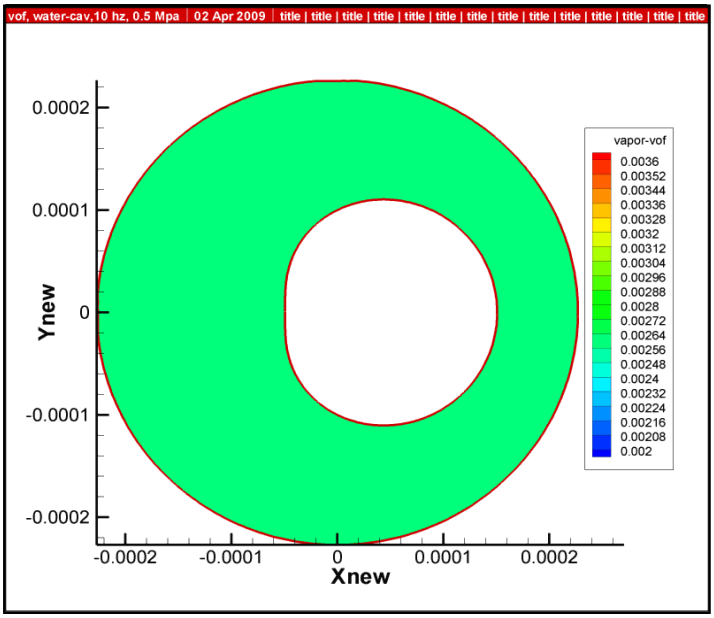

Figure 4.70 The volume fraction of the vapor at a frequency of 10 Hz, an amplitude of 0.002 inches, and an operating pressure of 0.5 MPa

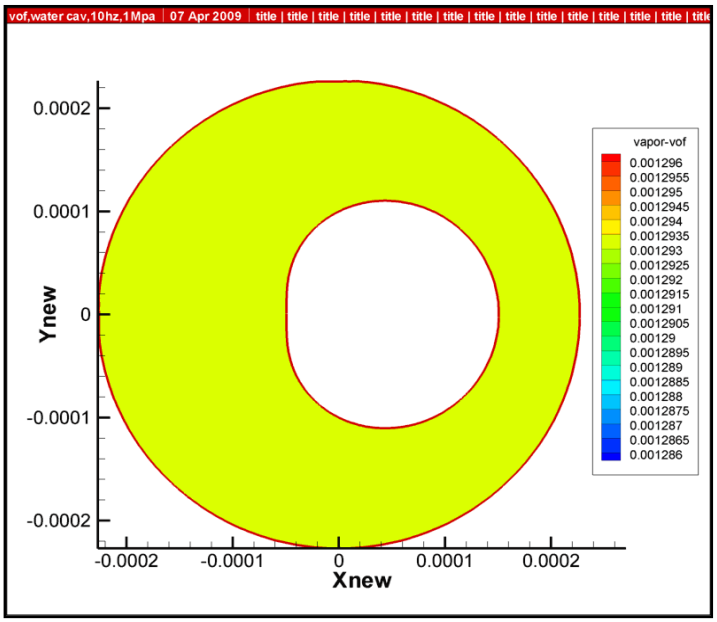

Figure 4.71 The volume fraction of the vapor at a frequency of 10 Hz, an amplitude of 0.002 inches, and operating pressure of 1 MPa

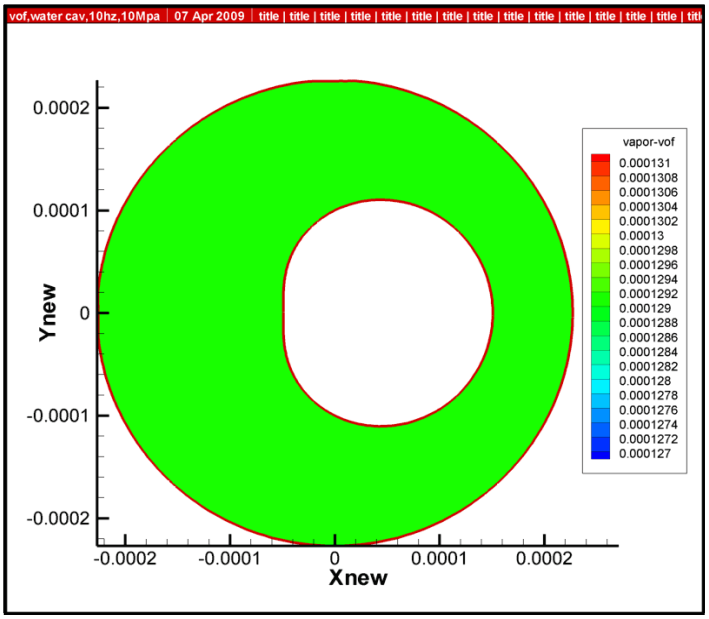

Figure 4.72 The volume fraction of the vapor at a frequency of 10 Hz, an amplitude of 0.002 inches, and operating pressure of 10 MPa

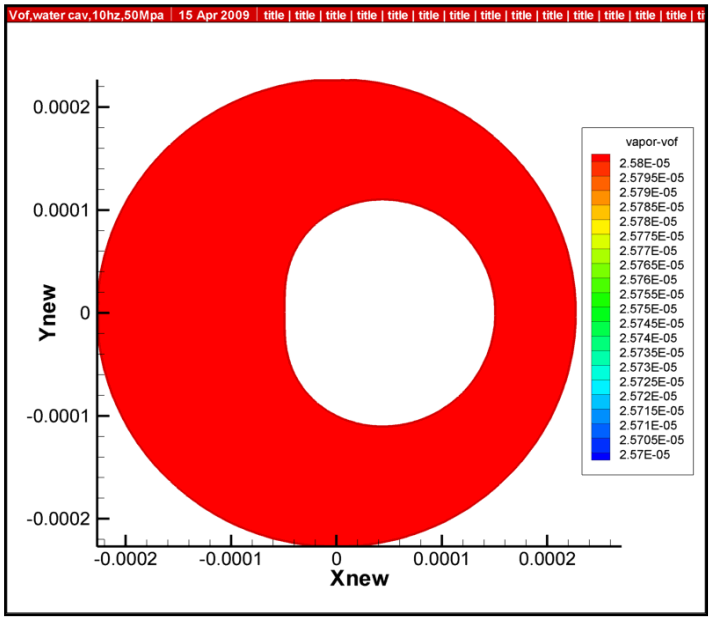

Figure 4.73 The volume fraction of the vapor at a frequency of 10 Hz, an amplitude of 0.002 inches, and operating pressure of 50 MPa

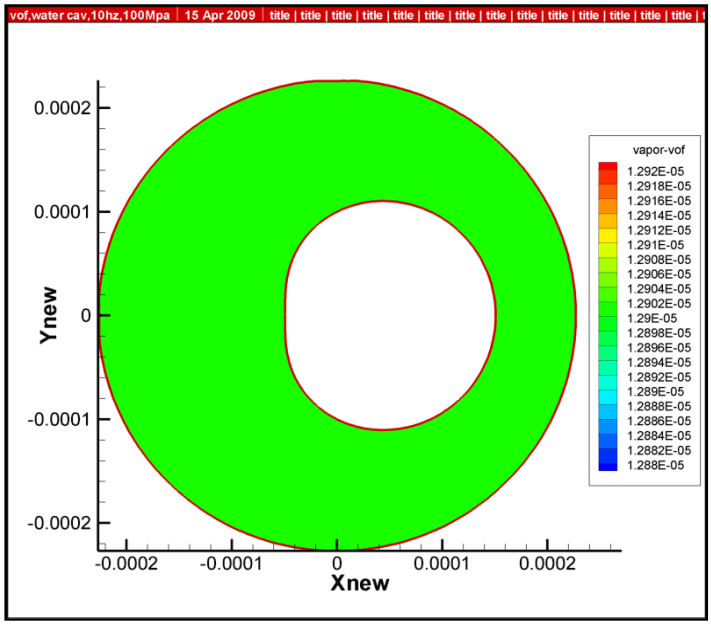

Figure 4.74 The volume fraction of the vapor at a frequency of 10 Hz, an amplitude of 0.002 inches, and operating pressure of 100 MPa

The Figure 4.75 shows the volume fraction of the vapor for the journal frequency of 50 Hz and the operating pressure of 0.001 Mpa. The squeeze film zone is totally full with vapor because the operating pressure of the system is less than fluid vapor pressure. The animation of the pressure field for the journal amplitude of 0.002 inches and the frequency of 50 Hz at different operating pressures of 1, 10, 50, and 100 MPa are depicted in the Figures 4.76 through 4.79. As the journal moves forward to the positive degrees from the start, the distribution consists of gradually increasing of the volume fraction from upstream to downstream and reaches the maximum value downstream at the position approaching to 90 degrees. The volume fraction of vapor suddenly falls to almost zero at 90 degrees and remain almost the same pattern until 180 degrees. The distribution of the volume fraction for the journal position from 180 to 360 is almost identical to that from 0 to 180 but is a mirror image. At the higher pressures the amount of gas present is minimal as would be implied by the pressure and velocity fields being essentially the same as a single phase fluid.

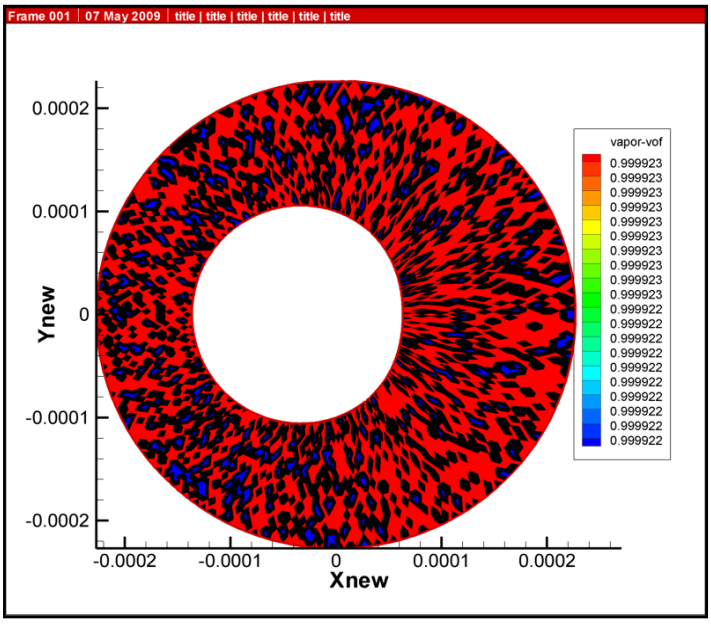

Figure 4.75 The volume fraction of the vapor at a frequency of 50 Hz, an amplitude of 0.002 inches, and operating pressure of 0.001 MPa

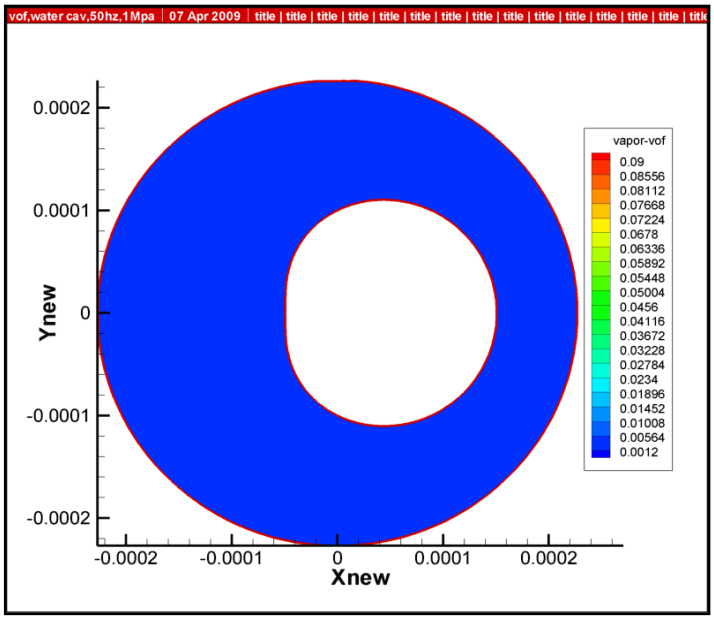
vof,water cav,50hz,1Mpa | 07 Apr 2009 | title | title | title | title | title | title

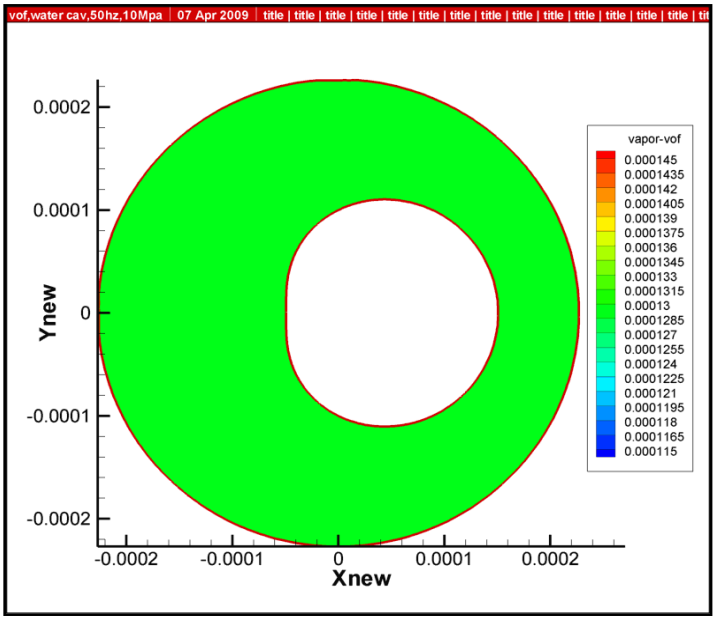

Figure 4.77 The volume fraction of the vapor at a frequency of 50 Hz, an amplitude of 0.002 inches, and operating pressure of 10 MPa

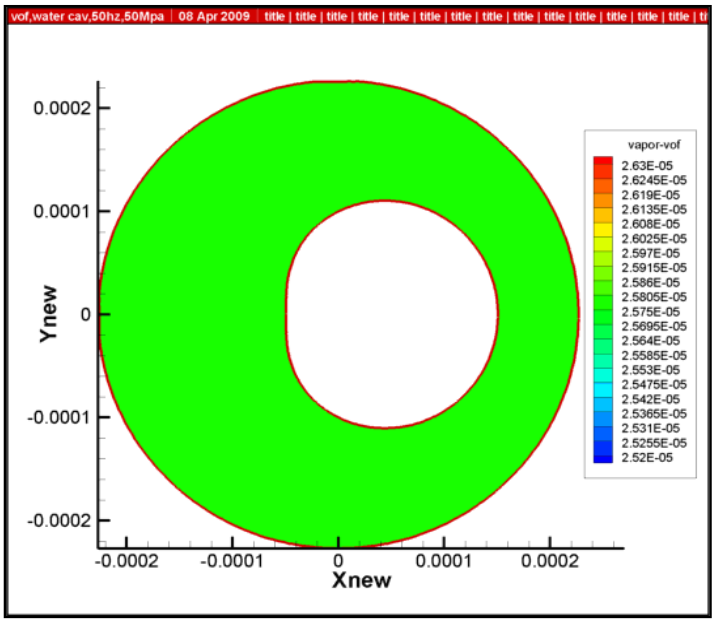

Figure 4.78 The volume fraction of the vapor at a frequency of 50 Hz, an amplitude of 0.002 inches, and operating pressure of 50 MPa

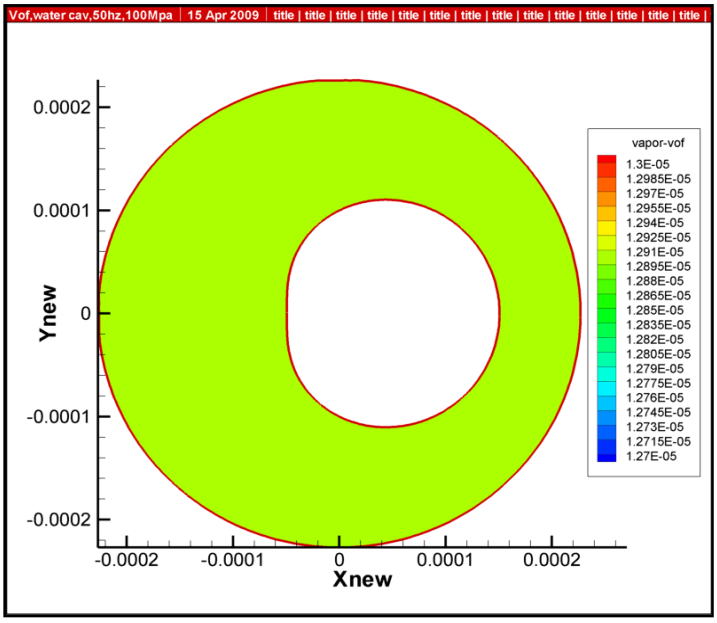

Figure 4.79 The volume fraction of the vapor at a frequency of 50 Hz, an amplitude of 0.002 inches, and operating pressure of 100 MPa

The Figure 4.80 shows the volume fraction of the vapor for the journal frequency of 100 Hz and the operating pressure of 0.001 Mpa. The squeeze film zone is totally full with vapor because the operating pressure of the system is less than fluid vapor pressure. The animation of the pressure field for the journal amplitude of 0.002 inches and the frequency of 100 Hz at different operating pressures of 10, 50, and 100 Mpa are depicted in the Figures 4.81 through 4.83. As the journal moves forward to the positive degrees from the start, the distribution consists of gradually increasing of the volume fraction from upstream to downstream and reaches the maximum value downstream at the position approaching to 90 degrees. The volume fraction of vapor suddenly falls to almost zero at 90 degrees and remain almost the same pattern until 180 degrees. The distribution of the volume fraction for the journal position from 180 to 360 is almost identical to that from 0 to 180 but is a mirror image.

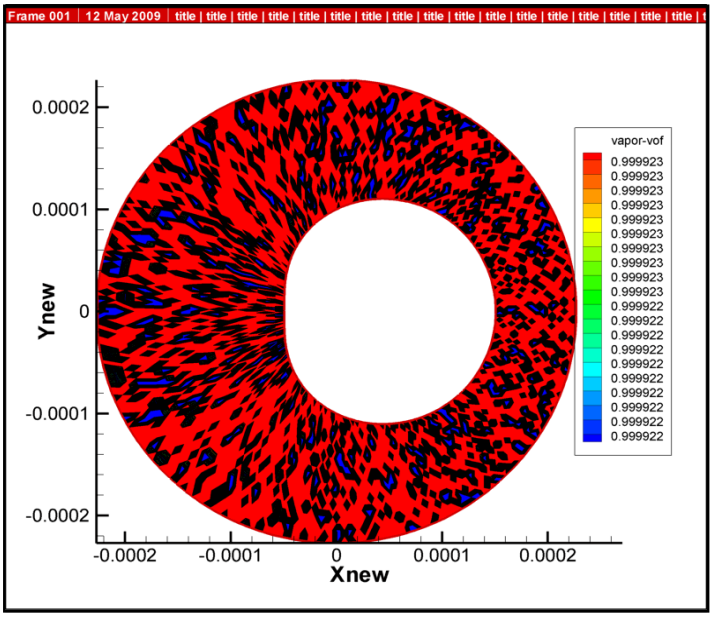

Figure 4.80 The volume fraction of the vapor at a frequency of 100 Hz, an amplitude of 0.002 inches, and operating pressure of 0.001 MPa

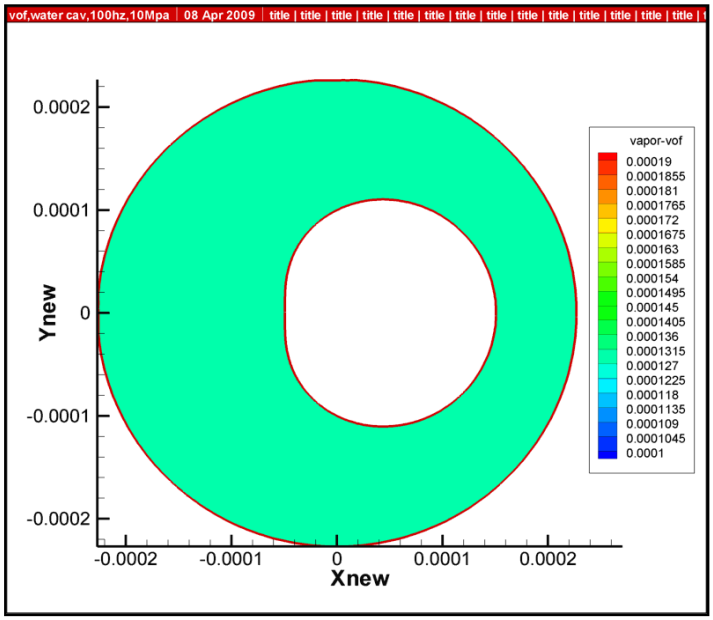

Figure 4.81 The volume fraction of the vapor at a frequency of 100 Hz, an amplitude of 0.002 inches, and operating pressure of 10 MPa

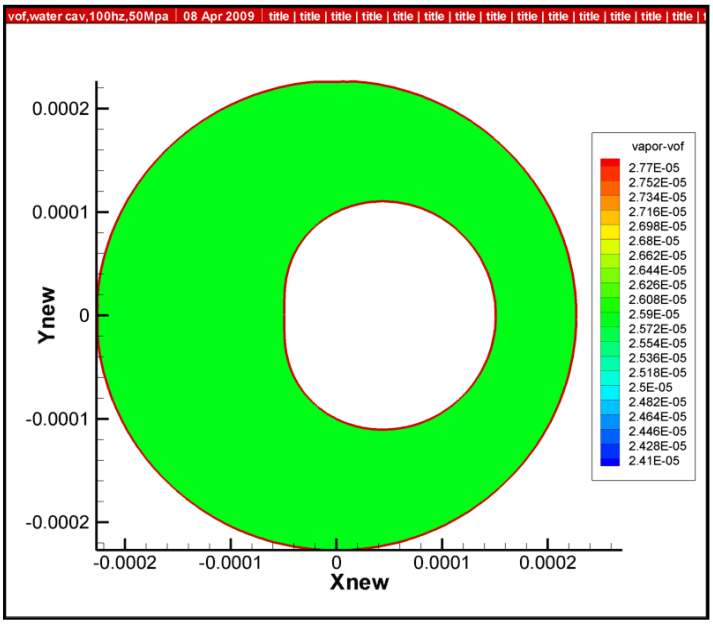

Figure 4.82 The volume fraction of the vapor at a frequency of 100 Hz, an amplitude of 0.002 inches, and an operating pressure of 50 MPa

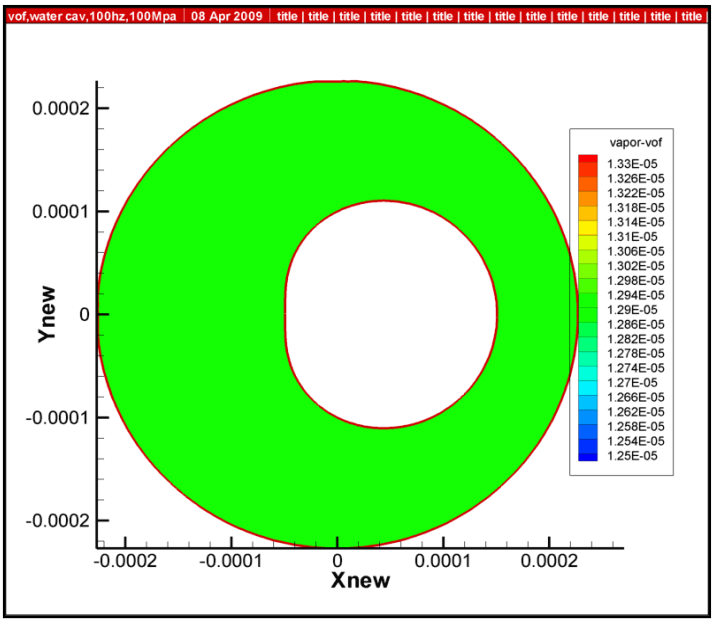

Figure 4.83 The volume fraction of the vapor at a frequency of 100 Hz, an amplitude of 0.002 inches, and an operating pressure of 100 MPa

Table 4.3 shows the maximum volume fraction of vapor. According to the table, the volume fraction of vapor depends on the operating pressure and vapor pressure. If the operating pressure is less than the vapor pressure, SFD is totally full with vapor. If the operating pressure is more than the vapor pressure, there is the volume fraction of vapor depending on how the operating pressure is close to the vapor pressure. For the same operating pressure, the volume fraction of vapor varies directly to the frequency.

Table 4.3 The maximum volume fraction of vapor for multiphase flow cases

Operating pressure (MPa)	Maximum volume fraction of vapor		
	10 Hz	50 Hz	100 Hz
0.001	1	1	1
0.01	0.95	N/A	N/A
0.05	0.53	N/A	N/A
0.1	0.33	N/A	N/A
0.5	0.0037	N/A	N/A
1	0.0015	0.09	N/A
10	0.00013	0.00015	0.0002
50	0.000026	0.000026	0.000028
100	0.000013	0.000013	0.000013

4.6 The Drag Forces

The drag force, F_d, exerting on the journal was a significant concern in this study. The Figure 4.84 depicts the drag force versus the angles for single phase whereas the Figures 4.85, 4.87, and 4.88 depict the drag forces versus the angles for the journal frequency of 10, 50, and 100 Hz, respectively. Note that the Figure 4.86 depicts the drag forces for 10 Hz at specific operating pressures which the cavitation effect is suppressed. Generally, the force is sinusoidal for all cases. As the journal moves forward to the positive degrees, the drag forces gradually increase and reach the maximum value

approximately at 90 degree. As the journal moves further, the drag forces decrease and reach zero at approximately 180 degrees. For the journal positions between 180 and 360, the forces are negative but have similar pattern to that of the positions between 0 and 180. However, there are large fluctuations at the angles of 90 and 270 degrees for certain multiphase flow cases. For certain operating pressures, i.e, 0.01, 0.05,and 0.1 MPa for 10 Hz. and 1 Mpa for 50 Hz, the force changes drastically as the journal moves through 90 and 270 degrees. These are the journal positions where minimum pressures occur. For these operating pressure, the water cavitates, changes phase, and the resulting high frequency pressure and velocity changes produce spikes in the force-time relationship. For the others operating pressure, the drag force is almost identical to that of single phase cases. At the higher operating pressures, no cavitation occurs and the force generate is identical for all cases as were the pressure and velocity fields. In addition, drag force is almost zero for the operating pressure of 0.001 MPa which is below the vapor pressure, or 0.00354 MPa.

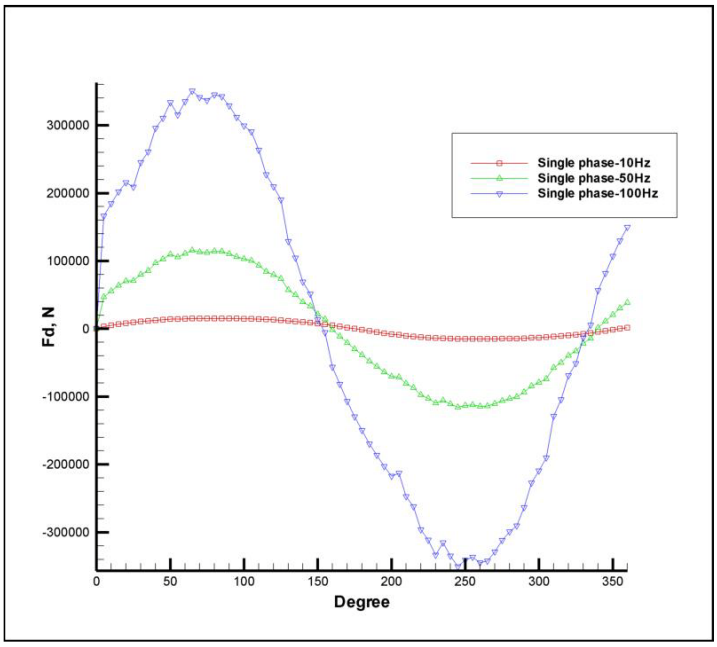

Figure 4.84 The drag forces(N/m) for the single phase flow

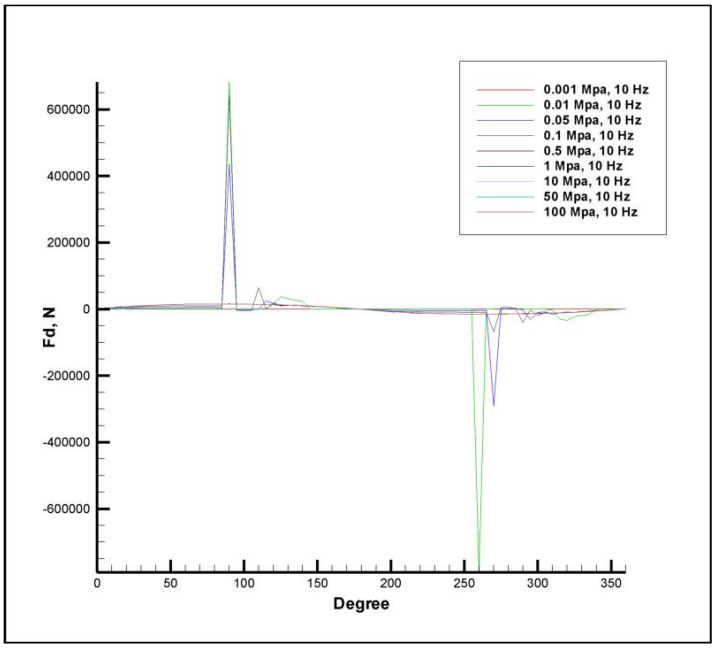

Figure 4.85 The drag forces(N/m) for the multiphase flow at the frequency of 10 Hz (all operating pressure cases)

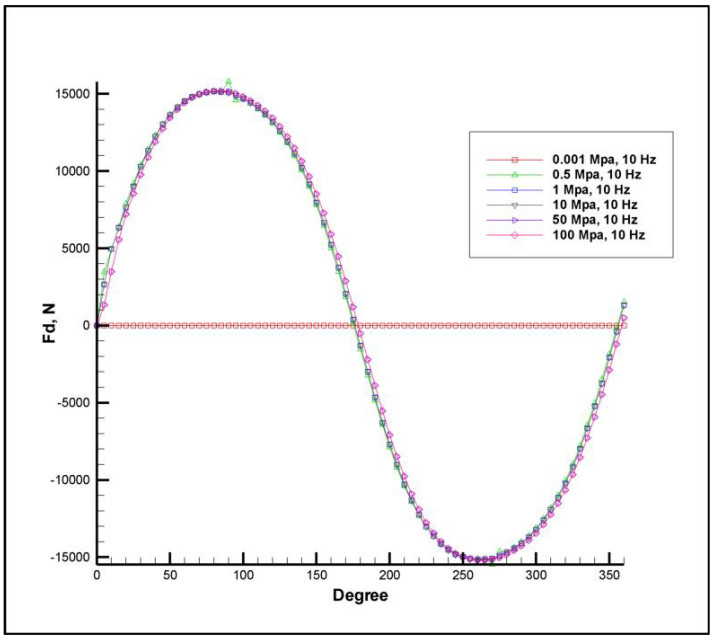

Figure 4.86 The drag forces(N/m) for the multiphase flow at the frequency of 10 Hz (certain operating pressure cases)

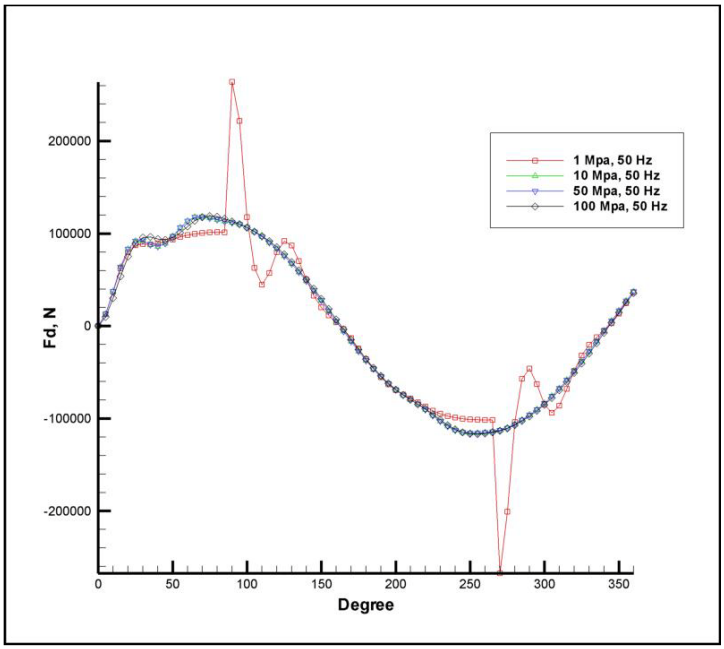

Figure 4.87 The drag forces(N/m) for the multiphase flow at the frequency of 50 Hz

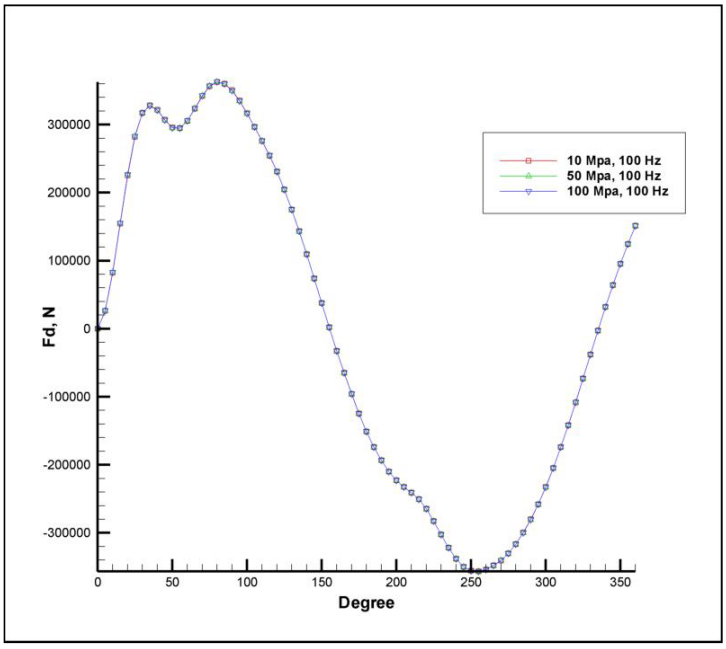

Figure 4.88 The drag forces(N/m) for the multiphase flow at the frequency of 100 Hz

Table 4.4 shows the maximum forces for single phase flow cases whereas Tables 4.5 through 4.7 show the maximum forces for multiphase flow cases with journal frequencies of 10, 50, and 100 Hz, respectively. The drag forces vary directly to the frequency. Generally, the forces are almost identical for the same frequency. However, for certain operating pressures, i.e, 0.01, 0.05,and 0.1 MPa for 10 Hz and 1 MPa for 50 Hz, the drag forces are greatly higher than the normal value due to the cavitation. In addition, the drag force is almost zero for the operating pressure of 0.001 Mpa which is below the vapor pressure, or 0.00354 MPa.

Table 4.4 The maximum forces for single phase flow cases

Frequency, Hz	Maximum positive force, N/m	Maximum negative force, N/m
10	15,018.77	-15,018.82
50	115,481.80	-115,584.96
100	345,056.60	-345,078.29

Table 4.5 The maximum forces for multiphase flow cases and the frequency of 10 Hz

Operating pressure, MPa	Maximum positive force, N/m	Maximum negative force, N/m
0.001	0.00	0.00
0.01	682,708.55	-791,200.80
0.05	436,821.54	-291,253.00
0.1	642,738.88	-67,664.39
0.5	15,786.30	-15,469.43
1	15,104.34	-15,092.47
10	15,072.90	-15,072.95
50	15,134.73	-15,134.60
100	15,134.95	-15,134.82

Table 4.6 The maximum forces for multiphase flow cases and the frequency of 50 Hz

Operating pressure, MPa	Maximum positive force, N	Maximum negative force, N
0.001	0.00	0.00
1	263,905.46	-267,374.02
10	118,140.30	-115,804.17
50	118,150.34	-115,798.33
100	118,991.97	-116,889.76

Table 4.7 The maximum forces for multiphase flow cases and the frequency of 100 Hz

Operating pressure, MPa	Maximum positive force, N	Maximum negative force, N
0.001	0.00	0.00
10	362,751.84	-356,706.08
50	362,965.45	-356,740.11
100	362,970.71	-356,745.12

CHAPTER V

SUMMARY AND CONCLUSION

A numerical study was conducted to investigate flow characteristics resulting from journal motion in the squeeze film damper. The two dimension SFD was modeled by using the Fluent software package. The study was divided into two different models including single phase flow model and multiphase flow model.

For the single phase model study, the 2-D SFD was modeled with three different journal amplitudes, i.e. 0.002, 0.001, and 0.0005 inches, and three different journal frequencies, i.e. 10, 50, and 200 Hz. The k-ε model in FLUENT was used to perform to numerical predictions of pressure, velocity and force. Based on numerical predictions, the results for single phase flow may be summarized as follows:

1. The distributions of pressure and velocity have the same pattern for all cases. The maximum pressures and velocities vary directly with the journal amplitude and frequency.
2. The curves of drag force versus angle for call case are sinusoidal. The maximum forces vary directly with the journal amplitude and frequency.

For the multiphase model study, the 2-D SFD was modeled with the journal amplitudes of 0.002 and three different journal frequencies, i.e. 10, 50, and 100 Hz. The operating pressures, i.e. 0.001, 0.01, 0.05, 0.1, 0.5, 1, 10, 50, 100 MPa, were included for cavitation study. Unfortunately, for certain operating pressures, it was not possible to simulate the rapid cavitation and its resulting pressure and velocity variations. The k-ε model integrated with the mixture model in FLUENT was used to obtain numerical predictions of pressure, velocity, volume fraction of vapor and force. In addition, the single phase flow case was also modeled for comparison purpose. Based on numerical predictions, the results may be summarized as follows:

1 The cavitation phenomenon renders the distribution of pressure and velocity different from the single phase flow case, especially the cases for which operating pressures are close to the vapor pressure. The squeeze film zone is filled with vapor for operating pressures below vapor pressure. The increase in the operating pressure away from the vapor pressure reduces the volume fraction of vapor in the squeeze film zone and consequently lessens the effect of cavitation. For the operating pressures which are high enough, i.e. 0.5 MPa for 10 Hz. frequency case and 10 MPa for 50 and 100 Hz frequency case, the pressure and velocity distributions are identical to that for the single phase case as these high operating pressures eliminate cavitation.

2 As a result of the deviation of the pressure from the single-phase-flow pressure mentioned above, the force for the operating pressure close to the vapor pressure is relatively high compared to that for the other cases. From this evidence, the cavitation obviously affects the force exerted on the system and its effect can be attenuated by increasing the operating pressure. The force is composed of a large spike in time as the cavitation occurs. The magnitudes can be large enough to cause considerable damage to the machine.

The results of this study show that the journal amplitude and frequency affect flow and consequently force in the SFD. The operating pressure shows a prominent role in reducing the effect of cavitation. More numerical investigations for multiphase flow study are needed in order to predict the proper operating pressure for the SFD to operate without experiencing the cavitation.

REFERENCES

[1] Zeidan, F., San Andrés, L., and Vance, J., 1996, "Design and Application of Squeeze Film Damper in Rotating Machinery," Proceeding of the 25th Turbomachinery Symposium, Turbomachinery Laboratory, Texas A&M University, pp. 169-188.

[2] Pietra, L.D., and Adiletta, G., 2002, "The Squeeze Film Damper over Four Decades of Investigations. Part I: Characteristics and Operating Features," The Shock and Vibration Digest, **34** (1), pp. 3-27.

[3] Pietra, L.D., and Adiletta, G., 2002, "The Squeeze Film Damper over Four Decades of Investigations. Part II: Rotor Dynamic Analyses with Rigid and Flexible Rotor," The Shock and Vibration Digest, **34** (2), pp. 97-126.

[4] Vance, J., 1988, *Rotor Dynamics of Turbomachinery*, John Wiley and Sons, New York.

[5] Diaz, S., and San Andrés, L., 2000, "Obit-Based Identification of Damping Coefficients on Off-centered Squeeze Film Dampers Including Support Flexibility," the International Gas Turbine & Aeroengine Congress & Exhibition, Munich, Germany, ASME Paper 2000-GT-0394.

[6] El-Shafei, A., and Eranki, R., 1994, "Dynamic Analysis of Squeeze Film Damper Supported Rotors Using Equivalent Linearization," Journal of Engineering for Gas Turbines and Power, **116** (3), pp. 682-691.

[7] Lubell, D., and San Andrés, L., 1998, “Imbalance Response of a Rotor Test Rotor Supported on Squeeze Film Dampers,” ASME Journal of Engineering for Gas Turbines and Power, **120** (2), pp. 397-404.

[8] De Santiago, O., and San Andrés, L., 2000, “Dynamic Response of a Rotor-Integral Squeeze Film Damper to Couple Imbalances,” the International Gas Turbine & Aeroengine Congress & Exhibition, Munich, Germany, ASME Paper 2000-GT-0388.

[9] De Santiago, O., and San Andrés, L., 1999, “Imbalance Response and Damping Force Coefficients of a Rotor Supported on End Sealed Integral Squeeze Film Dampers,” the International Gas Turbine & Aeroengine Congress & Exhibition, Indianapolis, Indiana, ASME Paper 99-GT-203.

[10] De Santiago, O., San Andrés, L., and Oliveras, J., 1999, “Imbalance Response of a Rotor Supported on Open-Ended, Integral Squeeze Film Damper,” ASME Journal of Gas Turbines and Power, **121** (4), pp. 718-724.

[11] Arauz, G., and San Andrés, L., 1997, “Experiment Force Responses of a Grooved Squeeze Film Damper,” Tribology International, **30** (1), pp. 77-86.

[12] Arauz, G., and San Andrés, L., 1996, “Experimental Study on the Effect of a Circumferential Feeding Groove on the Dynamic Force Response of a Sealed Squeeze Film Damper,” ASME Journal of Tribology, **118** (4), pp. 900-905.

[13] San Andrés, L., and Arauz, G., 1993, “Experimental Pressure and Film Forces in a Squeeze Film Damper,” ASME Journal of Tribology, **115**, pp. 134-140.

[14] Arauz, G., and San Andrés, L., 1994, “Effect of a Circumferential Feeding Groove

on the Force Response of a Short Squeeze Film Damper," ASME Journal of Tribology, **116** (2), pp. 369-377.

[15] San Andrés, L., 1992, "Analysis of Short Squeeze Film Dampers with a Central Groove," ASME Journal of Tribology, **114** (4), pp. 659-665.

[16] Diaz, S., and San Andrés, L., 1998, "Measurements of Pressure in a Squeeze Film Damper with Air/Oil bubbly Mixture," STLE Tribology Transactions, **41** (2), pp. 282-288.

[17] Diaz, S., and San Andrés, L., 1999, "Reduction of the Dynamic Load Capacity in a Squeeze Film Damper Operating with a Bubbly lubricant," ASME Journal of Gas Turbines and Power, **121** (2), pp. 703-709.

[18] San Andrés, L., and Diaz, S., 2003, "Flow Visualization and Forces from a Squeeze Film Damper with Natural Air Entrainment," ASME Journal of Tribology, **125** (2), pp. 325-333.

[19] Tao, L., Diaz, S., San Andrés, L., and Rajagopal, K.R., 2000, "Analysis of Squeeze Film Dampers Operating with Bubbly Lubricants," ASME Journal of Tribology, **122** (1) , pp. 205-210.

[20] Zeidan, F., and Vance, J., 1990, "Cavitation Regimes in Squeeze Film Dampers and their Effect on the Pressure Distribution," STLE Tribology Transactions, **33** (3), pp. 447-453.

[21] San Andrés, L., 1996, "Theoretical and Experimental Comparisons for Damping Coefficients of a Short Length Open-Ended Squeeze Film Damper," ASME Journal of Engineering for Gas Turbines and Power, **118** (4), pp. 810-815.

[22] Robinson, M., Arauz, G., and San Andrés, L., 1995, "A Test Rig for the Identification of Rotor Dynamic Coefficients Fluid Film Bearings," ASME Turbo Expo'95 Land, Sea, and Air Conference, Houston , ASME Paper 95-GT-431.

[23] San Andrés, L., and Vance, J., 1988, "Effect of Fluid Inertia on the Performance of Squeeze Film Damper Supported Rotor," ASME Journal of Engineering for Gas Turbines and Power, **110** (1), pp. 51-57.

[24] Chen, P., and Hahn, E., 1998, "Use of computational fluid dynamics in hydrodynamic lubrication," Proceedings of the Institute of Mechanical Engineers, **212**, part J.

[25] Xing, L., Braun, M.J., and Li, H., 2010, "Damping and Add Mass Coefficients for a Squeeze Film Damper Using the Full 3-D Navier-Stokes Equation," Tribology International, **43** (3), pp. 654-666.

[26] Xing, L., Braun, M.J., and Li, H., 2009, "A Three-Dimensional Navier-Stokes-Based Numerical model for Squeeze Film Dampers. Part 1--Effects of Gaseous Cavitation on Pressure Distribution and Damping Coefficients without Consideration of Inertia," STLE Tribology Transactions, **52** (5), pp. 680-694

[27] Xing, L., Braun, M.J., and Li, H., 2009, "A Three-Dimensional Navier-Stokes-Based Numerical model for Squeeze Film Dampers. Part 2--Effects of Gaseous Cavitation on the Behavior of the Squeeze Film Damper," STLE Tribology Transactions, **52** (5), pp. 695-705.

[28] FLUENT 6.3 Documentation, 2006, "FLUENT 6.3 User's Guide," ANSYS, Inc, Canonsburg, Pennsylvania.

APPENDIX A

Pressure solution from Reynolds equation and Fluid inertia Effect

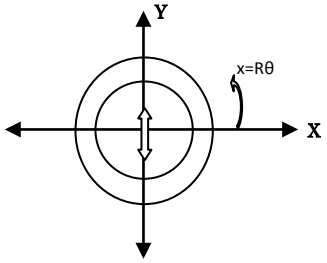

Dynamic film thickness, *h*, is defined by:

$$h = c - e_x \cos\theta - e_y \sin\theta$$

Let $e_x = 0$, $e_y = e\sin(\omega t)$, $\varepsilon = e/c$, $\tau = \omega t$

$$e_y^{\bullet} = e\omega\cos(\omega t)$$

$$\frac{\partial h}{\partial t} = -e_y^{\bullet}\sin\theta = -e\omega\cos(\omega t)\sin\theta\,, \quad \frac{\partial h}{\partial \theta} = -e_y\cos\theta = -e\sin(\omega t)\cos\theta$$

Reynolds Equation:

$$\frac{1}{R^2}\frac{\partial}{\partial\theta}\left(\frac{h^3}{12\mu}\frac{\partial P}{\partial\theta}\right) = \frac{\partial h}{\partial t}$$

$$\frac{\partial P}{\partial\theta} = \frac{12\mu R^2}{h^3}\int\frac{\partial h}{\partial t}d\theta = \frac{12\mu R^2}{h^3}\int\left[-e_y^{\bullet}\sin\theta\right]d\theta$$

$$\frac{\partial P}{\partial\theta} = \frac{12\mu R^2}{h^3}e_y^{\bullet}\cos\theta$$

$$P = 12\mu R^2\int\frac{e_y^{\bullet}\cos\theta}{h^3}d\theta = \frac{12\mu R^2 e\omega}{c^3}\int\frac{\cos(\omega t)\cos\theta}{\left[1-\varepsilon\sin(\omega t)\sin\theta\right]^3}d\theta$$

$$P = \frac{12\mu R^2}{c^2}\varepsilon\cos(\omega t)\int \frac{\cos\theta d\theta}{\left[1-\varepsilon\sin(\tau)\sin\theta\right]^3} \quad \text{let } C_p = 12\mu\omega\left(\frac{R}{c}\right)^2$$

$$P(\tau,\theta) = \varepsilon\cos(\tau)\int_0^{\theta} \frac{\cos\theta d\theta}{\left[1-\varepsilon\sin(\tau)\sin\theta\right]^3} * C_p$$

Fluid inertia Effect:

Governing Equation;

$$\frac{\partial}{\partial x}(hV_x) + \frac{\partial h}{\partial t} = 0 \tag{1}$$

$$-h\frac{\partial P}{\partial x} + \Delta\tau_{xy} = \rho\left[\frac{\partial}{\partial t}(V_x h) + \frac{\partial I_{xx}}{\partial x}\right] \tag{2}$$

where $I_{xx} = \int_0^h \bar{u}^2 dy, V_x = \frac{1}{h}\int_0^h \bar{u} dy$, Let $\Delta\tau_{xy} = h\frac{\partial P}{\partial x} = -\frac{12\mu V_x}{h}$, $I_{xx} = 1.2V_x^2 h$

From (1),

$$\frac{1}{R}\frac{\partial}{\partial\theta}(hV_x) + \frac{\partial h}{\partial t} = 0$$

$$V_x = -\frac{R}{h}\int\frac{\partial h}{\partial t}d\theta = -\frac{R}{h}\int -\left(e\omega\cos(\omega t)\sin\theta d\theta\right) = -\frac{R}{h}e\omega\cos(\omega t)\sin\theta d\theta$$

From (2),

$$-\frac{h}{R}\frac{\partial P}{\partial\theta} - \frac{12\mu V_x}{h} = \rho\left[\frac{\partial}{\partial t}(V_x h) + \frac{1.2\partial}{R\partial\theta}\left(V_x^2 h\right)\right]$$

$$-\frac{\partial P}{\partial\theta} = \frac{12\mu R V_x}{h^2} + \rho\frac{R}{h}\left[h\frac{\partial V_x}{\partial t} + V_x\frac{\partial h}{\partial t} + \frac{1.2}{R}\left(h\frac{\partial V_x^2}{\partial\theta} + V_x^2\frac{\partial h}{\partial\theta}\right)\right]$$

$$P(\tau,\theta) = -\int_0^{\theta}\left[\frac{12\mu R V_x}{h^2} + \rho\frac{R}{h}\left(h\frac{\partial V_x}{\partial t} + V_x\frac{\partial h}{\partial t} + \frac{1.2}{R}\left(h\frac{\partial V_x^2}{\partial\theta} + V_x^2\frac{\partial h}{\partial\theta}\right)\right)\right]d\theta$$

$$P(\tau,\theta)=\int_0^{\theta}\frac{12\mu R^2 e\omega\cos\tau\cos\theta}{(c-e\sin\tau\cos\theta)^3}d\theta-\int_0^{\theta}\frac{\rho R^2 e\omega^2\sin\tau\cos\theta}{(c-e\sin\tau\cos\theta)}d\theta-\int_0^{\theta}\frac{\rho(R.e\omega\cos\tau)^2\sin\theta\cos\theta}{(c-e\sin\tau\sin\theta)^2}d\theta$$

$$-\int_0^{\theta}\frac{2.4\rho(R.e\omega\cos\tau)^2\sin\theta\cos\theta}{(c-e\sin\tau\sin\theta)^2}d\theta+\int_0^{\theta}\frac{1.2\rho R^2 e^3\omega^2\cos^2\tau\sin\tau\cos^3\theta}{(c-e\sin\tau\sin\theta)^3}d\theta$$

VITA

Name:	Terdsak Neadkratoke
Address:	Department of Mechanical Engineering c/o Dr. Gerald Morrison Texas A&M University College Station TX 77843-3123
Email Address:	terdsakx@yahoo.com
Education:	B.Eng., Kasetsart University, Bangkok, Thailand, 1998 M.S., Mechanical Engineering, Texas A&M University, 2011